HAL
open science

Nano-optomechanics of suspended SiC nanowires down to cryogenic temperatures : exploration of optical and photothermal responses

Clement Gouriou

To cite this version:

Clement Gouriou. Nano-optomechanics of suspended SiC nanowires down to cryogenic temperatures : exploration of optical and photothermal responses. Physics [physics]. Université Grenoble Alpes [2020-..], 2023. English. NNT : 2023GRALY053 . tel-04444724

HAL Id: tel-04444724

https://theses.hal.science/tel-04444724v1

Submitted on 7 Feb 2024

HAL is a multi-disciplinary open access archive for the deposit and dissemination of scientific research documents, whether they are published or not. The documents may come from teaching and research institutions in France or abroad, or from public or private research centers.

L'archive ouverte pluridisciplinaire **HAL**, est destinée au dépôt et à la diffusion de documents scientifiques de niveau recherche, publiés ou non, émanant des établissements d'enseignement et de recherche français ou étrangers, des laboratoires publics ou privés.

THÈSE

Pour obtenir le grade de

DOCTEUR DE L'UNIVERSITÉ GRENOBLE ALPES

École doctorale : PHYS - Physique
Spécialité : Nanophysique
Unité de recherche : Institut Néel

Nano-optomécanique des nanofils suspendus à basse température

Nano-optomechanics of suspended SiC nanowires down to cryogenic temperatures : exploration of optical and photothermal responses.

Présentée par :

Clément GOURIOU

Direction de thèse :

Eddy COLLIN DIRECTEUR DE RECHERCHE, CNRS DELEGATION ALPES	Directeur de thèse
Olivier ARCIZET CHARGE DE RECHERCHE HDR, CNRS DELEGATION ALPES	Co-directeur de thèse

Rapporteurs :

LUDOVIC BELLON
DIRECTEUR DE RECHERCHE, CNRS DELEGATION RHONE AUVERGNE
ALESSANDRO SIRIA
DIRECTEUR DE RECHERCHE, CNRS DELEGATION PARIS CENTRE

Thèse soutenue publiquement le **6 octobre 2023**, devant le jury composé de :

LUDOVIC BELLON DIRECTEUR DE RECHERCHE, CNRS DELEGATION RHONE AUVERGNE	Rapporteur
ALESSANDRO SIRIA DIRECTEUR DE RECHERCHE, CNRS DELEGATION PARIS CENTRE	Rapporteur
ILARIA ZARDO ASSOCIATE PROFESSOR, UNIVERSITÄT BASEL	Examinatrice
OLIVIER BOURGEOIS DIRECTEUR DE RECHERCHE, CNRS DELEGATION ALPES	Examinateur
TRISTAN BRIANT MAITRE DE CONFERENCES, SORBONNE UNIVERSITE	Examinateur
LAËTITIA MARTY CHARGEE DE RECHERCHE HDR, CNRS DELEGATION ALPES	Examinatrice
DAVID FERRAND PROFESSEURE DES UNIVERSITES, UNIVERSITE GRENOBLE ALPES	Président

Nano-optomechanics of suspended SiC nanowires down to cryogenic temperatures :
exploration of optical and photothermal responses

Candidate
Gouriou Clement
Institut Néel

Advisors
Olivier Arcizet
Institut Néel

Advisors
Benjamin Pigeau
Institut Néel

Supervisor
Eddy COLLIN
Institut Néel

Academic Year : 2022/2023

Acknowledgement

During my experience as a student I was often told that my grades and achievements depend mainly on the work I put in, meaning I am the engineer of my success. I learn to disagree with this idea, and this flawed view crumbles even more when applied to my PhD, because no amount of work could have ever replaced the precious help, support and supervision I was so lucky to receive during my time.

It goes without saying that the supervision I received from Olivier Arcizet and Benjamin Pigeau was precious and essential. They are both exceptional researchers in which I found a bottomless source to satisfy my scientific curiosities. So many discussions we had ended up reviving the interest in my work. Among an overwhelming quantity of other things, I learn how great of a quality it is to be able to inspire interest in people during conversations about various subjects. With their tenacity and enthusiasm, they were a beacon that helped me navigate my work outside trouble waters. Ironically, I would never get tired of the exceptionally long Monday morning group meetings. More seriously, although it was hard to get constantly focused those meetings allowed to understand all aspects of the research group subjects, but mostly demonstrated how well Oliver and Benjamin were invested in our work. It was quite fortunately that Benjamin's determination also showed in sustaining the constant supply of home-made pastries, cakes and cookies in those everlasting morning meetings. Determination, I had to return in biking so as to assist the dinner at Benjamin's house (thankfully you do not live higher in the mountain). I cannot express enough the gratitude for the tremendous amount of feedback Olivier gave me during my manuscript writing. It was a lot of work and much patience was needed but, although not very gratifying for me, I don't believe it would have been less of a mess had I chosen to write the manuscript in French. But more than that, my gratitude goes beyond the quantity of correction I received, I thank you for the persistent availability in addressing all the problems I encountered, and for the perpetual guiding I was provided.

To Eddy Collin I give my entire gratitude for blindly trusting me to be my official advisor. Your enthusiasm and interest in my work was always a pleasure to met whenever the occasion presented itself.

Thanks to the Néel institute's director Laurence Magaud, and her predecessor Etienne Bustarret, that maintained and continue developing the working conditions that altogether give place to state-of-the-art research while facilitating accessibility for students to be trained. To Jean Philip Poizat I give my thanks, for encouraging the new generation of researchers to fly with their own wings by developing the non-permanent seminar in which I had the pleasure to meet fellow colleagues.

I also give my gratitude to all the members of the administration that made my staying at the Néel possible, but also who helped made my life easier and allowed me to organise my working trips, especially the wonderful night train I took to go in Palermo. Thanks to F. Pois, A. Laurent, M. Boyer, S. Gadal, C. Bartoli, Y. Milin and E. Ferrara.

I would like to deeply thanks, but also congratulate the reviewers of my manuscript, Alessendro Siria and Ludovic Bellon, who survived the reading and gave me utmost relevant feedbacks. I thank Tristan Briant, Laetitia Marry, David Ferrand, Ilaria Zardo and Olivier Bourgeois for being part of the defence jury.

My PhD was not only made of work in the lab, but also punctuated with summer schools that kept me invested and updated on other subjects revolving around my work. It allowed me as well to meet and connect with peers. Thus, I deeply thank the organisers Quentin Glorieux and Antoine Browaeys, for coordinating the summer school of Les Houches in Septembre 2020 within the turmoil of the Covid pandemia, and allowing us hiking in the mountain which was so refreshing after months of lockdown. I also give my gratitude to the coordinators and organisers of the Cryocourse in 2021: Christian Enss, S. Bühler-Paschen, E. Collin, G.R.P. Pickett, P. Skyba, H. Suderow, J. Tuoriniemi. The time I spend there allowed me to deepen my understanding in cold physics as well as meeting new friends.

All this thesis work rests upon the shoulder (or one may say, upon the cold plate) of the Sionludi instrument, which is an easy to work with, performant, and extraordinary apparatus, designed and realised by Eric Eyraud and Wolfgang Wernsdorfer. To them, I can merely be thankful enough for their advice, their expertise, and their time in explaining the functioning of the instrument. None of this would have been possible without their essential work. Thanks to Olivier Bourgeois who gave us some of his time in helping us to understand low temperature physics that apply to our experiments. I also would like to thank Nicolas Roch, Julien Renard, Clemens Winkelmann, for the sharing of their expertise and advises. Thanks to the team of cryogenic engineers, R. Iannone, K. Herbe, J. Guilhot, that worked hard in providing a reliable source for the precious liquid helium throughout the years, even in difficult times.

In all the experiments I had the chance to work on, we always had to use custom parts. I can only thank the talented mechanical engineers that guided me in designing such parts, and be amazed in the skills they put in crafting elegantly the various elements. Equally, I thank the electronic engineers for providing us with utmost performant devices. It is with such help that I was able to carry out measurements with confidence in the setup. So thanks to J. Jarreau, L. Del Rey, D. Dufeu, R. Haettel, D. Lepoittevin, J. Minet, G. Bres, P. Charecchio, C. Hoarau, S. Triqueneaux, G. Donnier-Valentin, D. Jegouso, V. Reita and S. Le Denmat. Thanks to D. Lepoittevin who helped us design future components and took the time to address my interest in electronic design.

Thanks to the computer scientists P. Belmain and J. Michel that helped me chose and take care of the computer I did all my data analysis, the numerical simulations, the writing of the manuscript including the current acknowledgement. I thank the entire nanofab team for their work as well as facilitating the access to instruments when needed.

To my closest colleagues I cannot stress enough the help and support that kept me going in the most difficult times. More than that, I am mainly grateful for the joyful atmosphere resulting from your presence. The time we spent outside, around beers, having fun, was precious to me. I am thankful to Antoine Reigue who helped me as much in understanding the optical part of my subject, as our discussion on politics were interesting. Especially thanks to Francesco Fogliano who took the time to teach me his accumulated expertise during his last moment as PhD, while passing the torch to the cryogenic experiment I inherited from him. His formidable work laid the foundation of mine and made my start so much easier, while giving me standards for better achievements. Thanks to Philip Heringlake, always available whenever I asked questions, and always giving precious advises. I also would like to thank Laure Mercier de Lepinay, though you left before I even arrived, your tremendous work has left archaeological traces in the group that helped me better understand almost every aspect of the variety of subjects I encountered. Thanks to Alex Fontana for his help and support during his staying, as well as the time we passed in Palermo. The delicious pizzas, the spritz and the profound discussions we had were delightful. Thanks to Michael Croquette and Jonathan Laurent for being consistent in the fun I have when spending time with you.

To my PhD buddy Hugo Weltz, it was fun to have you with me and I enjoyed the shared time we had, I promise I will try your best restaurant recommendations. To Chao Zang, I can only hope for the success of your experiments and wish you good luck if you ever try combining your work with the cryostat. I took great care of it, it can only work. Thanks to Cattleya Dousset for your late but valuable contributions in my PhD. You only begin your PhD work and I wish you the best of luck, may it *shines bright like a diamond*... with a NV-centre in it.

Thanks to my colleagues with whom I could escape work within the workspace. I will cherish all the enriching moments I spend with you. In particular, I will remember those numerous outdoor coffee conversations with Maria accompanied by the unmovable wooden box, or the plentiful meal share with Lucien with whom the discussion could easily go into unexpected directions. My deepest desire being to one day share a pizza in your homemade oven. To Lucas, I value very much the long discussion and shared moment we had, during the time we could make for ourselves.

I also thank S. Zanier for trusting me with the teaching of experimental physics. It allowed me to learn and improve myself as a teacher while taking pleasure in teaching practical science in the most enjoyable environment.

Thanks to the comrades I had the pleasure to meet outside the working environment in the many gathering of people which have strong opinion about grabbing on living in good conditions. Had I more energy in that time, I would have joined in your union.

Of course, even though it is obvious to me, I can only be profoundly thankful for all the support I received from my friends, but also all

they inspired in me. I was very lucky to be surrounded by part of you who were present in the beginning, other in the end, and some who stayed all along. It had been of huge help to start my PhD knowing I had friends already living in Grenoble, spending time cheering, playing to boardgames around beers. I also give my ever lasting thanks to my roommates which made the lockdown as pleasant as it could be. I will never forget the many SuperTuxKart games I definitely always won... But my staying with you was much more than that, and I am grateful of the time I spent sharing that part of my life. Let's not forget my long distant friends which were always a pleasure to visit, whenever I returned in my birth region. Whenever we met again, it was as if time never really passed, and filled me with happiness. For my beloved, with whom I shared incalculable happy times, and with whom I was able to be true to myself, I give my deepest gratitude and love, but also my greatest congratulations on supporting me in my most annoying sates.

We often tend to forget all the invisible work that facilitates so much our working environment. The cleaning service that provided in the building and offices which made it pleasant to work in. The technicians that made sure the coffee machine was always operational. But let's not forget the collective work put in open source tools and programming languages. Python was of incredible help, providing me with free of charge competitive tools in order to best perform in my work. I insist on the tremendous long term gain we get from investing time and effort in open source community-developed tools. I also thank all the staff in the variety of services that were available in the laboratory, such as Service Achats Magasin, or Service Reprographie.

At last but not least, je ne remercierai jamais assez ma famille qui a été d'un grand support distanciel tout au long de cette thèse, mais qui surtout s'est toujours battu pour m'offrir les opportunités qui m'ont permises d'arriver jusqu'ici. Bien que mes parents ne comprenaient quasiment rien à ce que je faisais, iels ont gardé un intérêt constant pour ce que je faisais. *Mais à quoi ça sert ?* me demandaient t'iels constamment. Je peux maintenant vous répondre fièrement : à pas grand-chose, fin je crois. A ma famille je dis un grand merci.

Preface

When I started my PhD thesis my predecessor, Francesco Fogliano, had finally succeeded in cooling a nanowire to (almost) the base temperature of the cryostat I went on working on. It had been a challenge to painstakingly isolate the nanowire from the spurious mechanical vibrations produced by the dilution process that artificially heated up the sample position noise temperature. On the other hand, another PhD student, Philip Heringlake, was working on protocols for high speed force microscopy with nanowires in the group. I remember thinking I was lucky and that it would be a more or less straight forward path to tackle the project I was given : implementing force microscopy with nanowires at cryogenic temperatures to investigate new physics. I was wrong ("obviously" a more experienced researcher would say). Still, I was indeed lucky to have been presented to a functioning, well-designed experimental setup, and our work lead us to investigate a branch of physics rather new for the group : thermal physics of nanoscale objects at low temperatures.

The first questions we had on thermal transport occurring in our nanowire appeared from the measurement of the optical heating curves of nanowires. Upon investigating the thermal response of the nanowires, we observed unexpected and non-trivial dependencies in the injected optical power, with heating rates strongly varying bellow 10 K. We developed new tools to probe the thermal physics of the system, which allowed us to investigate the dynamical response of the nanowires to light induced thermal waves. The large variety of effects that we encountered (thermal expansion, refractive index modulation, elongation, bilayer effect, modulation of the cross section) lead us to progressively improve the experimental and analytic tools to investigate in greater detail the physics at play in our system.

In this context the present thesis manuscript does not follow the chronological order of our work. Instead, we present the different techniques and observations that helped us refine our understanding on the thermal physics involved in our nanowires. This is why we will deal with room temperature characterisations that have been developed consequently to observation realised at low temperature, and aim to be implemented in future measurement at cryogenic temperatures.

Author's contribution In this thesis work we investigated in greater detail the thermal properties of the nanowires at low temperatures, following the PhD work of F. Fogliano that demonstrated it was possible to cool down and observe a nanowire at dilution temperatures. The puzzling optical heating curves, that seemed common to multiple nanowires, let us know that the nanowire was transiting from different regimes of heat conduction below 10 K. To complement those static measurements and to better understand the conduction properties of our nanowires in such cold environment, we developed and performed dynamical measurement using a pump-probe configuration. During our investigations, we often alternated between observations of photothermal effects at low temperatures and room temperature characterisation. In the late stage of the thesis work, those

characterisations gain from the help of the internship student C. Dousset who helped carry out some measurements while the analysis was realised in regard to the model and theory developed in parallel.

To further investigate the light nanowire interaction, that is per essence at the source of its photothermal response, we designed and implemented a new experimental setup to better understand the role played by the internal optical resonances of the nanowire (Mie resonances). This study, which was based on the analysis of lateral light scattering polar diagrams, gave us some refined experimental and analytical tools to investigate the internal Mie optical resonance, whose strong role in the photothermal response of the nanowires was subsequently investigated.

Chapter 1 will present the motivation and context of our work. We will introduce the formalism used to describe the mechanical properties of the nanowires used in our group. To better understand the optomechanical experiments, we describe the 2D readout measurement principles that will be used in this thesis work. We then conclude presenting the various projects started in the group using the nanowire platform.

Chapter 2 focuses on the optical properties of 3C-SiC nanowires and to how they couple to light. Indeed, under white light illumination, one can observe the great variety of colours a nanowire can display for different diameters. We will use the framework of Mie scattering to explain how this colouration appears. In a second time we will describe the new experimental setup developed in order to probe the scattering properties of the nanowires. The analysis of the angular scattering diagrams of several nanowires will confirm the robustness of the Mie scattering theory in describing the light-nanowire interaction. This formalism also pave the path towards a better description of the absorption properties of the nanowires, that will be investigated in chapter 5.

Chapter 3 describes the cryostat experimental apparatus that has been used for the investigation of the thermal properties of nanowires at low temperature. We will present in great detail the different elements composing the suspended optomechanical setup as well as the readout channels. We then expose the experimental achievements in thermalising nanowires at cryogenic temperatures, as well as the non-trivial evolution of the noise temperature of our nanowires with the optical power, which relates to the conduction properties of the resonator. The chapter concludes with a summary of the expected heat conduction regimes occurring in nanostructures at low temperature.

Chapter 4 aims at exposing the specificities of the pump-probe optomechanical setup that was used in this PhD thesis work. We present the standard protocols that are used to characterise the nanowire mechanical properties. We then show a typical broadband response, which is a central measurement class in this thesis, and explain its specificities when employed using the interferometric readout channel. After exposing first results in measuring thermal effect on the

nanowire reflectivity, we conclude the chapter by formalising the framework of the Fourier heat diffusion dynamics in a 1D system, and how the non-homogeneous temperature profile along the nanowire can affect our measurements of its thermal noise.

Chapter 5 deals with the different characterisation techniques developed to study of the nanowires thermal properties at room temperature. After observing non-trivial photothermal effects at low temperature, we used a room temperature experimental setup in order to investigate the dynamics of several thermomechanical effects. After presenting the measurement setup, we analyse the elongation dynamics of the nanowire consecutive to light absorption at different wavelength. From those measurements, we can retrieve several properties, such as the calibrated absorption and its wavelength dependence, which is strongly structured by the Mie resonances. In a different set of experiments, we analysed the impact of the thermal contact resistance between the nanowire and its clamping on the photothermal response, allowing us to refine our heat propagation model. We then come back on the nanowire lateral displacements generated by the thermomechanical deformation at the clamping, and we present the study of the evolution of the response profile when scanning the pump laser position along the nanowire. To better model the clamping thermomechanical dynamics, we implemented numerical simulations using the COMSOL software which helped us relate this thermal effect to the temperature modulation at clamping. We finish the chapter by reporting on the interplay between the thermal and the optical effects, with the presentation of the thermally induced optical force modulation response measurements. Scanning the pump laser colour around an optical resonance reveals the interplay between the optically induced temperature modulation at the laser position and the temperature dependent light-nanowire interaction (which is strongly structure by its internal optical resonances).

Chapter 6 presents the measurements realised to explore the nanowire thermal properties at low temperatures. We start by comparing the broadband responses from room to medium temperature (10 K), and exploit the room temperature observations to analyse how the different thermal mechanisms evolve at low temperatures. We then highlight the non-linearity of the thermal response at low temperature which strongly varies with the mean optical power employed, that lead us investigate the heat wave propagations when the heat conductivity and the heat capacity are allowed to vary with temperature, and thus with the position within the nanowire. At colder temperature we show resonantly driven responses that are dominated by thermomechanical effects and how they relate to the non-linear diffusion of heat. We conclude the chapter with the analysis of the nanowire resonant frequency shift dependence to the optical power, as well as how it varies when we scan the pump position along the nanowire. We analyse the frequency shift in relation to the non-homogeneous temperature profile.

CONTENTS

Acknowledgement v

Preface ix

1 SiC nanowires as an ultrasensitive force probe platform 1
Introduction ... 1
1.1 Context of the thesis - Mechanical resonators at low temperature and nano-thermometry ... 2
1.2 Nanowire resonators as force sensor ... 5
1.2.1 Vibrations of a clamped-free nanowire ... 5
1.2.2 Brownian motion of the nanowire ... 12
1.3 β-Silicon Carbide nanowires ... 14
1.4 Optical readout and projective measurements ... 15
1.4.1 Free space measurement ... 16
1.4.2 Interferometric measurement ... 16
1.5 Overview of past experiments realised in the host group ... 17
1.6 Chapter summary ... 21

2 Light-nanowire interaction and internal Mie resonances 23
Introduction ... 23
2.1 Optical properties ... 24
2.2 Mie resonances ... 25
2.2.1 Description of the EM Fields ... 25
2.2.2 Radiometric quantities associated to the scattering of a nanowire ... 30
2.2.3 Optical cross-section ... 35
2.3 Investigation of angular scattering diagrams ... 36
2.3.1 Measurement setup ... 36
2.3.2 Diagram evolution with wavelength ... 39
2.3.3 Reflectivity ... 42
2.4 Perspective ... 43
2.4.1 Thermal modulation of Optical Forces ... 43
2.4.2 Nanowire under Gaussian illumination ... 44
2.5 Chapter summary ... 44

3 Cryogenic optomechanical setup 47
Introduction ... 47
3.1 Description of the Cryostat ... 48

3.1.1 Helium circulation ... 49
3.1.2 Temperature control ... 50
3.2 Cooling down the experiment ... 52
3.3 Optical head ... 54
3.3.1 The suspended optomechanical setup ... 54
3.3.2 Interferometric fibred objectives ... 57
3.3.3 Detectors ... 61
3.3.4 Imaging and communication with the instruments ... 64
3.4 Interferometric readout of the nanowire vibrations ... 65
3.5 Thermalizing a nanowire resonator at cryogenic temperature ... 66
3.5.1 Reduction of thermal noise ... 66
3.5.2 Linearity of the mechanical response ... 68
3.5.3 Optical heating and heat propagation regimes ... 68
3.6 Chapter summary ... 75

4 Exploring the heat propagation dynamics within nanowires **77**
Introduction ... 77
4.1 Pump probe experimental setup ... 78
4.2 Measurement protocol ... 80
4.2.1 Nanowire reflectivity ... 81
4.2.2 Fitting the Brownian motion ... 81
4.2.3 Response measurements ... 84
4.3 Measurement channel ... 85
4.3.1 Interferometric readout ... 85
4.3.2 Vertical readout ... 89
4.4 Reflectivity measurements ... 89
4.5 Model for the thermal response ... 91
4.5.1 Diffusion model ... 91
4.5.2 Static profile ... 93
4.5.3 Periodic excitation ... 93
4.6 Thermal noise under non-homogeneous temperature profile ... 95
4.7 Chapter summary ... 97

5 A compilation of photothermal mechanisms within the SiC nanowires **99**
Introduction ... 99
5.1 Thermal elongation of the nanowire length ... 100
5.1.1 Measurement of the nanowire elongation response ... 101
5.1.2 Absorption inhomogeneities ... 104
5.1.3 Mie enhanced absorption ... 105
5.2 Heat diffusion coefficient of the nanowires and thermal contact resistance ... 109
5.3 Thermal lateral deformation ... 113
5.4 Profile structure of the low frequency lateral deformation response ... 115
5.5 Modelling of the thermomechanical effect at the clamping ... 118
5.6 Thermal modulation of the optical cross-section ... 124
5.7 Electrostriction ... 127
5.8 Chapter summary ... 128

6 Thermal response from Room to Cryogenic temperature **129**
Introduction ... 129
6.1 Photothermal responses at low temperature ... 130
6.2 Thermal waves in a non-linear regime ... 137

6.2.1 Heat diffusion when C_p, κ, vary with temperature 137
6.2.2 Stationary temperature profile 138
6.2.3 Dynamical heat diffusion in the non-linear regime 140
6.3 Frequency shift with temperature 150
6.3.1 Two level system (TLS) contribution 151
6.3.2 Non-homogeneous temperature profile 153
6.4 Dynamical investigation of the photothermal modulation of the mechanical resonance 156
6.5 Chapter summary 161

Conclusion **163**

A Annexe : Additional heat diffusion problems **169**
A.1 Static temperature profile with a transition regime of the heat conductivity temperature dependence 169
A.2 Thermal response accounting for the thermal contact resistance inertia 172
A.3 Heat diffusion under Gaussian-shaped heat sources 176
A.3.1 Static profile with constant heat capacity and conductivity 176
A.3.2 Periodic excitation with constant diffusion coefficient 177
A.3.3 Stationary temperature profile with the heat capacity and conductivity varying with the temperature 178

B Annexe : Ellipse on a tilted plane **181**

C Annexe : Some mathematical demonstrations **185**
C.1 Getting T_{noise} from integrating Nanowire PSD Brownian motion 185
C.2 Demonstration of the limiting value of Mie coeff $C_{m,l}^{\parallel,\perp}$ 187

D Annexe : Unsolved problems **189**
D.1 Convergence speed of Z-configuration mirror alignment 189
D.2 Mueller's matrices and wave plates 190

Bibliography **191**

Summary ADUM **205**

THÈSE

Pour obtenir le grade de

DOCTEUR DE L'UNIVERSITÉ GRENOBLE ALPES

École doctorale : PHYS - Physique
Spécialité : Nanophysique
Unité de recherche : Institut Néel

Nano-optomécanique des nanofils suspendus à basse température

Nano-optomechanics of suspended SiC nanowires down to cryogenic temperatures : exploration of optical and photothermal responses.

Présentée par :

Clement GOURIOU

Direction de thèse :

Eddy COLLIN DIRECTEUR DE RECHERCHE, CNRS DELEGATION ALPES	Directeur de thèse
Olivier ARCIZET CHARGE DE RECHERCHE HDR, CNRS DELEGATION ALPES	Co-directeur de thèse

Rapporteurs :

LUDOVIC BELLON
DIRECTEUR DE RECHERCHE, CNRS DELEGATION RHONE AUVERGNE
ALESSANDRO SIRIA
DIRECTEUR DE RECHERCHE, CNRS DELEGATION PARIS CENTRE

Thèse soutenue publiquement le **6 octobre 2023**, devant le jury composé de :

LUDOVIC BELLON DIRECTEUR DE RECHERCHE, CNRS DELEGATION RHONE AUVERGNE	Rapporteur
ALESSANDRO SIRIA DIRECTEUR DE RECHERCHE, CNRS DELEGATION PARIS CENTRE	Rapporteur
ILARIA ZARDO ASSOCIATE PROFESSOR, UNIVERSITÄT BASEL	Examinatrice
OLIVIER BOURGEOIS DIRECTEUR DE RECHERCHE, CNRS DELEGATION ALPES	Examinateur
TRISTAN BRIANT MAITRE DE CONFERENCES, SORBONNE UNIVERSITE	Examinateur
LAËTITIA MARTY CHARGEE DE RECHERCHE HDR, CNRS DELEGATION ALPES	Examinatrice
DAVID FERRAND PROFESSEURE DES UNIVERSITES, UNIVERSITE GRENOBLE ALPES	Président

1.1 Context of the thesis - Mechanical resonators at low temperature and nano-thermometry

It is difficult to mention optomechanical system without mentioning gravitational wave detection [1] (approx. 14k referenced citations on Google Scholar), since it illustrates the versatility of mechanical systems in bridging different domain of physics. In this case, astronomical events are now measured with squeezed light in 3-4 km long interferometers in which the sensitivity optimisation now needs to take into account the quantum nature of the light fields [2] as well as the momentum transfer between the light and the mass mirrors, with precision partly limited by the thermal noise of the mirrors coating.

On the other hand, micro and nano-mechanical resonators provide large force sensitivities due to their light masses and susceptibilities. They have helped to probe physics at the nanoscale benefiting from the constant progresses observed in micro and nano-structure fabrication techniques. In parallel, coupling large systems such as mechanical oscillators to quantum states would allow to deepen our understanding in the mechanisms involved in quantum decoherence and quantum measurements [3, 4] while improving precision [5, 6]. Demonstration of such interactions have been made using coupling of mechanical oscillator to superconducting qubits [7]. The low mass of micro/nano-mechanical oscillator combined with decent quality factors, offer excellent sensitivity for force measurements, sufficient to detect the force produced by a single electron spin [8]. Oscillators have also been built from a large variety of materials and geometrical forms, such as nanotubes, graphene, nanowires [9, 10, 11], or using optically trapped particles [12, 13, 14, 15].

Lowering the temperature of the such probes is also a permanent objective in the field [19]. Apart from the gain in force sensitivity that originates from a quieter environment (which reduces the thermal noise), as well as the decrease of the mechanical damping rates (generally observed at low temperatures) ; cooling down such systems would allow investigating the intrinsic thermal and physical properties of the resonators in their lowest excitation states. Active cooling using radiation pressure [20], have succeeded in bringing a specific mode of a nano-mechanical oscillator down to its ground state in the resolved sideband regime [17, 21, 22, 23], the material remaining at higher temperature in general. Direct cooling to ultra-low temperatures [18], opens perspectives for the above-mentioned perspectives. Reaching such quantum state with macroscopic mechanical resonator also holds intrinsic value, such as the need for massive quantum oscillator in order to probe properties of space-time at its fundamental scale [24, 25].

Nonetheless, dynamical back action cooling does not necessarily improve the bare force sensitivity of the oscillator as it also reduces its mechanical susceptibility. Passively cooling to a quantum ground state has been recently achieved for a macroscopic mechanical resonator [18], but has for the moment been only performed on high fre-

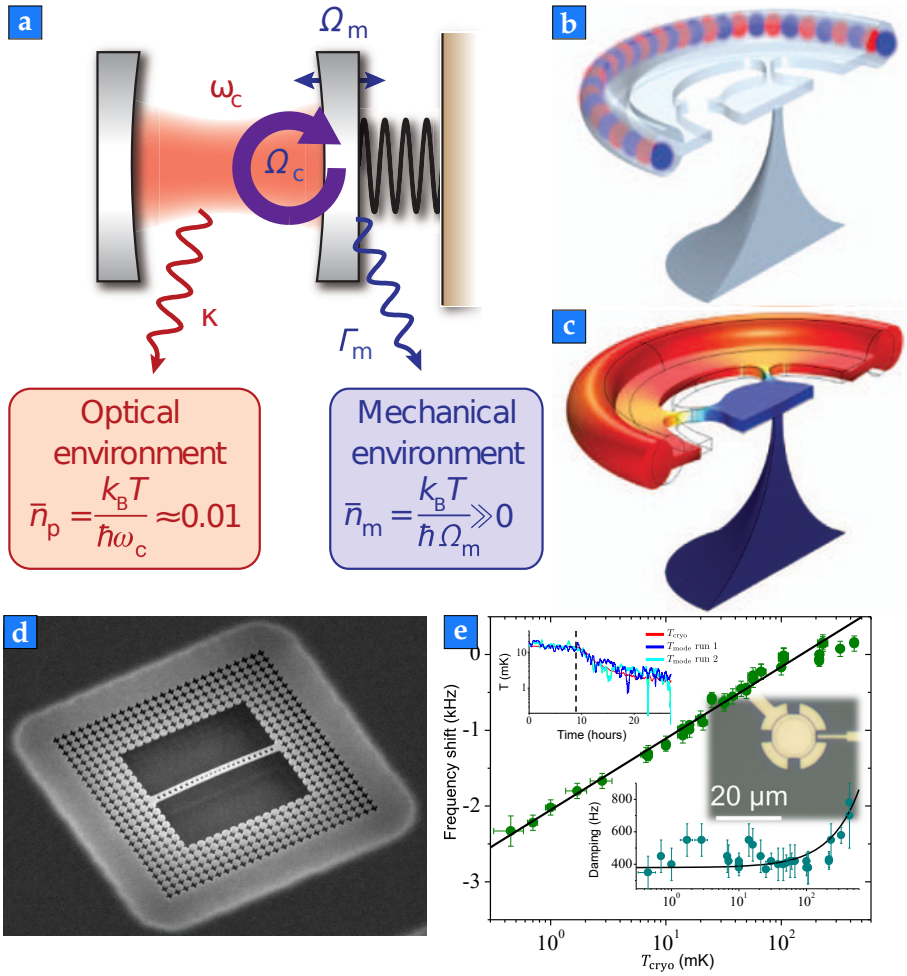

Figure 1.1: Examples of cold mechanical oscillator. (a) Principle of optomechanics [16]. Figures (b),(c) show the profiles of the optical mode (top) and the radial displacement of the fundamental breathing mode (bottom) of a toroidal resonator used in cavity optomechanics [16]. (d) SEM image of an optomechanical resonator with phononic shield, which was laser cooled into its quantum ground state [17]. (e) First passively cooled mechanical resonator observed in its quantum ground state of motion (adapted from [18]). The main graph corresponds to the shift of the resonant frequency with temperature, with respect to $\omega_0/2\pi \simeq 15.1$ MHz (black line is a logarithmic fit). The top inset shows the concomitant evolution of the cryostat temperature (T_{cryo} in red line) and the mechanical mode temperatures for two distinct runs (T_{mode} in blue lines). The bottom inset graph corresponds to the mechanical damping with a linear fit in black. An optical picture of the device is shown.

quency mechanical oscillators, which are very stiff and do not present a very large force sensitivity. Furthermore, it remains a very difficult task as one needs to decouple the mechanical oscillator from its support which is hardly compatible with optical readout which requires an efficient heat evacuation. Additionally, when cooling down nanomechanical resonators, apart from the reduction of the thermal noise, there often comes a reduction of the heat conductance of the samples. This reduces the coupling of the oscillator with the cold thermal bath, while increasing its sensitivity to perturbation induced by the readout probe : Joule heating when measured with RF fields [26, 27, 28, 29], or optical absorption when measured by optical means, making use or not of optical cavities [30, 31, 32, 33].

In addition, regimes of heat conduction are known to present a large physical richness at low temperatures and for nano sized systems, where the different finite dimensions of the system introduce temperature cutoffs when the system dimensions start to compare to the phonon mean free path or the dominant phonon wavelength [39]. Investigating these exotic regimes allows probing how phonons propagate and behave at those scales. In some cases, the thermodynamic definition of temperature no longer holds and leads to non-trivial considerations on how the nanoresonator properties are affected by the phonon dynamics. One must find ways to measure and characterise

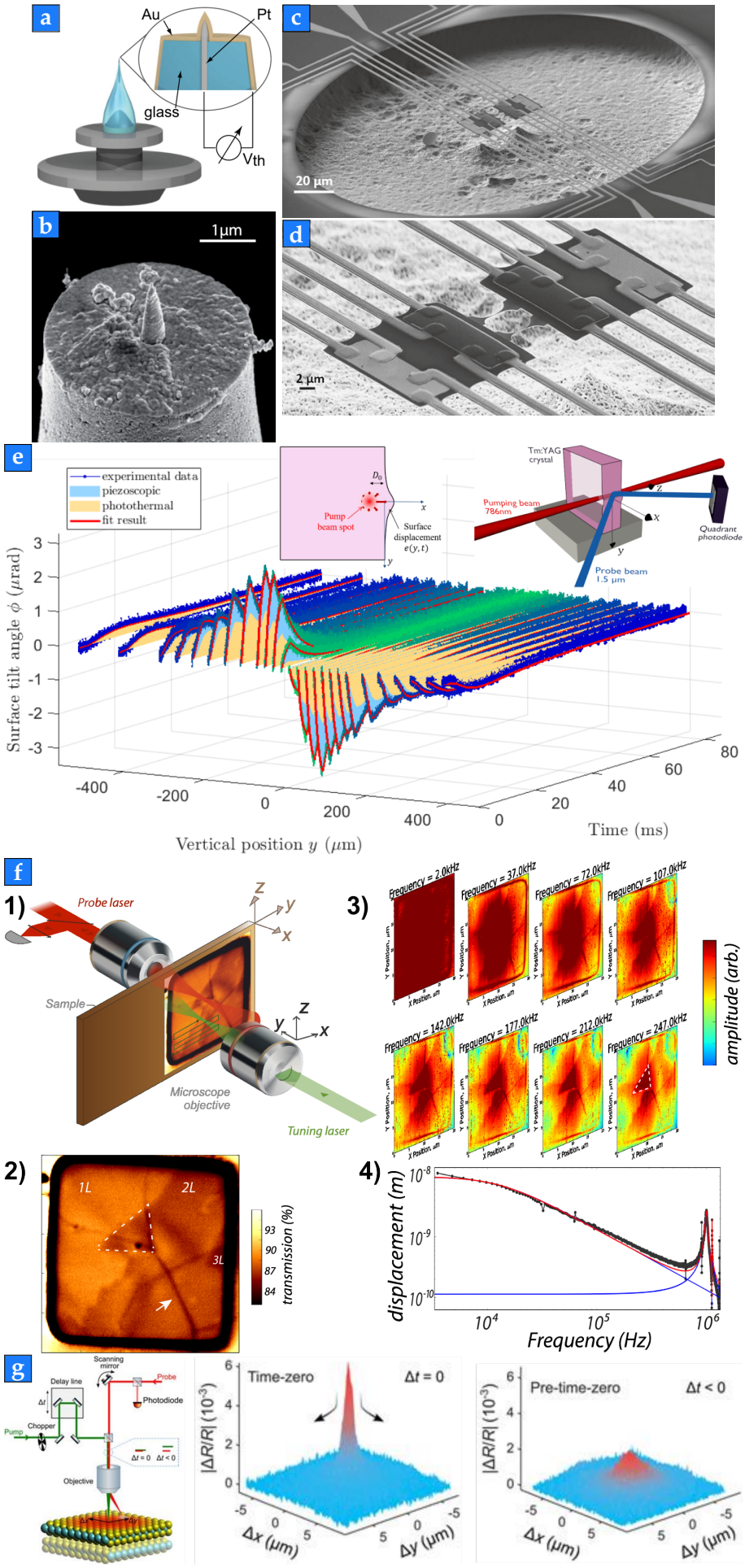

Figure 1.2: Examples of different heat probes and techniques used for thermal measurements on nanostructures. (a), (b) Illustration of a probe used in Scanning thermal Microscopy, and SEM image of the tip presented in [34]. Figures (c), (d) show SEM images of a suspended silicon nitride measurement platform used for heat conduction measurements in nanostructures [35]. (e) Heat diffusion measurements by photodeflection on the surface of a bulk Tm:YAG crystal, where the thermal dynamic couples to the optomechanical backaction, from [36]. (f) Measurements of the dynamical thermal properties of a graphene membrane, in a pump probe experimental configuration where the pump laser (green) is scanned across the sample area ((f).1). Figure ((f).2) shows the collected transmitted intensity of the graphene resonator. The figures in ((f).3) show the response amplitude maps of the deformation at different fixed modulation frequencies of the pump intensity. On the other hand, the figure ((f).4) show the deformation amplitude response over a large frequency range when the pump is positioned at a fixed at the centre of the sample. In blue lines a thermal low-pass filter model and a mechanical Lorentzian for two coupled modes, while the red line corresponds to the sum of the two contributions. Adapted from [37] (g) Representation of the pump-probe microscopy setup with adjusting delay between the pump and the probe, while using reflectivity signal to probe the heat diffusion from the pump [38].

those quantities, relying on different actuation phenomena. Assuming thermalisation to the thermal bath, researchers used on-chip noise thermometers [29], or used directly the mechanical and optical properties of the optomechanical resonators [40] for joint thermometry measurements with objective of pushing those measurement principles down to the quantum regimes of the optomechanical interaction [40].

Other measurement channels can be used to probe the temperature or the heat propagation inside nanostructures. The measurements of the mechanical frequency shifts have been used to analyse the temperature profile inside cantilevers [41] and the impact of their non-homogeneity on the vibrational noise temperature of the systems. Raman thermometry can give local information on the temperature and the stress within nano-oscillators [42, 43, 44, 45]. Heat conduction properties are also probed using on-chip resistive thermometers [35], sample surface deformation [36], near field heat transfer [34], or more directly Scanning thermal microscopy [46, 47]. Pump probe methods, closer to what will be use in this thesis project, involve opto-thermal effects such as reflectivity change with temperature [38]. These methods were also used in the group during the PhD of Cornelia Schwarz on suspended graphene membranes [37, 48], and before to investigate the photothermal response of macroscopic cavity mirrors [49].

In this context, we will present in the following how we use SiC nanowires as force field sensors and the different techniques we developed in order to probe their thermal properties. Following the work initiated during the PhD of F. Fogliano, where a $40\mathrm{zN}/\sqrt{\mathrm{Hz}}$ force sensitivity was demonstrated using nanowires at dilution temperatures, we aim at characterising the dynamical photothermal response of the nanowires and further investigate how it impacts the use of silicon carbide nanowires in our low temperature force measurements.

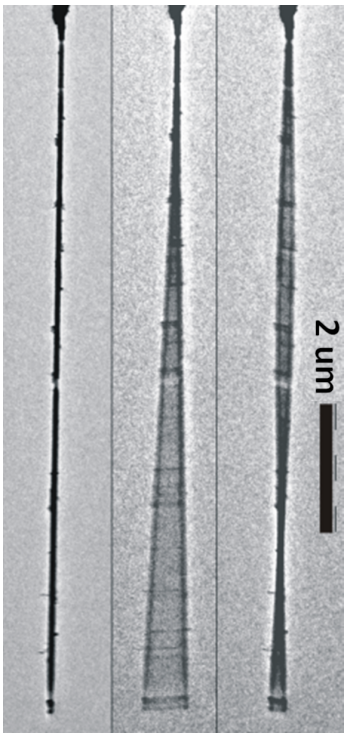

Figure 1.3: Nanowire picture using a SEM. From left to right : picture taken when the nanowire is at rest, resonantly driven to its first, and to its second mode.

1.2 Nanowire resonators as force sensor

In this section we derive the main equations and expressions that will be use for describing the mechanical behaviour of our suspended nanowires, see Fig. 1.3. While most the derivation can be found in the literature, we adapted the notation to suit the conventions use in our research group.

We first establish the fundamental equations that describe the resonant behaviour of the suspended nanowires in 1D without loss of generality. Then, we describe the effect of an external force field acting on the 2D dynamics of the nanowires. We finish formalising the interaction of the nanowire with a thermal bath.

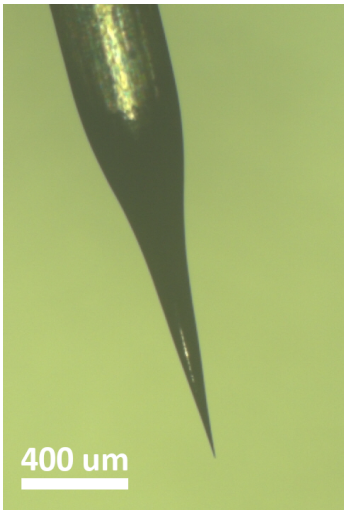

Figure 1.4: Image taken with an optical microscope of the etched tip of a tungsten wire, used as a nanowire support.

1.2.1 Vibrations of a clamped-free nanowire

In our experiments, we use nanowires that are clamped in one end to an etched tungsten tip, see Fig. 1.4, while freely moving to the other end. The motion of such system is well modelled by a clamped-free stiff beam and described by the Euler-Bernoulli equation. For the sake of wholeness we will present a brief derivation of the aforementioned equation, starting from the continuous medium framework [50]. The

demonstration follows the more general derivation found in Ref. [51], and we will proceed using a variational method making use of the Hamilton's principle and functional derivation. For a more detailed approach about vibration of continuous medium, one can refer to Ref. [52].

Considering a section of a beam, of length $\mathrm{d}L$, cross-section S, and volume $\mathrm{d}V = S\,\mathrm{d}L = \mathrm{d}^3 r$, the strain energy resulting from a small deformation of the total beam is given at first order by,

$$U = \frac{1}{2}\int_V \sigma_{ij}\,\epsilon_{ij}\,\mathrm{d}V, \tag{1.1}$$

where σ_{ij} is the stress tensor, and ϵ_{ij} is the strain tensor (or deformation tensor), and we adopted the Einstein summation notation. The kinetic energy of the section is given by,

$$T = \frac{1}{2}\int_V \rho\,(\partial_t u)_i\,(\partial_t u)_i\,\mathrm{d}V, \tag{1.2}$$

where $\mathbf{u}$ is the displacement vector field. We also consider an external volumetric force source, q, applied to the elementary volume. This force exerts a work such as,

$$W = \int_V q_i(\mathbf{r})\,u_i\,\mathrm{d}V. \tag{1.3}$$

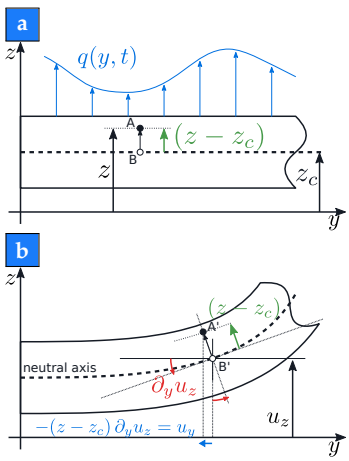

Figure 1.5: Notation scheme for the derivation of the Euler-Bernoulli equation.(a) Before deformation. (b) After deformation.

Considering the geometry of the beam problem undergoing flexural deformation, one can express the displacement vector such as (see Fig. 1.5),

$$\mathbf{u} = \begin{bmatrix} u_x \\ u_y \\ u_z \end{bmatrix} = \begin{bmatrix} 0 \\ -(z-z_c)\partial_y u_z(y) \\ u_z(y) \end{bmatrix}. \tag{1.4}$$

The strain tensor relates to the displacement vector field, $\mathbf{u}$, such as $\epsilon_{ij} = \frac{1}{2}(\partial_j u_i + \partial_i u_j)$. Moreover, in the linear regime of small deformation, we can relate the strain to the stress tensor using the generalised Hook's law either in stress with $\sigma_{ij} = \lambda\,\epsilon_{ll}\,\delta_{ij} + 2\,\mu\,\epsilon_{ij} = \frac{\nu\,E}{(1+\nu)(1-2\,\nu)}\,\epsilon_{ll}\,\delta_{ij} + \frac{E}{(1+\nu)}\,\epsilon_{ij}$, or in strain with $\epsilon_{ij} = \frac{1+\nu}{E}\,\sigma_{ij} - \frac{\nu}{E}\,\sigma_{ll}\,\delta_{ij}$, where $\epsilon_{ll} = \mathrm{Tr}(\boldsymbol{\epsilon}) = \boldsymbol{\nabla}\cdot\mathbf{u}$, $\sigma_{ll} = \mathrm{Tr}(\boldsymbol{\sigma})$, while λ, μ are the Lamé coefficients, and E, ν are the Young modulus and the Poisson coefficient respectively. Under uniaxial loading condition along the y-axis (corresponding to uniaxial stress), it follows the only non-zero component of the stress tensor due to flexural deformation is given by,

$$\sigma_{yy} = E\,\epsilon_{yy} = -(z-z_c)\,E\,\partial_{yy}u_z(y). \tag{1.5}$$

Introducing the area inertial momentum, $I = \int_S (z-z_c)^2\,\mathrm{d}^2 r$, we can express the Lagrangian,

$$L = T - U + W, \tag{1.6}$$

$$= \int_0^L \left(\rho\,A\,(\partial_t u_z(y))^2 - E\,I\,(\partial_{yy}u_z(y))^2 + q\,u_z(y)\right)\,\mathrm{d}y, \tag{1.7}$$

then using the Hamilton's principle with,

$$S[u_z] = \int_{t_0}^{t_1} L(u_z, \partial_t u_z, \partial_y u_z, \partial_{yy} u_z, y, t)\mathrm{d}t, \qquad \frac{\delta S}{\delta u_z} = 0. \tag{1.8}$$

Carrying out the functional derivative, we get,

$$\left[-\rho\, S\, \partial_t(\partial_t u_z) - \partial_{yy}(E\, I\, \partial_{yy} u_z) + q\right] = 0. \tag{1.9}$$

The equation (1.9) is the Euler-Bernoulli equation with a force per unit length term q. In the following, we will denote $u_z \equiv r$ as the displacement of the neutral axis from the resting position of the beam to its deformed position.

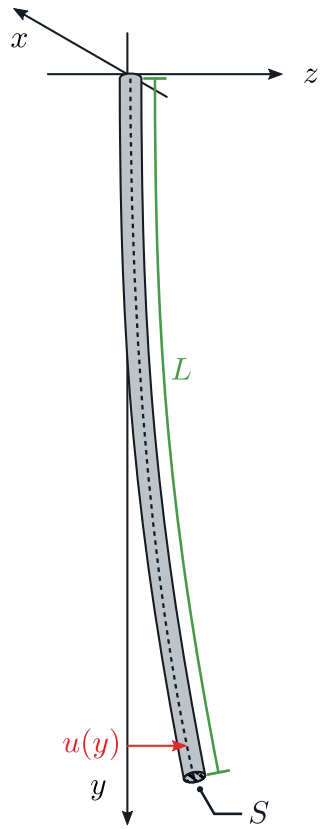

Figure 1.6: System of axis chosen for deriving the mechanical behaviour of a nanowire resonator.

Free oscillations

The dynamical motion of the lateral displacement, r, of a suspended nanowire of radius R, follows then Euler-Bernoulli equation [53],

$$\rho\, S\, \partial_t^2 r(y,t) + E\, I\, \partial_y^4 r(y,t) = 0 \tag{1.10}$$

where E is the Young modulus, ρ its volumetric mass, $S = \pi R^2$ the cylinder cross-section and $I = \frac{\pi R^4}{4}$ the cylinder inertial momentum. We use the coordinate system as illustrated in Fig. 1.6.

Although it is not always the case, we assume for simplicity's sake E and I to be constants of the altitude, y. Equation (1.10) is solved using the ansatz, $r(y,t) = a(t)\, u(y)$, and upon substitution we get a set of two equations.

$$\partial_t^2 a(t) = -\Omega^2\, a(t), \qquad \partial_y^4 u(y) = k^4\, u(y), \tag{1.11}$$

where k is the wave vector and Ω is the frequency of oscillation. The two equations are related by the dispersion relation, $\Omega = k^2\sqrt{\frac{E\,I}{\rho\, S}} = k^2\sqrt{\frac{E\,R^2}{4\rho}}$. The set of solutions for u are given by eq. (1.12),

$$u[y,\Omega] = A\cos(ky) + B\sin(ky) + C\cosh(ky) + D\sinh(ky), \tag{1.12}$$

while constrained by the boundary conditions defined in eq. (1.13),

$$u[0,\Omega] = 0, \quad \partial_y u[0,\Omega] = 0, \quad \partial_y^2 u[L,\Omega] = 0, \quad \partial_y^3 u[L,\Omega] = 0, \tag{1.13}$$

where the boundaries account for a fixed clamping (two first), the free end is curvature free, and no momentum (*i.e* no load) is applied at the tip.

The set of solutions that satisfies the above equations are given by solving,

$$\begin{bmatrix} 1 & 0 & 1 & 0 \\ 0 & 1 & 0 & 1 \\ -\cos(k\,L) & -\sin(k\,L) & \cosh(k\,L) & \sinh(k\,L) \\ \sin(k\,L) & -\cos(k\,L) & \sinh(k\,L) & \cosh(k\,L) \end{bmatrix} \begin{bmatrix} A \\ B \\ C \\ D \end{bmatrix} = \begin{bmatrix} 0 \\ 0 \\ 0 \\ 0 \end{bmatrix}, \tag{1.14}$$

Figure 1.7: Nanowire mechanical normal mode for 5 first family.

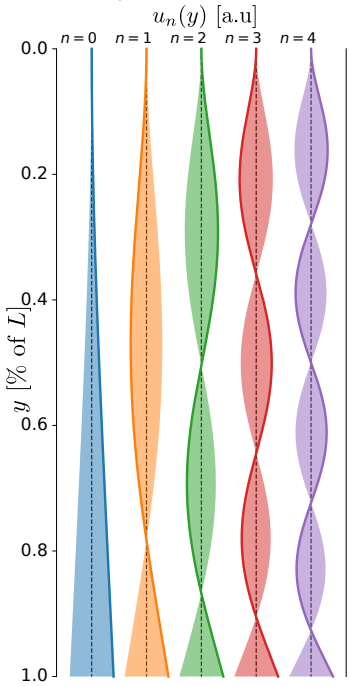

leading to the mode equation for non-trivial solutions to exist,

$$\cos(k\,L)\cosh(k\,L) = -1. \tag{1.15}$$

Solutions for such equation are found numerically using root-finding methods, and each discrete solution is a resonant mode referred with the subscript n. One can note the cosh term imposes an exponential precision for the roots, such that for high order modes (typically above $n > 20$) quantitative prediction becomes undermined as the gap from theory will diverge exponentially due to the cosh and sinh terms in the analytical solution.

The resonant frequencies of the nanowire are then given by,

$$\Omega_n = k_n^2\sqrt{\frac{EI}{\rho S}} = (k_n\,L)^2\,\Omega_0, \tag{1.16}$$

$$\Omega_0 = \sqrt{\frac{E}{4\rho}\,\frac{R}{L^2}} \simeq 10^4\,[\text{rad.s}^{-1}.\text{m}]\,\frac{D}{L^2}, \tag{1.17}$$

with $(k_n\,L)$ the solution of eq. (1.15), and D the nanowire diameter. We considered the material properties of 3C-SiC evaluating the Young's modulus at $E \simeq 400\,\text{GPa}$, and a material density of $\rho = 3200\,\text{kg.m}^{-}3$. It follows the family of solutions that solve for the motion of the nanowire lateral displacement is given with,

$$r_n(y,t) = a_n\,u_n(y)\,e^{-i\,\Omega_n\,t}, \tag{1.18}$$

$$u_n(y) = \left[\cos(k_n\,y) - \cosh(k_n\,y) - \frac{\cos(k_n\,L)+\cosh(k_n\,L)}{\sin(k_n\,L)+\sinh(k_n\,L)}\,(\sin(k_n\,y) - \sinh(k_n\,y))\right], \tag{1.19}$$

where a_n is the amplitude coefficient associated to the resonant mode n, and we define the normal mode profile, u_n, represented in Fig. 1.7. It is important to note that the set of normal modes, $\{u_n\}_{n\in\mathbb{N}}$, forms an orthonormal basis in the Hilbert space of functions defined in $[0, L]$ under the scalar product, $\langle a,\,b\rangle = \frac{1}{L}\int_0^L a(y)\,b(y)\,\mathrm{d}y$. Meaning that, $\langle u_i,\,u_j\rangle = \delta_{i,j}$, with $\delta_{i,j}$ the Dirac coefficient. It can be shown that, from eq. (1.15), all normal modes equate in amplitude at the tip of the nanowire, $|u_n(L)| = 2$, $\forall n \in \mathbb{N}$.

Additionally, one can compute the eigenfrequency of the modes using the expression related to the kinetic and potential energy. Indeed, injecting the solution $r_n(y,t) = a_n\,u_n(y)\,e^{-i\,\Omega_n\,t}$ in eq. (1.1,1.2), one gets by energy conservation,

$$\Omega_n^2 = \frac{\int_0^L E\,I\,(\partial_y^2 u_n(y))^2\,\mathrm{d}y}{\int_0^L \rho\,S\,u_n^2(y)\,\mathrm{d}y}. \tag{1.20}$$

This formulation will be useful to estimate frequency shift with material properties that are temperature dependent, see sec. 6.3.

Modal analysis - response of a nanowire

The normal modes of the nanowires form an orthonormal basis. The nanowire lateral displacement dynamics can then be expressed as $\delta r(y,t) = r(y,t) - r_0(y) = \sum_n \delta r_n(t)\, u_n(y)$, where r_0 is the equilibrium position without external drive. Projecting the Euler-Bernoulli equation onto the normal mode basis (**Galerkin's method**), $\langle (1.10), u_n \rangle$, one gets the dynamic equation on the elements $\delta r_n(t)$.

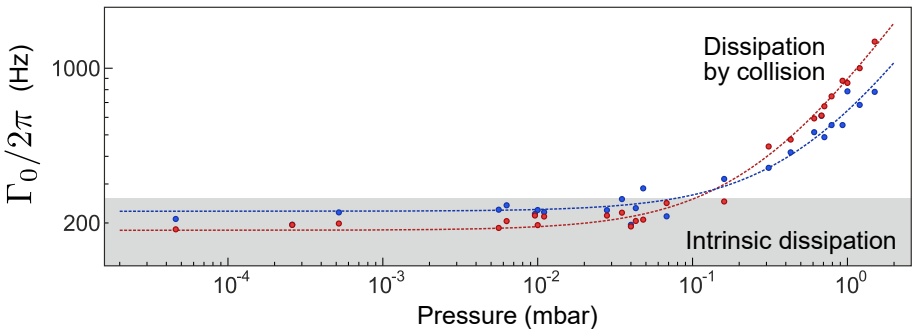

Figure 1.8: Acoustic dissipation measurement at different environment pressures, for both mechanical polarisation of the first mode family (in red the low frequency polarisation, in blue the high frequency one). The grey area represent the region where the intrinsic dissipation dominates, while above the dissipation by collision dominates. Adapted from [54]

In addition, for a more realistic description, we manually introduce a damping rate, Γ_n, associated to the mode n, that is related to several dissipation mechanisms. There are multiple contributions for the dissipation in our nanowires. At room pressure, the dominant mechanism has been shown to be **acoustic dissipation** [54]. For the first mode family, one can approximate the term,

$$\Gamma_0 \simeq 2\pi \frac{P}{\rho\, R} \sqrt{\frac{m_g}{k_B\, T}} \times 0.580, \tag{1.21}$$

where P is the pressure surrounding the nanowire, ρ the nanowire density, R its radius, m_g the molecular mass of the surrounding gas. Measurements were made during the PhD of L. Mercier de Lépinay, and shown in Fig 1.8.

More generally, as described in [55], each resonant mode acts as a harmonic oscillator, in which the dissipation is associated to a **Langevin** force, $\delta F_{\text{thm},n}$, which describes the coupling of the mode to a thermal bath, which will be more detailed in sec. 1.2.2. The dynamics of the mode can then be expressed,

$$\partial_t^2 \delta r_n(t) - \Gamma_n\, \partial_t \delta r_n(t) + \Omega_n^2\, \delta r_n(t) = \frac{1}{M_{\text{eff}}} \left(\langle f_{\text{ext}}, u_n \rangle + \delta F_{\text{thm},n} \right), \tag{1.22}$$

with M_{eff} the mode dynamical mass, and f_{ext} an external linear test force. In the frequency domain, this translates into,

$$\delta r_n[\Omega] = \chi_n[\Omega]\, \left(\langle f_{\text{ext}}, u_n \rangle [\Omega] + \delta F_{\text{thm},n}[\Omega] \right), \tag{1.23}$$

where we define the mode susceptibility $\chi_n[\Omega] = \left[M_{\text{eff}} \left(\Omega_n^2 - \Omega^2 - i\, \Omega\, \Gamma_n \right) \right]^{-1}$. Assuming each mode are independent, which is a good approximation in the case of our nanowires

due to their good quality-factor, the modal analysis states that the response of the nanowire is given by the coherent sum of individual mode response convoluted by the probing profile [55].

When observing the nanowire displacement, using a probe having a probing profile h, such that $\langle h, h\rangle = 1$, we can then express the nanowire response as $\delta r[\Omega] = \sum_n \delta r_n[\Omega]\,\langle h, u_n\rangle$.

In eq. (1.22) the force drive is projected onto the normal mode. Thus, depending on the linear distribution profile of the external force, $f(y)$, the drive can act very differently on different modes. We denote the external linear force such as, $f_{\text{ext}}(y,t) = F_{\text{ext}}(t)\,f(y)$, with $\langle f, f\rangle = 1$. In the case of an optical driving by the radiation pressure exerted by a focused laser beam on the nanowire, the force profile can be modelled as a Dirac distribution, since in practice the laser waist w_0 is in the order of 500 nm, thus much smaller than the nanowire length ($2R < w_0 \ll L$). In such case the external force is $f_{\text{ext}}(y,t) = F_{\text{rad}}(t)\,\delta(y - y_0)$, with y_0 the position of the laser along the nanowire, and we have $f_{\text{ext},n} = F_{\text{rad}}(t)\,u_n(y_0)$ which as no effect on a mode if the laser is positioned at one of its nodes, see Fig. 1.9.

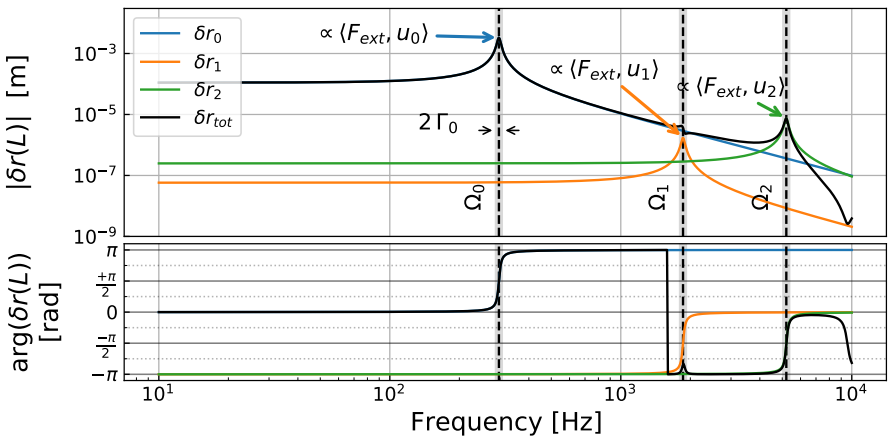

Figure 1.9: Bode diagram of the mechanical lateral deflection of the nanowire vibrating tip expected in response to a pointlike force modulation. We considered a nanowire of length 200 μm, and radius 120 nm, while the force modulation amplitude is taken at 1 pN. The external force is positioned here close to the node of the second mode profile.

A striking demonstration in [55], is that within the approximation of mode independence, we can attribute an effective susceptibility to the nanowire which relates to the mode susceptibility such as,

$$\delta r[\Omega] = \chi_{\text{eff}}[\Omega]\;\left(F_{\text{ext}}[\Omega] + \delta F_{\text{thm}}\right), \tag{1.24}$$

$$= \sum_n \chi_n[\Omega]\;\left(F_{\text{ext}}[\Omega]\langle f, u_n\rangle + \delta F_{\text{thm},n}\right)\;\langle h, u_n\rangle. \tag{1.25}$$

It was shown the effective Langevin force, δF_{thm}, also follows the fluctuation-dissipation theorem with χ_{eff}. In the case of our nanowires, the low frequency contributions of the modes in the susceptibility decrease rapidly with the mode number. One can then approximate most of the nanowire response, and noise temperature using the measure of the first mode family response.

The effective mass, M_{eff}, we referred in the above equations is defined with eq. (1.24), and often associated to the fundamental mode. In the more general case, when considering a mode family, n, the ef-

fective mass is expressed as,

$$M_{\text{eff},n} = M_{\text{nw}} \frac{\langle u_n, u_n \rangle}{\langle h,\, u_n \rangle^2}, \tag{1.26}$$

with $M_{\text{nw}} = \rho\, \pi\, R^2\, L$ the geometrical mass of the nanowire. When measured at the vibrating tip of the nanowire with a focused laser beam, $\langle h,\, u_n \rangle = u_n(L) = 2$, and $M_{\text{eff},n} = M_{\text{nw}}/4$, $\forall n \in \mathbb{N}$.

Dressing of a nanowire by a force

In reality, the nanowire identically vibrates in the two directions transverse to its axis, which in principle would have involved a 2-fold degeneracy of the modes due to the symmetries of the geometry. However, because of inhomogeneities inside the nanowire structure, as well as how the nanowire is clamped on its support, one always observe a breaking of symmetry and a lift of degeneracy of the lateral vibration resonant frequency when considering a mode family, n. For each mode the eigenvectors, see Fig. 1.10, are orthogonal in the absence of a force field gradient. Those **mechanical polarisations**, form a natural basis $(\mathbf{e}_1,\, \mathbf{e}_2)$, on which we can project the 2D motion of the nanowire lateral deformations.

In the presence of an external force field, $\mathbf{F}_{\text{ext}}$, the mechanical polarisation basis can be modified if the eigenmodes are subjected to cross-couplings in shearing force fields [54]. Considering the nanowire undergoing a small displacement within a spatially varying external force field, one can express the impact of the force field gradient on the considered mode dynamics using a first order development,

$$\mathbf{F}_{\text{ext}}(\mathbf{r}(t)) = \mathbf{F}_{\text{ext},n}(\mathbf{r}_0 + \delta\mathbf{r}), \tag{1.27}$$

$$= \mathbf{F}_{\text{ext}}(\mathbf{r}_0) + \delta\mathbf{r} \cdot \boldsymbol{\nabla} F_{\text{ext}}(\mathbf{r}_0) + o(\delta\mathbf{r}). \tag{1.28}$$

Denoting $g_{ij} \equiv \frac{1}{M_{\text{eff}}}\, \partial_i F^j_{\text{ext}}(\mathbf{r}_0)$, we can write the 2D lateral displacement dynamics of a considered resonant mode family, such as,

$$\partial_{tt}\delta\mathbf{r}(t) + \begin{pmatrix} \Omega_1^2 & 0 \\ 0 & \Omega_2^2 \end{pmatrix} \cdot \delta\mathbf{r}(t) - \begin{pmatrix} \Gamma_1 & 0 \\ 0 & \Gamma_2 \end{pmatrix} \cdot \partial_t \delta\mathbf{r}(t) + \begin{pmatrix} g_{11} & g_{12} \\ g_{21} & g_{22} \end{pmatrix} \cdot \delta\mathbf{r}(t) = \frac{1}{M_{\text{eff}}} \left(\delta\mathbf{F}_{\text{ext}}(\mathbf{r}(t)) + \delta\mathbf{F}_{\text{th}}(t) \right), \tag{1.29}$$

where $\Omega_i/2\pi$, $\Gamma_i/2\pi$ are the resonant frequencies and damping rate of the i-th polarisation. The new susceptibility of the systems becomes,

$$\underline{\underline{\chi}}^{-1}[\Omega] = M_{\text{eff}} \begin{pmatrix} (\Omega_1^2 - \Omega^2) - i\,\Omega\,\Gamma_1 + g_{11} & g_{12} \\ g_{21} & (\Omega_2^2 - \Omega^2) - i\,\Omega\,\Gamma_2 + g_{22} \end{pmatrix}. \tag{1.30}$$

In this sense, the gradient of force, dresses the nanowire dynamics.

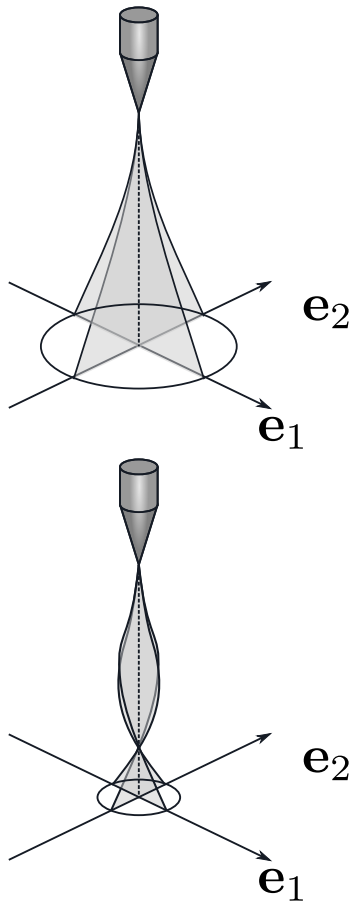

Figure 1.10: Schematic of a nanowire mechanical orthogonal polarisation for the first and second vibration mode.

The different spatial variation of the force gradients will have different impact on the nanowire response, see Fig 1.11. Thus recording how the mechanical polarisation modes change when the nanowire position is dressed by the force, allows us recover the local gradient of the acting force field.

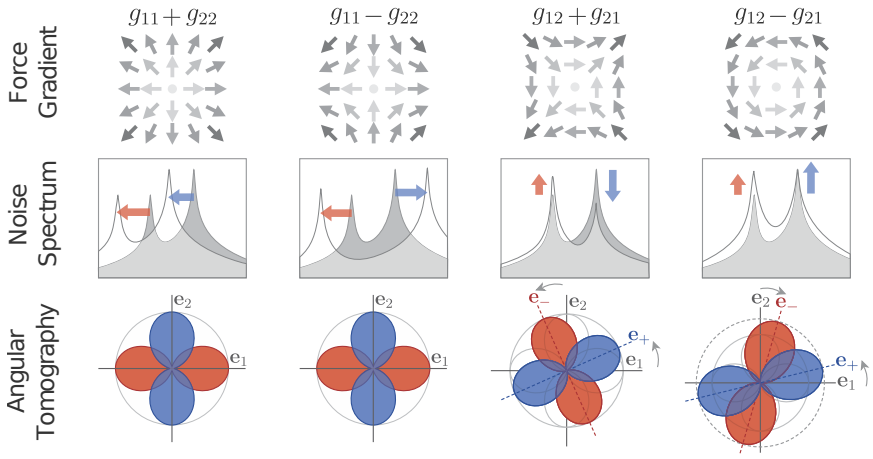

Figure 1.11: Impact of the different elements of the 2D force fields gradients on the nanowire dynamics. The noise spectral densities, are obtained when using a read-out vector oriented between both polarisations. From [54].

1.2.2 Brownian motion of the nanowire

An oscillator at finite temperature without an external drive presents position fluctuations due to thermal fluctuations. Thermal noise thus sets some fundamental limit to force sensitivity when using resonators as sensors. For instance the thermal motion of the coating used in gravitational waves detection [56], limits their sensitivity.

Thermal noise and mechanical damping are closely linked. Indeed, when an oscillator is in equilibrium with a thermal bath, the **Fluctuation-Dissipation** theorem [57, 58] applies and relates the observed position fluctuations, the bath temperature and the dissipation of the system (the damping in the case of an oscillator). Not accounting for environmental damping mechanism, there are various sources of internal dissipation in a mechanical oscillator. Concerning SiC nanowires, one can consider the non-exhaustive list : viscoelastic damping (internal friction) [59, 60, 61, 62], point defects, clamping losses [63], Two-Levels-Systems (see sec. 6.3). In our experiments, the mechanical susceptibility has been verified to follow the one of a viscously damped oscillator on all the frequency and temperature ranges that we will be exploring in the following. No signature of other types of dissipation (such as solid friction) could be observed.

In the case of our resonators, the thermal fluctuation of the nanowire position is also called its **Brownian motion**. It is modelled by an effective stochastic thermal force, the **Langevin force** which follows the Langevin equation [54, 64], and will be denoted $\delta F_{\text{thm}}(t)$. We denote T the temperature of the thermal bath and Γ the damping coefficient of the oscillator.

Properties of the Langevin force

By construction, the Langevin force follows a Markovian random process and has null time average: $\langle \delta F_{\text{thm}} \rangle_t = 0$. The spectral density of the Langevin force is defined as,

$$2\pi\,\delta(\Omega + \Omega')\,S_{F_{\text{thm}}}[\Omega] = \langle \delta F_{\text{thm}}[\Omega]\,\delta F_{\text{thm}}[\Omega'] \rangle, \tag{1.31}$$

and its value is given by,

$$S_{F_{\text{thm}}}[\Omega] = 2\,M\,\Gamma_{\text{m}}\,k_B\,T, \tag{1.32}$$

with $\Gamma_{\text{m}}/2\pi$ the damping rate of the mechanical oscillator. The above spectral density is governed by the **Fluctuation-Dissipation** theorem [57, 58, 65], such as,

$$S_{F_{\text{thm}}}[\Omega] = -\frac{2\,k_B\,T}{\Omega}\,\text{Im}\left(\frac{1}{\chi[\Omega]}\right), \tag{1.33}$$

with $\chi[\Omega] = \left[M\,(\Omega_{\text{m}}^2 - \Omega^2 - i\Omega\,\Gamma_{\text{m}})\right]^{-1}$ is the susceptibility of an harmonic oscillator with resonant frequency $\Omega_{\text{m}}/2\pi$ and damping rate $\Gamma_{\text{m}}/2\pi$. We note that the viscously damped susceptibility is also associated to a zero memory bath since,

$$C_{F_{\text{thm}}}(\tau) = \langle \delta F_{\text{thm}}(t)\,\delta F_{\text{thm}}(t+\tau) \rangle_t = 2\,M\,\Gamma\,k_B\,T\,\delta(\tau), \tag{1.34}$$

Thermal fluctuation of the nanowire position

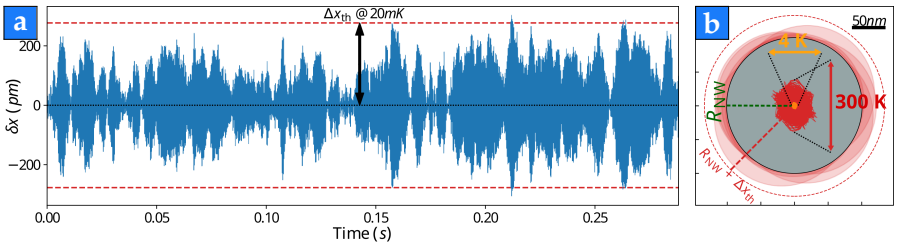

Figure 1.12: Simulation of the Brownian thermal motion of a SiC nanowire: (a) temporal evolution of the position of the resonator extremity, for a 300 µm long, 200 nm thick NW thermalised at 20 mK. (b) Comparison between the NW diameter and the spreading of the thermal fluctuations at 300 K and 4 K. Adapted from [66].

The spectral noise of the nanowire tip motion due to the coupling with the thermal bath when considering a given mode family, is given by,

$$S_{\delta\mathbf{r}}[\Omega] = \left|\underline{\underline{\chi}}[\Omega]\right|^2 S_{F_{\text{thm}}}[\Omega], \tag{1.35}$$

$$= \left|\underline{\underline{\chi}}[\Omega]\right|^2 2\,M_{\text{eff}}\,\Gamma\,k_B\,T, \tag{1.36}$$

where M_{eff} is the effective mass of the oscillator, $\Gamma/2\pi$ its effective damping rate and $\underline{\underline{\chi}}$ is the effective susceptibility associated to the mode [55]. In the case of our nanowires, the fundamental mode dominates the dynamics of the lateral displacement at the tip on a broad

frequency range. The spreading of the nanowire tip displacement fluctuation is given by the variance of the position noise. Integrating the PSD over all frequencies we get,

$$\Delta r^2 \equiv \int_{-\infty}^{\infty} S_{\delta r}[\Omega] \, \frac{d\Omega}{2\pi} = \frac{k_B}{M_{\text{eff}} \, \Omega_m^2} \, T, \tag{1.37}$$

with Ω_m the mechanical resonance of the first mode family. Thus, the size of the area spanned by the oscillator is $\Delta r = \sqrt{k_B \, T / (M_{\text{eff}} \, \Omega_m^2)}$, see Fig. 1.12.

When considering the dynamics of a mode, it can be assimilated as a mechanical harmonic oscillator. In its quantum ground state, it is expected to observe fluctuation of its position and momentum due to the Heisenberg's uncertainty principle. In such case, treating the position and momentum as quantum operators, one can express the **zero point fluctuations (ZPF)** of the mechanical oscillator to be,

$$\delta r_{\text{ZPF}} = \sqrt{\frac{\hbar}{2 \, M_{\text{eff}} \, \Omega_m}}, \qquad p_{\text{ZPF}} = \sqrt{\frac{\hbar \, M_{\text{eff}} \, \Omega_m}{2}}, \tag{1.38}$$

where p_{ZPF} is the zero point fluctuations momentum of the mode. The ZPF of the position typically falls in the pm range for our nanowires. In the following, even if the temperature of the nanowire will be cooled down cryogenic temperatures, we will always have a large remaining thermal phonon number populating each mode.

1.3 β-Silicon Carbide nanowires

Silicon carbide (SiC) is used in a variety of application [67]. It is a hard ceramic, morphing into a multitude of polytypes in its solid state. Among those, the most occurring one is the α-SiC (or 6H-SiC) which is a hexagonal phase, while the β-SiC is the only polytype with a SiC cubic structure, see Fig. 1.13a. Due to its low thermal expansion, hardness and good thermal conductivity, its usage can spread from automobile application in brake disks, to nuclear fuel coating, as well as the base material for mirrors in astronomy [68, 69]. The

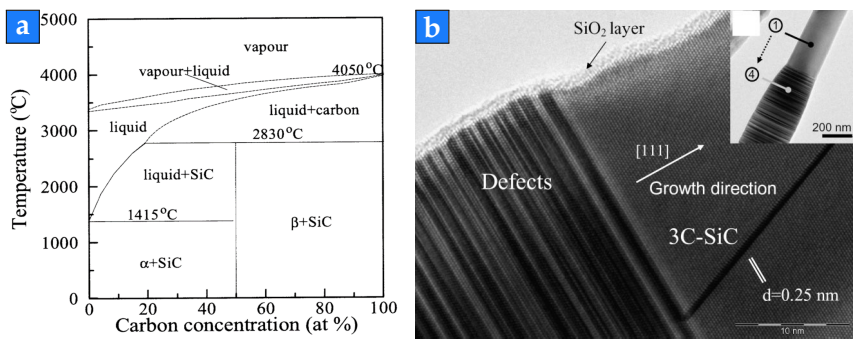

Figure 1.13: (a) Phase diagram of the different SiC polytype phases [70]. (b) TEM image of a region of a SiC nanowire close to a structural defect [71].

rising interest in using SiC as the main component in microelectronics and transistor fabrication, stems from its high thermal conductivity that allows for good heat transfer, which raises the question on how

the heat transfer is modified by shrinking the size of the components down to the nanometric scale. Moreover, those studies were heavily aimed at characterising the material from room to high temperature. Developing methods to study the material and its thermal properties at cryogenic temperature is both challenging and relevant to better understand the behaviour of nanoscale structure of SiC.

In our experiments, we mainly use the β polytype phase SiC, also known as the **3C-SiC**. The longitudinal axis of our nanowires is aligned with the growth direction, along the [111] direction. Our nanowires have diameters usually ranging from 100 to 500 nm. Impurities and growth defects can appear along the nanowires, and visible with a SEM or more precisely with a TEM microscope, see Fig. 1.13b. They have a mass density $\rho = 3200$ kg.m^{-3}, and a Young modulus of approximately $E = 400$ GPa.

For thermal studies, it is important to know the temperature dependency of the main material properties, such as its thermal expansion, its heat capacity or its conductivity, but also other properties that can structure the nanowire interaction with light, such as its reflective index. The thermodynamic properties of SiC will be addressed in the last section of chap. 3, while the optical properties are presented in chap. 2.

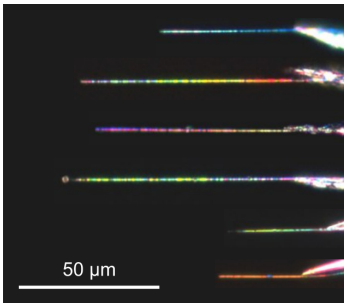

Figure 1.14: Picture under an optical microscope of several nanowires under a given polarised white light. The colour originates for the resonant interaction of the SiC nanowires with light, and depends on the nanowires diameter. The granularity stems from the inhomogeneities in the crystalline structure of some nanowires, as well as possible defects.

1.4 Optical readout and projective measurements

Looking at our 3C-SiC nanowires under an optical microscope illuminated with a white light, see Fig. 1.14, one can observe the nanowires to be coloured very differently. This is due to their resonant interaction with light. Indeed, silicon carbide nanowires have a high refractive index, $n_{\text{SiC}} \simeq 2.6$ [72, 73], which given their diameter range (100 - 500 nm) can sustain several light oscillations across their cross-section. The nanowires interact resonantly with the incident light following well the **Mie theory** [74], which will be more detailed in chap. 2.

Due to this high interaction with light, we designed optical readout protocols to measure the 2D deformations of the nanowire vibration. Those protocols rely on a projective measurement, meaning that the measured quantity (photon flux modulation encoded on the photodiode output channels) is proportional to the nanowire vibrations projected on the vectorial readout profile, $\mathbf{h}$. When using focussed laser beams, the readout profile extension is of the size of the laser waist at the focal point (approximately 500 nm for focused beam). It can thus be modelled by a Dirac distribution, $\mathbf{h}(y) = \delta(y - y_0)\,\mathbf{e}_\beta$, where y_0 is the position of the laser along the nanowire axis and $\mathbf{e}_\beta$ the **measurement vector**. We will see that the latter will be connected to the gradient of the reflectivity maps obtained when scanning the nanowire rest position with respect to the laser spot. The projected displacement thus takes a local character, and denoted,

$$\delta r_\beta = \langle \delta\mathbf{r}, \mathbf{h} \rangle = \delta\mathbf{r}(y_0) \cdot \mathbf{e}_\beta. \tag{1.39}$$

1.4.1 Free space measurement

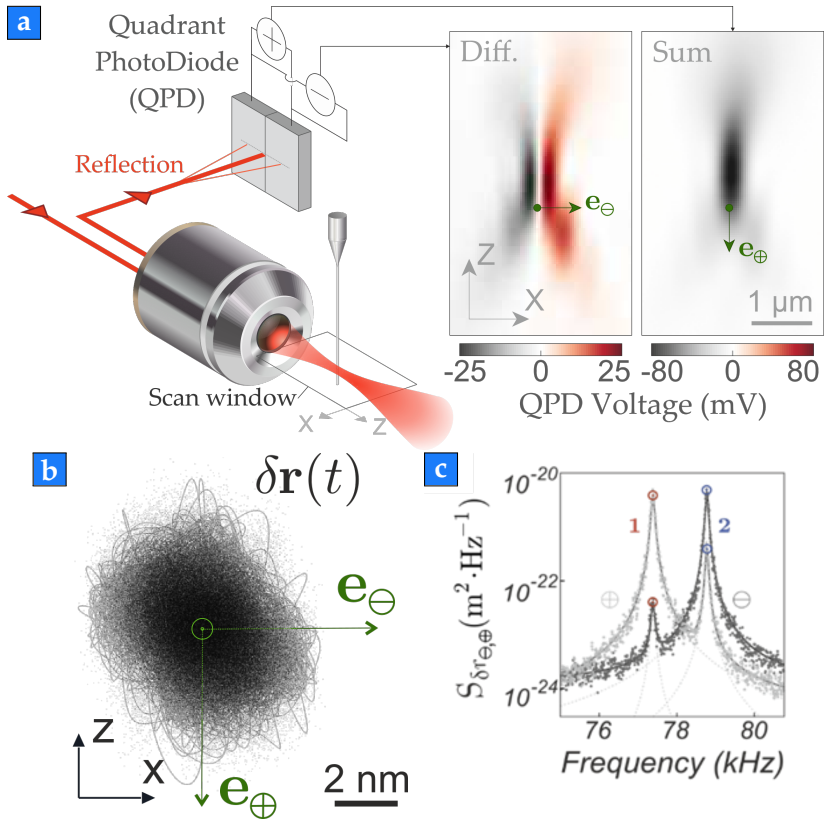

Figure 1.15: Free space optical readout scheme. (a) A laser beam is focused on the nanowire using a microscope objective. The reflected light is collected and sent to a quadrant-Avalanche Photo-Diode (Q-APD) where the signal is processed. A scan of the nanowire position in the laser waist allows generating 2D maps for the sum and difference channel. (b) 2D representation of the reconstructed Brownian motion displacement of the tip of the nanowire. (c) Power spectral density (PSD) of the projected Brownian motion along the e_+ and e_- measurement vectors.

In the free space configuration, we focus a laser on the nanowire using a microscope objective. The light scattered by the nanowire is collected back by the objective and collimated at the middle of the **Avalanche Quadrant Photo-Diode** (AQPD). Scanning the nanowire position inside the laser waist, we reconstruct the 2D XZ-maps for the sum and difference output channel of the AQPD. One can relate the nanowire displacement in those fields to a modulation of the output intensity. The intensity gradients in those maps give us the measurement vectors. Placing the nanowire at a given position, see Fig. 1.15a, gives us two projections of the nanowire displacements and allows us to reconstruct its trajectory in the 2D plane, see Fig. 1.15b.

From the temporal signal, we measure the **Power Spectral Density** (PSD), giving us access to the resonant frequencies of the nanowire modes, their quality factor and the noise temperature. However, this scheme needs to directly bring the laser beam to the nanowire in free space, using transparent windows between the closed environment surrounding the nanowire and the optic table where the detectors are placed. This configuration is not optimal when dealing with experiments inside a cryostat, where we use optical fibres to carry the signal in and out of the cryostat.

1.4.2 Interferometric measurement

In chap. 4, we will detail the readout scheme when using fibred interferometric objectives developed within the Institute. In this readout

scheme, the probe laser beam is injected inside a fibre whose output is collimated by a set of two lenses, see Fig. 1.16. When moving the nanowire inside the laser focal point, because part of the collected reflected light is injected back into the fibre, we only have one readout channel at our disposal. The only information we get is the collected reflection intensity. Nonetheless, we use the dephasing acquired by the light during its return trip from the reflection to generate an interference on the photodetector. Scanning the nanowire position inside the laser waist, returns an interference pattern that reproduces the structure of the focussed light field in amplitude and in phase.

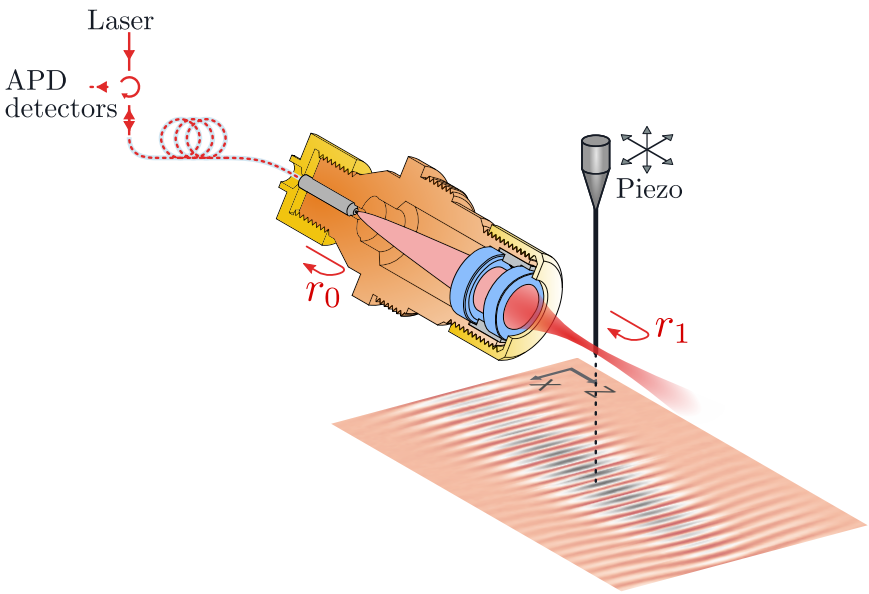

Figure 1.16: Interferometric optical readout scheme. A laser injected to a fibre is focused on the nanowire using a two lenses objective. A first reflection occurs at the fibre end within the objective (with reflectivity r_0). Part of the reflected light by the nanowire (with reflectivity r_1) is injected back into the fibre and sent to a photodetector, after passing through an optical circulator.

In this scheme, the measurement vector is given by the gradient of the reflected photon flux measured along the interference pattern. What we lose in having only one measurement vector, we gain by increasing our sensitivity to the nanowire displacements. Indeed, the interferometric nature of the readout structures the readout efficiency at a scale given by the radiation wavelength, and not by the laser spot size, as in the free space readout scheme.

1.5 Overview of past experiments realised in the host group

Because of their low mass, high aspect ratio, high stiffness and good thermal conductivity, SiC nanowires have been used as highly sensitive force sensors in our group. Adapting the nanowire diameters and the aspect ratio allows to use the nanowires in a variety of applications. Figure 1.17 presents a summary of the mechanical properties dependence and the optical readout efficiency of the nanowires as a function of their length and diameter. The force sensitivity is limited by the thermal fluctuations of the nanowire, and equates the Langevin

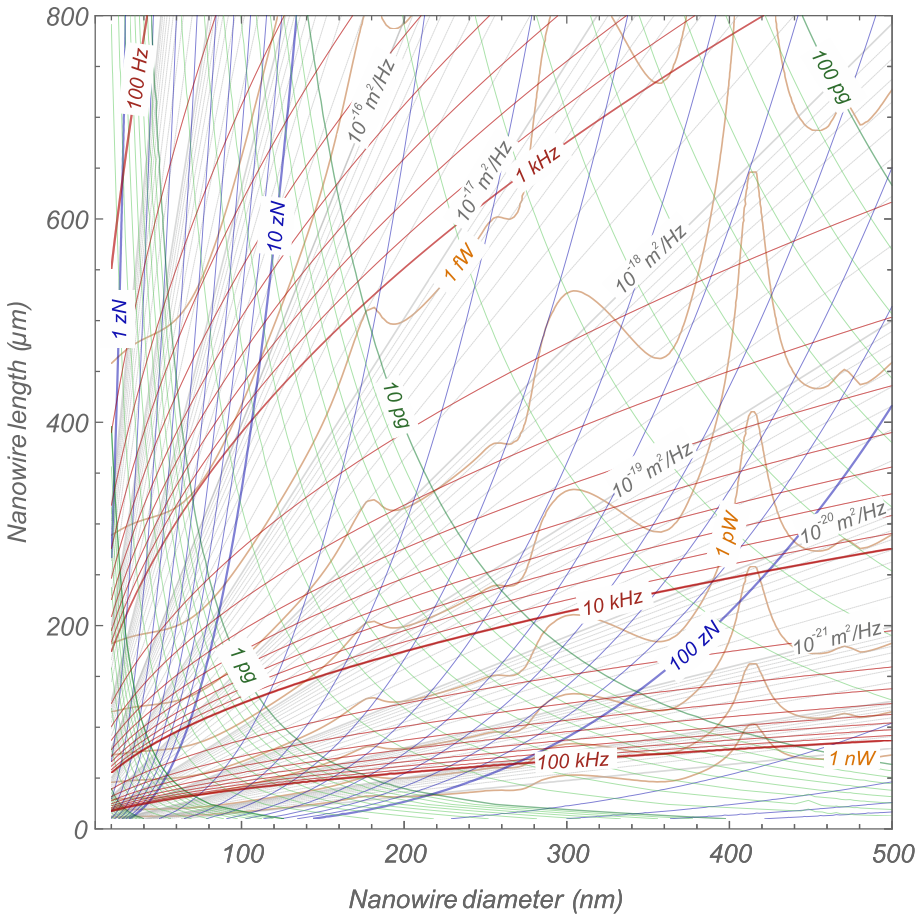

Figure 1.17: Abacus : Mechanical properties of the nanowires (assumed to be perfect cylinders) depending on their geometry. In red the mechanical resonance of the fundamental modes. In green the effective mass. In blue the minimum force sensitivity at 20 mK, while in grey the resonant thermal noise amplitude at 20 mK. We assumed a constant quality-factor over all the map ($Q = 10^5$). We represent in orange the minimum optical power needed to detect the thermal noise at 20 mK while having a signal to shot noise ratio of 1. From [66]-SI.

force noise, which gives,

$$\delta F_{\text{min}} = \sqrt{2\, M_{\text{eff}}\, \Omega_m\, k_B\, T/Q} \propto \frac{D^{3/2}}{L^{1/2}}, \tag{1.40}$$

using the double-sided spectral convention, with M_{eff} being the effective mass, Q the resonator quality factor, $\Omega_m/2\pi$ the mechanical resonance frequency, k_B the Boltzmann's constant and T the temperature of the thermal bath, while D and L are the diameter and length of the nanowire respectively. The thermal noise at resonance is given by, $S_{\delta r_\beta}[\Omega_m] = 2\, k_B\, T\, Q/(M_{\text{eff}}\, \Omega_m^3) \propto L^5/D^5$.

The nanowire force sensing platform offers a certain variety of applications, with demonstrated capacity to probe optical, electrostatic and proximity force fields, which can each be greatly optimised with a careful pre-selection of the nanowire geometry. Sensitivity to 10 aN/$\sqrt{\text{Hz}}$ has been achieved at room temperature during the thesis of A. Gloppe [75]. In such context, 2D vector force field measurements have been carried out using pump-probe measurements to map the optical force exerted on a nanowire plunged into a focused laser beam [75], see Fig. 1.18b. The electrostatic force field of an AFM tip was also measured [54], by measuring the perturbation induced on the nanowire mechanical properties by the force field gradients produced by the tip, see Fig. 1.18d.

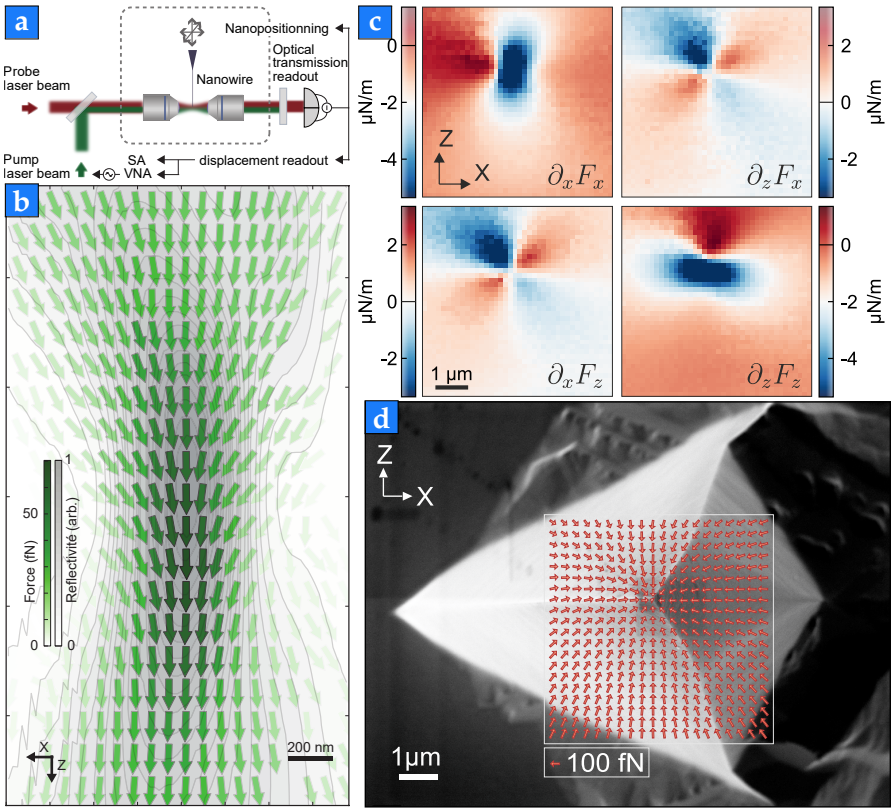

Figure 1.18: (a) Measurement setup for mapping the optical force exerted on the nanowire within the waist area, as shown in (b) which was measured in a pump-probe experimental configuration [75]. (c) Maps of the 2D force field gradients generated by a voltage biased AFM tip [54]. The integrated force field produced by a 1 V bias voltage is shown in (d) where it is super-imposed on a STEM image of the tip.

Cooling down the nanowire reduces its thermal noise while also increasing its quality-factor. Force sensitivity, up to the 40 $zN/\sqrt{Hz}$ at 40 mK has been demonstrated, [66]. To give an order of magnitude, this level of sensitivity corresponds to the electrostatic Coulomb interaction between two electrons separated by 100 μm. Our recent measurements realised during the PhD of P. Heringlake and H. Weltz have shown that it is possible to generate charges at the nanowire extremity using optical wavelength close to the semiconductor gap of the nanowire, which suggests that the nanowire could prove useful at dilution temperatures to investigate nano-electronic samples.

Selecting the nanowire diameter is also important to tune the optical interaction with light. Going beyond the initial optomechanical experiments realised in a focused laser beam, experiments making use of optical cavities were subsequently developed. There the nanowire is inserted in the intracavity field of high-Q microcavities, which can be mapped out using the parametric interaction along both directions: first by measuring how the nanowire perturbs the intracavity field, then by measuring the optomechanical force exerted on the nanowire, see Fig. 1.19a. This experiment demonstrated the possibility to reach the single photon regime of cavity optomechanics, at the condition to reduce the nanowire thermal noise [66, 76]. This can be largely achieved in the dilution cryostat used during this PhD since a temperature of only 4K should be sufficient. However, the implementation of such a fibre microcavity is very complex in the cryogenic environment, and this lead to the investigation of the optomechanical coupling to another class of microcavity, such as a photonic-crystal cavity, which

is the current PhD subject of C. Zhang, see Fig. 1.19b.

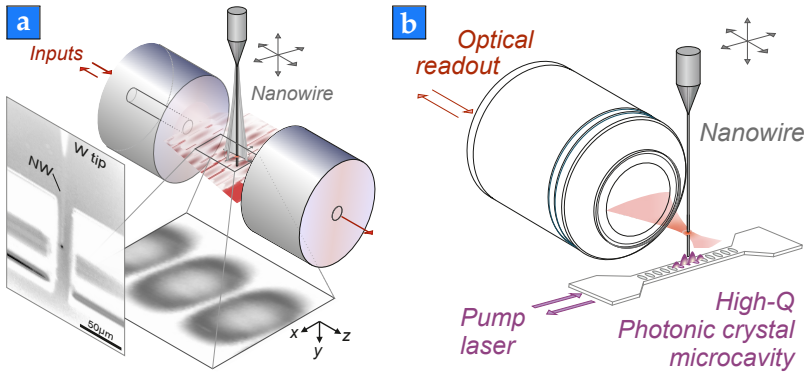

Figure 1.19: Cavity nano-optomechanics: (a) a nanowire is inserted in the mode volume of a fibre microcavity [66, 76] during the PhD of F. Fogliano and postdoc of A. Reigue and (b) inserted in the mode volume of a photonic crystal developed at C2N in the group of R. Braive during the PhD of C. Zhang.

In parallel, the group functionalised the nanowire with diamond nanocrystals hosting single nitrogen-vacancy defects in order to study the parametric coupling of the mechanical modes of the nanowire to the two-level systems formed by the NV-centre spin, see Fig. 1.20a. This coupling which arises in a strong magnetic field gradient, as in the Stern and Gerlach experiment, would allow to project the spin-state of the NV defect onto the nanowire vibrations [77, 78].

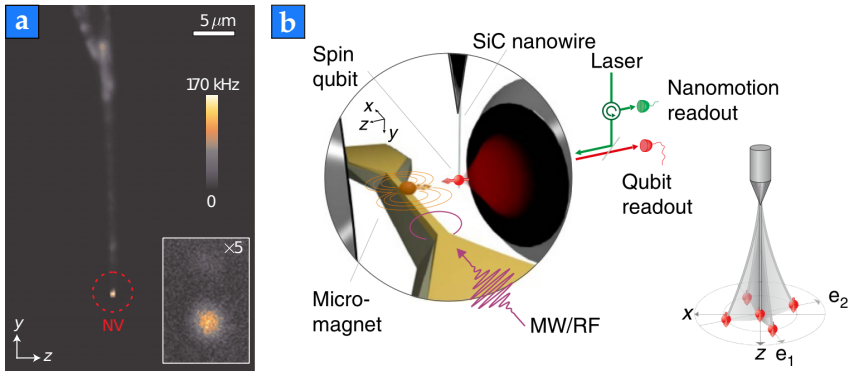

Figure 1.20: Hybrid spin-nanomechanical system. (a) Fluorescence image of a nanowire functionalised with a single NV defect. (b) Measurement setup used for investigating the spin-nanowire interaction in a strong magnetic field gradient, leading to the observation of an equivalent phononic Mollow triplet [77, 78].

Significant improvements on the 2D force field imaging using coherently driven trajectories instead of random thermal noise motion [79] led to faster and finer measurements of force fields above nanostructure and approaching a quasi-realtime measurement rate (10/s). It allowed in particular the investigation of electrostatic and proximity force fields, as well as the investigation of electrostatic patches due to sample surface imperfection, see Fig. 1.21a. Those patches generate an electrostatic force background that can hinder the observation of weaker proximity forces, such as Casimir forces. Strategies to compensate the electrostatic background have been developed, such as on-chip field compensation using external electrodes as shown in Fig. 1.21b. Adding a strong electrostatic field around the nanowire, allowed the observation of a so called electro-optical force, which originates from the light induced creation of electron-hole pairs when illuminating the nanowire with a strong optical pump. Part of the charges being channelled along the nanowire and leading to a lateral force in presence of electrostatic fields. The characterisation of this phenomenon is primordial in order to gain fine control over the field compensation for proximity force measurement and was the topic of

H. Weltz PhD thesis.

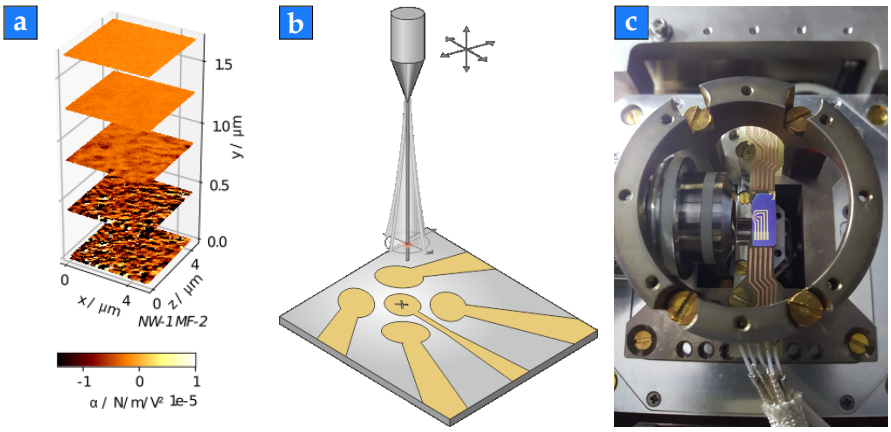

Figure 1.21: (a) Measurement of the force field divergence at different altitude over a planar metal surface. (b) Illustration of the sample design with control electrodes in order to generate arbitrary homogeneous electrostatic field around the nanowire, and (c) picture of the implemented chip inside the measurement setup.

All in all, the variety of applications using nanowires in our group allowed to highlight several intricate phenomena that need to be better characterised in order to push forward finer force sensing measurements. The implementation of the advanced force sensing protocols and measurement techniques (developed at room temperature) at the cryogenic temperatures, should allow for the investigation of new physics at low temperature, and was a strong incentive to this PhD project. In particular, it is necessary to carefully investigate the impact of the optical probe on the nanowires, which becomes extremely invasive at dilution temperature and was the central objective of the PhD.

1.6 Chapter summary

Using nano-mechanical oscillators to measure forces is not new. We started this chapter presenting a non-exhaustive list of different experiments using nano-sized mechanical actuators used to investigate physics at the nanoscale. However, we need to account that in every mechanical oscillator system there is a spurious vibrational noise due to the finite temperature of those resonators, which ultimately limits the force sensitivity of the system. In addition, at those scale, the readout method that probes the nano-oscillator state brings noise and can have a back-action effect subsequent to the optomechanical coupling (often used to improve the readout sensitivity of the mechanical system). The perturbations brought by the probe is especially important to be tackled with at cryogenic temperatures (used for the reduction of the thermal noise), as it can also become a source of heat killing the purpose of cooling down the nanoresonator. This task is particularly difficult since at low temperature the heat propagates exotically in nanostructures. We listed multiple experiments trying to better understand and measure the heat propagation at the nanoscale, accounting for the decoupling of multiple heat conduction mechanisms.

Our work fits in those fields of research by trying to better understand the thermomechanical properties of our nanomechanical systems, when they are cooled down. Doing so, we hope to reduce the probing perturbation while increasing the force sensitivity of our

nanowires. Ultimately, we aim at taking advantage of the low noise environment, provided by cooling down the whole optomechanical setup, in order to access new physics at low temperature with our resonators.

We continued the chapter presenting the general feature and properties of our 3C-SiC nanowires, as well as the mathematical framework we use to describe the mechanical response of our resonators to a modulated force and a force field gradient. The different measurement methods we use (free space and interferometric), allow us to carry out a variety of experiments. From force field measurement, to small mode volume cavity-optomechanical coupling, as well as hybrid spin-nanomechanical systems, we illustrated the large range of application in using quasi-1D nanomechanical oscillators in optomechanical coupling.

CHAPTER 2

LIGHT-NANOWIRE INTERACTION AND INTERNAL MIE RESONANCES

Contents

Introduction 23
2.1 Optical properties 24
2.2 Mie resonances 25
2.2.1 Description of the EM Fields 25
2.2.2 Radiometric quantities associated to the scattering of a nanowire 30
2.2.3 Optical cross-section 35
2.3 Investigation of angular scattering diagrams 36
2.3.1 Measurement setup 36
2.3.2 Diagram evolution with wavelength 39
2.3.3 Reflectivity 42
2.4 Perspective 43
2.4.1 Thermal modulation of Optical Forces 43
2.4.2 Nanowire under Gaussian illumination 44
2.5 Chapter summary 44

Introduction

In this chapter, we detail the specificities of the interaction between the light and our nanowires. Due to their large refractive index (approximately 2.6), our SiC nanowires can sustain internal optical resonances in the visible domain, which strongly affect their interaction with the focussed laser beams we employ for optical readout or for local excitation. Those Mie resonances are responsible for the colourful images of the nanowires one can obtain in a microscope under white light illumination, see Fig. 2.1, which originate from their spectrally selective interaction with the light, but also from the peculiar scattering diagrams which are associated to those resonances. In this chapter we present an experiment that was built to investigate the scattering properties of the nanowire, to measure their scattering diagrams for different colours. Beyond providing a better understanding

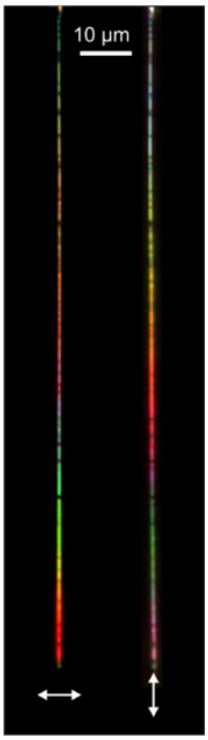

Figure 2.1: Microscope image of the same nanowire under polarized white light (left perpendicular, right parallel), using a 50X objective. The multiple colours along the nanowire are due to its conical form.

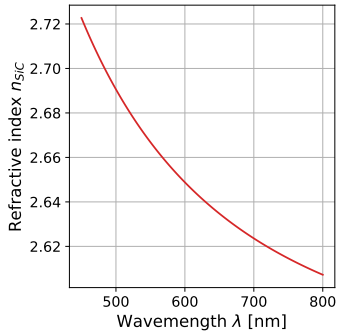

Figure 2.2: Refractive index of 3C-SiC with the incident wavelength.

of the light-nanowire interaction, which is essential for many applications in the group experiments, those measurements also open the way towards advanced observations, such as their impact on the optomechanical force field experienced by the nanowire.

2.1 Optical properties

The dependence of the SiC refractive index on the light wavelength [72], can be adjusted with,

$$n = 2.5538 + 3.42 \times 10^{-14}\,\lambda^{-2}, \tag{2.1}$$

where λ is the propagating wavelength expressed in vacuum in [m], see Fig. 2.2. Although decreasing with the wavelength, the average refractive index is high enough for visible light to sustain internal resonances within our nanowire of diameter ranging from 150 nm to 600 nm. The variation of the refractive index with temperature will ultimately also impact the optical readout. One can find in the literature the thermo-optic coefficient of 3C-SiC to be $\alpha_n(T) = \frac{1}{n(T)} \left.\frac{\partial n}{\partial T}\right|_T$, which can vary around $2.9 - 5.7 \times 10^{-5}$ K^{-1} [80, 81] at room temperature. This feature will be dealt in more detail in chap. 5.

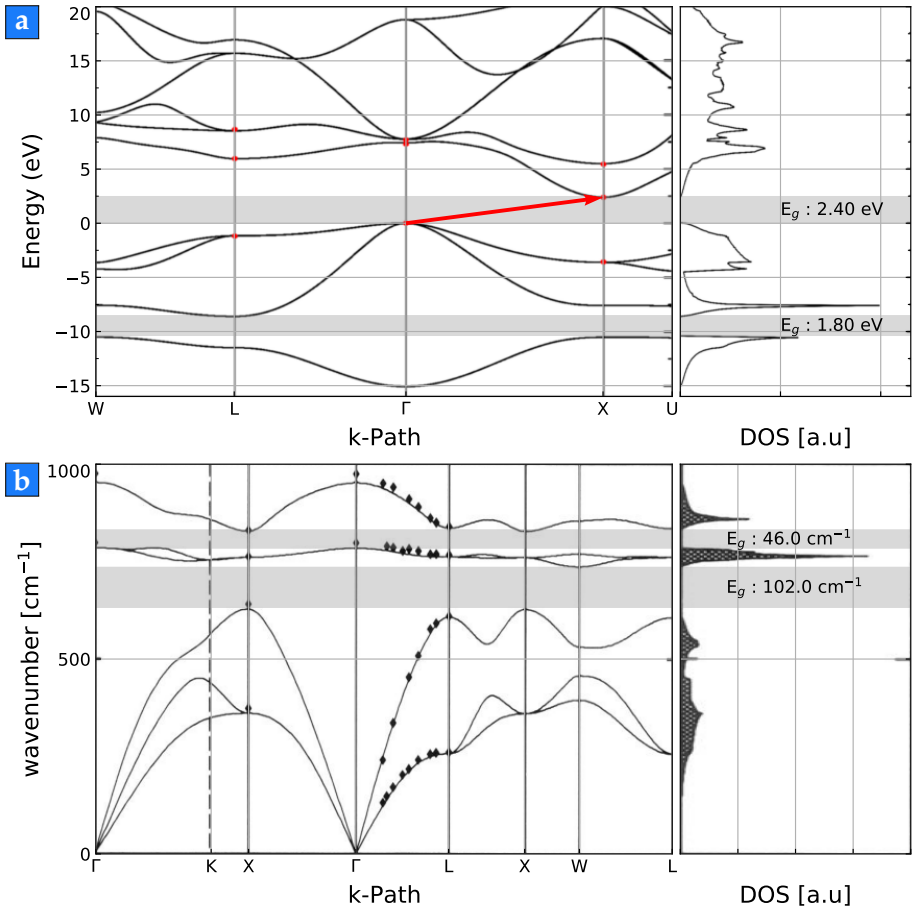

Figure 2.3: (a) Electron dispersion band-diagram for 3C-SiC with the indirect bandgap (red arrow) and its associated Density of State for 3C-SiC [82]. (b) 3C-SiC phonon-dispersion band diagram [83].

3C-SiC has an indirect electronic bandgap at around 2.40 eV, see Fig. 2.3a. This means it starts to increasingly absorb light of wavelength

below 515 nm. As the band gap varies with the temperature, so the absorption at a given wavelength, see Fig. 2.4.

For comparison, we show the phonon band diagram that is associated to the heat propagation properties of 3C-SiC.

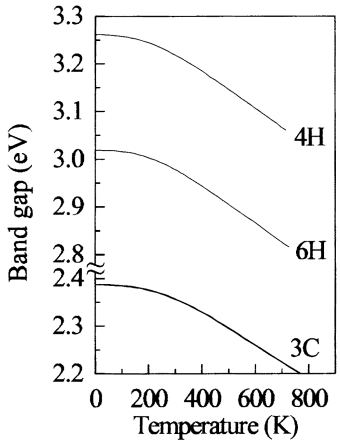

Figure 2.4: Evolution of the SiC indirect band gap with temperature [84].

2.2 Mie resonances

In this section, we will briefly derive the main expressions used for characterising the nanowire interaction with light.

Gustave Mie initially developed the theory in 1908, to explain the diversity of colours observed for nanoscale gold colloidal particles of the same material but differing in size [74]. However, Mie was not the first to tackle such problem. Before him, Alfred Clebsch [85], Ludvig Lorenz [86, 87], and Peter Debye [88], had already given great contribution in solving light scattering by a perfect sphere. On the other hand, Peter Debye is better known for developing a similar theory to describe the radiation pressure on astronomical dust. History retained Mie as the name of the scattering regime for nanoscale objects whose dimensions are comparable to the optical wavelength, but previous contributions should still be acknowledged.

As a general description, Mie theory is an exact resolution of the Maxwell's equations, accounting for boundary condition, when considering the scattering of light by nanometric particles. For objects of non-perfect geometry, Mie scattering constitutes a good first order approximation of the scattering properties of such object.

In the following, we will model the nanowire as an infinite cylinder illuminated by a transverse light field, a situation that is very close to the experimental case, as long as the laser is not too close to the nanowire extremities. The mathematical development will closely follow the one of Ref. [89].

2.2.1 Description of the EM Fields

From now on, we closely follow the derivation of Mie theory for an infinite cylinder found in [89], illuminated by a plane wave with normal incidence. Let us consider an infinite cylinder along the y-axis, of radius R, and refractive index n, see Fig. 2.5. We consider the nanowire surrounded by vacuum. Due to the translational symmetry, we can remove the y-dependence for the physical quantities. Considering a monochromatic incident plane wave, with wave-vector, $k_0 = \omega/c$, ω being the radiation pulsation while c the light celerity. We decompose the incident radiation over the parallel and orthogonal polarizations ($\mathbf{E}_i^{\parallel}$, $\mathbf{E}_i^{\perp}$) with respect to the nanowire that are respectively oriented along $\mathbf{e}_y$ and $\mathbf{e}_x$.

The electromagnetic field follows the Maxwell's equations inside ($\mathbf{E}_1, \mathbf{H}_1$) and outside ($\mathbf{E}_2, \mathbf{H}_2$) the nanowire, which can be written in absence of free charges and currents as,

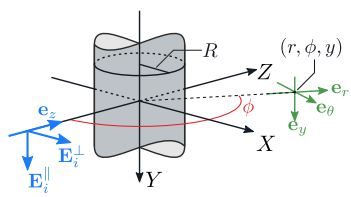

Figure 2.5: Chosen system of axis for Mie theory calculation, in the case of plane wave illumination with normal incidence.

$$\nabla \cdot \mathbf{E}_1 = 0, \quad \nabla \cdot \mathbf{H}_1 = 0, \quad \nabla \times \mathbf{E}_1 = +i\mu_0\omega\mathbf{H}_1, \quad \nabla \times \mathbf{H}_1 = -i\epsilon_r\,\epsilon_0\omega\mathbf{E}_1, \tag{2.2}$$

$$\nabla \cdot \mathbf{E}_2 = 0, \quad \nabla \cdot \mathbf{H}_2 = 0, \quad \nabla \times \mathbf{E}_2 = +i\mu_0\omega\mathbf{H}_2, \quad \nabla \times \mathbf{H}_2 = -i\epsilon_0\omega\mathbf{E}_2, \tag{2.3}$$

with μ_0 the vacuum permeability, ϵ_0 the vacuum permittivity and ϵ_r the relative permittivity of the medium. We remind the relation between the total magnetic field and the induced one: $\mathbf{B}_{1,2} = \mu_0\,\mathbf{H}_{1,2}$. At the interface of two media, although the quantities are strictly speaking continuous, they vary over space scale much smaller than the radiation wavelength in question. They thus appear discontinuous and justify the boundary conditions when we are only interested in macro-scale quantities,

$$[\mathbf{E}_1(\mathbf{r}) - \mathbf{E}_2(\mathbf{r})] \times \mathbf{e}_n = 0, \tag{2.4}$$

$$[\mathbf{H}_1(\mathbf{r}) - \mathbf{H}_2(\mathbf{r})] \times \mathbf{e}_n = 0. \tag{2.5}$$

The tangent component of the EM-field is continuous at any interface of directional vector $\mathbf{e}_n$. It follows from Maxwell's equations that the EM-field satisfies the Helmholtz equation in vacuum and in the nanowire,

$$\nabla^2\mathbf{E}_1(r,\phi) + n\,k_0^2\mathbf{E}_1(r,\phi) = 0, \tag{2.6}$$

$$\nabla^2\mathbf{E}_2(r,\phi) + k_0^2\mathbf{E}_2(r,\phi) = 0, \tag{2.7}$$

where n is the nanowire refractive index.

Cylindrical harmonics

The above equations are an eigenvalue problem for the operator Laplacian. The eigenvector solutions will be the **cylindrical harmonics**. This equation is solved by searching a solution $\mathbf{M}$ of the form,

$$\mathbf{M}(\mathbf{r}) = \nabla \times (\mathbf{c}\,\psi(\mathbf{r}))\,, \tag{2.8}$$

where ψ is a scalar field, and $\mathbf{c}$ a constant vector also referred as the pilot vector. Using the vector product identities, we have that,

$$\nabla^2\mathbf{M} + k^2\,\mathbf{M} = \nabla \times \left(\mathbf{c}\left[\nabla^2\psi + k^2\,\psi\right]\right). \tag{2.9}$$

It follows that, for $\mathbf{M}$ to satisfy eq. (2.6 or 2.7), it is sufficient that ψ satisfies the scalar Helmholtz equation. In addition, we define a vector field, $\mathbf{N} = (\nabla \times \mathbf{M})/k$, and will also be a solution of the Helmholtz equation. Both fields $\mathbf{M}$ and $\mathbf{N}$ follow the same relations than the EM-field, thus allowing $\mathbf{E}$ and $\mathbf{H}$ to be expressed as combinations those fields.

From the symmetry of the scattering particle, here a cylinder, we can try to find solutions for ψ in the form, $\psi(r,\phi) = R(r)\, e^{i\,m\,\phi}$, with $m \in \mathbb{Z}$. This leads to the equation on R, such as

$$r\,\partial_r\,(r\,\partial_r R) + \left[r^2\,k^2 - m^2\right]\,R = 0, \tag{2.10}$$

whose solutions are **Bessel's functions**. The periodicity in $e^{i\,m\,\phi}$ and the choice of the proper Bessel functions will depend on the pumping conditions, while their argument $k\,r$ must be adapted if we work in the vacuum ($r\,\omega/c$) or in the nanowire ($n\,r\,\omega/c$).

We introduce $\rho = k\,r$ as the dimensionless variable for the radial solution functions. We denote $Z_m^{(l)}(\rho)$, with $l = 1,2,3,4$, such as,

$$Z_m^{(1)} = J_m, \qquad Z_m^{(3)} = H_m^{(1)} = J_m + iY_m, \tag{2.11}$$

$$Z_m^{(2)} = Y_m, \qquad Z_m^{(4)} = H_m^{(2)} = J_m - iY_m, \tag{2.12}$$

which involves the Bessel (J_m, Y_m) and Hankel ($H_m^{(1)}$,$H_m^{(2)}$) functions, of the first and second kind.

Taking $\mathbf{e}_y$ as the pilot vector, the expression of the vector cylindrical harmonic fields are,

$$\mathbf{M}_m^{(l)} = \boldsymbol{\nabla} \times \left(\mathbf{e}_y\,\psi_m^{(l)}\right) = -\mathbf{e}_y \times \boldsymbol{\nabla}\psi_m^{(l)} \tag{2.13}$$

$$= k\left(im\frac{1}{\rho}Z_m^{(l)}\,\mathbf{e}_r - (\partial_\rho Z_m^{(l)})\mathbf{e}_\phi\right)e^{i\,m\,\phi}, \tag{2.14}$$

$$\mathbf{N}_m^{(l)} = \frac{1}{k}\boldsymbol{\nabla} \times \mathbf{M}_m^{(l)}, \tag{2.15}$$

$$= k\,Z_m^{(l)}(k\,r)\,e^{i\,m\,\phi}\,\mathbf{e}_y. \tag{2.16}$$

The vector harmonics $\mathbf{M}_m, \mathbf{N}_m$ constitutes a basis on which each solution of the vector Helmholtz equation can be decomposed. Moreover, the orthogonality of the cos, sin function, make the vector harmonics an orthogonal basis, $\langle \mathbf{M}_m, \mathbf{M}_n\rangle = \langle \mathbf{M}_m, \mathbf{N}_n\rangle = \langle \mathbf{N}_m, \mathbf{N}_n\rangle = 0$, if $m \neq n$, with the following scalar product,

$$\langle \mathbf{U}, \mathbf{V}\rangle = \int_0^{2\pi} \mathbf{U}\cdot\mathbf{V}^*\mathrm{d}\phi. \tag{2.17}$$

As such, in the following, we will first expand the incoming pump light on this base.

Incident EM-field: ($\mathbf{E}_i$, $\mathbf{H}_i$)

We now solve the EM solution under plane wave illumination while taking into account the boundary conditions at the vacuum-nanowire interface. We denote the incident EM-field, ($\mathbf{E}_{\text{inc}}$, $\mathbf{H}_{\text{inc}}$), the scattered fields, ($\mathbf{E}_s$, $\mathbf{H}_s$). Furthermore, we introduce the total fields inside the nanowire, ($\mathbf{E}_1$, $\mathbf{H}_1$), and the total fields outside the nanowire, ($\mathbf{E}_2$, $\mathbf{H}_2$). Because of eq. (2.2,2.3), computing the expression of the electric field is sufficient to also determine the magnetic field.

We first expand the incident plane wave on the vector cylindrical harmonics,

$$\mathbf{E}_{\text{inc}} = E_{\text{inc},0}\, e^{i\,\mathbf{k}_{\text{inc}}\,\mathbf{r}}\, \mathbf{e}_{\text{inc}} = E_{\text{inc},0}\, e^{-i\,r\,k_0\,\cos(\phi)}\, \mathbf{e}_{\text{inc}} = \frac{E_{\text{inc},0}}{k_0} \sum_m \left(a_m^{\text{inc}}\, \mathbf{N}_m + b_m^{\text{inc}}\, \mathbf{M}_m \right), \tag{2.18}$$

where we chose to prefactor $\frac{E_{i,0}}{k_0}$ in order for a_m^i and b_m^i to be dimensionless. Due to the orthogonality of the radial harmonic we can retrieve the coefficient with,

$$a_m^{\text{inc}}\, \frac{E_{\text{inc},0}}{k_0} = \frac{\langle \mathbf{E}_{\text{inc}},\, \mathbf{N}_m \rangle}{\langle \mathbf{N}_m,\, \mathbf{N}_m \rangle}, \qquad b_m^{\text{inc}}\, \frac{E_{\text{inc},0}}{k_0} = \frac{\langle \mathbf{E}_{\text{inc}},\, \mathbf{M}_m \rangle}{\langle \mathbf{M}_m,\, \mathbf{M}_m \rangle}. \tag{2.19}$$

Sparing the computational steps, we end up finding the EM-fields expanded in the vector cylindrical harmonics such as,

$$\mathbf{E}_{\text{inc}}^{\parallel} = \frac{E_{\text{inc},0}}{k_0} \sum_{m=-\infty}^{\infty} a_m^{\text{inc}}\, \mathbf{N}_m^{(l)}, \qquad \mathbf{E}_{\text{inc}}^{\perp} = \frac{E_{\text{inc},0}}{k_0} \sum_{m=-\infty}^{\infty} b_m^{\text{inc}}\, \mathbf{M}_m^{(l)}, \tag{2.20}$$

$$\mathbf{H}_{\text{inc}}^{\parallel} = -i\, \frac{k_0}{\omega\, \mu_0}\, \frac{E_{\text{inc},0}}{k_0} \sum_{m=-\infty}^{\infty} a_m^{\text{inc}}\, \mathbf{M}_m^{(l)}, \qquad \mathbf{H}_{\text{inc}}^{\perp} = -i\, \frac{k_0}{\omega\, \mu_0}\, \frac{E_{\text{inc},0}}{k_0} \sum_{m=-\infty}^{\infty} b_m^{\text{inc}}\, \mathbf{N}_m^{(l)}, \tag{2.21}$$

where $a_m^{\text{inc}} = (-i)^m$ and $b_m^{\text{inc}} = -i\, a_m^{\text{inc}}$. One can note that $a_{-m}^{\text{inc}} = (-1)^m\, a_m^{\text{inc}}$.

Internal, ($\mathbf{E}_1$, $\mathbf{H}_1$), and scattered, ($\mathbf{E}_s$, $\mathbf{H}_s$), EM-fields

Up to now we have not specified which kind of Bessel's function is used in the cylindrical harmonic expressions. Indeed, Y_m and $H_m^{(2)}$, diverge at the origin, and thus are not physical concerning the internal radiation that must be finite inside the nanowire. Outside the cylinder, both J_m and Y_m are well-behaved, but only $Z_m^{(3)}$ satisfies the asymptotic behaviour.

After expressing the incident plane wave radiation in terms of the vector cylindrical harmonics, we want to know how the internal and scattered field respond to such excitation. The internal, $\mathbf{E}_1$ and the scattered field, $\mathbf{E}_s$, in the nanowire are expressed as,

$$\mathbf{E}_s^{\parallel} = \frac{E_{\text{inc},0}}{k_0} \sum_{m=-\infty}^{\infty} a_m^{\text{inc}}\, a_m^s\, \mathbf{N}_m^{(3)}(k_0,\, r,\, \phi), \qquad \mathbf{E}_s^{\perp} = \frac{E_{\text{inc},0}}{k_0} \sum_{m=-\infty}^{\infty} b_m^{\text{inc}}\, b_m^s\, \mathbf{M}_m^{(3)}(k_0,\, r,\, \phi), \tag{2.22}$$

$$\mathbf{E}_1^{\parallel} = \frac{E_{\text{inc},0}}{k_0} \sum_{m=-\infty}^{\infty} a_m^{\text{inc}}\, a_m^1\, \mathbf{N}_m^{(1)}(n\, k_0,\, r,\, \phi), \qquad \mathbf{E}_1^{\perp} = \frac{E_{\text{inc},0}}{k_0} \sum_{m=-\infty}^{\infty} b_m^{\text{inc}}\, b_m^1\, \mathbf{M}_m^{(1)}(n\, k_0,\, r,\, \phi), \tag{2.23}$$

where we choose to keep a_m^{inc}, b_m^{inc}, in order to explicitly discriminate what comes from the incident field to what comes from the resonant behaviour due to the boundary conditions. To compute the coefficients, we make use of the boundary relations at the interface of the nanowire. The outside field is given by,

$$\mathbf{E}_2 = \mathbf{E}_{\text{inc}} + \mathbf{E}_s, \tag{2.24}$$

while for the intra-nanowire fields, the wave vector becomes $n\,k_0$, and solve the Helmholtz equation: $\nabla^2 \mathbf{E}_1 + (n\,k_0)^2\,\mathbf{E}_1 = 0$. From the boundary conditions,

$$0 = [(\mathbf{E}_{\text{inc}}(r,\phi) + \mathbf{E}_s(r,\phi)) - \mathbf{E}_1(r,\phi)] \times \mathbf{e}_r, \tag{2.25}$$
$$0 = [(\mathbf{H}_{\text{inc}}(r,\phi) + \mathbf{H}_s(r,\phi)) - \mathbf{H}_1(r,\phi)] \times \mathbf{e}_r, \tag{2.26}$$

getting a system of four equations. Combining the above equations, we get the scattering and internal coefficients for the fields such as,

$$a_m^s = -\frac{Z_m^{(1)}(n\,k_0\,R)\,\dot{Z}_m^{(1)}(k_0\,R) - n\,\dot{Z}_m^{(1)}(n\,k_0\,R)\,Z_m^{(1)}(k_0\,R)}{Z_m^{(1)}(n\,k_0\,R)\,\dot{Z}_m^{(3)}(k_0\,R) - n\,\dot{Z}_m^{(1)}(n\,k_0\,R)\,Z_m^{(3)}(k_0\,R)}, \tag{2.27}$$
$$b_m^s = -\frac{n\,Z_m^{(1)}(n\,k_0\,R)\,\dot{Z}_m^{(1)}(k_0\,R) - \dot{Z}_m^{(1)}(n\,k_0\,R)\,Z_m^{(1)}(k_0\,R)}{n\,Z_m^{(1)}(n\,k_0\,R)\,\dot{Z}_m^{(3)}(k_0\,R) - \dot{Z}_m^{(1)}(n\,k_0\,R)\,Z_m^{(3)}(k_0\,R)}, \tag{2.28}$$
$$a_m^1 = +\frac{\dot{Z}_m^{(3)}(k_0\,R)\,Z_m^{(1)}(k_0\,R) - Z_m^{(3)}(k_0\,R)\,\dot{Z}_m^{(1)}(k_0\,R)}{n\,\dot{Z}_m^{(3)}(k_0\,R)\,Z_m^{(1)}(n\,k_0\,R) - n^2\,Z_m^{(3)}(k_0\,R)\,\dot{Z}_m^{(1)}(n\,k_0\,R)}, \tag{2.29}$$
$$b_m^1 = +\frac{Z_m^{(3)}(k_0\,R)\,\dot{Z}_m^{(1)}(k_0\,R) - \dot{Z}_m^{(3)}(k_0\,R)\,Z_m^{(1)}(k_0\,R)}{n\,Z_m^{(3)}(k_0\,R)\,\dot{Z}_m^{(1)}(n\,k_0\,R) - n^2\,\dot{Z}_m^{(3)}(k_0\,R)\,Z_m^{(1)}(n\,k_0\,R)}, \tag{2.30}$$

with n the refractive index of the nanowire, k_0 the amplitude of the wave vector in vacuum, and R the radius of the cylinder, and $Z_m^{(1)} = J_m$ and $Z_m^{(3)} = H_m^{(1)}$. The full expression of the scattered fields are,

$$\mathbf{E}_s^{\parallel} = \frac{E_{\text{inc},0}}{k_0} \sum_{m=-\infty}^{\infty} a_m^{\text{inc}}\,a_m^s\,\mathbf{N}_m^{(3)}, \qquad \mathbf{E}_s^{\perp} = \frac{E_{\text{inc},0}}{k_0} \sum_{m=-\infty}^{\infty} b_m^{\text{inc}}\,b_m^s\,\mathbf{M}_m^{(3)}, \tag{2.31}$$
$$\mathbf{H}_s^{\parallel} = -i\,\frac{k_0}{\mu_0\,\omega}\,\frac{E_{\text{inc},0}}{k_0} \sum_{m=-\infty}^{\infty} a_m^{\text{inc}}\,a_m^s\,\mathbf{M}_m^{(3)}, \qquad \mathbf{H}_s^{\perp} = -i\,\frac{k_0}{\mu_0\,\omega}\,\frac{E_{\text{inc},0}}{k_0} \sum_{m=-\infty}^{\infty} b_m^{\text{inc}}\,b_m^s\,\mathbf{N}_m^{(3)}, \tag{2.32}$$

where we remind that $a_m^{\text{inc}} = (-i)^m$ and $b_m^{\text{inc}} = -i\,a_m^i$. Similarly, the internal EM-fields across the nanowire cross-section are given by,

2

$$\mathbf{E}_1^{\parallel} = \frac{E_{\text{inc},0}}{k_0} \sum_{m=-\infty}^{\infty} a_m^{\text{inc}}\, a_m^1\, \mathbf{N}_m^{(1)}, \quad \mathbf{E}_1^{\perp} = \frac{E_{\text{inc},0}}{k_0} \sum_{m=-\infty}^{\infty} b_m^{\text{inc}}\, b_m^1\, \mathbf{M}_m^{(1)}, \tag{2.33}$$

$$\mathbf{H}_1^{\parallel} = -i\,\frac{n\,k_0}{\mu_0\,\omega}\,\frac{E_{\text{inc},0}}{k_0} \sum_{m=-\infty}^{\infty} a_m^{\text{inc}}\, a_m^1\, \mathbf{M}_m^{(1)}, \quad \mathbf{H}_1^{\perp} = -i\,\frac{n\,k_0}{\mu_0\,\omega}\,\frac{E_{\text{inc},0}}{k_0} \sum_{m=-\infty}^{\infty} b_m^{\text{inc}}\, b_m^1\, \mathbf{N}_m^{(1)}, \tag{2.34}$$

where one must account that the wave vector amplitude is $k = n\,k_0$.

The expression of those fields describes the whole optical interaction of our SiC nanowires with an incident plane wave illumination. Although working with focused gaussian beam, the plane wave approximation works well in our case for low numerical aperture objectives and because the nanowires are smaller than the laser waist.

2.2.2 Radiometric quantities associated to the scattering of a nanowire

Under illumination, the nanowire scatters light all around itself. In the following we will derive some of the most important quantities in radiometry that characterise the scattering of the nanowire and how it impacts the measurements.

Poynting vector

The time average Poynting vector of the EM-fields is defined as,

$$\mathbf{S} = \frac{1}{2}\,\text{Re}(\mathbf{E} \times \mathbf{H}^*), \tag{2.35}$$

which gives the EM energy flow per unit of surface, $[|\mathbf{S}|]$ =W.m^{-2}. The incident plane wave, polarized in the xOy plane and propagating along the z-axis, has a Poynting vector such as,

$$\mathbf{S}_{\text{inc}} = \frac{1}{2}\,\text{Re}(\mathbf{E}_{\text{inc}} \times \mathbf{H}_{\text{inc}}^*) = \frac{k}{2\mu\omega}\,E_{\text{inc},0}^2\,\mathbf{e}_z = \frac{\epsilon_0\,c}{2}\,E_{\text{inc},0}^2\,\mathbf{e}_z, \tag{2.36}$$

because we have $i\,\mu_0\,\omega\,\mathbf{H} = i\,\mathbf{k}_0 \times \mathbf{E}$, for a plane wave in vacuum. We note that the Poynting vector is indeed aligned with the propagation direction. Concerning the scattered EM-fields, the longitudinal and orthogonal power irradiated by the nanowire are given by,

$$\mathbf{S}_s^{\parallel} = \frac{1}{2}\,\text{Re}(\mathbf{E}_s^{\parallel} \times (\mathbf{H}_s^{\parallel})^*), \qquad \mathbf{S}_s^{\perp} = \frac{1}{2}\,\text{Re}(\mathbf{E}_s^{\perp} \times (\mathbf{H}_s^{\perp})^*), \tag{2.37}$$

where the detailed expressions are given by the fields computed in the above section.

Note that the Poynting vector of the scattered field alone does not represent a physical quantity. In order to estimate the optical forces resulting from the interaction with light, one needs to consider the entire

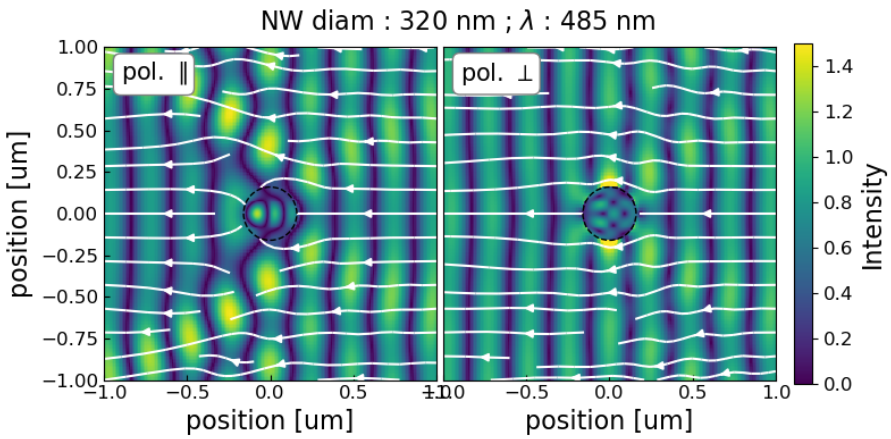

Figure 2.6: Representation of the electromagnetic field amplitude outside and inside the nanowire for parallel and perpendicular incident polarisations. The stream plot in white solid lines represents the amplitude of the local Poynting vector for the total field outside the nanowire.

field. As an illustration, in Figure 2.6 is represented the total electric field intensity for the two incident light polarisations, with a stream plot of the Poynting fields for a given wavelength and nanowire diameter. Nonetheless, looking at the scattered light in the far-field, the contribution of the scattered field alone is sufficient to estimate the scattering properties of the nanowire. Indeed, we computed the fields for a given incident plane wave, which has an infinite extension. In practice, incident plane wave approximation is sufficient describing the nanowire in the waist of lasers of non too tightly focused beam, but one should not forget that the incident light is confined in the direction outside the optical axis of the source. Thus, in the far field, only the scattered light by the nanowire is non-vanishing.

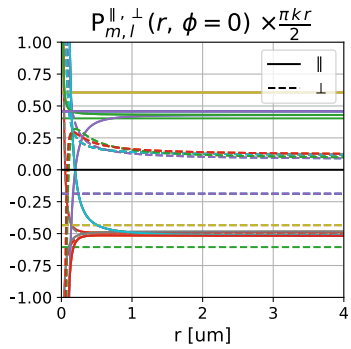

Figure 2.7: Convergence of the coefficient $P_{m,l}$ (defined in eq. (2.39 and 2.40)), with the distance of observation, computed for a nanowire of diameter 300 nm. We chose $m, l \in \{-2, -1, 0, 1, 2\}$. We observe the transition between near-field and far-field approximation, at approximately five time the nanowire diameter.

Radiated intensity

We define the **radiant intensity** per unit length of the nanowire, I_r in [W.sr^{-1}.m^{-1}], as the density of radiated flux per unit angle emitted by an illuminated elementary section in a given direction, with respect to the pump laser optical axis. When measuring this radiated intensity at a distance r of the nanowire, we have,

$$I_r(\phi)\,\mathrm{d}\phi\,\mathrm{d}h = \mathbf{S}(r,\phi)\cdot\mathbf{e}_r(\phi)\,r\,\mathrm{d}\phi\,\mathrm{d}h. \tag{2.38}$$

We now focus our attention on the scattered field, and thus look at the scattering contribution in the Poynting vector. As mentioned above, even though it does not refer to a physical quantity in the vicinity of the nanowire, it is the surviving term when looking far from the nanowire off the optical axis.

From the field expressions we can derive the radiated flux of the scattered light in a given direction $\mathbf{e}_r$, at a distance r from the nanowire, such as,

2

$$\mathbf{S}_s^{\parallel} \cdot \mathbf{e}_r = \frac{c\,\epsilon_0\,E_{\text{inc},0}^2}{2} \sum_{m,l} \text{Re}\left[i\,(-i)^{m-l}\,a_m^s\,(a_l^s)^* \quad \left[+Z_m^{(3)}(k\,r)\,(\dot{Z}_l^{(3)}(k\,r))^*\right]\,e^{i\,(m-l)\,\phi}\right] \quad = |\mathbf{S}_{\text{inc}}| \sum_{m,l} P_{m,l}^{\parallel}, \tag{2.39}$$

$$\mathbf{S}_s^{\perp} \cdot \mathbf{e}_r = \frac{c\,\epsilon_0\,E_{\text{inc},0}^2}{2} \sum_{m,l} \text{Re}\left[i\,(-i)^{m-l}\,b_m^s\,(b_l^s)^* \quad \left[-(Z_l^{(3)}(k\,r))^*\dot{Z}_m^{(3)}(k\,r)\right]\,e^{i\,(m-l)\,\phi}\right] \quad = |\mathbf{S}_{\text{inc}}| \sum_{m,l} P_{m,l}^{\perp}, \tag{2.40}$$

with $|\mathbf{S}_{\text{inc}}| = \frac{1}{2}\,c\,\epsilon_0\,E_{\text{inc},0}^2 = I_{\text{inc},0}$, the incident intensity.

Near-field vs Far-field

The terms, $P_{m,l}^{\parallel,\perp}$, hold an explicit but complex dependence on r, involving Bessel's functions. However, they quickly converge to limiting behaviours in $\frac{1}{r}$, see Fig. 2.7. Over few μm (approximately five times the nanowire diameter), the field around the nanowire is very structured in ϕ and r. Still, when computing the Poynting vector field of the scattering field, see Fig. 2.8, the radiated power began to be constant in a given direction. On top of that, looking at the distribution of the terms in the far-field, with the indices m and l, we can see some symmetry in the distribution, see Fig. 2.9a and 2.9b.

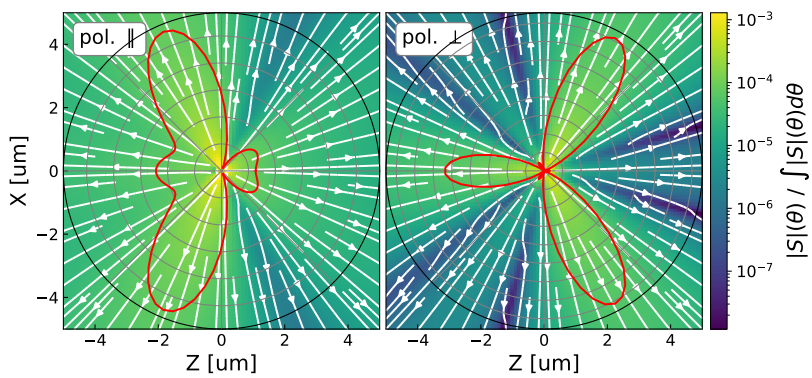

Figure 2.8: Poynting stream plot of the scattered field for a Nanowire of diameter 320 nm under an illumination at 485 nm.

Looking how the different coefficients $P_{m,l}^{\parallel,\perp}$ converges, see Fig. 2.9, we group the terms that have the same far-field limit together such as,

$$\begin{aligned}\Gamma_{m_0,l_0}^{\parallel,\perp}(r \to \infty) &= P_{m_0,l_0}^{\parallel,\perp} + P_{-m_0,l_0}^{\parallel,\perp} + P_{m_0,-l_0}^{\parallel,\perp} + P_{-m_0,-l_0}^{\parallel,\perp} \\ &\quad + P_{l_0,m_0}^{\parallel,\perp} + P_{-l_0,m_0}^{\parallel,\perp} + P_{l_0,-m_0}^{\parallel,\perp} + P_{-l_0,-m_0}^{\parallel,\perp} \qquad (2.41)\\ &= (-1)^{m_0-l_0}\,\epsilon_{m_0,l_0}\,\frac{2}{\pi\,k\,r}\,\text{Re}\left[c_{m_0}^s\,(c_{l_0}^s)^*\right] \\ &\quad \times \cos(m_0\,\phi)\,\cos(l_0\,\phi), \qquad (2.42)\end{aligned}$$

where m_0, l_0 are positive index in $\mathbb{N}^2$, and $\epsilon_{m_0,l_0} = 8/(1+\delta_{m_0,l_0} + \delta_{0,l_0} + \delta_{m_0,0} + 4\,\delta_{m_0,l_0}\,\delta_{0,l_0}\,\delta_{m_0,0})$, while c_i^s refers to a_i^s or b_i^s whether we consider the parallel or perpendicular polarization respectively. The above expressions make use of the properties : 1) $Z_{-m} = (-1)^m\, Z_m$, 2) $a^s_{-m} = a^s_m$ and $b^s_{-m} = b^s_m$. The prefactor $2/(\pi\, k\, r)$ comes from the limit value of the Bessel's function product,

$$C^{\parallel}_{m,l} = +Z^{(3)}_m(k\,r)\,(\dot{Z}^{(3)}_l(k\,r))^* \underset{r\to\infty}{\sim} -i\,(-i)^{m-l}\,\frac{2}{\pi\,k\,r}, \quad (2.43)$$

$$C^{\perp}_{m,l} = -(Z^{(3)}_l(k\,r))^*\dot{Z}^{(3)}_m(k\,r) \underset{r\to\infty}{\sim} -i\,(-i)^{m-l}\,\frac{2}{\pi\,k\,r}. \quad (2.44)$$

Note that $\mathrm{Im}(C^{\parallel,\perp}_{m,m}) = \frac{2}{\pi\,k\,r}$ exactly for all r.

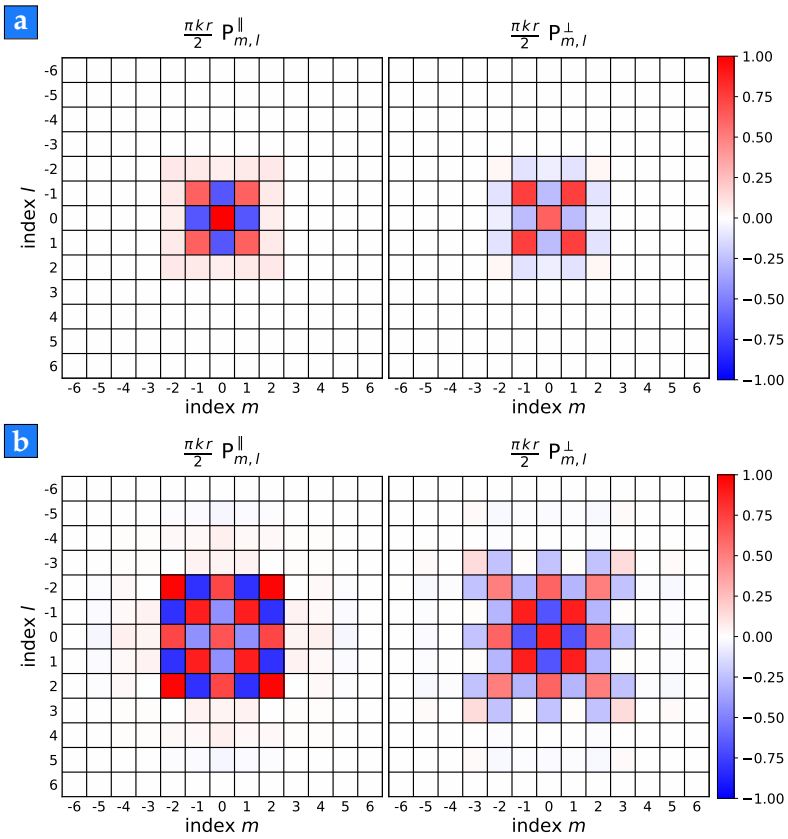

Figure 2.9: Matrix representation of the far-field value of the $P^{\parallel,\perp}_{m,l}$ coefficients at $\phi = 0$, for two nanowire diameter (a) 250 nm, (b) 600 nm, under an incident plane wave with wavelength of 633 nm. The quick vanishing of the high harmonics contributions allows for great reduction in computational power as the truncation of the sum leads to good approximation.

Figure 2.10: Mie scattering diagrams for an infinite cylinder with different diameters, for an incident wavelength of $\lambda_{\text{inc}} = 633$ nm.

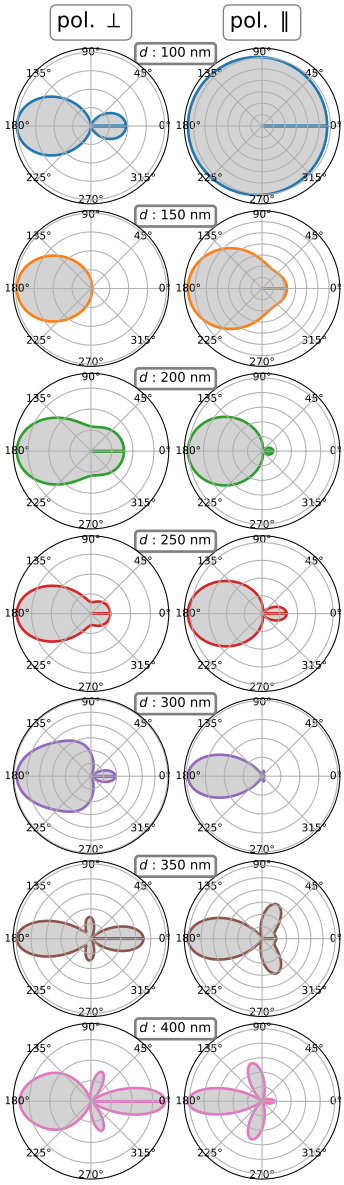

Figure 2.11: (a) Spectrum of the scattered light intensity (black line), as well as the back collection with objectives of two different NA (blue and red solid lines), for a parallel incident illumination on a nanowire of radius 150 nm, expressed in terms of an optical cross-section $\sigma_s^{\parallel}$. (b) Abacus for nanowire diameter preselection. Both figures adapted from [54]

In the end, the radiated intensity in the far field can be written,

$$I_r^{\parallel,\perp}(\phi) = I_{\text{inc},0} \sum_{m_0=0, l_0 \leq m_0}^{\infty} r\,\Gamma_{m_0,l_0}^{\parallel,\perp}, \tag{2.45}$$

$$= \frac{2\,I_{\text{inc},0}}{\pi\,k_0} \sum_{m_0=0, l_0 \leq m_0}^{\infty} (-1)^{m_0-l_0}\,\epsilon_{m_0,l_0} \times \text{Re}\left[c_{m_0}^s\,(c_{l_0}^s)^*\right] \cos(m_0\,\phi)\,\cos(l_0\,\phi), \tag{2.46}$$

where ϵ_{m_0,l_0} is as defined in the framed text, $c_i^s = a_i^s$ or $c_i^s = b_i^s$ depending on whether we consider the parallel or perpendicular polarization respectively, k_0 the incident wave vector in vacuum, and $I_{i,0} = \frac{1}{2}\,c\,\epsilon_0\,E_{i,0}^2$ the incident intensity in W.m^{-2}. We note that $I_r^{\parallel,\perp}$ (in W.sr^{-1}.m^{-1}) does not depend on the distance of observation, r, as expected. Figure 2.10 shows the scattering diagrams for different nanowire diameters under the illumination of a plane wave at fixed wavelength 633 nm. They structure the perceived colour and allow us to quantify the reflectivity of the nanowires in use.

The total optical power per unit length of the scattered light, is given by integrating the radiated intensity all around the cylinder, see black solid line in Fig. 2.11a,

$$\Phi_s = \int_{-\pi}^{+\pi} I_r(\phi)\mathrm{d}\phi = \underbrace{\frac{4\,I_{\text{inc},0}}{k} \sum_{m=-\infty}^{\infty} |a_m^s|^2}_{\Phi_s^{\parallel}} + \underbrace{\frac{4\,I_{\text{inc},0}}{k} \sum_{m=-\infty}^{\infty} |b_m^s|^2}_{\Phi_s^{\perp}}. \tag{2.47}$$

The expression simplifies by taking advantage of the orthogonality of the cylindrical harmonics. Moreover, from the radiated intensity one

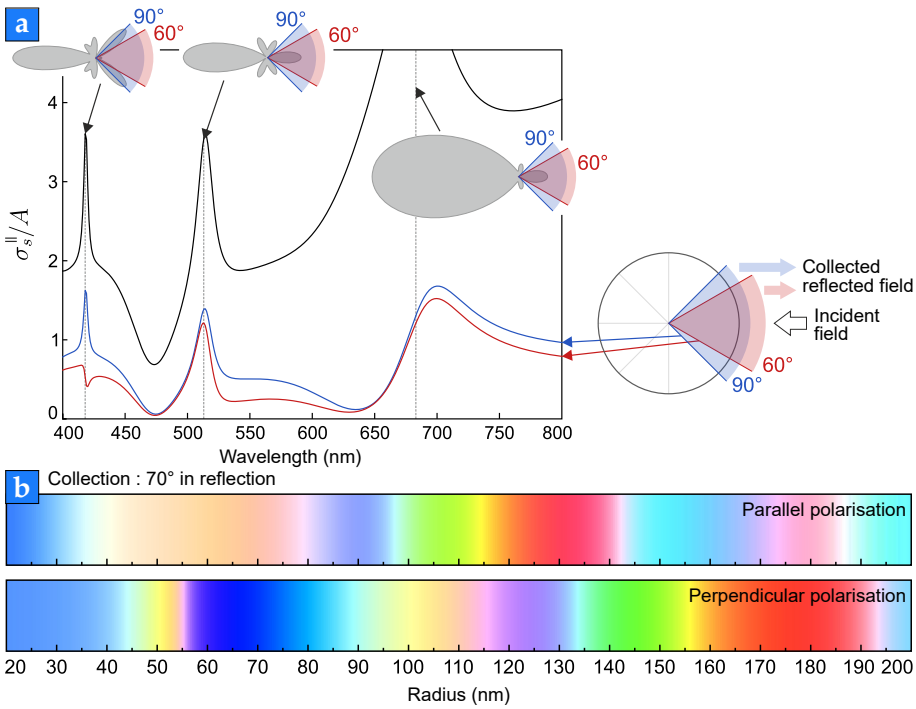

can compute the amount of expected back scattering by integrating the intensity over the numerical aperture (NA) angle of the objective used to focus light on the nanowire, see Fig. 2.11a. Taking into account the camera specification and the spectrum of the incident light, L. Mercier de Lépinay [54] applied the theory to compute an abacus of the reflected perceived colour when a nanowire is illuminated by a white light (typically when observed in an optical microscope) for both polarisation, as a function of its diameter, see Fig. 2.11b. This provides a good estimation (5-10 nm error) of the nanowire diameter and allows for easy preselection of nanowires before experimenting.

2.2.3 Optical cross-section

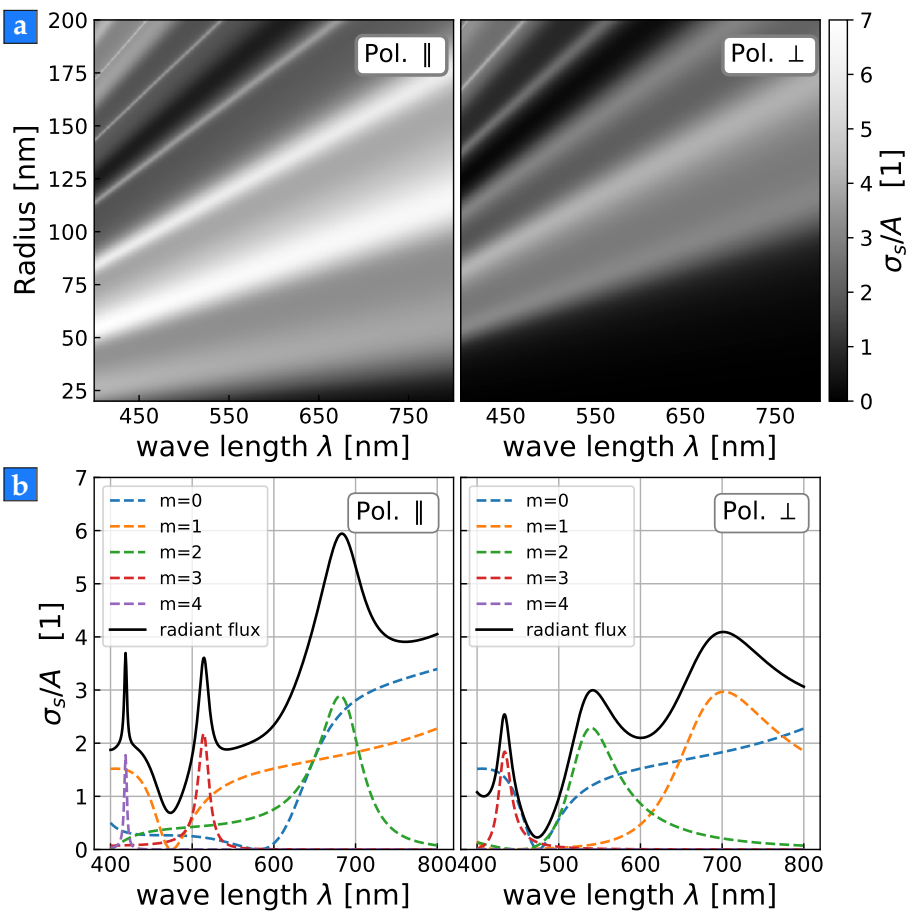

Figure 2.12: (a) Relative optical cross-section with varying radius and wavelength. (b) Contributions to the optical cross-section for a nanowire of diameter 300 nm.

The Mie resonances increase the interaction between the nanowire and the illuminating radiation. We define the **optical cross-section** as the ratio between the total scattered power by the nanowire, $\Phi_s \, \mathrm{d}h$ and the incident power impinging on the geometrical cross-section, $I_{i,0} \, 2 \, R \, \mathrm{d}h$, with R the nanowire radius. We thus have,

$$\frac{\sigma_s^{\parallel,\perp}}{A} = \frac{\Phi_s^{\parallel,\perp} \, \mathrm{d}h}{I_{i,0} \, 2 \, R \, \mathrm{d}h} = \frac{2}{k \, R} \sum_{m=-\infty}^{\infty} |c_m^s|^2, \tag{2.48}$$

where $A = 2 \, R \, \mathrm{dh}$, $c_i^s = a_i^s$ or b_i^s for the parallel or orthogonal polarization respectively. Figure 2.12a shows Mie resonances can enhance

the interaction of the nanowire with light, up to seven times its geometrical cross-section.

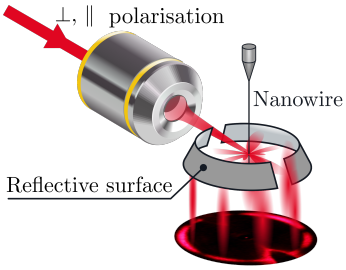

Figure 2.13: Experimental scheme for angular scattering measurement setup.

2.3 Investigation of angular scattering diagrams

To further investigate the light nanowire interaction and the impact of the internal Mie resonances, we developed a dedicated experiment allowing to collect the angular profiles of the light laterally scattered by the nanowires, Fig. 2.13. To do so, we made use of a tunable laser source, a filtered supercontinuum laser, and a specific imagery system. We start the section by describing the experimental setup we developed, the procedure to measure the angular scattering profiles, and their theoretical analysis.

2.3.1 Measurement setup

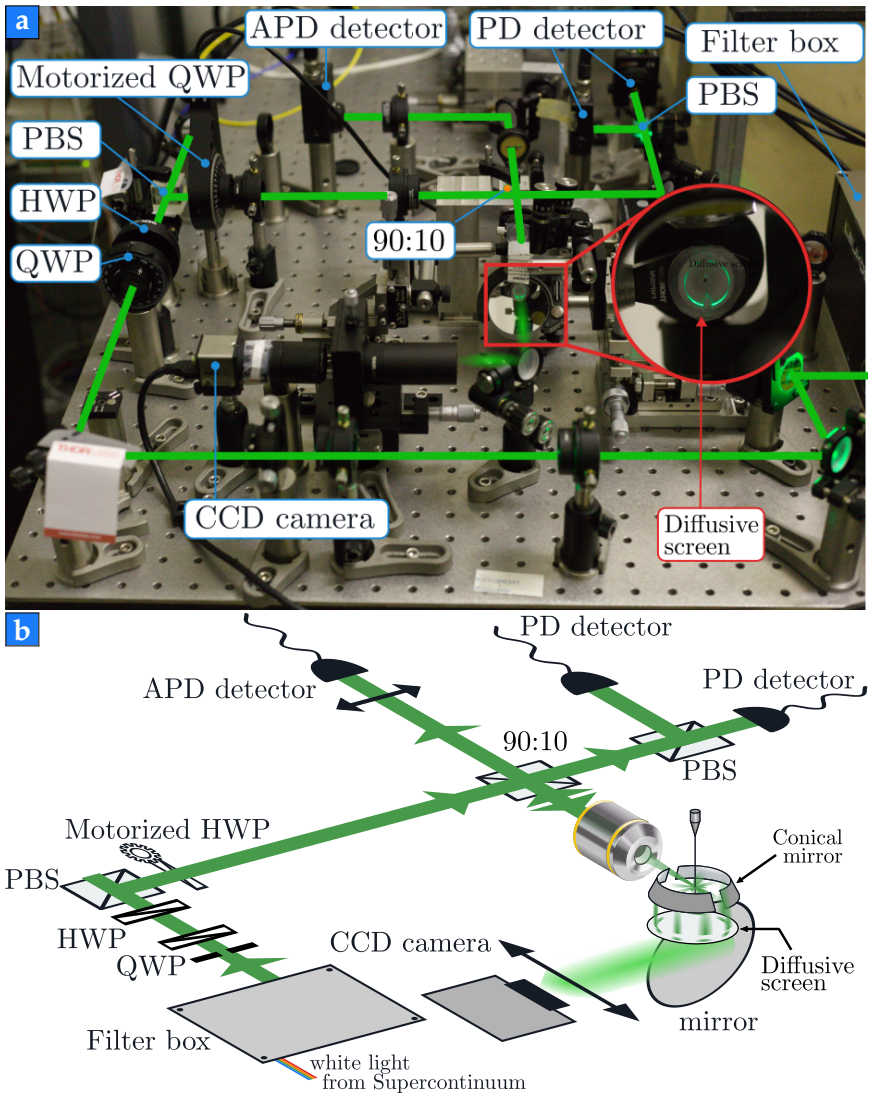

Figure 2.14: Experimental setup for studying scattering diagrams of a nanowire under low NA focused laser illumination. (a) Picture of the setup with annotations and super-imposed laser path, (b) illustration scheme of the experimental setup. The white laser light from the Supercontinuum passes through a filter box, selecting the desired wavelength with a bandwidth of 5 nm. The succession of a quarter waveplate (QWP), a half waveplate (HWP) and a polarising beam splitter (PBS) of large bandwidth correct the residual ellipticity of the filtered light. A motorised HWP is used to rotate the incident polarisation of the focused laser beam on the nanowire. We use a 90:10 beam splitter (90% in transmission) to collect the back scattering of the nanowire onto an avalanche photodiode (APD). The lateral scattered light is projected on a diffusive screen using a conical mirror, and the angular diagram is imaged on a CCD camera. Two photodiodes (PDs) after a PBS measure the incident light state.

To measure the scattered diagram at a given radiation wavelength, we implemented a measurement scheme where we project the scattered light to a bottom lying diffusive screen which is then imaged on a CCD camera, see Fig. 2.14b. A laser beam is focused on a nanowire by a long working distance microscope objective (10x/0.1 NA). It presents a smaller numerical aperture compared to the optics we usually use in our experiments, which allows to assume that the illumination at the focal point is very close to the plane wave situation. The scattered light is projected on a diffusive screen using a pierced conical mirror surrounding the illuminated nanowire section. We then use a ThorCam camera to image and capture the scattering diagram. The output illumination side of the conical mirror is also drilled in order to avoid saturation of the illumination since the output beam can be much brighter than the scattered light.

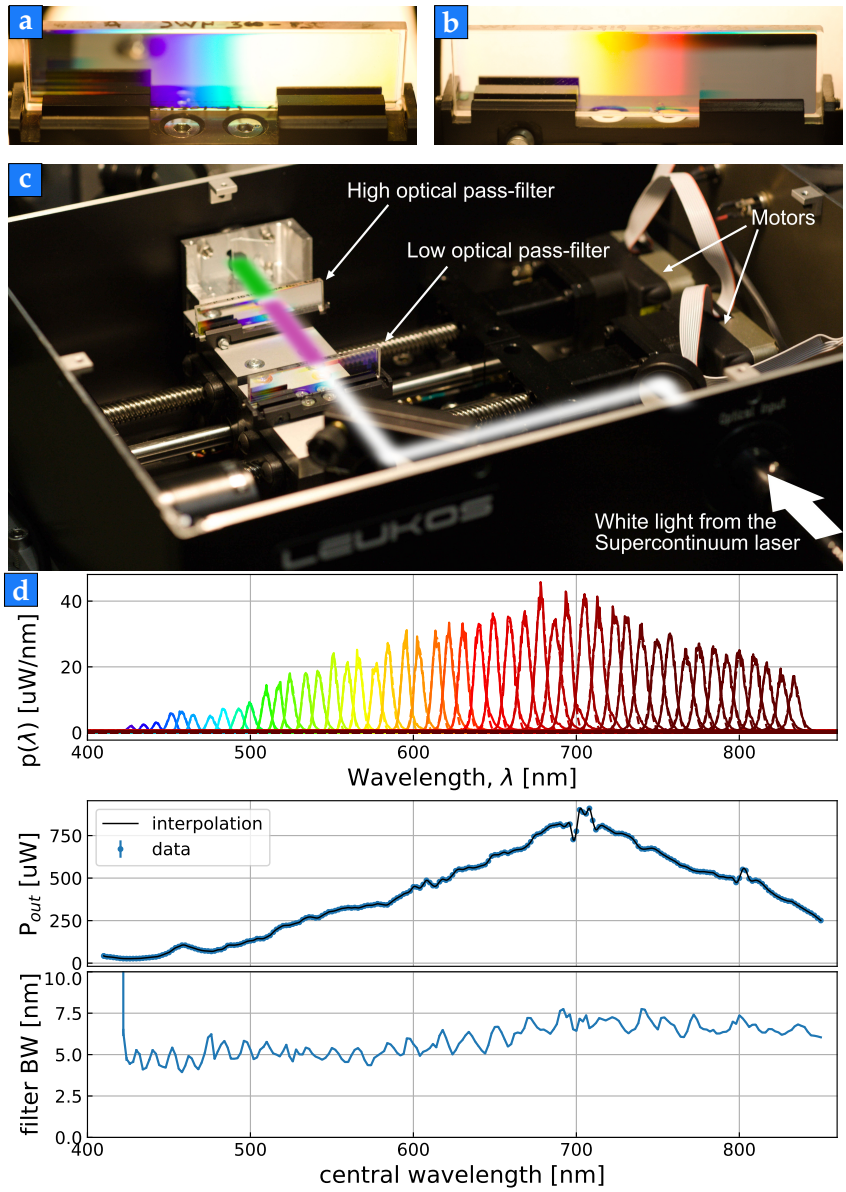

Figure 2.15: Supercontinuum laser Leukos filter box. In picture (a) a high pass wavelength filter, in (b) a low pass wavelength filter, in (c) a large picture of the filter box picture where the collimated white laser is sandwiched through the optical filters. The filtered color and the optical bandwidth can be adjusted using motorised translation on the optical filters. Figure (d) shows the calibration of the filter box output, using a fibred spectrometer placed at the focal point of the objective in the setup shown in Fig. 2.14b. For the smallest filtered bandwidth, we report the output wavelength spectral distribution of several colour configurations (top panel). The middle panel shows the output optical intensity when we vary the central wavelength of the filtering. The bottom panel shows the evolution of the spectral filtering bandwidth with the central wavelength, which can be considered between 5-7 nm.

We make use of a **Supercontinuum** laser (Leukos), which generates an output beam spreading over a broad wavelength spectrum (at

40 MHz repetition rate). We select the wanted wavelength through a filter box using two optical filters mounted on motorised translation stages (Fig. 2.15c) : a High pass (Fig. 2.15a) followed by a Low pass filter (Fig. 2.15b). We characterised the filter box specifications using the minimum filtering bandwidth (approximately 5 nm here), see Fig. 2.15d, in order to get quantitative measurement of the illumination spectrum.

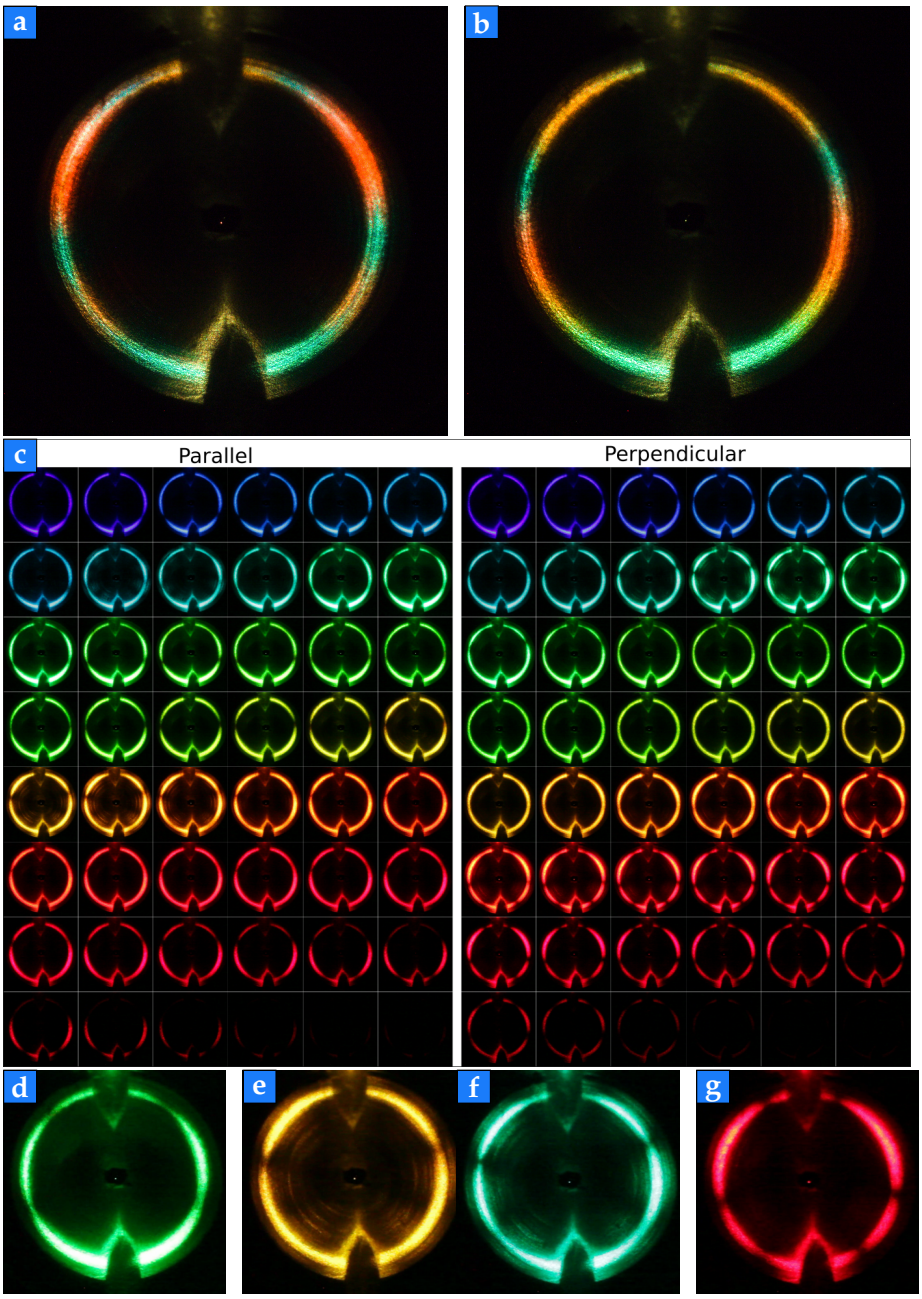

Figure 2.16: Coloured picture of the scattering diagram of a nanowire of diameter 450 nm, under white light illumination with (a) parallel incident polarisation, and (b) perpendicular. (c) Multi-colour scattering diagrams for the same nanowire, upon scanning the incident wavelength. Images (d), (e) are diagrams chosen to show the spectacular structuration of the radial scattering of the nanowire under parallel polarisation illumination, while under perpendicular polarisation illumination for the images (f), (g).

In figure 2.16c, we show the different lateral scattering diagrams measured when sweeping the wavelength of the incident radiation, captured by a Camera *Canon EOS 5D Mark II*. Each image represents the radial scattering image of the nanowire, the laser coming from the top of the image. While the wavelength is changed, we observe the appearance, rotation, and disappearance of nodes in the angular

diagrams, indicating weakly scattering orientations.

2.3.2 Diagram evolution with wavelength

From each captured image, we can reconstruct the polar distribution of the scattered light intensity, see Fig. 2.17a. Figure 2.17b shows the analysis protocol from the diagram picture to the angular intensity. We start from a grey-scaled image returned by the ThorCam camera. After determining the centre, the incidence angle of the laser and the angle of the dead-zone (open area of the conical mirror), we transform the image from XY-pixel coordinate to radius-angle coordinate. To retrieve the angular intensity, we integrate the pixel value over a radius range that captures the width of the diagram, without integrating the spurious light. Then, we smooth the radial intensity using multi-passing of a rectangular integrating gate. It allows us to retrieve the local maximum and minimum of the angular scattered intensity, measured at a given incident wavelength.

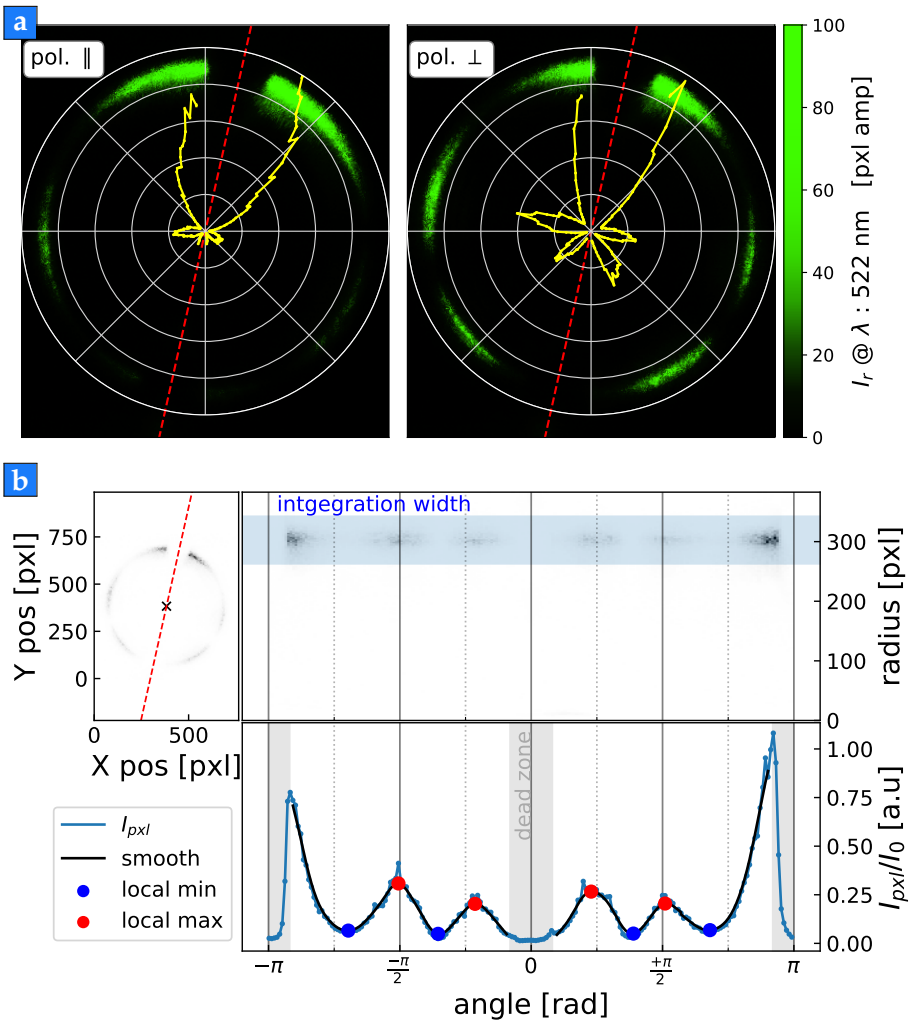

Figure 2.17: Angular scattered intensity measurement. (a) Polar scattering diagram in far-field, where the max value is set to best observe the contrast. (b) Data exploitation scheme from the ThorCam picture to the normalised angular scattering intensity.

Since we were merely interested in the scattering diagrams, we did not need to calibrate the above diagrams in absolute term. Instead, we placed a photodiode in reflexion in order to record and calibrate

the reflected power, after having taken into account the variations of injected power with the colour. The polar variation of the intensity are well captured in the diagrams. If we look at the angular local extrema of the scattered intensity diagrams, we can follow their evolution when scanning the incident wavelength, as shown in Figure 2.18a. We compared those measurements to the analytical expression derived from the Mie theory given in eq. (2.46) by adjusting the fitted nanowire diameter to a value of 450 nm. Those diagrams are like *fingerprints* of the nanowire optical response.

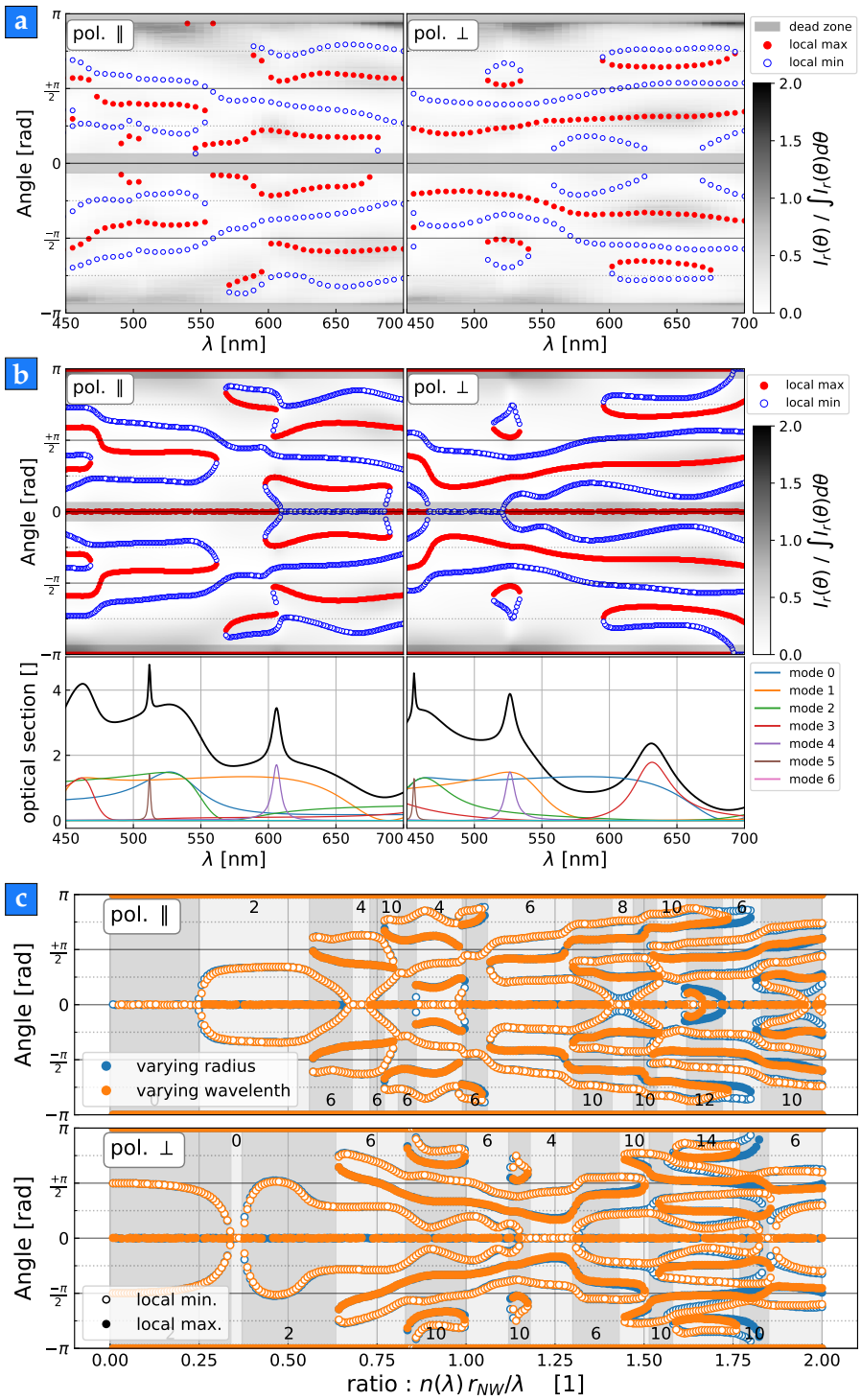

Figure 2.18: From picture to Mie diagram fingerprint. (a) Diagram maps with different wavelength, compared to a theoretical one with a nanowire of 450 ± 10 nm. (b) Theoretical Mie diagram fingerprints. Figure (c) shows the dependence on the angular extrema with respect to the optical depth ratios nR/λ. For the two incident polarisations, we compare the evolution of the diagrams between changing the radius at fixed wavelength $\lambda = 633$ nm (blue markers), or when varying the wavelength at fixed nanowire radius $R = 200$ nm (orange markers). The filled markers represent the local maxima, while the white filled markers represent the local minima. We also divide the diagrams in zones of same number of local extrema (minimum and maximum) while discarding the extrema along the optical, *i.e* at 0 or π. It shows, the knowledge of the number of extrema from the two polarisations at a given wavelength already allows for quick estimation of the nanowire radius.

Upon inspecting again eq. (2.46), we realise the optical resonances variability between nanowires are only encoded in the coefficients c_m^s (where $c_m^s = a_m^s$ for parallel incident polarisation, and $c_m^s = b_m^s$ for a perpendicular one), which only depend on two parameters, the refractive index $n(\lambda)$ and the ratio $n(\lambda)\,R/\lambda$, where R is the nanowire radius, and λ the incident radiation wavelength in vacuum. Figure 2.18c shows how the angular extrema evolve with this ratio, whilst varying either the radius or the wavelength accounting the dispersion of the material. It is indeed very interesting to compare the experimental results with the theory using only a single parameter. In the particular case of 3C-SiC, a deformation arises at large $n\,R/\lambda$ ratios, if we properly take into account the material dispersion, since the refractive index change with the wavelength has an increasing rate for lower wavelength. However, this deformation affects little our analysis, because the range of radius and wavelength used in our experiments belongs to the matching zone, and can be used elegantly to compare the scattering diagrams of different nanowires.

We can use those measurements to determine the nanowire diameter from the fits of the scattering diagrams with the theory map. In Figure 2.20a we plot the extrema measurement as squares that represent the error obtained when analysing the scattering diagrams. The metric used is the sum of the overlapping area between a measured point and its theoretical position when computed from the expressions at a given radius. If we sweep the estimated radius and compute the

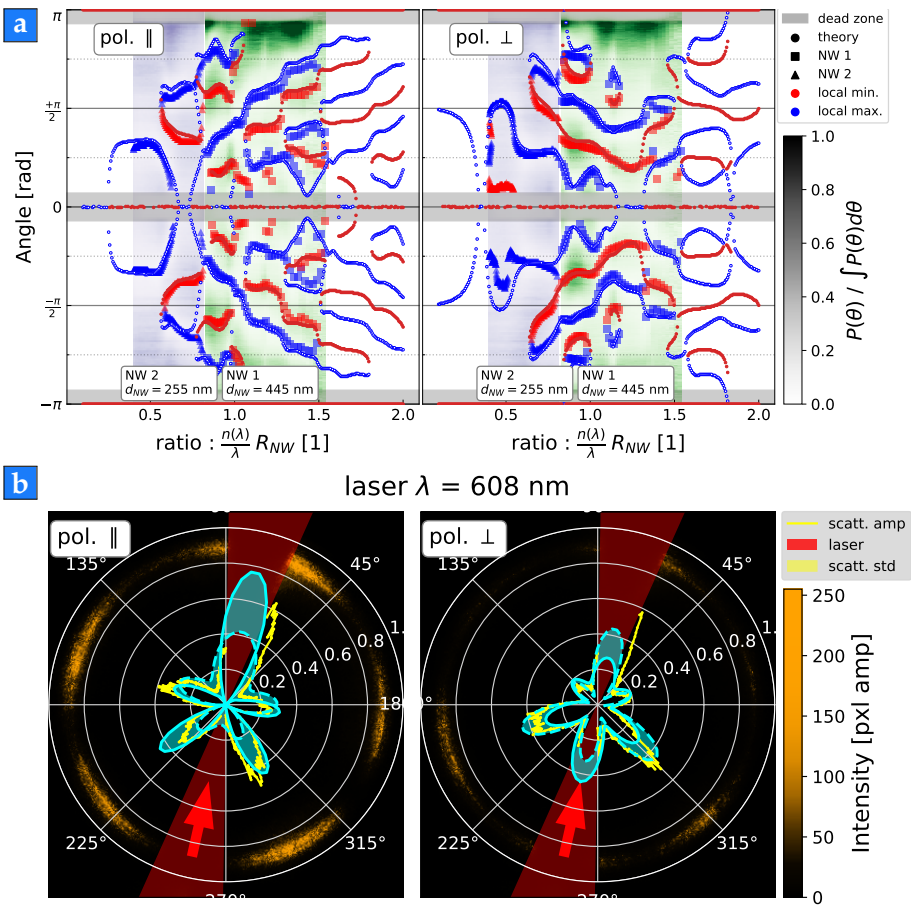

Figure 2.19: (a) Illustration of the overlapping rectangle method to quantitatively estimate the nanowire radius from comparison to theory. The rectangle size is given by the angle uncertainty of the extrema position for its height, and by the ratio uncertainty for its width. (b) Sweeping the radius and computing the total overlapping of the measured points to the theory. For the Nanowire 1 in Fig. 2.20a.

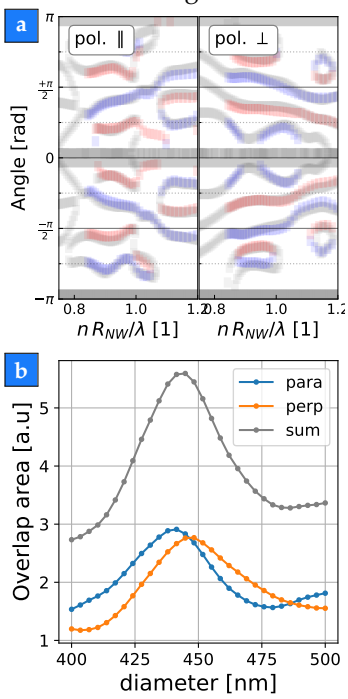

Figure 2.20: (a) Measurement of the local extrema dependence with the ratio $n\,R/\lambda$ for two different nanowires, super-imposed on the theory. The blue markers are the local minima, while the red ones are the local maxima. For nanowire 1 (NW 1) we computed the ratio with the fitting diameter $d_{\text{fit}} = 445$ nm, while for nanowire 2 (NW 2) we chose the fitting diameter $d_{\text{fit}} = 255$ nm. On the other hand, Figure (b) shows a direct fitting of a scattering diagram. We plot the theoretical expected diagram in cyan for 440 nm and 450 nm diameter at the measured wavelength.

total overlapping between the theoretical and the experimental diagram, we can construct a metric to estimate the error on the radius, see Fig. 2.20b.

Doing so, we show in Figure 2.20a the applied method on two measured nanowires. When fitting directly a single scattering diagram taking a single wavelength, depending on the chosen colour, one can get various uncertainties on the nanowire diameter evaluation, especially if the measurement ratio sits around, 0.2, or 0.4, where the diagram does not vary much with the radius at fixed wavelength. That is why, by measuring at several wavelengths, we get much better estimations of the nanowire radius, and the precision is all the more increased when involving higher order Mie resonances.

Figure 2.20b shows the fitting of a scattering diagram measured at a fixed wavelength, using the expected radiated angular intensity with a 10 nm uncertainty range on the chosen nanowire radius. It demonstrates that with a single shot measure of the scattering diagram of a nanowire, one can get its diameter efficiently. The downside of this single shot method is that one has to choose carefully the wavelength that will generate a very distinctive diagram.

2.3.3 Reflectivity

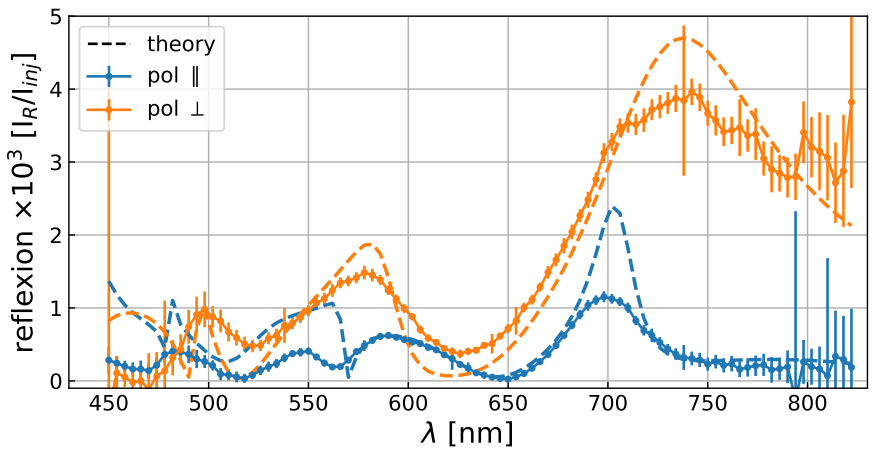

Figure 2.21: Measurement of the reflected intensity by a SiC nanowire of diameter $d_{\text{fit}} = 420$ nm, at different illumination wavelength.

On top of measuring the angular scattering diagrams, the experimental setup in Fig. 2.14a allows to measure the back reflexion intensity of the illuminated nanowire. Figure 2.21 shows the measured reflected intensity normalised by the injected power, for a nanowire of diameter 416 nm. For comparison, we also show the expected profile of the reflexion with the theory, where we adjust the amplitude with an arbitrary constant. We observe the large scale variations follow roughly the theory, but the setup is not sensitive enough to the sharp variation of reflexion due to Mie resonances. The spectral width of the incident wavelength not being pure, might explain the loss in details, not accounting for spurious light (such as reflexion of the incident beam on the objective).

2.4 Perspective

In the future, one can increase the efficiency of the measurement by selecting a discrete set of measurement wavelength that optimises the overlapping discrimination. With increasing precision, one could gain access to more refined effects, such as the contribution of the oxide crust (approximately 5 nm), which is known to cover the nanowires.

Mie resonances structure how the nanowires interact with light, and thus the amplitude of the optical force that can drive the nanowire dynamics. In the following chapter, we will encounter pieces of evidence that the temperature change due to the modulation of the absorbed optical power inside the nanowire will generate a modulation of the optical forces. Indeed, upon changing the local temperature under the illuminating laser, the nanowire radius undergoes thermal expansion, but the refractive index also shifts by a quantity given by the thermo-optic coefficient, α_n. To investigate the general evolution of this thermally induced optical force modulation, we aim to compute the **Lorentz forces** acting on the nanowire illuminated by a plane-wave, while varying the refractive index and the nanowire radius.

2.4.1 Thermal modulation of Optical Forces

The total optical forces acting on a nanowire in an EM field is computed by integrating the Maxwell's tensor through a closed surface [90]. In our case, we solve the EM field equations for an incident plane wave with normal incidence, illuminating an infinite dielectric cylinder, resulting in the Mie resonances (see above section), while the integration will take part over a surface cylinder in the vacuum surrounding the nanowire. In such case, the time average Maxwell's tensor reads,

$$\underline{\underline{\mathbf{T}}} = \left[\epsilon_0\, \mathbf{E}_2 \otimes \mathbf{E}_2^* + \mu_0\, \mathbf{H}_2 \otimes \mathbf{H}_2^* - \frac{1}{2}\left(\epsilon_0\, \|\mathbf{E}_2\|^2 + \mu_0\, \|\mathbf{H}_2\|^2\right) \underline{\underline{\mathbf{I}}}\right], \quad (2.49)$$

where $\underline{\underline{\mathbf{T}}}$, $\underline{\underline{\mathbf{I}}}$ are the Maxwell's tensor and the unity tensor of order 2 respectively, while ($\mathbf{E}_2$, $\mathbf{H}_2$) is the external EM field around the nanowire, computed in sec. 2.2.

The total Lorentz force acting on the nanowire, is then given by,

$$\mathbf{F} = \oint_{\partial A} \underline{\underline{\mathbf{T}}} \cdot \mathbf{n}\, \mathrm{d}\sigma, \quad (2.50)$$

with $\mathbf{n}$ the normal to the infinitesimal integration surface $\mathrm{d}\sigma$, and ∂A the closed cylinder surface around the nanowire. The thermal expansion coefficient, α_l, can be found ten times smaller in amplitude than the thermo-optic one, α_n. As they play a similar role in the Mie resonances (considering the ratio $n\,R/\lambda$), we assume the shift in refractive index is the dominant effect that modulates the optical forces under a temperature change. To estimate the force shift with temperature, we compute the Lorentz force when changing the refractive index at different temperature, such as $n(\lambda, \delta T) = n(\lambda)\,(1 + \alpha_n\, \delta T)$. Figure 2.23

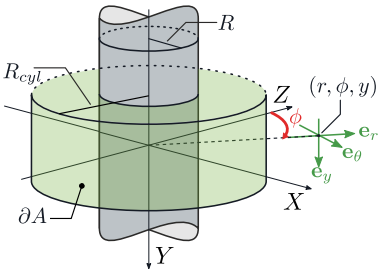

Figure 2.22: Integration scheme, and main notations used for expressing the optical force exerted on a section of the nanowire.

shows the evolution of the Lorentz force for a given nanowire with diameter 555 nm (we expect greater sensitivity to thermal optical force modulation with respect to small diameter nanowires). We also show the expected force sensitivity to temperature change defined such as,

$$F_Z(T_0 + \delta T) = F_Z(T_0) + \partial_T F_Z|_{T_0}\, \delta T, \tag{2.51}$$

with F_Z the force value along the optical axis of the illuminating laser.

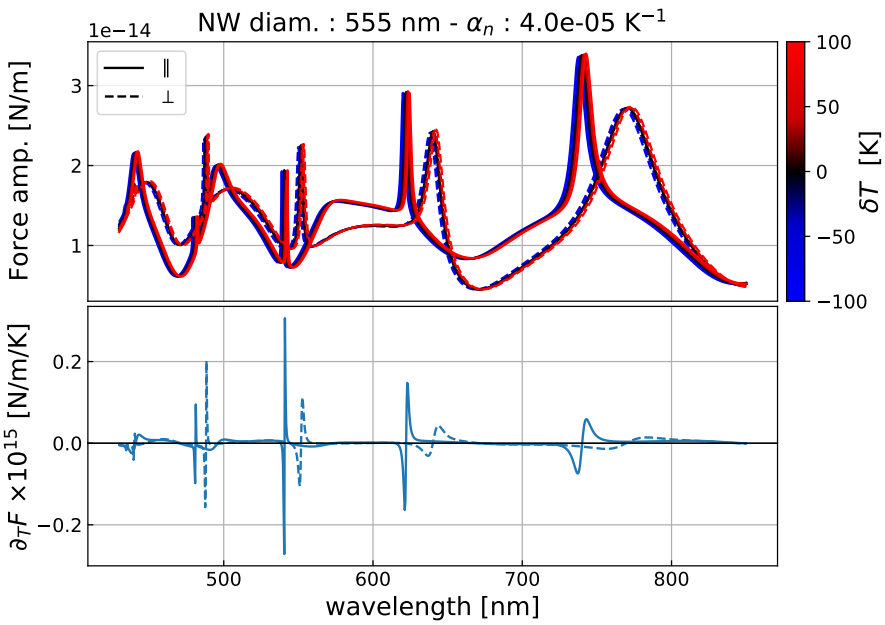

Figure 2.23: Top panel is the computed optical force along the optical axis, when inducing a refractive index change $\delta n = n(\lambda)\,\alpha_n\,\delta T$. Bottom panel is the computed gradient of force with the temperature shift.

2.4.2 Nanowire under Gaussian illumination

In order to get quantitative results in the optical forces acting on the nanowires, one needs to account for realistic incident illumination. We developed a code to project a paraxial gaussian beam onto the plane wave basis, then sum over all the contributions to obtain the scattered field (A. Reigue). This was used to investigate the light-nanowire interaction [76] in the cavity nano-optomechanical experiments conducted in the group [91]. Doing so, one may expect exotic regimes where the total contribution of the optical force is in the opposite direction of the incident radiation propagation which was predicted in ref. [92]. This work is still under investigation and will be subject to further studies, as the interaction with the incident optical field can give rise to non-trivial optical tweezing effects [93, 94].

2.5 Chapter summary

In this chapter we presented the formalism we used to describe the interaction between our 3C-SiC nanowires and an incident plane wave illumination, which involves Mie resonances. It allowed for a quantitative description of the scattering properties of the nanowires, where

the far field angular scattered light was measured using a novel experimental setup. We then described the calibration and the protocols we used with this new setup.

Accessing the angular scattering diagram allows going beyond colorimetric considerations, which requires calibration of the incident white light colour spectrum as well as the colour response of the capturing camera and the display screen. Along with a new method of measuring the nanowires' diameter, we also deepen our understanding in the light-nanowire interaction. It lays the ground for quantitative consideration about the nanowires reflectivity, their enhanced light absorption coefficients (see sec. 5.1.3), as well as grasping the expected properties of the optical force field acting on the nanowires. We provided a mean to compare the different nanowires interacting with the visible light by using a singular parameter, the ratio between the incident wavelength and the effective radius of the nanowire. This method maps all the scattering diagrams and the thus expected interactions of our nanowires with an incident laser light source.

We concluded this chapter teasing future works and refinements we aim at implementing. A more realistic description of the light-nanowire interaction will account for the focusing of the gaussian laser beam, which in the case of large numerical aperture objectives is far from the plane wave approximation.

Picture of the Sionludi cryostat built for optomechanical experiments. The cryostat has been entirely built by E. Eyraud with the help of W. Wernsdorfer while the optical head was realized by J. Jarreau.

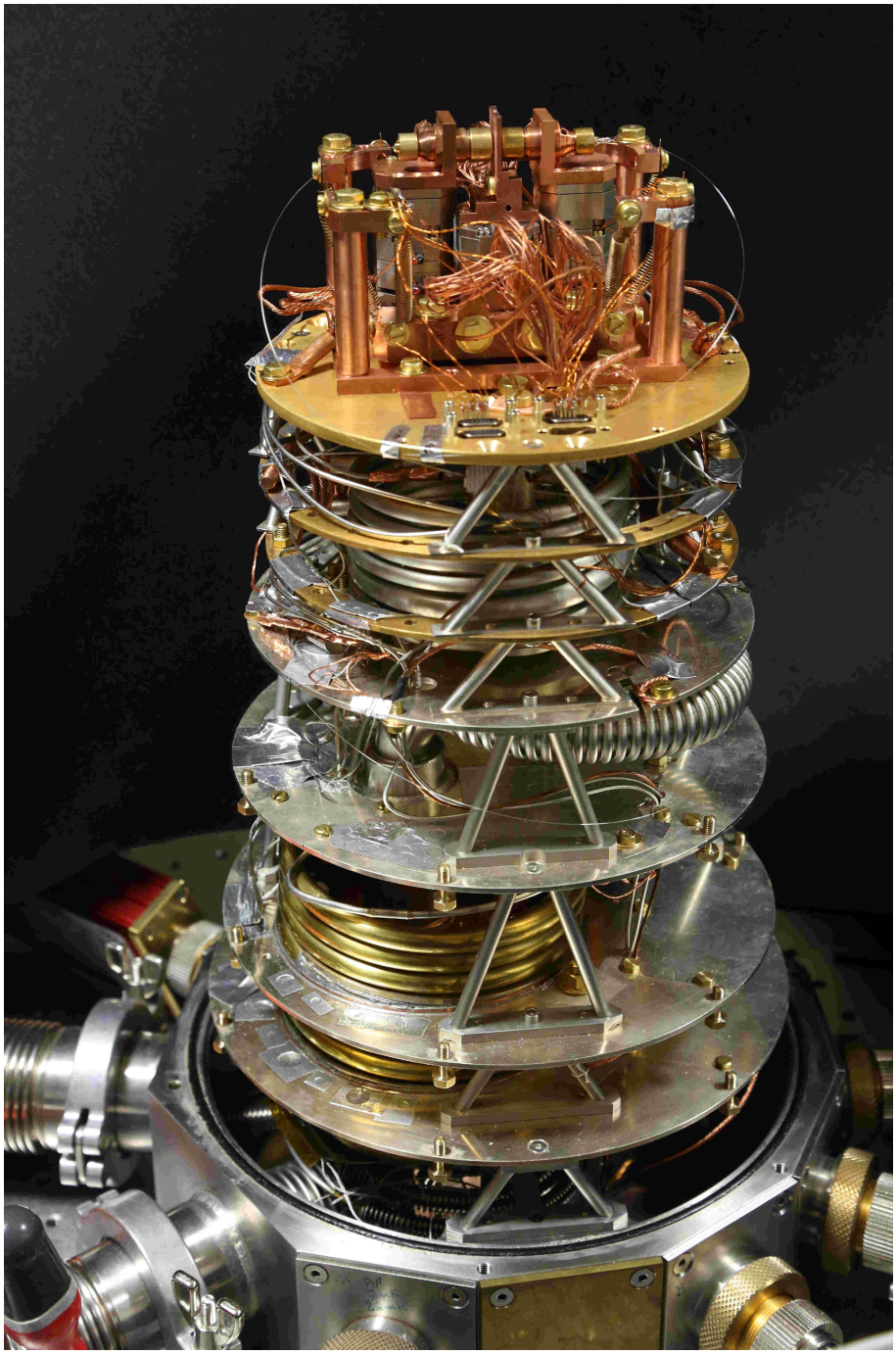

CHAPTER 3

CRYOGENIC OPTOMECHANICAL SETUP

Contents

Introduction **47**
3.1 Description of the Cryostat **48**
3.1.1 Helium circulation 49
3.1.2 Temperature control 50
3.2 Cooling down the experiment **52**
3.3 Optical head **54**
3.3.1 The suspended optomechanical setup 54
3.3.2 Interferometric fibred objectives 57
3.3.3 Detectors 61
3.3.4 Imaging and communication with the instruments 64
3.4 Interferometric readout of the nanowire vibrations **65**
3.5 Thermalizing a nanowire resonator at cryogenic temperature **66**
3.5.1 Reduction of thermal noise 66
3.5.2 Linearity of the mechanical response 68
3.5.3 Optical heating and heat propagation regimes 68
3.6 Chapter summary **75**

Introduction

In this chapter we will present the experimental setup used for studying SiC nanowires at cryogenic temperatures. First the general working principle of a cryostat will be presented, as well as the specificities of the **Sionludi** design. That design allows us to implement an optical setup on the cold plate of the cryostat, which was used to perform optomechanical experiments down to 20 mK. In a second time, the different elements composing the optical head developed to study the heat propagation within nanowires will be presented. Finally, we present the first thermalisation results, where we demonstrated it was possible to observe a nanowire featuring a noise temperature of about 30 mK temperature. We also show the investigation of the nanowires force sensing properties at low temperatures.

Thermal noise is the limiting factor in force sensing experiments at room and dilution temperature. Going at low temperatures not only allows to observe an increase in Q-factor, but also the overall improvement of the spatial stability, as well as a dramatic increase in the oscillator frequency stability. It opens great promises for exploring new physics at low temperature via ultrasensitive force sensing experiments.

However, thermalizing nanomechanical resonators at mK temperature is not an easy task as they couple easily to spurious environmental vibration, often due to the cryostat functioning as well as electric fluctuations [95].

3.1 Description of the Cryostat

The Néel Institute is well known for its expertise in cryogenics. Imagined by A. Benoit in 1990, the upside-down design for dilution refrigerators was subsequently optimised by several generations of researchers and engineers at the Institute. Among them, Wolfgang Wernsdorfer and Eric Eyraud realized a systematic optimisation of the concept, and produced several generations of **Sionludi** (where the name relate to the reverse of Dilution referring to the vertical inversion of the functioning of the cryostat). Their work features a constant improvement in the cryostat performances while also aiming at standardizing the instrument operation and its environment (pumping group, software, etc). We benefited from their incredible expertise, and with the help of other colleagues in the Institute, we built an experimental platform dedicated to the realization of ultrasensitive force measurements at dilution temperatures, see Figure on the left of the chapter title page. Contrary to traditional cryostat, the cold plate is at the top of the apparatus, which is interesting for its compatibility with optical experiments. Three internal shields are used to thermally insulate the different stages of the cryostat, see Fig. 3.1.

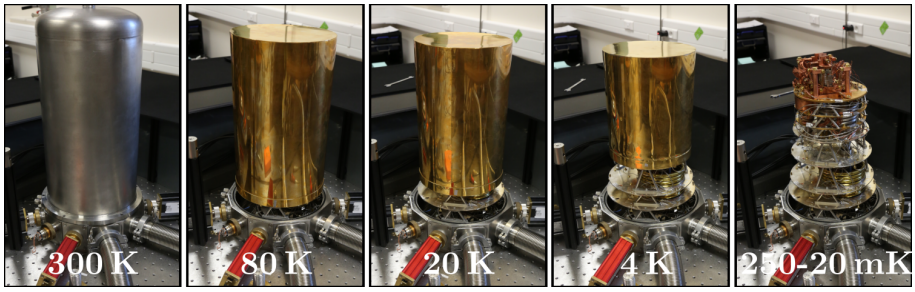

Figure 3.1: Picture of the thermal shield use to thermally isolate each stage. The overall setup is like a russian doll.

3.1.1 Helium circulation

The working principle of the Sionludi cryostat stays the same as any other dilution fridges [96]. The cryostat is made of various stages with decreasing temperature from the bottom to the top stages, Fig. 3.2. He^4 liquid is used to cool down the first three stages (80 K, 20 K, 4 K), see Fig. 3.3a. The 4 K stage has a great cooling power allowing for a quick thermalisation of bulky elements. During the cooling phase, a heat exchanger precools the He^3He^4 mixture circulating inside the **fast injection** in gaseous form, see Fig. 3.3b, allowing a quick thermalisation of the upper stages down to 4 K. In the normal dilution mode, this short circuit is not used, and the mixture takes the **normal injection** path, Fig. 3.3c, and circulates first through a counter-flow heat exchanger with the He^4 evacuation from the 4 K box. Then the mixture undergoes a Joule-Thomson expansion in a heat exchanger, that also collects the return of the mixture from the coldest area. After a condensation impedance, the mixture becomes liquid, then falls into the mixing chamber where the dilution process operates. The pumped phase passes through the still where He^3 is continuously extracted during the steady-state operation, and whose cold vapour serves to precool the incoming mixture (in the Joule-Thomson heat exchanger).

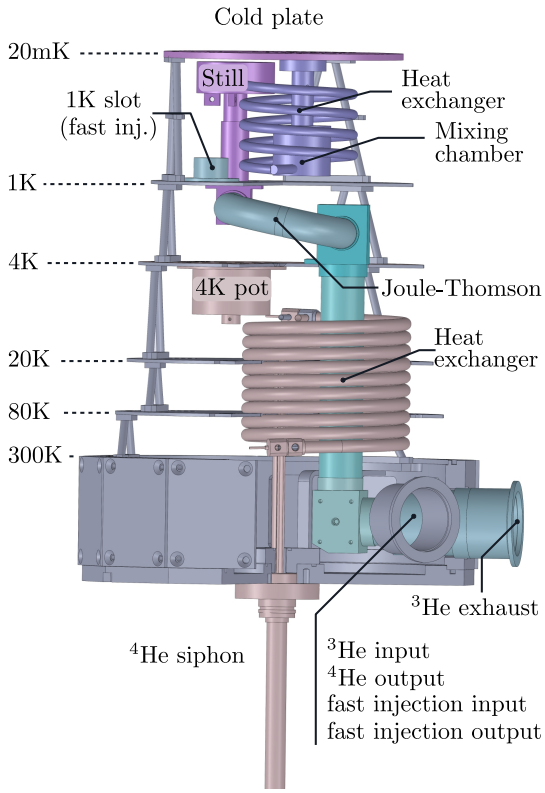

Figure 3.2: Schematic of the **Sionludi** cryostat overlayed with colours to highlights the important elements.

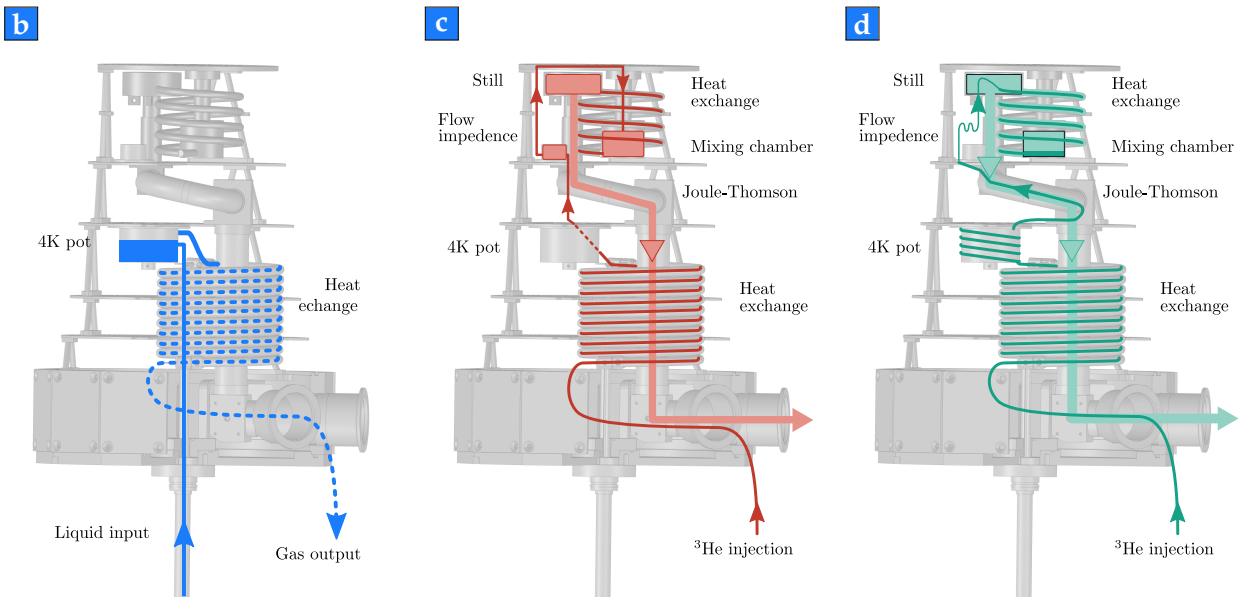

Figure 3.3: Schematic of the **Sionludi** cryostat overlayed with colours to highlights the important elements, 3.2, and circulation systems, such as (a) the He^4 circulation. (b) the **fast** injection. (c) the **normal** injection.

Figure 3.4: Picture of one thermo-resistor thermally coupled to a cryostat stage.

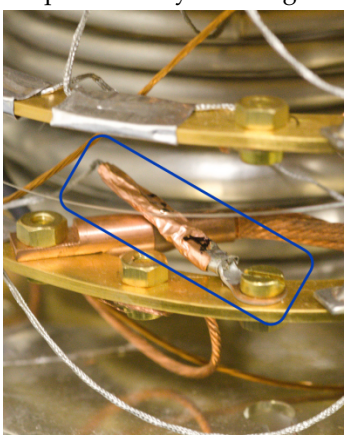

3.1.2 Temperature control

The cryostat is equipped with three sets of thermometers in order to measure the temperature at the different stages, Fig. 3.4.

Two thermometers are installed on the experimental setup, allowing us access to the temperature close to the studied sample, while six others are permanently connected to the cryostat itself. The thermometers are made of a combination of Platinum (Pt100), Carbon (C100), Ruthenium oxide (RuO_2), see Fig. 3.5a. Those materials present a rapidly changing resistivity with temperature, and different combinations of those elements allows building thermometers suited for the different temperature stages. Their temperature dependence in shown in Fig 3.5b.

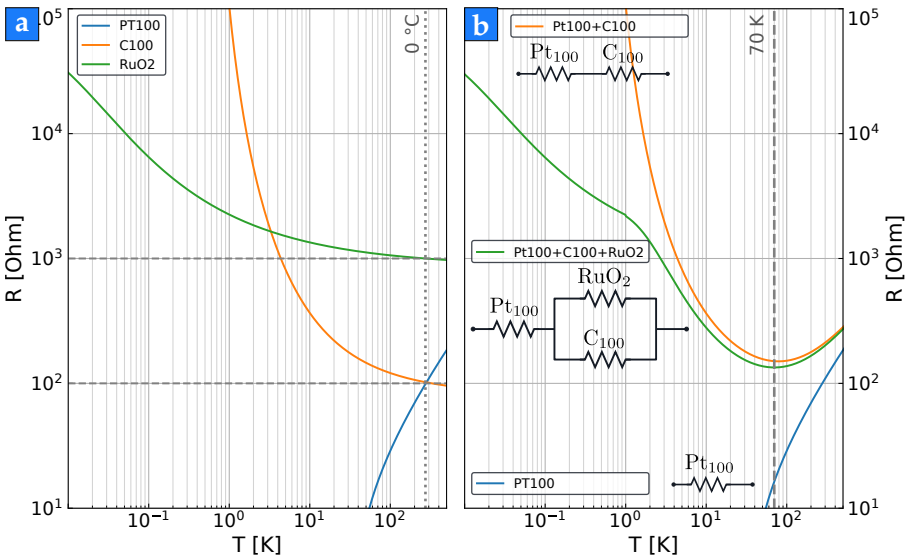

Figure 3.5: Thermo-resistor function used to measure the temperature at the different stages inside the cryostat. (a) Material resistance with the temperature. (b) Thermometer resistance with temperature.

The 80 K thermometer is made of a single Pt100 resistor. The 4K and 20 K thermometers combine a Pt100 and a C100. The coldest thermometers are made of Pt100 in series with a Ru02 and a C100, which provide a rapidly changing resistance over a large temperature range, except in the region of 70 K, which is of lower importance. This configuration is used in the thermometers used for the mixing chamber, for the still, and for the experimental platform. Additional thermometers, only made of Ru02 are used as complementary measurements (on the 50 mK ring, on the mixing chamber and on the 1st plate).

To measure the resistance, we perform a **4-terminal sensing** using two MMR3 modules developed by the electronic department of the Institute, Fig. 3.6b, which can simultaneously read three different thermo-resistors. Those modules are interfaced with a TCPIP protocol, and we have implemented a parallel readout sequence, based on UDP protocols, to provide a more readable interface for the cryostat, see Fig. 3.6e. On top of that, one can heat the sample using a 1 kΩ heating element controlled by a stable electrical source via a MGC3 module. They jointly work with the MMR3s and allow to implement a **PID** loop to have reliable control over the sample temperature, Fig. 3.6d. In practice, the cryostat stability is sufficient not to activate any

active stabilisation loop.

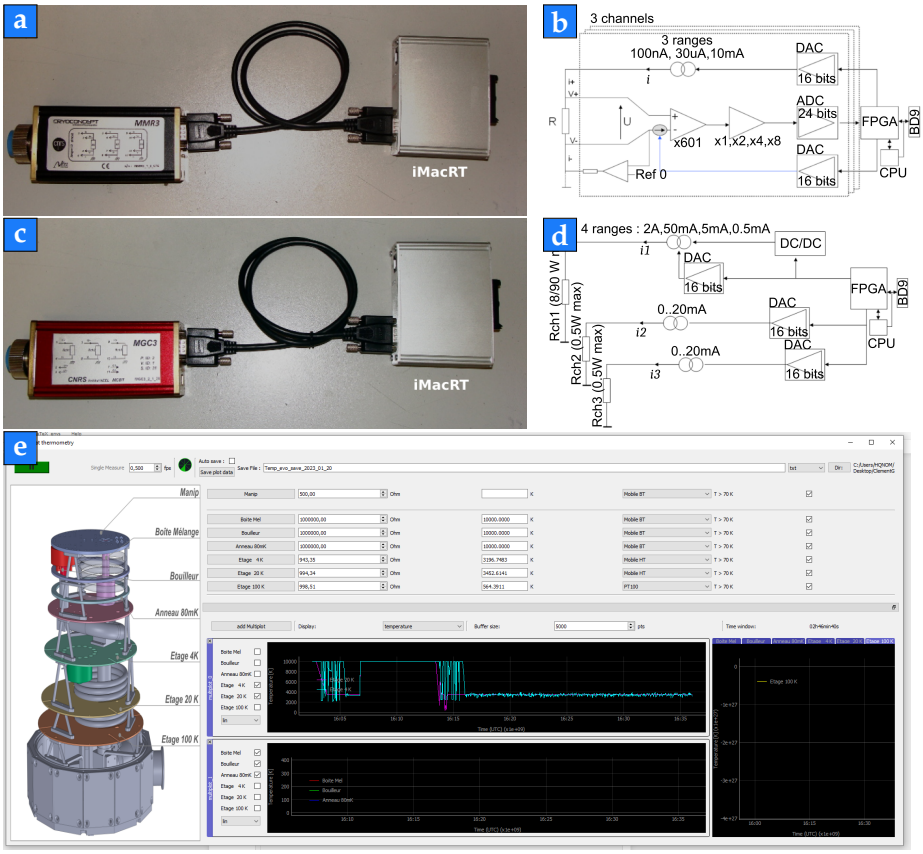

Figure 3.6: (a) Picture of the MMR3 box used to measure the temperature inside the cryostat, and its functioning diagram (b). (c) Picture of the MGC3 box used to measure resistively heat up the nanowire sample holder, and its functioning diagram (d). More information at the technicians' webpage `http://elec.neel.cnrs.fr/macrt/index.php`. (e) Shows the python-based User Interface for thermometer readout developed during the PhD thesis. The interface makes use of PyQT and pyqtgraph modules.

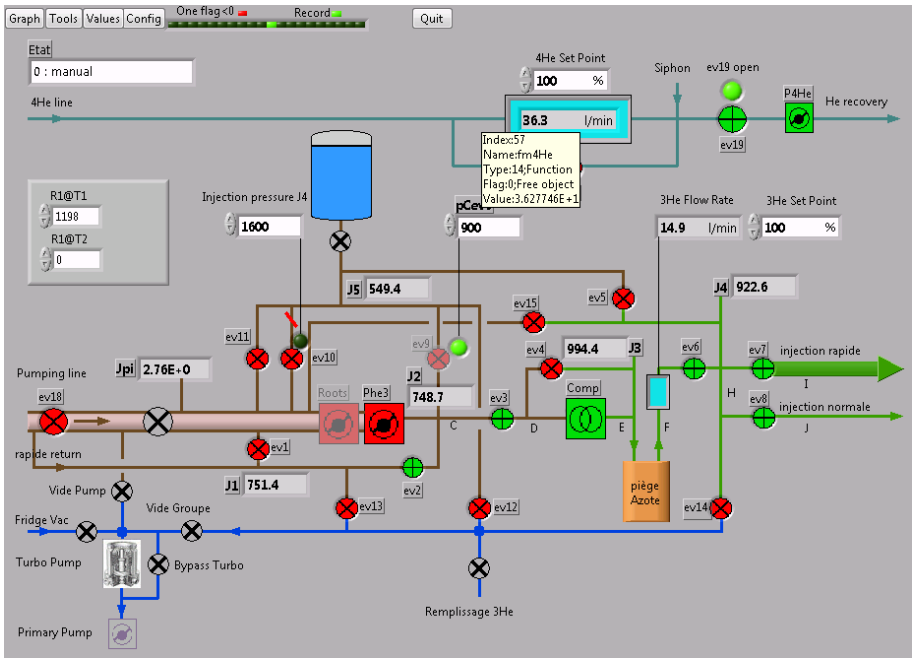

Figure 3.7: *Cryoptic* interface. Software that controls the solenoid valves that manage the circulation of the helium insides cryostat.

3.2 Cooling down the experiment

The cryostat is controlled using a LabView interface, Fig. 3.7, originally developed by P. Gandit. The software manages a set of solenoid valves and flow controllers that regulate the fluid circulation in the cryostat. There are two independent piping systems : one for the He^4, Fig. 3.9a, and one for the helium mixture He^4He^3, Fig. 3.9b.

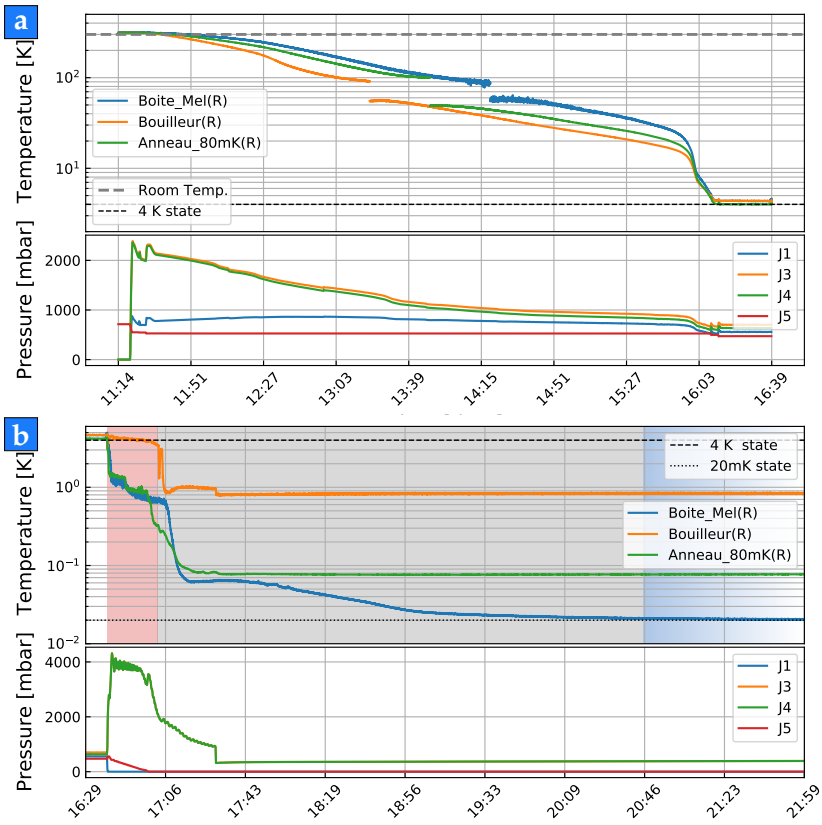

Figure 3.8: (a) Temperature evolution during a cooldown from room temperature to 4 K state. (b) Temperature evolution when the dilution starts and reaches its stationary regime. The red background colour corresponds to the **fast precooling** configuration of the *Cryoptic* interface, while the grey background to the **continuous precooling** configuration. The blue background correspond to the stable 4 K state reached by the cryostat.

To make the description of a typical cooldown more clear, we define three main states that the cryostat will reach during the process: the **300 K state**, the **4 K state**, and the **20 mK state**. A typical temperature evolution during the pre-cooling phase, from 300 K to 4 K, is showed in Fig. 3.8a. For our experiments, the pre-cooling phase lasts typically 4 hours, which is convenient since one needs to constantly track optically the nanowire in order to compensate misalignment due to thermal contraction of the different elements composing the setup. Still it could be done at a higher pace (down to 2 hours) at the price of a higher He^4 consumption. In our case 8 to 10 L of He^4 are used to reach 4K.

Starting from 300 K, the *Fast-precooling* mode uses two injection channels in order to quickly cool down the cryostat. During this phase, one injects a fraction (approx 10%) of the total He^4He^3 mixture in circulation, which serves as a coolant gas and is subsequently pumped away at room temperature. The injected mixture is also precooled by the Nitrogen "booster" (only for the rapid injection channel).

Then after typically 15 minutes, we pass to the *Continuous-precooling* mode. The He^4 flow rate is now stabilized to a smaller value (16% of

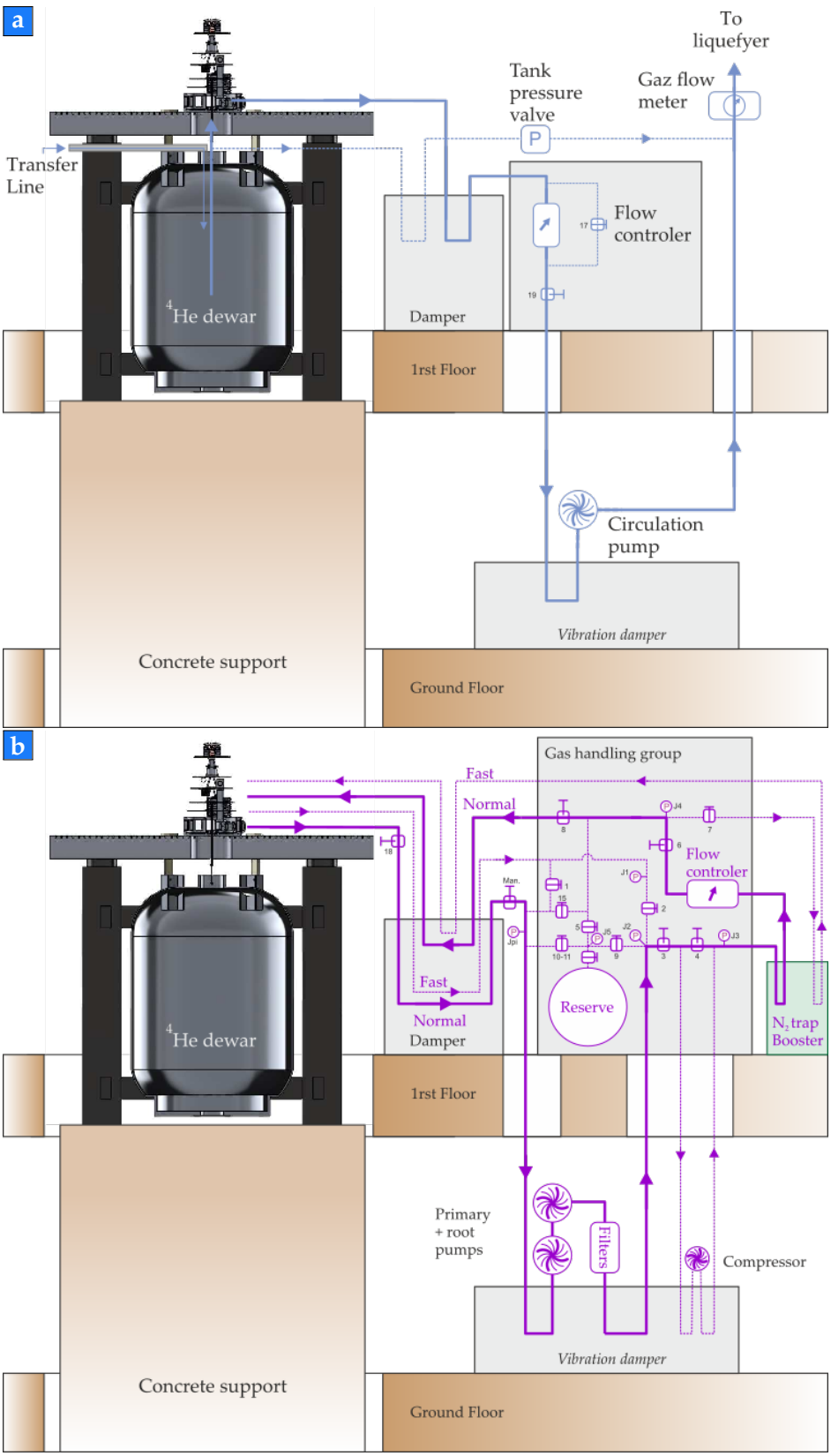

Figure 3.9: (a) He^4 pumping circulation. (b) Mixture pumping circulation: normal and fast.

the maximum flow) to optimise the cooldown rate and the He^4 consumption. When the head of the cryostat has reached 4 K, we typically wait for 30 minutes before initiating the condensation of the mixture.

During this phase the fast injection channel is closed and the totality of the mixture is progressively injected in the cryostat, thereby initiating the condensation. After about 30 minutes, most of the mixture has been condensed, the still as well as the mixing chamber temperatures go below 1 K, and the dilution process starts. In less than 20 minutes the base temperature has reached 30 mK, and it will take around 30 minutes more to reach its lower temperature (20 mK). After the cryostat has achieved 20 mK, the program goes to Operating mode where only the injection flow is regulated.

3.3 Optical head

The core experimental apparatus that was employed at the beginning of my PhD, developed during the PhD of F. Fogliano, is shown in Fig. 3.10 and in more detail in Fig. 3.11. It was meant to investigate the possibility to employ our silicon carbide nanowires at dilution temperatures, so as to improve their force sensitivity, as well as to access novel physics at low temperatures. We chose to employ a fibre optical readout, for the sake of compactness and long term stability. As comparison, a free space approach requires complex viewport systems and suffers a lot from temperature induced misalignments. We had to develop our own objectives, compatible with dilution temperatures. The alignment of the experiment was insured by a set of piezo positioners, and we also had to include a suspension apparatus to isolate the nanowire from the vibration generated by the cryostat as a result of the fluid circulation. Those different aspects are summarized in the following section.

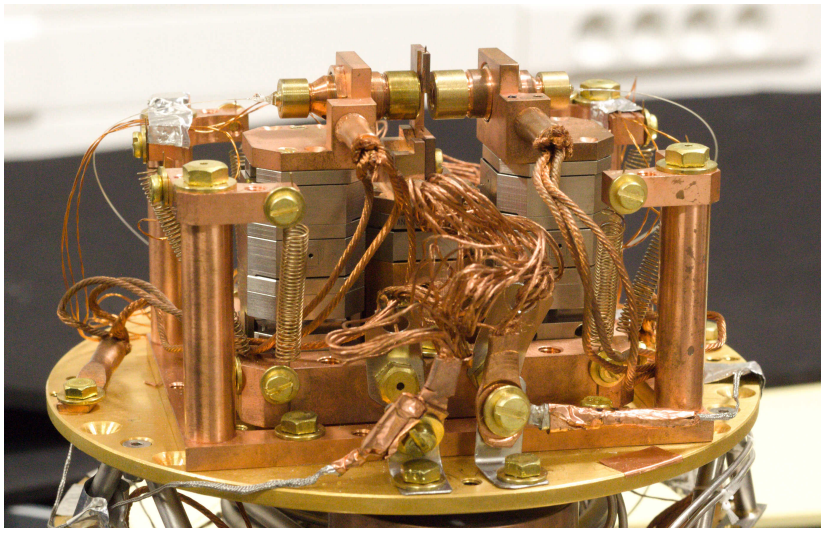

Figure 3.10: Picture of the optical head mounted on the 20 mK stage of the Sionludi cryostat.

3.3.1 The suspended optomechanical setup

We implemented a fully suspended optomechanical setup, Fig. 3.11, to isolate the nanowire from the vibration noise generated by the fluid circulation. This problem was first spotted when we intentionally froze the still (by temporarily stopping the injection) and observed

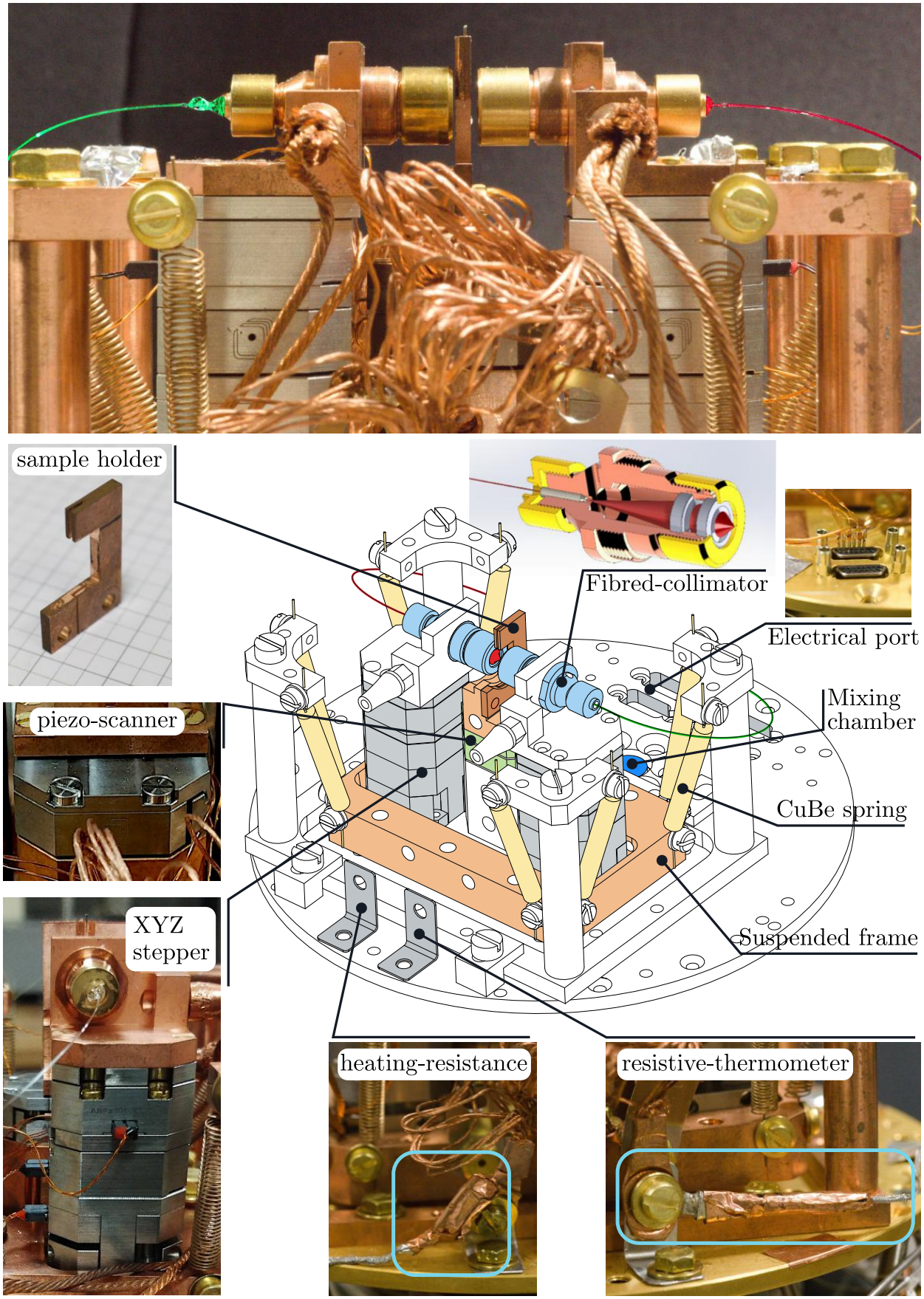

Figure 3.11: (Top picture) Close up picture of the optical head, with a super-imposed camera exposition showing the coloured laser circulating in the fibres. (Annotated schematic) Compilation of pictures of the different elements composing the optical head setup, and their associated placement in the Solidworks blue-print.

a dramatic reduction in the noise temperature of the nanowire. The vibration noise at the base of the cryostat was estimated at the level of a few pm/$\sqrt{\text{Hz}}$ at 4 kHz which was sufficient to produce an excess of artificial noise of approximately 200-400 mK. The designed suspension is made of 8 beryllium-copper springs with stiffness of approximately 30 N.m^{-1} (elongation of 20 mm for a total setup mass of 500 g).

The nanowire is attached to a tungsten tip, which is in turn clamped on a copper sample holder, see inset in Fig. 3.11. The support is mounted on an AttoCube piezo scanner, allowing to move the nanowire in a 3D XYZ volume of (27 x 5.4 x 27) μm^3 at room temperature. This volume shrinks down to (7 x 1.4 x 7) μm^3 at low temperatures due to the reduction of the piezoelectric efficiency. The scanner is controlled by a National Instrument card, through an amplifier.

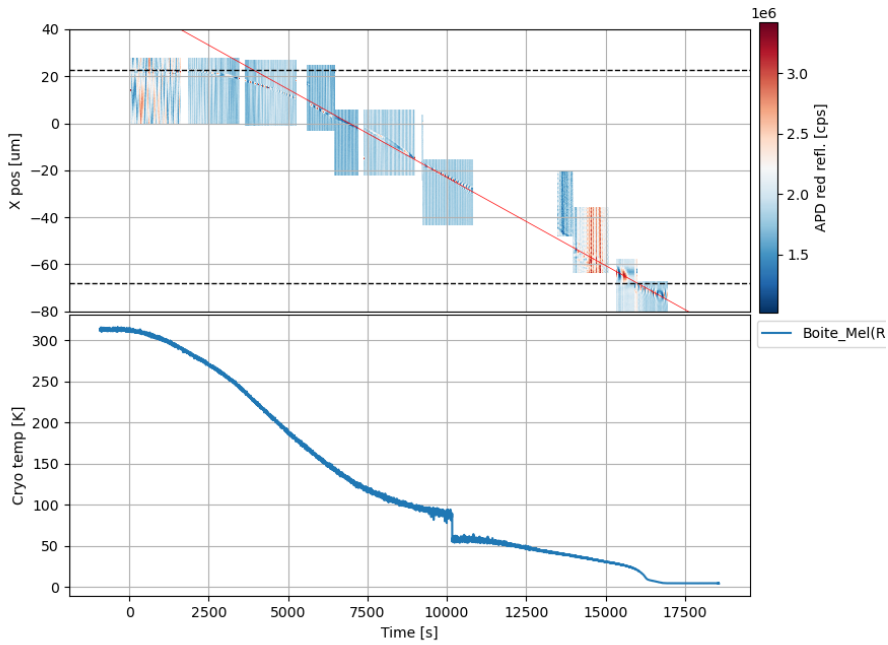

Figure 3.12: Measurement of the lateral displacement due to thermal expansion during cooldown. While cooling down, we follow the nanowire with the collimator using the steppers, in order to keep the nanowire in focus. This can gives the rate of thermal shift. Each inset image is the reflected photon flux upon scanning the nanowire in the laser waist. The red line correspond to an estimation of the shift rate to 7.5 nm.s^{-1}, which is very reproducible between different cool downs.

To perform the readout of the nanowire displacements, specific fibred interferometric objectives were developed in the Institute (machined by J. Jarreau). Using two of those collimators we are able to focus a laser on the nanowire, while collecting the reflected and transmitted light. Alternatively we can inject two different colours at different positions along the nanowire. Those objectives are mounted on titanium AttoCube Steppers, which are used to adjust the relative position of the laser spot and the nanowire in order to compensate for thermal expansion and deformation within the cryo-head during the cooldown, see Fig. 3.12. During this tracking phase, we only adjust the XZ horizontal degrees of freedom. Concerning the vertical axis, since the copper is contracting more than the titanium, the nanowire has a tendency to "plunge" into the laser spot, so there is no risk of loosing it vertically. Once the cryostat is cold, we can find the nanowire extremity by progressively lowering the objective support.

With all these elements, good thermalisation is assured thanks to soft copper cables. Those braided cable made of pure OFHC copper, are connected from the objective support, from the nanowire holder and from copper suspended plate, down to the 20 mK plateau and to the mixing chamber. They also provide a damping for the spring suspension, without which long-lasting oscillations (already 2 minutes at room temperature and in air) could become a problem.

3.3.2 Interferometric fibred objectives

We designed and fabricated specific fibred objectives to install in the optical head so as to increase the compactness as well as the stability of the optomechanical setup. The objectives are made using two aspheric lenses : a first lens of focal $f = 15.29$ mm serves to collimate the laser beam, while a second lens of numerical aperture $NA = 0.7$ focusses the laser down to an approx. 500 nm spot. To adjust the objectives, we displace the single mode fibre inside the ferrule, measure the optical waist profile for each position and then glue it (using a UV curing glue) at the optimal position.

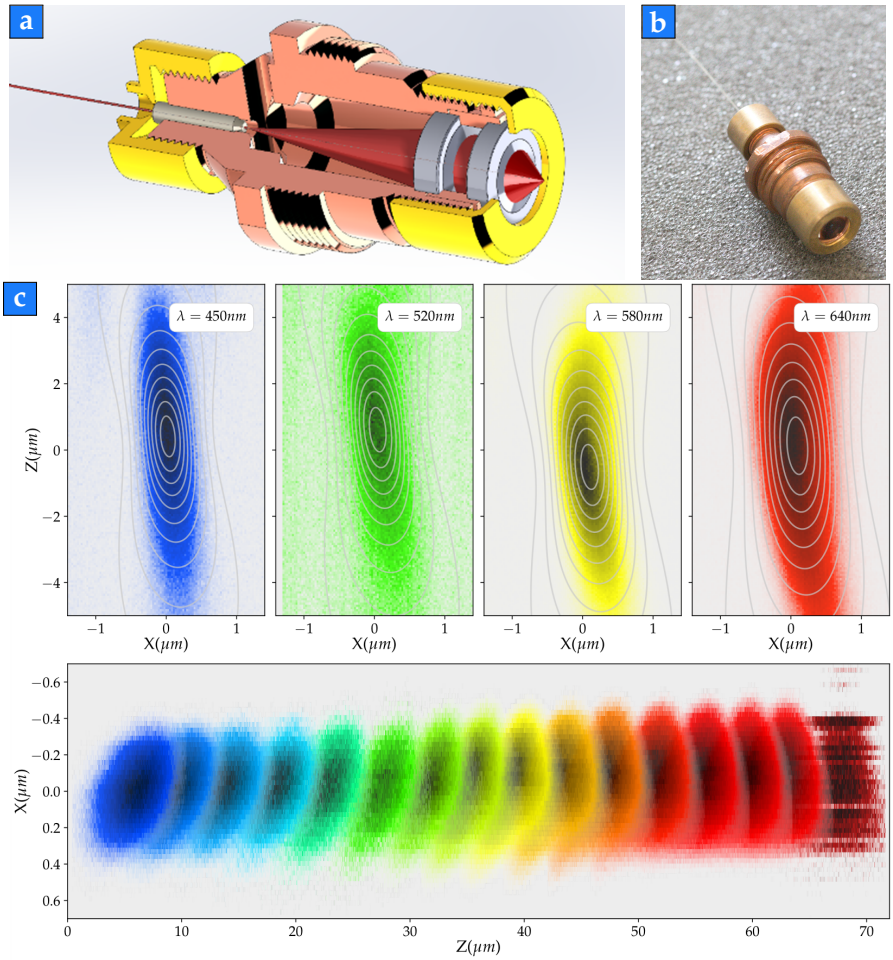

Figure 3.13: Crafted fibered objectives, (a) Solidworks blue-print of the crafted objective. (b) Picture of a mounted collimator. (c) Achromaticity characterisation of the objectives, from [66].

We characterised the achromaticity using a Supercontinuum laser, Fig. 3.13c, which was done during the PhD of F. Fogliano. Because the temporal coherence of the Supercontinuum is short, we do not resolve

the interference pattern upon scanning the nanowire in the optical waist of the objective. Still we can recover the gaussian shape of the focused beam and calibrate the achromaticity of the objectives.

To tackle the polarimetry characterisation, we use the standard framework in linear optics [97, 98]. It assumes that the output fields of an optical system is a linear combination of the input fields components. In order to deal with real systems that can have depolarisation effect, the state of polarisation is described by the Stokes vectors, $\mathbf{S} = (S_0, S_1, S_2, S_3)$, and we use Mueller matrices to describe the optical elements [99].

To characterise the fibred objectives, we aim to compute the Mueller matrix for each objective by analysing the polarisation transformation undergone by an incoming laser beam. We implement a rotating quarter-wave plate method [100], to measure the Stokes parameters of the light. As a remark, it is important to notice that experimentally the polarisation of a laser beam is not well conserved when it is reflected by mirrors in an optical bench, except when it is in the S/P-polarisation state. This is why we took care of measuring the polarisation state just after re-collimation of the output of the fibred collimators, see Fig. 3.14a.

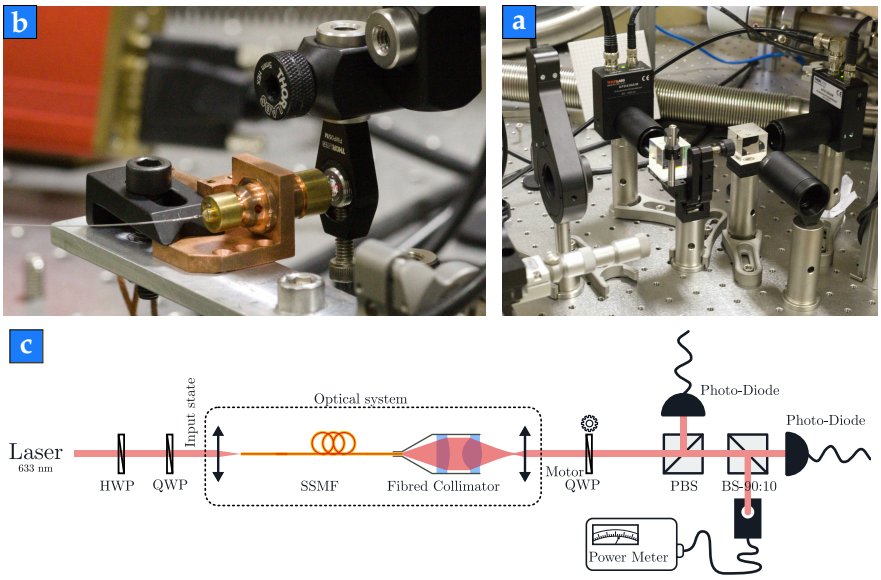

Figure 3.14: Setup used for the measurement of the polarisation properties of the interferometric fibre objectives. The Stokes parameters of the injected light and the transmitted light, (b) picture of the setup, (a) picture of the re-collimated transmitted light, (c) setup scheme. We use a Polarising Beam Splitter (PBS) with photo-diodes and a power meter for redundancy.

The notation we use follows closely the article [100]. Any beam of radiation can be considered as a mixture of unpolarised light (*i.e* random dephasing between fields components) and completely polarised light. When considering polarised radiation E-fields, in the Horizontal/Vertical reference framework,

$$E_H(z,t) = E_{H,0}\cos(\omega t - kz + \delta_H), \tag{3.1}$$
$$E_V(z,t) = E_{V,0}\cos(\omega t - kz + \delta_V), \tag{3.2}$$

where $E_{H,0}, E_{V,0}$ are the amplitude of the fields components, ω the radiation pulsation, k the wave vector and δ_H, δ_V an initial phase. Our measurement setup is only sensitive to the intensity of the radiation, this is why using the Stokes parameters that relate the time average

quadratic field components to the state of polarisation is most relevant.

$$\mathbf{S} = \begin{pmatrix} S_0 \\ S_1 \\ S_2 \\ S_3 \end{pmatrix} = \begin{pmatrix} E_{H,0}^2 + E_{V,0}^2 \\ E_{H,0}^2 - E_{V,0}^2 \\ 2\,E_{H,0}\,E_{V,0}\,\cos(\delta) \\ 2\,E_{H,0}\,E_{V,0}\,\sin(\delta) \end{pmatrix}. \tag{3.3}$$

Now considering the Stokes vector of a real state which is partially polarised, $\mathbf{S} = (S_0', S_1', S_2', S_3')$, one can compute the degree of polarisation with,

$$P = \frac{\sqrt{(S_1')^2 + (S_2')^2 + (S_3')^2}}{S_0'}, \tag{3.4}$$

where $0 \leq P \leq 1$. P is unity for completely polarised light. As mentioned before, $\mathbf{S}$ can be expressed as the sum of unpolarised light and completely polarised one, such as

$$\mathbf{S} = (1-P)\begin{pmatrix} S_0 \\ 0 \\ 0 \\ 0 \end{pmatrix} + P\begin{pmatrix} S_0 \\ S_1 \\ S_2 \\ S_3 \end{pmatrix} = (1-P)\,\mathbf{S}_{\mathrm{UNP}} + P\,\mathbf{S}_{\mathrm{CP}}, \tag{3.5}$$

with $S_0 = S_0'$. From a measurement of the partially polarised Stokes parameters, one retrieve the completely polarised ones,

$$\mathbf{S}_{\mathrm{CP}} = \begin{pmatrix} S_0 \\ S_1 \\ S_2 \\ S_3 \end{pmatrix} = \frac{1}{P}\begin{pmatrix} S_0' \\ S_1' \\ S_2' \\ S_3' \end{pmatrix} - \frac{1-P}{P}\begin{pmatrix} S_0' \\ 0 \\ 0 \\ 0 \end{pmatrix}. \tag{3.6}$$

The polarimetry measurement consists in passing the polarised light through a quarter wave plate with fast angle rotated by θ with respect to a polariser. In our experiment we use a Polarising Beam Splitter (PBS). The transmitted intensity after the PBS of the light is,

$$I(\theta) = \frac{1}{2}\left(S_0 + S_1\,\cos^2(2\,\theta) + S_2\,\cos(2\,\theta)\,\sin(2\,\theta) + S_3\,\sin(2\,\theta)\right). \tag{3.7}$$

Figure 3.16 shows the expected signal when applying the measure for linearly polarised light, as well as circular one.

In figure 3.15 we show the ellipse representation of the polarisation state and how the ellipse parameters relate to the Stokes ones.

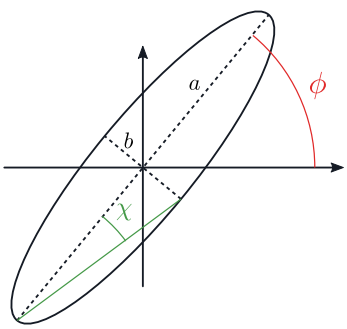

Figure 3.15: Ellipse representation of a polarisation state. The ellipse parameters are given with the relation $S_1 = I_0\,\cos(2\,\Phi)\,\cos(2\,\chi)$, and $S_2 = I_0\,\sin(2\,\Phi)\,\cos(2\,\chi)$.

One can either fit the resulting pattern, or expand eq. (3.7) in a truncated Fourier series,

$$I(\theta) = \frac{1}{2}\left(a_0 + b_2\,\sin(2\,\theta) + a_4\,\cos(4\,\theta) + b_4\,\sin(4\,\theta)\right), \tag{3.8}$$

with the relation, $a_0 = S_0 + \frac{S_1}{2}$, $b_2 = S_3$, $a_4 = \frac{S_1}{2}$, $b_4 = \frac{S_2}{2}$. Using the

Fourier series analysis,

$$a_0 = \frac{1}{T} \int_T I(\theta) \mathrm{d}\,\theta, \tag{3.9}$$

$$a_n = \frac{2}{T} \int_T I(\theta)\ \cos(n\,\theta)\,\mathrm{d}\theta, \tag{3.10}$$

$$b_n = \frac{2}{T} \int_T I(\theta)\ \sin(n\,\theta)\,\mathrm{d}\theta, \tag{3.11}$$

with T the period, thus here $T = 2\,\pi$.

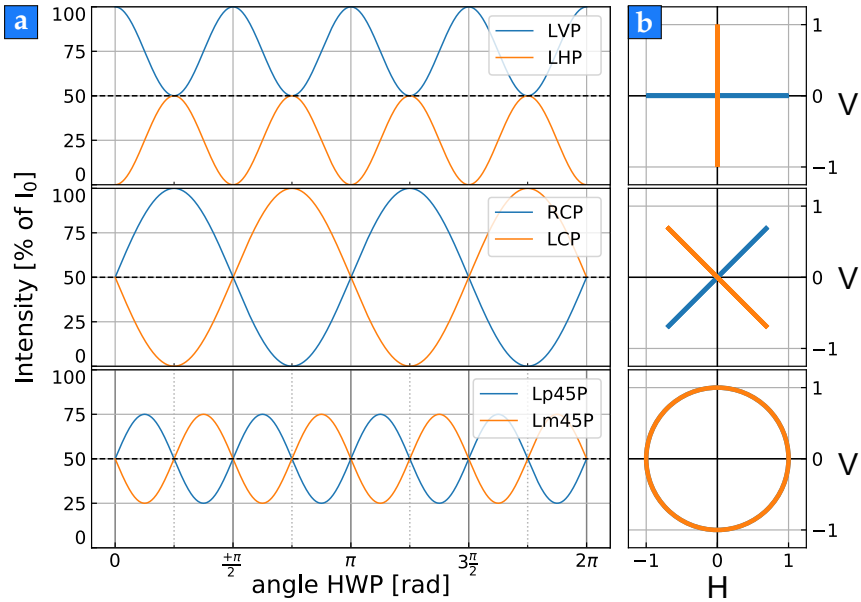

Figure 3.16: Expected evolution of the measured intensity with the rotation of the HWP in the polarisation state measurement setup. (a) Relative intensity normalised by the incident intensity : horizontal and vertical output polarisation (top panel), diagonal polarisation (middle panel), left and right circular polarisation (bottom panel), p and m in the label standing for *plus* and *minus* respectively. (b) Corresponding ellipse representation of the measured Stokes parameters, normalised by the intensity. The correspondence between the Stokes parameters and the ellipse is given in Fig. 3.15.

In figure 3.17 is presented the results from the measurement of the output polarisation state for various input polarisation state. The actual optical system is composed of the lens use to inject light into the single mode fibre, and the objective 1 and 2 that focus the light onto the nanowire. There is an additional lens that collimate back the focused beam, in order to send the light into the rotating wave polarisation state measurement setup. Figure 3.17b, shows the extracted Mueller matrix coefficients for both objectives in the case where we normalised the output intensity so that we account losses due to not perfect injection into the fibred objectives.

Characterising the polarisation behaviour of the objective is important to better control the polarisation of the incident radiation acting on the nanowire. Indeed, the nanowire is a highly birefringent optical system due to its geometry and the Mie resonances, and thus very sensitive to the incoming light polarisation. This sensitivity can be used in order to measure the local change of temperature in the nanowire that will induce a change in the nanowire reflectivity. However, the above characterisation is a first step toward a full control of the incident light polarisation interacting with the nanowire. The fibred objective had to be displaced into the polarisation measurement setup, and thus when put back on the optical head in the cryostat, the bending of the fibres can induce a change in the birefringence of the whole fibred objective optical system. On top of that, after cooling down the cryostat, one

expect a change in the polarisation properties of the fibred objectives as well.

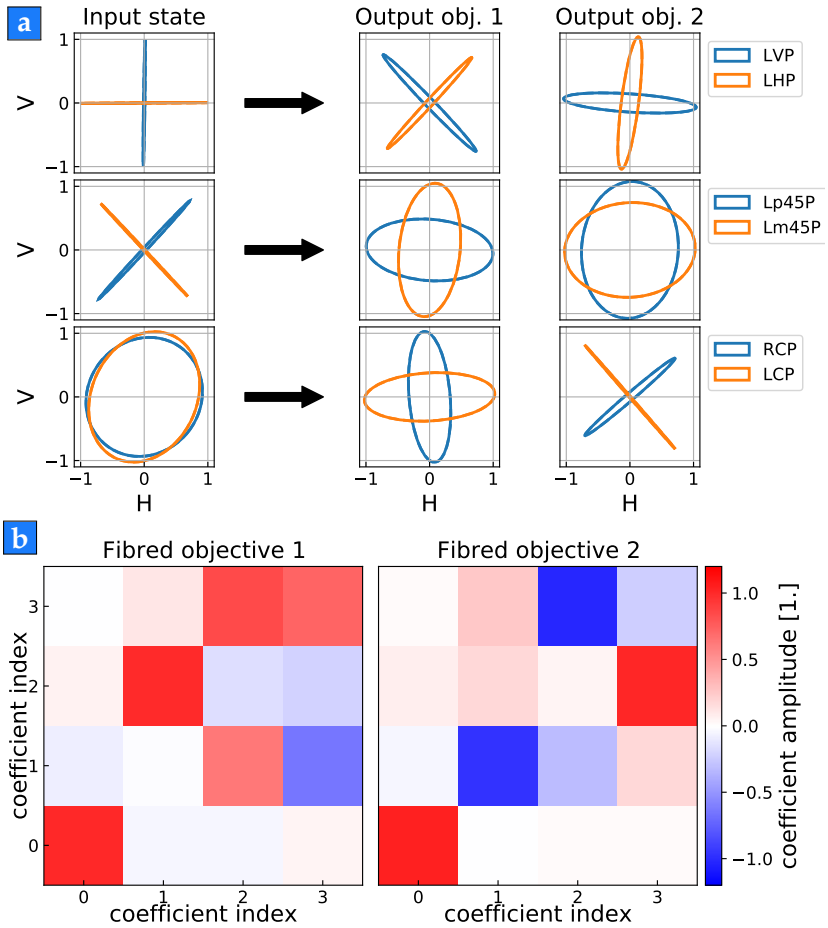

Figure 3.17: Polarisation measurement for collimator characterisation, (a) Elliptical representation of the measured polarisation states, (b) Computed Mueller matrix of the fibred collimators.

3.3.3 Detectors

Because heating the nanowire due to light absorption is not negligible at cryogenic temperature, we have to work at very low optical power: sub-pW of injected optical power while in our room temperature experiment we operate between 1 and 100 μW). At such low optical powers, we would be totally blinded by the dark noise of the photodiodes amplifiers we use. Instead, we choose to operate with reliable Avalanche Photo-Diodes (APD), operating in the photo-counting regime. The Excelitas APD (Fig. 3.18a), operated in the Geiger mode,

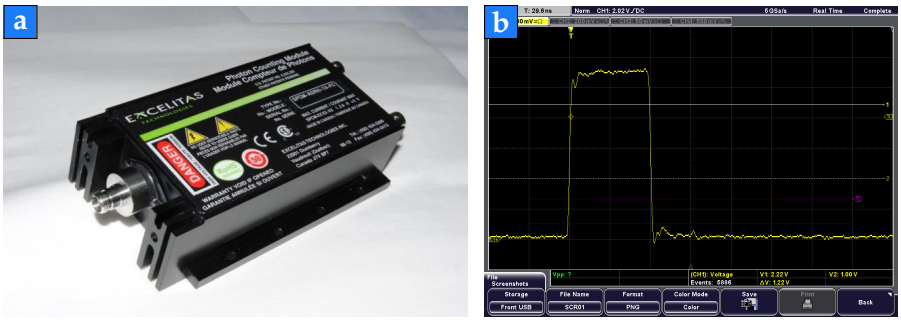

Figure 3.18: (a) Avalanche Photo Diode (APD) used for low intensity interferometric readout. (b) Signal pulse shape associated to a detection event.

produces an electrical pulse of 20 ns length for each photon detected, see Fig. 3.18b, which is done with a quantum efficiency of about 65% at 633 nm. The nanowire vibrations will be encoded as a sequence of pulses which require a proper calibration in order to convert it into an equivalent flux modulation.

The analogous measurement instruments are in general used with continuously varying input signals, which are very different from the sequence of pulses produced by the APDs. Particularly, the Spectrum Analysers (SA) as well as the Zurich Instrument (ZI) demodulator, operate via a demodulation of the input signals, and one needs to estimate the conversion factor from the optical flux modulation seen by the APDs and the demodulated signal strength computed by the devices. This conversion factor is later called the **Click to Volt (CtV)** coefficient, and will be used to convert the demodulated amplitudes in Volt to its equivalent flux modulation amplitude. We then convert later into an equivalent displacement using the measurement vector (in cps/m) computed by the static routine, developed in the imaging interface introduced in sec. 3.3.4. The principle of this calibration

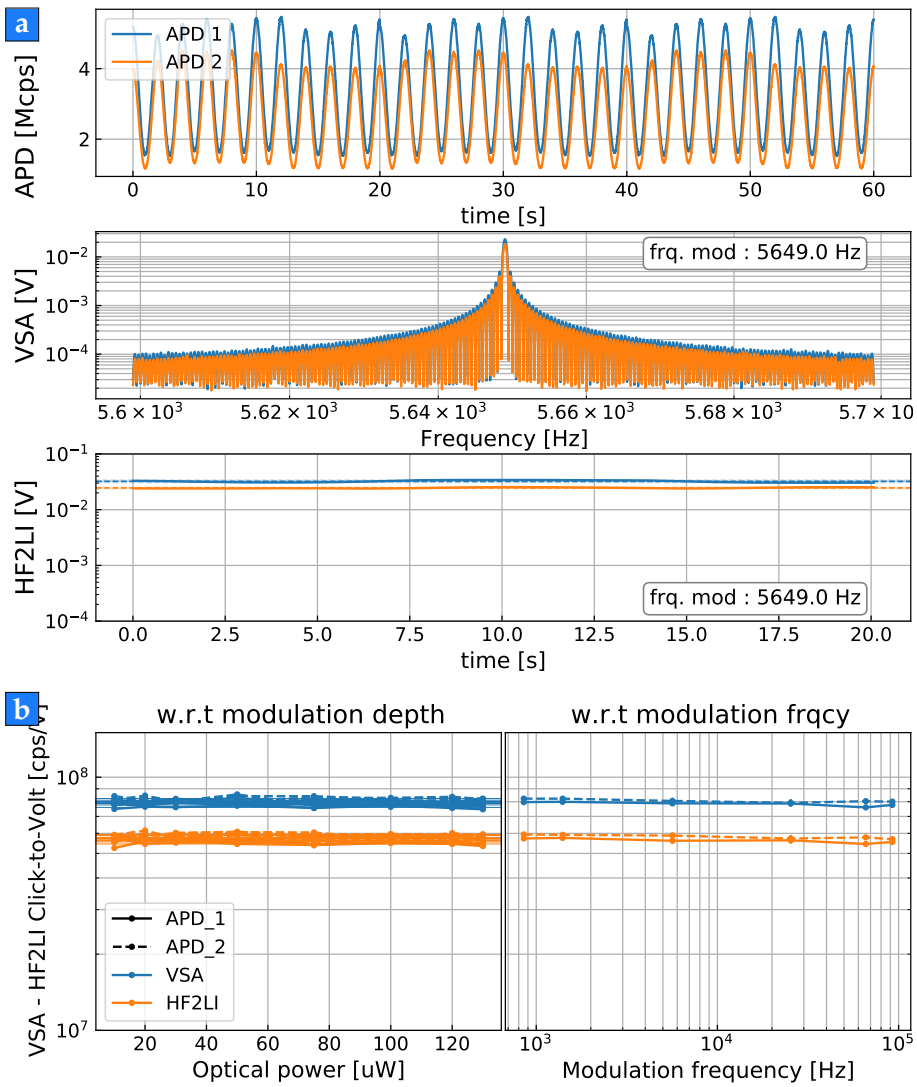

Figure 3.19: Direct measurement of the Click-to-Volt (CtV) conversion factor. (a) We first modulate the optical intensity using the Zurich Instrument (HF2LI model) at low frequency (0.5 Hz because of the time resolution of our NI-card) and measure the modulated signal on the APDs with a NI-card (top panel). We then set the modulation frequency we want to test and measure the PSD with the VSA instrument (middle panel), as well as the demodulated signal on the HF2LI (bottom panel). (b) We obtain the conversion between those different quantities by comparing the computed quadrature of the NI time-trace (in cps) with the mean value of the demodulated signal by the HF2LI and with the maximum of the PSD (both in V). In the legend, APD 1 and 2 correspond to the two probe line and pump line.

measurement is to generate a known intensity modulation with the AOM, then measure its amplitude using the photon counter (in cps) and the demodulated (SA or ZI) amplitude, see Fig. 3.19. This can be done at different modulation frequencies, after having verified on a standard photodiode, the spectral response of the AOM (which is flat from 0 to 10 MHz typically).

In the following we formalize the measurement principle in the photon counting regime.

Calibration of the demodulated signals

The Avalanche Photo-Diode (APD) sends a square pulse signal for each detected photon from the collected reflected signal when the nanowire is in the waist of the laser. The signal received by the Spectrum Analyser (SA) is then a succession of similar pulses defined as,

$$\Pi(t) = \begin{cases} V_\pi & \text{, if } t \in [0,\, T_\pi] \\ 0 & \text{, ohterwise} \end{cases}, \tag{3.12}$$

with V_π the voltage amplitude of the signal, T_π its width.

In the limit of small optical fluxes, *i.e.* when the mean temporal separation between pulses is smaller than the pulse duration or the APD dead time (a few 10 ns), meaning for optical fluxes smaller than 10 Mcps, the APD output signal is the sum of delayed identical pulses. The Power Spectrum Density (PSD) of the signal is computed from its autocorrelation function using the Wiener-Khintchine theorem. Each individual pulse will give a contribution in the spectrum, Fig. 3.20, while the photon statistic will give a weighting function.

The weighting function stems from the probability of measuring a photon reflected from the nanowire, which is proportional to the intensity of the radiation field at the nanowire position, $\mathbf{r}(t)$. The oscillation of the nanowire around the position being small, we can develop the reflected photon flux in perturbation:

$$\Phi_R(\mathbf{r}(t)) = \Phi_R(\mathbf{r}_0 + \delta\mathbf{r}(t)) = \Phi_R(\mathbf{r}_0) + \nabla\Phi_R(\mathbf{r}_0)\cdot\delta\mathbf{r}(t), \tag{3.13}$$

$$= \Phi_R(\mathbf{r}_0) + \|\nabla\Phi_R(\mathbf{r}_0)\|\,\delta r_\beta(t), \tag{3.14}$$

where $\delta r_\beta = \delta\mathbf{r}\cdot\mathbf{e}_\beta$ is the projected displacement along the measurement vector $\mathbf{e}_\beta = \nabla\Phi_R(\mathbf{r}_0)/\|\nabla\Phi_R(\mathbf{r}_0)\|$. In the end one can arrive to the following expression (SI of ref. [91]),

$$S_V[\Omega] = V_\Pi^2 T_\Pi^2 \mathrm{sinc}^2(\Omega\frac{T_\Pi}{2})\left[\Phi_R(\mathbf{r}_0) + \|\nabla\Phi_R(\mathbf{r}_0)\|^2 S_{\delta r_\beta}[\Omega]\right], \tag{3.15}$$

$$= S_V^{\text{shot}}[\Omega] + S_V^{\text{signal}}[\Omega]. \tag{3.16}$$

The first term, S_V^{shot}, is proportional to the photon flux shot noise consequence of the photon statistic [6]. Indeed, experimentally we average the measured spectrum over multiple acquisitions, allowing us to consider the noise as an average over many realisation, in particular over many random trajectories of the nanowire. As a consequence

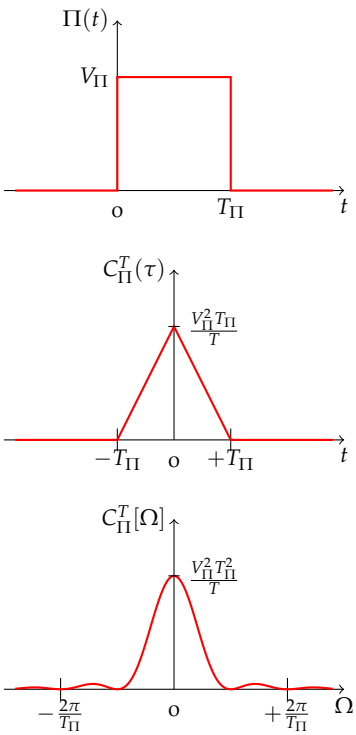

Figure 3.20: From top to bottom: pulse shape of a photo detection, its autocorrelation and its Fourier transform.

the first term is only proportional to the mean reflected flux by the nanowire around its resting position. On the other hand, the second term shows how the displacement signal is transduced by the local slope of the interference pattern. Thus, the conversion factor between the SA measured PSD and the displacement PSD of the nanowire is given by,

$$S_{\delta r_\beta}[\Omega] = \frac{S_V^{\text{signal}}[\Omega]}{\eta^2 \, \|\nabla \Phi_R(\mathbf{r}_0)\|^2}, \tag{3.17}$$

where $\eta = \sqrt{2\pi}\, V_\Pi \, T_\Pi$ in V/cps (the $\sqrt{2\pi}$ accounting for the conversion between the f-space to the Ω-space), and where $\|\nabla \Phi_R(\mathbf{r}_0)\| = \beta$ is the conversion amplitude between the flux modulation and the nanowire displacement. Taking $T_\Pi = 20$ ns and $V_\Pi = 0.55$ V (pulse of 5.5 V followed by 10dB of attenuation), we estimate $\eta = 2.8 \times 10^{-8}$ V/cps.

A direct corollary is that the minimum detectable thermal noise of the nanowire motion is given by,

$$S_{\delta r_\beta}^{\text{thm,min}}[\Omega] = \frac{\Phi_R(\mathbf{r}_0)}{\|\nabla \Phi_R(\mathbf{r}_0)\|^2}. \tag{3.18}$$

To find the optimal Signal to Noise Ratio (SNR), one must minimize the above expression. In practice, we look for maximizing the measurement slope while minimizing the average optical power.

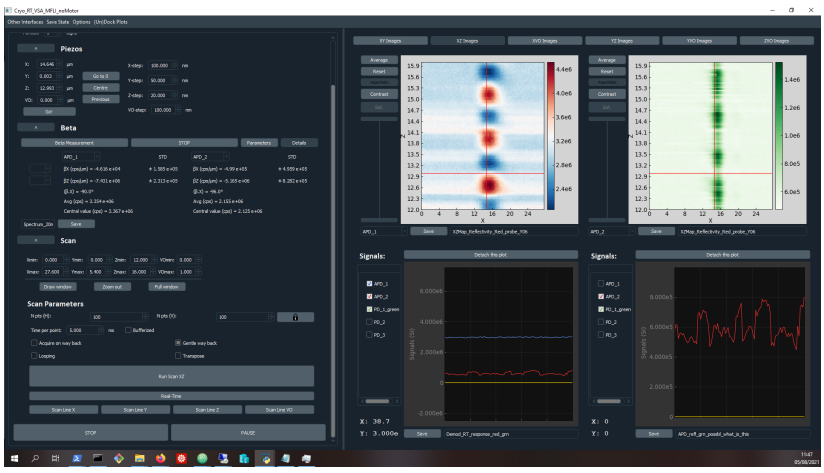

Figure 3.21: Home-made python interface, initially developed by L. Mercier de Lépinay, to allow communication with different hardware (Piezo controller, Spectrum analyser, NI-card, etc...) and perform imaging. On the left side is the interface to enter the imaging parameters. On the right side is shown to XZ-maps of the reflected photon flux by the nanowire upon scanning its position into the laser waist for the pump (green map on the top right) and the probe (red-blue map on the top left). The two plots at the bottom are the real-time signals measured by the NI-card.

3.3.4 Imaging and communication with the instruments

To perform measurements it is essential to communicate and synchronise several instruments and pieces of hardware that allow us to manipulate the nanowire and retrieve signals. To do so we designed a Python-based program, developed during the PhD of L. Mercier de Lépinay prior to my arriving, which has been enriched by every generation of PhD students afterward. A user interface allows accessible and quick preliminary imaging measurement, see Fig. 3.21. We then use python scripts to produce long measurements while scanning several parameters (position, optical power, modulation frequency, *etc*).

3.4 Interferometric readout of the nanowire vibrations

When a fibred objective focuses light on the nanowire, the injected light gets first reflected into the fibre upon reflection at the fibre end side inside the objective. It is modelled by an amplitude reflection coefficient r_0. A second reflection occurs on the nanowire, modelled by a coefficient r_1, which is collected back by the objective, see Fig. 3.22. Using a 90/10 fibre splitter, both reflected flux interfere on the detector. Moving the nanowire in the XZ-plane, the nanowire will scatter back part of the local field allowing to image its focussed/defocussed wave fronts.

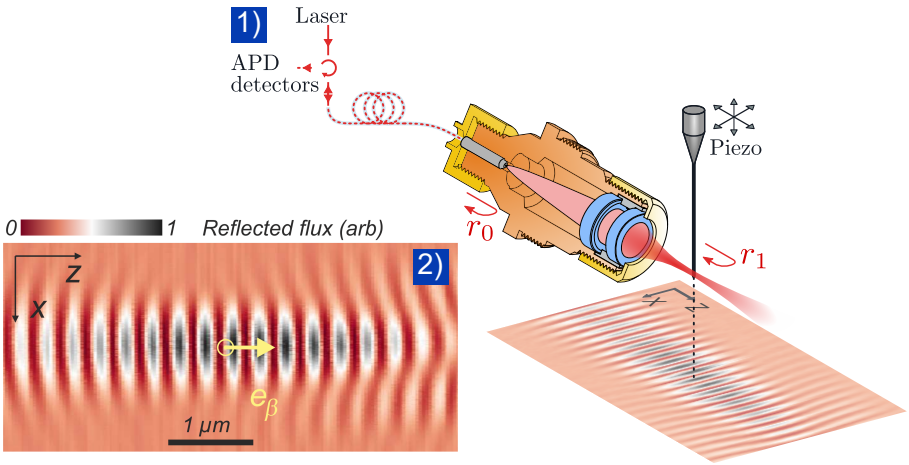

Figure 3.22: 1) Scheme of the interferometric readout principle use for the cryostat optical head. 2) Reflection image obtained when scanning the nanowire in the laser spot, revealing the focussed/defocussed wave fronts before and after the waist area, as well as non paraxial effects (the structuration on the right side). We position the nanowire on the optical axis, close to the locations of maximum slope, and the measurement vector is indicated by a yellow arrow.

A typical measured map is shown in Fig 3.22.2). The maps feature a well contrasted interference pattern along the optical axis, which is a signature that the magnitudes of each interfering signal are quasi identical, around 4%. This interference can then be used to probe the vibrations of the nanowire around its rest position, $\mathbf{r}_0$, with an efficiency proportional to the interference slope at the measurement position:

$$\delta\Phi_R(t) = \nabla\Phi_R|_{\mathbf{r}_0} \cdot \delta\mathbf{r}(t), \tag{3.19}$$

reproducing the projective measurement of the 2D transverse motion of the nanowire on a measurement vector, $\mathbf{e}_\beta$, that depends on the position of the nanowire in the interference figure. Similarly to the free-space readout scheme, the measurement vector is the local gradient of the reflected flux in the XZ-plane, at the position of the nanowire, Fig. 3.22. The estimation of the measurement slope is computed by scanning the nanowire around the measurement position, which allows to estimate the tangent plane to the reflected map, using a scanning protocol developed by L. Mercier de Lépinay [54].

3.5 Thermalizing a nanowire resonator at cryogenic temperature

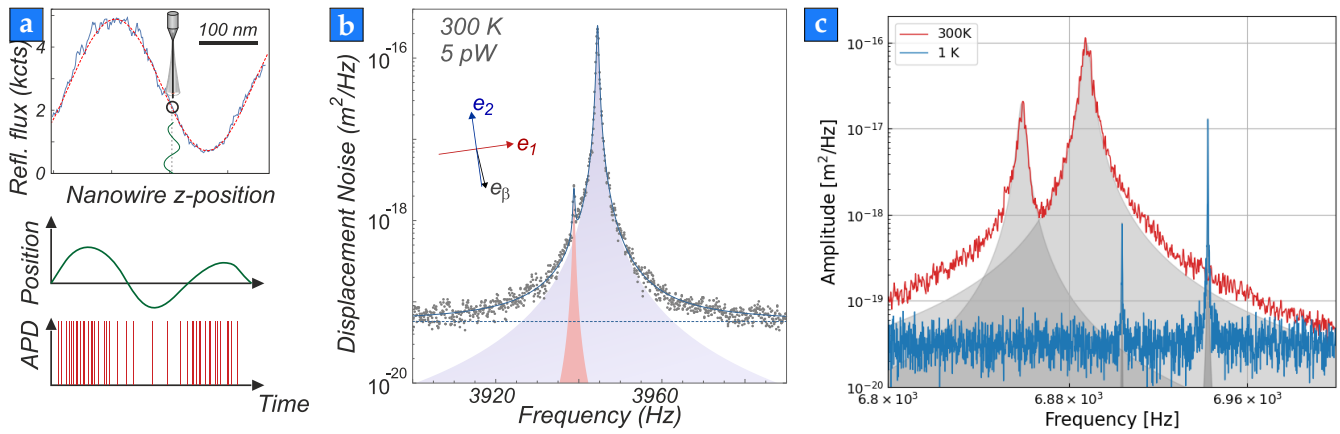

Figure 3.23: (a) Illustration of the vibration measurements from the nanowire vibrating within the interference pattern, to train of pulses generated by the APD from a continuous signal, and ((b)) the resulting displacement noise measurement of the Brownian Motion with the cryostat optical head setup (image adapted from [91]). (c) Comparison of the Brownian Motion of the nanowire between room temperature (red) and 1 K temperature (blue).

3.5.1 Reduction of thermal noise

After mounting the optical setup, we measured the vibration noise of the nanowires while cooling down the cryostat from room to cryogenic temperature [91], during the course of the PhD of Francesco Fogliano. From the measurement of the nanowire thermal noise spectra, one can retrieve its noise temperature as well as the evolution of its mechanical properties by adjusting the measured spectra with the expression,

$$S_{\delta r_\beta}[\Omega] = \sum_{m=1,2} \frac{2\,k_B\,T_{\text{eff}}\,\Gamma_m}{M_{\text{eff}}} \frac{1}{(\Omega_m^2 - \Omega^2)^2 + \Omega^2\,\Gamma_m^2} \tag{3.20}$$

as shown in Fig. 3.23. The effective mass, M_{eff}, is calibrated by measuring the nanowire noise motion at room temperature under low probe optical power, assuming the nanowire is fully thermalised with the support. Because of the good quality factor of the nanowire resonators, one can approximate its thermal motion by treating each mode family independently. As a consequence, we can directly compute the noise temperature by integrating the noise spectra and get,

$$T_{\text{eff}} = \frac{M_{\text{eff}}\,(\Omega_1^2 + \Omega_2^2)}{\pi\,k_B}\,I_{\text{B.M}}, \tag{3.21}$$

where $I_{\text{B.M}} = \int S_{\delta r_\beta}[\Omega]\,\mathrm{d}\Omega$, integrated over several Γ around the mode family.

Figure 3.23c shows the evolution of the nanowire thermal noise from 300 K to 1 K of noise temperature. Different measurements of the noise temperature are reported in Fig. 3.24a for a given nanowire, and one can verify that the noise temperature follows the one of the cryostat cold plate. The grey area is the range of noise temperature that was only possible to measure in absence of suspension. The

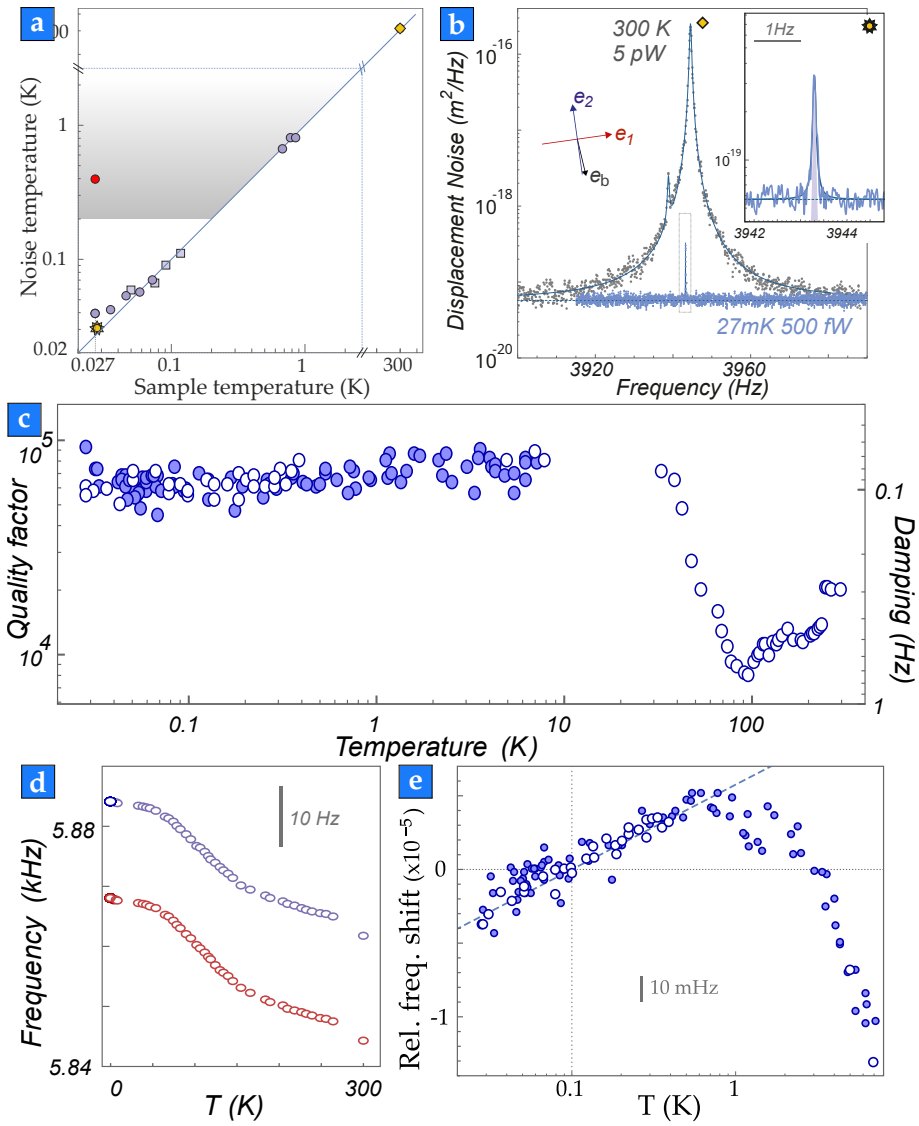

Figure 3.24: (a) Noise temperature of the nanowires measured for decreasing cryostat temperatures. The yellow diamond corresponds to the noise temperature measure at room temperature (shown in (b)), while the yellow star corresponds to the lowest noise temperature measured on a nanowire (also shown in (b)). The square data points are measurements carried out with the spring suspensions. The circle data points are measurements done without the suspension while stopping the cryostat mixture injection, or with the injection on (red circle). The grey shaded area shows the limited region of possible noise temperature without the spring suspension. (b) Comparison of thermal noise spectra measured at 300 K and 27 mK (sample thermometer). (c) Evolution of the mechanical quality factor with the cryostat temperature. (d) Mechanical frequency shifts of the fundamental mechanical modes during a cooldown, as a function of the cryostat temperature (open symbols). (e) relative frequency shift measured and as a function of the nanowire temperature (full symbols) when increasing the optical power, compared to the relative frequency shift when increasing the cryostat temperature without optical heating (open symbols). All figures are from [91].

nanowire was observed being thermalised at 27 mK, with a readout optical injected power of 100 fW, Fig. 3.24b. The quality factors of the nanowire are reported in Fig. 3.24c. When lowering the temperature, they present a strong degradation around 100 K, but improve down to 10 K up to 8-10$\times 10^4$, a value that is not significantly evolving at lower temperatures, probably indicating a limiting clamping loss level. The mechanical frequency of the two fundamental modes first increases when lowering the temperature down to 500 mK, see Fig. 3.24d, but then present an inverted evolution at lower temperatures showing a characteristic logarithmic slope. This behaviour is typical of resonators made from amorphous materials [101, 102]. Indeed, although the nanowires are made from crystalline 3C-SiC, a small layer of amorphous oxide covers the nanowire (1 to 10 nm thick). The logarithmic slope of the relative frequency shifts is indeed of only 1% of the slope observed for fully amorphous materials, which is likely related to the percentage of amorphous material in the nanowire.

3.5.2 Linearity of the mechanical response

For vectorial force sensing application, it is imperative the nanowire remains in the linear deformation regime, with its eigenmodes not being cross coupled, except via the external force field gradients. After having verified the linearity of the nanowire response (see Fig 3.25a), we drive one mechanical polarisation with a piezoelectric element, while measuring the Brownian motion of the second one, Fig. 3.25c, and verify that driving one mode does not heat the second one.

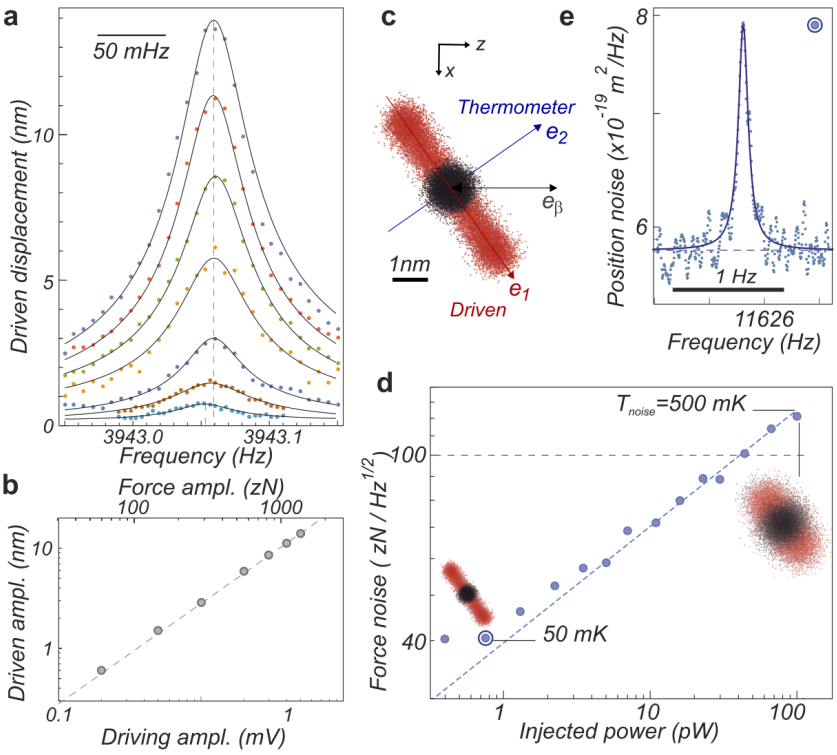

Figure 3.25: (**a**,**b**) Verification of the linearity of nanowire mechanical response under increasing piezo drive up to relatively large force amplitudes (1.5 aN). (**c**,**d**,**e**) Verification of the independence of the eigenmodes: we measured the thermal noise of mode 2, while driving mode 1 with a rather large force modulation. No significant cross coupling could be observed, and the second mode was observed thermalizing down to 50 mK. The force sensitivity achieved with the 11kHz nanowire reached approximately 40 zN/$\sqrt{\text{Hz}}$. (data from F. Fogliano [91])

3.5.3 Optical heating and heat propagation regimes

Figure 3.26a shows the noise temperature of the nanowire when increasing the optical power used for mechanical readout. It shows different sublinear heating regimes, with $P^{1/2}$, $P^{1/5}$ and $P^{1/2}$ (or $P^{1/3}$ depending on the nanowire) slopes in the (20-100) mK, (100-200) mK, (200-1000) mK temperature intervals. In particular in the range of 100-200 mK, a strong sublinear regime appears: increasing $\times 100$ the optical power, only doubles the noise temperature of the nanowire, which provides a great working regime to increase the readout SNR without increasing too much the nanowire noise temperature.

The power dependence of the static optical heating with the laser optical power, is connected to the temperature dependence of the SiC nanowire conductance. Indeed, in the stationary regime, the heat flux

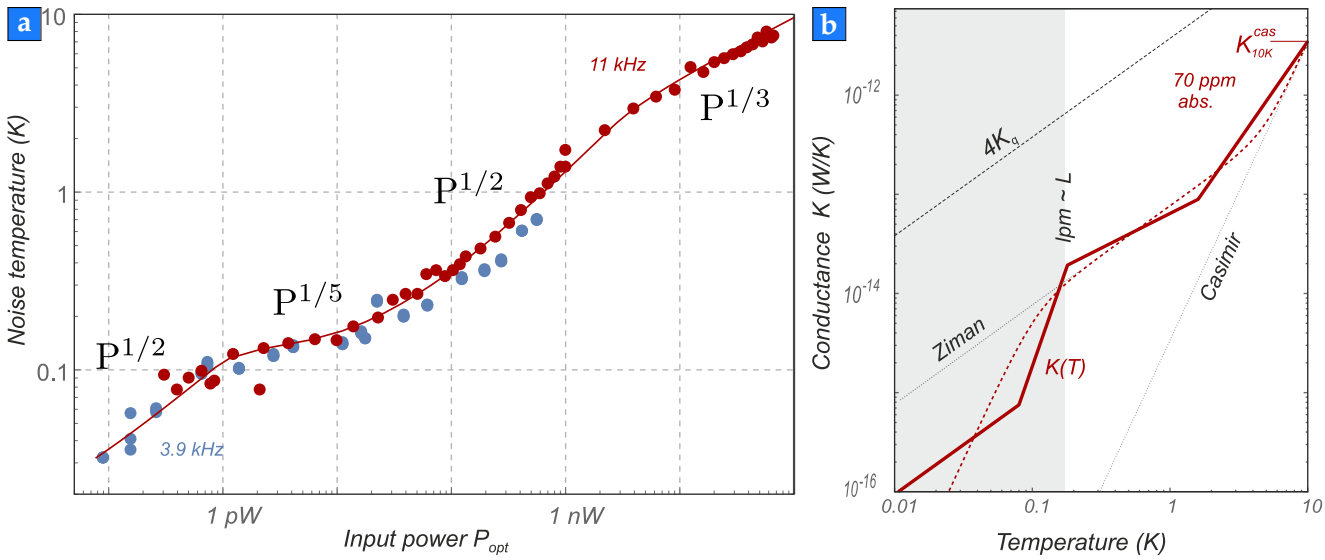

Figure 3.26: (a) Evolution of two nanowires (blue and red dots) noise temperature with the injected optical power. Those measurements allow to extract the evolution of the heat conductance of the nanowire with temperature (assuming a constant optical absorption), as reported in panel (b). This estimation can then be compared to the different theoretical regimes expected for our nanowire. See the discussion in sec. 3.5.3. (data from F. Fogliano [66])

along the nanowire is constant and equates to,

$$j_{\text{th}} = \frac{P_{\text{abs}}}{S}, \tag{3.22}$$

where $P_{\text{abs}} = P_0 A_{\text{abs}}$ is the absorbed optical power with the absorption coefficient, A_{abs}. Assuming that the noise temperature of the nanowire is a good estimator of the temperature at its vibrating extremity (and that it can be properly defined in the whole temperature range), we obtain,

$$P_0 = \int_{T_{\text{cryo}}}^{T_{\text{noise}}} \frac{K(T)}{A_{\text{abs}}} \, \mathrm{d}T, \tag{3.23}$$

where T_{cryo} and $T(y = L) \simeq T_{\text{noise}}$ are the temperatures at the nanowire clamping and at its vibrating tip respectively, while $K(T)$ is the conductance of the nanowire (which equates to $\kappa S/L$ in the diffusive regime).

In this case, if the conductance follows a power law dependence in the temperature, $K \propto T^{\mu}$, then the noise temperature will follow a dependence on the pump power of $T_{\text{noise}} \propto P_0^{1/(\mu+1)}$. Under those assumptions, the measurement of the noise temperature evolution with the injected optical power can be exploited using,

$$\frac{K(T)}{A_{\text{abs}}} = \frac{\partial P_0}{\partial T_{\text{noise}}}. \tag{3.24}$$

This approximation may be relatively rough in the general case, especially assuming the Fluctuation-Dissipation theorem can be applied to the system, although the temperature is not strictly uniform. However, when the conductance of the system rapidly increases with the temperature, all the temperature gradients should be concentrated in

the clamping area, where the nanowire is the coldest. As such the temperature profiles within the nanowire should be relatively homogeneous, as if it was warmed up by the cryostat directly. Of course instead of this cumulative integration, it would have been more adequate to increase the sample temperature to a given temperature using the cryostat, and subsequently measure a heating curve. However, at that time we could not satisfyingly stabilize the cryostat in the 500-1000 mK temperature range. The measurements exposed in chapter 6 will make use of two different lasers, and will help to get more insights on the optical heating curves.

Within those limitations, the behaviour shown in Fig. 3.26a was similarly observed on all the nanowires investigated at low temperatures: in particular the quasi plateau observed below 200 mK was very reproducible, even if the heating rates observed above varied a bit in the $P^{1/2}$, $P^{1/3}$ range depending on the nanowire.

We thus adjusted those measurements using a conductance that was varying with different power laws in the different temperature ranges (see Table 3.1).

$K(T) \propto$	Range
$(T/10K)^2$	1.6 K <T< 10 K
$(T/1.6K)^{0.7}$	140 mK <T< 1.6 K
$(T/140mK)^5$	80 mK <T< 140 mK
$(T/80mK)^2$	20 mK <T< 80 mK

Table 3.1: Conductance power dependence of the temperature in the different regimes, determined from the measurement shown in Fig. 3.26a. (from [66])

Figure 3.26b shows the deduced conductance obtained from this analysis. Note that we only determine the K/A_{abs} ratio, so we assumed that the absorption was temperature independent, which corresponds to a 70 ppm absorption coefficient as we set the nanowire conductance to the value given by the Casimir model at large temperature (10 K). Since then, we developed alternative measurements of the nanowire absorption coefficient by investigating the light induced elongation of the nanowire. This method is relatively robust and is explained in chapter 5. At room temperature, we obtained absorption coefficients up to a few percent, when positioning the laser on a "hot spot" where fully benefiting from the Mie enhancement of the absorption. Those values are significantly larger than what was obtained in this measurement sequence, but one should aim at reproducing those elongation measurements at low temperatures for comparison.

The observed different regimes of conduction are in principle related to different propagation regimes of heat inside nanostructures [39, 103, 104]. We will now qualitatively describe those regimes and their relation to the previous measurements. Part of the following discussion can be found in the SI of Ref. [91] or the thesis manuscript [66].

The heat propagation in nanostructures differs from the one observed in bulk material. In bulk materials, the conductivity is related to the heat capacity through the kinetic theory,

$$\kappa = \frac{1}{3} C_p \, \rho \, v_s \, \Lambda, \tag{3.25}$$

where C_p is the mass heat capacity, ρ the density of the material, Λ the mean free path of the heat carriers, and v_s the velocity of the carriers. In the case of our SiC nanowires, we neglect the electronic contribution of heat from residual doping or impurities and only consider phonons as the main heat carriers. Bulk properties of SiC follow well the established model for crystalline materials: the Einstein model at high temperature, Debye model at low temperature, or Born-von Kármán

model that account for the phonon dispersion that affects the density of states of phonons.

The thermal properties of the multiple allotropic phases of bulk SiC have been extensively studied in the literature but only down to temperatures around 4-10 K. In Figure 3.27, we show a compilation of the 3C-SiC bulk thermal coefficients and their temperature dependence. We used phenomenological models in order to implement those temperature dependent quantities in our analysis. The heat capacity of 3C-SiC, follows well the Debye model down to kelvin temperature. On the other hand, the thermal conductivity presents a very different peculiar temperature dependence.

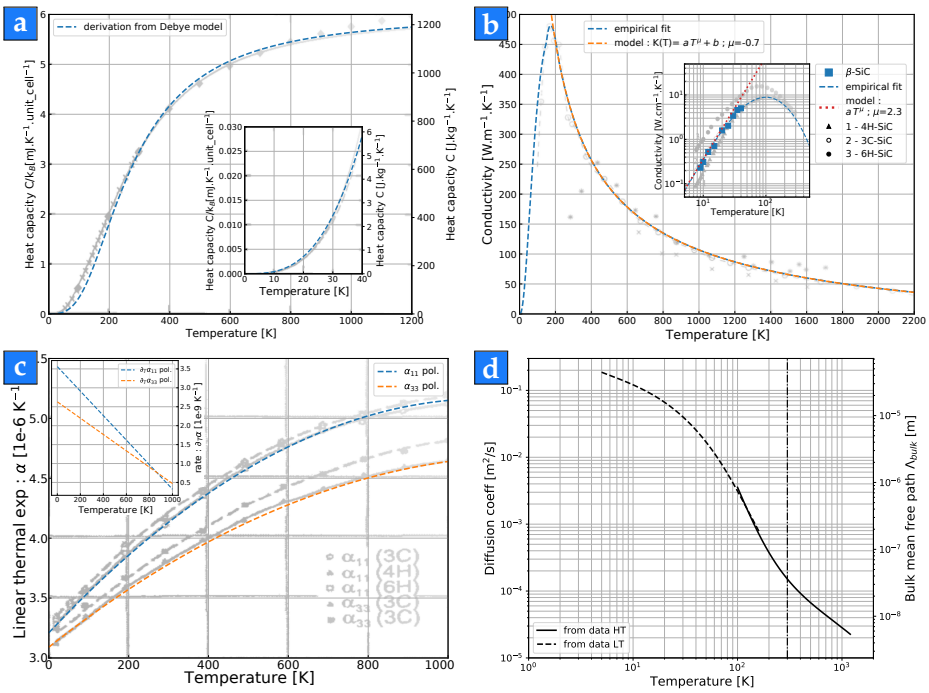

Figure 3.27: Compilation of the evolution of the 3C-SiC thermal properties with temperature, measured in the literature. The heat capacity in Figures (a) are from [105]. The thermal conductivity in Figures (b) are compiled from [106, 107]. The thermal expansion coefficient with temperature in (c) can be found in [108]. The inset figure shows the increase rate of the thermal expansion with temperature. The heat diffusion coefficient in panel (d) is computed from the fitting of the $\kappa(T)$, $C_p(T)$, and $\rho(T)$ with either theoretical models or empirical ones. Assuming the sound velocity does not vary significantly with the temperature and taken at $v_s = 12\,600\,\mathrm{m.s^{-1}}$, the expected bulk mean free path, Λ_{bulk}, is directly deduced from the heat diffusion coefficient using eq. 3.25.

The expected thermal diffusion coefficient, $D(T) = \frac{\kappa(T)}{\rho(T)\,C_p(T)}$, for bulk material is shown in Fig. 3.27d. It is expected to increase by a few orders of magnitude from room temperature to 4 K, but we will see in practice that this does not fit with our observations (where we measure only a very limited increase). From eq. (3.25), one can compute the evolution of the bulk mean free path for phonons with the temperature, see Fig. 3.27d and 3.28a. The expected phonon mean free path rapidly increases at low temperature. At room temperature, the mean free path of phonons (tens of nm) is smaller than the typical nanowire diameters (> 100 nm). However, at lower temperatures, Λ_{ph} rapidly becomes comparable to the nanowire diameter, and one has to investigate how the heat propagation is modified in such regimes in microscale/nanoscale structures [104].

Indeed, when the phonon mean free path increases, the phonons undergo scattering not only on internal defects but also on the surface boundaries of the nanowire. The "quality" of this boundary scattering (between an elastic/specular scattering, or an inelastic scattering) depends on the surface roughness and of the wavelength of the phonons

involved. The energy spectrum of phonons follows a black-body distribution, and the dominant phonon wavelength at a given temperature is given by,

$$\lambda_{\text{dom}} = \frac{h\, v_{ph}}{4.965\, k_{\text{B}}\, T}, \tag{3.26}$$

where h and k_{B} are the Planck and Boltzmann constants, and $v_{\text{ph}} \simeq 12\,600\,\text{m.s}^{-1}$ the sound velocity in silicon carbide [109]. Thus, we discern two limit regimes: the Casimir regime where the phonon wavelength is smaller than the rugosity of the boundary surface (which leads to limiting their mean free path to the nanowire diameter), and the Ziman regime where the phonons' wavelength are larger than the surface roughness (leading to consider phonons undergoing specular reflection, extending their mean free path beyond one scattering event).

In the Casimir regime the mean free path is fixed to the nanowire diameter since it is the limiting dimension, and the conductance follows the expression [110],

$$K_{\text{Cas}}(T) = 3200 \left(\frac{2}{5} \frac{\pi^2 k_{\text{B}}^4}{\hbar^3 v_{\text{ph}}^3} \right)^{2/3} \frac{\pi\,(d/2)^2}{L}\, \Lambda_{\text{Cas}}\, T^3 = \beta_{\text{Cas}}\, \Lambda_{\text{Cas}}\, T^3, \tag{3.27}$$

where $\Lambda_{\text{Cas}} = d$ is the Casimir phonon mean free fixed at the nanowire diameter. This T^3 law should in principle explain the first part of the optical heating down to 10 K of noise temperature. However, we observe a T^2 law, which could correspond to regime of conduction seen in amorphous material, that could originate from the oxide layer crust covering our nanowires, and limits our mechanical damping rates.

On the other hand, when the temperature gets lower, the dominant phonon wavelength starts to become larger than the rugosity of the nanowire boundary surface (estimated to a few nm *RMS*). The specularity of the scattering increases allowing the distance between inelastic collision to be larger than the nanowire diameter. Ziman introduced an effective mean free path,

$$\Lambda_{\text{Zim}} = \Lambda_{\text{Cas}} \frac{1+p}{1-p}, \tag{3.28}$$

where p is the specularity fraction of the scattering processes at the boundary. It represents the probability for a phonon to undergo an elastic reflection on the surface and is given by the Soffer's model, $p(\lambda, \eta) = e^{-(2\pi)^4 \eta^2 / (\pi \lambda_{\text{dom}}^2(T))}$, where η is the root-mean-square deviation of the boundary rugosity. When the temperature decreases, the dominant phonon wavelength vanishes, and thus p becomes very close to unity, leading to a divergence of the mean free path according to eq. (3.28). Using this limiting case one can show that at lower

temperatures the Ziman conductance follows the expression,

$$K_{\mathrm{Zim}}(T) \simeq \beta_{\mathrm{Zim}}\, \Lambda_{\mathrm{Cas}}\, T, \tag{3.29}$$

with β_{Zim} a constant of the temperature. The linear relation is in accordance with the power law for the optical heating measurement between 10 K and several 100 mK. More realistically, instead of considering a mean roughness value for the whole nanowire surface, one can consider a roughness distribution such as $P(\eta) = 1/\eta_0\, e^{-\eta/\eta_0}$, with η_0 being a cutoff value around 4 nm in the case of our nanowires [111]. This leads to a modified specular fraction,

$$\bar{p}(\lambda) = \int_0^{\infty} P(\eta)\, p(\lambda, \eta) \mathrm{d}\eta \simeq \int_0^{\frac{\lambda_{\mathrm{dom}}(T)}{4\pi}} P(\eta)\, \mathrm{d}\eta. \tag{3.30}$$

The subsequent Ziman mean free path follows $\Lambda_{\mathrm{Zim}} = \Lambda_{\mathrm{Cas}} \frac{2-e^{-\lambda_{\mathrm{dom}}/4\pi\eta_0}}{e^{-\lambda_{\mathrm{dom}}/4\pi\eta_0}}$, and is plotted in Fig. 3.28a. Figure 3.28b compares the different length scales involved in the heat propagation regimes, and their evolution with temperature.

Looking at the optical heating measurements, the regime in $P^{1/5}$ would correspond to the transition where the phonons contributing to the heat conduction have their mean free path comparable to the nanowire length. In this regime the phonons propagate ballistically and their dynamic is described by the Boltzmann equation. On the other hand, the stiff slope in T^3 that phenomenologically match the strong decrease of the conductance below 200 mK shown in Fig. 3.26b, was obtained using the following expression of the mean free path: $\Lambda^{-}1 = L^{-}1 + \Lambda_{Zim}^{-}1$, in the Casimir formula to account for the saturation of the mean free path to the nanowire length. Alternatively, this very strong decrease of the conductance could also originate from the contact interface (Kapitza mechanisms follow the same temperature trend).

Lastly the last regime below 100 mK of noise temperature correspond to a linear dependence in T of the conductance. This would be in accordance with a quantum conduction regime described by Landauer [103, 112] as,

$$4\, K_{\mathrm{q}} = \frac{4\, \pi^2\, k_{\mathrm{B}}^2}{3\, h}\, T, \tag{3.31}$$

with K_{q} the quantum of thermal conductance [113], which is the phononic equivalent of the quantum of electronic conductance, except there exist four quantum channels (the four phonon polarisations : 2 flexural, 1 dilatational, 1 torsional). This is a quantum limit for the maximum contribution of phonons to the heat conductance of a 1D system in case of perfect transmission which account for the four propagation modes. Even if the temperature definition in such regimes is ill-defined, this should set a fundamental limit in our experiments.

The mention of ballistic propagation in our nanowires make us pounder on some important and delicate questions such as : In our measurement setup are we sensitive to all types of phonons ? Indeed, do all phonons identically influence the mechanical properties of the nanowires and participate in their noise temperature ? In the

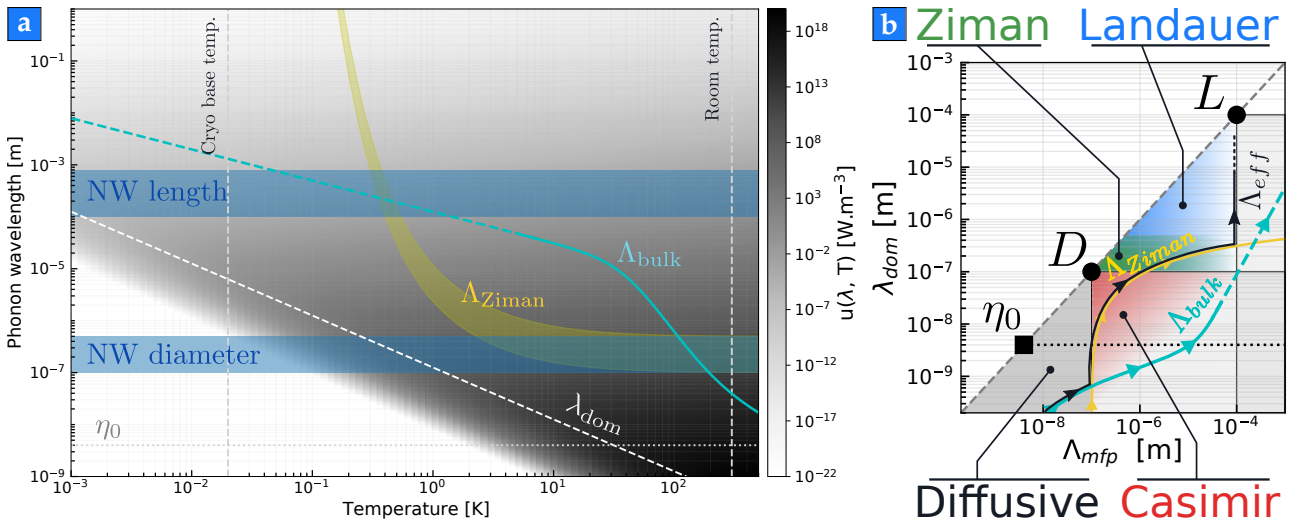

Figure 3.28: (a) Length scale diagram, comparing the different length parameter involved in the different thermal transport regimes with varying temperature. We represented the region of expected nanowire diameter and length, as well as the associated Ziman phonon mean free path. In cyan line, we overlayed the computed bulk mean free path from the data in the literature with the kinetic theory, where the dotted part represent the expected extrapolation to low temperature. (b) Expected phase diagram of the different heat propagation regimes for SiC nanowire experiments. The right figure is a representation of the nanowire parameters. The coloured regions are areas of parameter space associated to a certain heat propagation regime. The arrowed lines in cyan and yellow are the expected trajectory of the bulk and Ziman mean free path, when the temperature is decreasing from room to cryogenic temperatures.

following chapters, we will describe several thermal actuation mechanism, and one should wonder if those mechanisms are sensitive to all types of phonons. For instance, in the ballistic regime, as the mean free path is limited by the nanowire length, one can believe that the heat conduction measurements will more likely probe the boundary effects as well as the quality of the clamping interface rather than the nanowire thermal properties. It might be relevant to separate the phonon contributions to the heat transfer into two types: one contribution originating from diffusive phonons (thermalized with the lattice material) and another from ballistic phonons (decoupled from actuation mechanisms) [114]. More fundamentally, the definition of a local temperature is certainly ill-defined in the ballistic propagation regimes. Concerning our experimental setup, we probe the low frequency thermal response of the nanowire which corresponds to the time averaged propagation properties of the nanowires, while the ballistic dynamic would be in the few MHz range. Also, due to the need of using two different lasers, we could not significantly investigate the photothermal response of the nanowire in the ballistic or quantum regimes (below 200 mK).

As such we will aim at investigating how the heat diffusion model can be pushed down to low temperatures and still account for our observations. With these questions in mind, in order to further explore the heat propagation inside the nanowires, which are essential for our future experiments at dilution temperatures, we developed and analysed **pump-probe** measurements, which are presented in the following chapter.

3.6 Chapter summary

This chapter presents in detail the experimental apparatus used to study our nanowire down to cryogenic temperatures. We show and thoroughly describe the different elements that compose the optomechanical setup implemented on a Sionludi cryostat, which is a necessary step in order to better grasp the interpretation of our measurements. We calibrated and characterised the optical probing, as well as the measurement channel that make use of APDs.

In a second time, we presented our first results concerning the thermalisation of the nanowires with the cryostat. Preparatory work has been done in order to better characterise and control the polarisation of the incident light focused on the nanowires. The noise temperature with respect to the probing optical power demonstrates how sensitive our nanowires are to optical heating, and thus the need to work at very low intensity - up to nine order of magnitude less than in our room temperature measurement configurations. The nanowires mechanical polarisations has been shown to stay decoupled at milliKelvin temperatures and the nanowire response keeps it linearity over large range of driving amplitude, which allows us to reach force sensitivity as small as $40\,\mathrm{zN}/\sqrt{\mathrm{Hz}}$.

We conclude the chapter dealing with the non-trivial evolution optical heating curves, which gives us evidence that toward low temperature, we become sensitive to complex thermal physics occurring in our nanowires.

CHAPTER 4

EXPLORING THE HEAT PROPAGATION DYNAMICS WITHIN NANOWIRES

4

Contents

Introduction 77
4.1 Pump probe experimental setup 78
4.2 Measurement protocol 80
4.2.1 Nanowire reflectivity 81
4.2.2 Fitting the Brownian motion 81
4.2.3 Response measurements 84
4.3 Measurement channel 85
4.3.1 Interferometric readout 85
4.3.2 Vertical readout 89
4.4 Reflectivity measurements 89
4.5 Model for the thermal response 91
4.5.1 Diffusion model 91
4.5.2 Static profile 93
4.5.3 Periodic excitation 93
4.6 Thermal noise under non-homogeneous temperature profile 95
4.7 Chapter summary 97

Introduction

In this chapter we present the pump-probe experimental scheme that will be used to study thermal waves inside nanowires in the cryostat. Using pump-probe techniques to probe heat transport has already been used in the group leading to the observation of a retarded force related to thermal effects [75], as well as to qualitatively investigate heat propagation within graphene membrane during the PhDs of A. Gloppe and C. Schwarz [37].

In the following, we will describe the measurement protocols and the different steps undergone to characterise the optomechanical properties of the studied nanowire, such as its resonant frequencies, the direction of its mechanical polarisation basis, its effective mass, as well

as its reflectivity. We will then present the measurement of a broadband response to an optical intensity modulation of the pump laser, and its pre-analysis. These measurements shed light on the sensitivity of the readout scheme on various optomechanical and photothermal parameters. We thus describe the different kind of information which can be extracted from our interferometric measurement channel. In particular, for a specific thick nanowire we were able to measure the thermally induced reflectivity change along the readout interference, which has minimal impacts on more traditional nanowires except when we hit Mie resonances (see section 4.4). To better understand the thermal response following a modulation of the absorbed optical power that generates heat waves, we formalise the heat diffusion in the 1D case considering our configuration of a suspended nanowire. In such model, the temperature along the nanowire is not homogeneous, and we study its impact on the measured noise temperature extracted from the Brownian motion.

4.1 Pump probe experimental setup

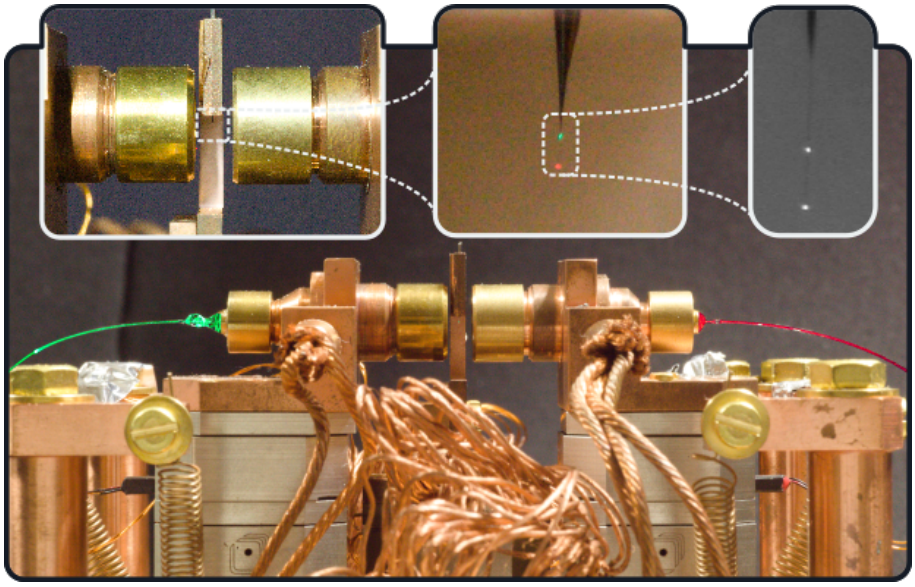

Figure 4.1: Pump-probe setup pictured at different scales. In large, we see the top of the optomechanical setup. The left inset shows a close up of the two objectives with the sample holder in the middle. We then zoom to see the laser spots of the laser on the nanowire (true colours, image taken with a simple camera) and a bigger close up on the right (taken with a monochrome CCD camera).

In this section we will describe in greater detail the experimental setup used for probing the heat propagation properties inside SiC nanowires. We implement a purely non-contact optical technique using two lasers in the pump-probe configuration. To do so, one laser (red) was used to probe the response of the nanowire while we modulated the intensity of the second laser (green) which induces thermal waves propagating within the nanowire consecutive to light absorption. In both cases we use visible light, but as we will see in later sections, the laser at 515 nm falls closer to the 3C-SiC indirect bandgap, making it more suitable for efficient thermal heating.

Figure 4.1 shows a close up of the optical head as well as the different scales present in the setup. Having a second fibred objective

mounted on XYZ-steppers allowed us to decouple the probing position from the pumping one, see Fig. 4.2.

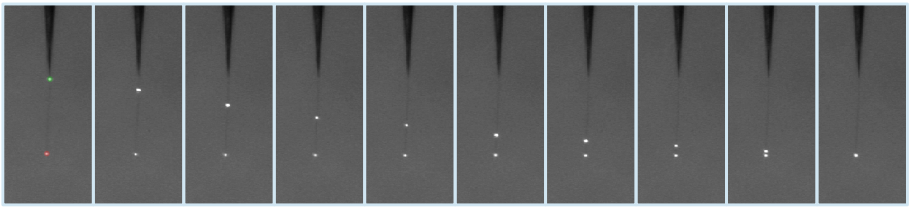

Figure 4.2: Pictures of the different focal spots scattered by the nanowire while we scan the position of the pump laser, colorized in green in the left picture. The bright spot at the bottom tip of the nanowire is the scattered light from the probe laser, colorized in red in the left picture.

The optical setup is shown in Fig. 4.3. It is divided in two channels. The probe channel uses a red HeNe laser at 633 nm, which is injected in a fibre. On the injection path we use a 99/01 integrated fibred splitter that plays the role of an optical circulator. It allows recovering 99% of the flux reflected by the nanowire-objective optical system. In this system, the light undergoes two reflections : one at the air-glass interface at the fibred output inside the objective, and one from the nanowire. Both signals interfere at the detector, an Avalanche Photo-Diode (APD), thus providing an interferometric readout. Likewise, in the pump channel, a green laser at 515 nm (Oxxius) follows the same trip but passes through an **Acousto-Optic Modulator (AOM)**, see Fig. 4.4, before being injected in the fibre. We use a 90/10 fibred splitter instead of a 99/01 one because in practice it provided better phase stability for the interferometric detection.

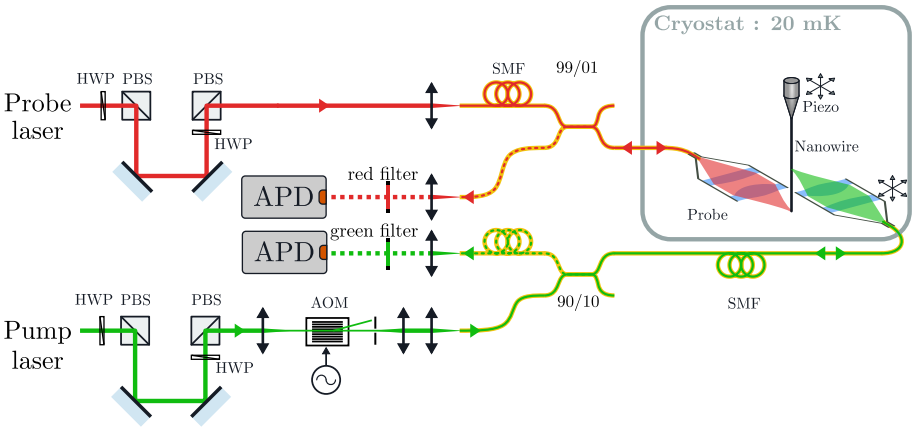

Figure 4.3: Optical scheme of the pump-probe setup for heat wave modulation. Both laser intensities are attenuated by a succession of half waveplate (HWP), Polarising Beam splitter (PBS) and an AOM. Concerning the probe line, the beam is then directly injected inside a Single Mode Fibre (SMF), while the pump line passes through an AOM before injection inside a SMF. The reflected signal is then collimated on APDs after passing through asymmetric fibred splitters, which collect most of the reflected light. We use a red filter (band-pass filter at 633 nm) and a green filter (band-pass filter at 515 nm) in front of the APD detection path for the red and green laser respectively, in order to avoid cross talking.

A **Zurich Instrument (HF2LI model)** lockin is used to control the pump laser power. We use that instrument to modulate the green intensity and demodulate the induced fluctuation in the probe signal. We calibrate the AOM transmission, relating the control voltage sent to the controller to the optical power send onto the nanowire, see Fig. 4.4d. As described in sec. 3.3.3, the APD converts the measured photon flux to a series of pulses. Christophe Hoarau designed a pulse repeater, based on high speed logical gates, that allows us to send the APD signal to various instruments (counters, oscilloscope, spectrum analyser, demodulators) without modifying the impedance seen by the APD, see Fig. 4.4c.

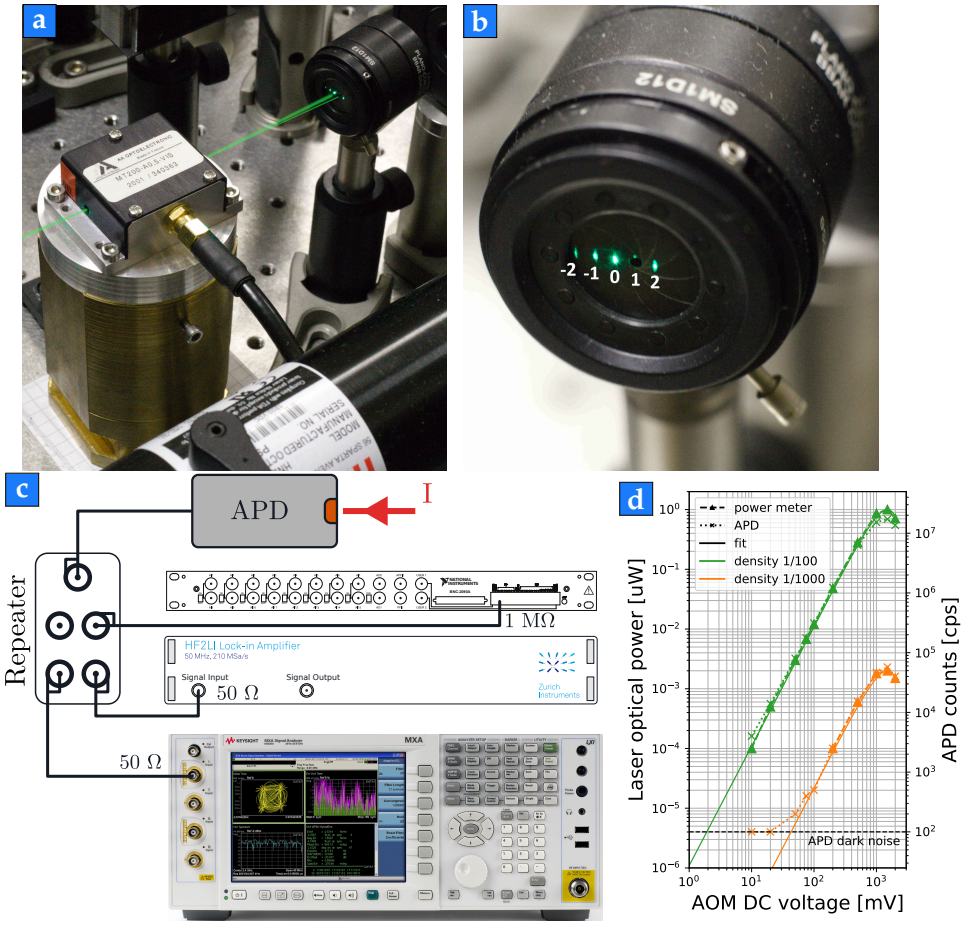

Figure 4.4: Picture of the Acousto-Optic Modulator inserted in the pump line. (a) Modified picture with green lines to illustrate the laser path. (b) Picture of the output order selected using a pinhole diaphragm. (c) Measurement scheme of the APD output signal. The input photon flux I is converted into a series of pulses, duplicated by the repeater into multiple outputs that are used for various instruments. From top to bottom we show the NI-card (used for imaging and measurement vector estimations), the HF2LI Zurich instrument and the Spectrum Analyser (SA) used for response and signal analyses. (d) AOM calibration measurements of the optical intensity versus the input voltage sent to the AOM driver. The two coloured lines plots correspond to measure with two different attenuations. The left axis indicates the optical power at the fibre injection of the pump laser into the cryostat, while the right axis corresponds to the click-per-second signal measured of the reflected signal by the APDs.

4.2 Measurement protocol

In this section we expose the classical measurements we realize in order to characterise the nanowires used in our experiments. Indeed, for each nanowire one needs to characterise its mechanical and geometrical properties.

The starting point is the measure of the room temperature Brownian motion at the vibrating tip of the nanowire. From that measurement we obtain the resonant frequencies, the quality factor of the nanowire modes and their effective mass, see Fig. 4.7. Contrary to our room temperature experiments which makes use of a dual photodiode, we note that we rely here on a single measurement channel (due to the use of a mono-mode fibre). As such we would need to realize noise measurements at different position within the interference pattern in order to vary the orientation of the measurement vector. In practice, we have verified multiple times that the eigenmode orientations were perpendicular within each longitudinal family, so that a single measurement can be sufficient to determine the angle formed by the eigenmodes and the measurement vector. This estimation can be further confirmed with a resonantly driven response measurement, see Fig. 4.8.

Knowing those intrinsic properties of the nanowire is a necessary

requirement prior to any measurement of its dynamical response to an intensity modulated pump signal.

4.2.1 Nanowire reflectivity

The contrast and amplitude of our interferometric readout depends on the nanowire reflectivity. As seen in chap. 2, the interaction of the nanowires with light is complex and structured. In sec. 4.3, we will discuss in more detail the implication of having a complex reflectivity coefficient in the readout. Instead, this section will focus on giving an estimation of our nanowire reflectivity.

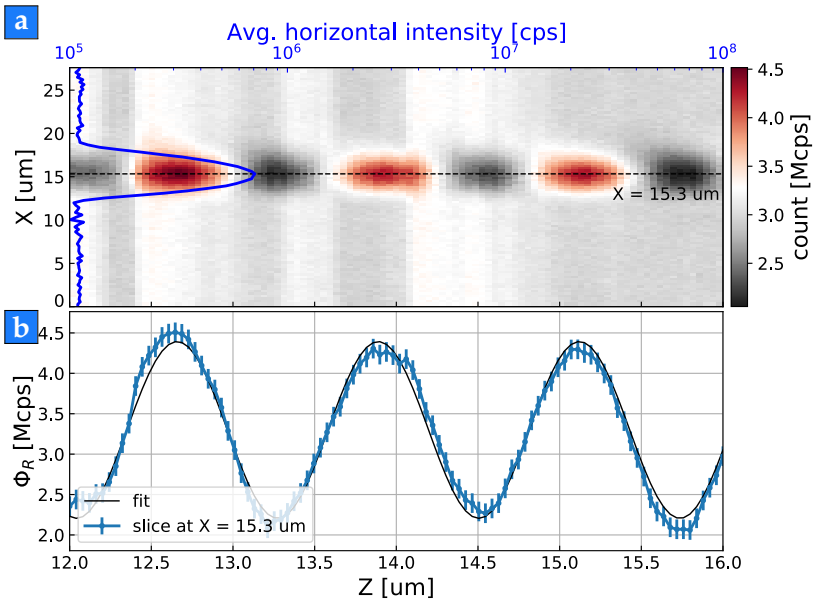

Figure 4.5: Reflectivity measurement using the interferometric readout objective with the probe laser (633 nm). (a) From the refection flux XZ-map, we identify the centre of the waist by the X position that maximises the absolute different to the total average reflected flux, averaged over the Z-axis, *i.e* that maximises $A(X) = \int_{Z_{min}}^{Z_{max}} \|\Phi(X,Z) - \langle\Phi\rangle\| \, dZ/(Z_{max} - Z_{min})$ where $\langle\Phi\rangle$ denote the average value over the XZ-map. (b) Fitted 1D interference pattern of the XZ-map slice, taken at $X = 15.3\,\mu$m.

When scanning the nanowire in the waist of the probe laser, one can access the interference pattern measured in the reflected flux. From the XZ reflectivity maps, one can retrieve the nanowire reflectivity using the contrast of the measured interference, see Fig. 4.5.

In Fig. 4.6 we show the reflectivity profile as we move the probe laser along the nanowire. We see a slightly decreasing reflectivity as we get close to the clamping area, and can be attributed to a slight radius change. Such measurements can also be reproduced for the two characteristic light polarisations, parallel and perpendicular to the nanowire axis. However, the spatial resolution here is too coarse to render the reflectivity inhomogeneities we observed in other measurements.

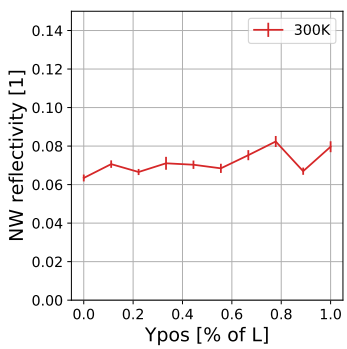

Figure 4.6: Average reflectivity, r_{NW}, of a nanowire measured at different altitudes derived from the contrast of the interferometric readout. Measurement at room temperature.

4.2.2 Fitting the Brownian motion

The spectrum analyser records the noise power of the photon flux measured by the APDs. The photon flux is directly related to the motion noise of the nanowire, projected on the measurement vector defined by the interference pattern. Figure 4.7 shows the converted power spectral density of the nanowire vibration at its first resonant mode family in absence of external force.

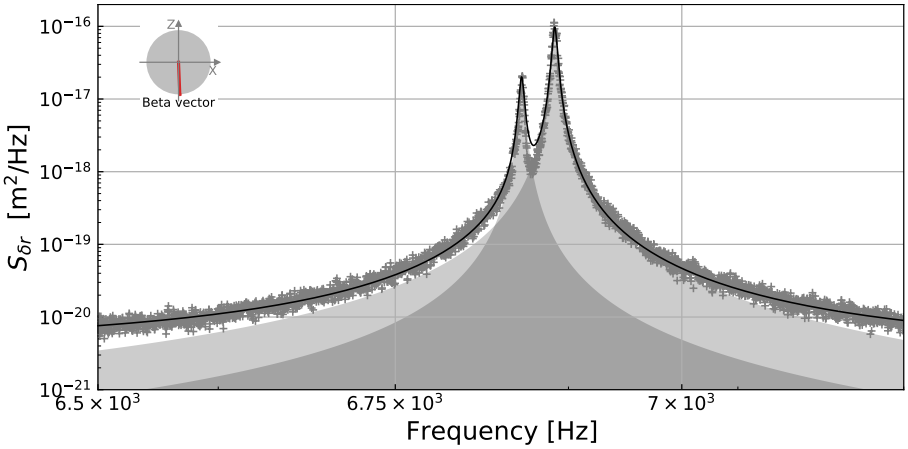

Figure 4.7: Measurement of the thermal noise displacement spectrum (averaged over 50 realisations, RBW=500 mHz) of a nanowire at room temperature at its fundamental mode. Using the measurement vector, represented in the inset panel, we converted the signal in Volt to displacement per unit Bandwidth. We fit the noise spectra using a Lorentzian for each mechanical polarisation (translucent grey area) and the total spectra (black solid line) is given by the incoherent sum of both resonances and a constant background related to the

Measuring the first mode family, the fitting model is,

$$S_{\delta r_\beta}[f] = A_1^2 \frac{f_1^2\, G_1^2}{(f_1^2 - f^2)^2 + f^2\, G_1^2} + A_2^2 \frac{f_2^2\, G_2^2}{(f_2^2 - f^2)^2 + f^2\, G_2^2} + \mathrm{B}^2, \tag{4.1}$$

$$= |\chi_{11}|[f]^2\, S_{\delta F_{\mathrm{thm}}}[f]\, (\mathbf{e}_\beta \cdot \mathbf{e}_1)^2 + |\chi_{22}|[f]^2\, S_{\delta F_{\mathrm{thm}}}[f]\, (\mathbf{e}_\beta \cdot \mathbf{e}_2)^2, \tag{4.2}$$

where A_i, f_i, G_i are the amplitude, the resonant frequency, the linewidth for the mechanical polarisation i respectively, and $S_{\delta F_{\mathrm{thm}}}$ is the PSD of the Langevin force. The constant B in the fitting model is the background noise level, related to the shot-noise of the laser and the dark noise of the detector. The vectors $\mathbf{e}_\beta$, $\mathbf{e}_i$ are the measurement vector and the mechanical polarisation vector. Because we exert not external force, only the diagonal elements of the susceptibility plays a role in the Brownian motion, and χ_{ii} represents the mechanical susceptibility of each eigenmode i.

The conversion between the raw measured data to the fitted data is,

$$S_{\delta r_\beta,\mathrm{fit}} = 10^{\frac{S_{\delta r_\beta,\mathrm{meas}}}{10}} \frac{\mathrm{CtV}^2}{\beta^2} \frac{50\,\Omega}{\mathrm{RBW}} \times 1\mathrm{mW}, \tag{4.3}$$

where P_{dBm} is the measured power spectral density in dBm, CtV is the click-to-volt conversion factor (in Hz/V), β is the norm of the measurement vector (in Hz/m) and $S_{\delta r_\beta,\mathrm{fit}}$ is the Spectral noise of the measured displacement in the direction of the measurement vector in m^2.Hz^{-1}.

Mode orientation measurements

From the Brownian motion we can retrieve the orientation of the nanowire mechanical polarisation, *i.e.* the transverse eigenmodes of

the considered mode family. The noise spectrum of the projected measurement along $\mathbf{e}_\beta$ is related to the Langevin force acting equally to the eigenmodes with,

$$S_{\delta r,\beta} = \cos^2(\gamma)\, S_{\delta r_1} + \sin^2(\gamma)\, S_{\delta r_2}, \tag{4.4}$$

where γ is the angle between the orthogonal eigenmode basis and the measurement vector.

Alternatively, the stationary trajectory followed by the nanowire when driven at a fixed frequency is an ellipse in the XZ transverse plane. Converting a response measurement obtained by sweeping the driving tone across both eigenfrequencies allows to obtain a set of ellipses which allow to directly visualize the eigenmode orientations in the real plane, see Fig. 4.8.

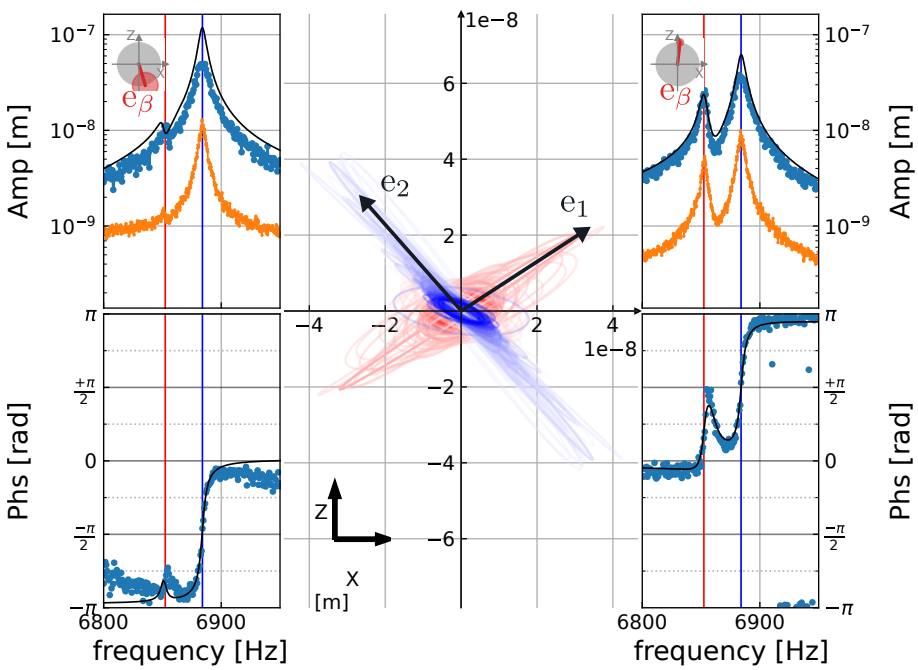

Figure 4.8: Response measurements for two different measurement vectors when the nanowire is driven around resonance (blue data in the left and right panel). In orange is the measured amplitude of the thermal motion. The centre panel is the ellipse representation of the nanowire tip displacement for each driving tone. This representation allows determining unambiguously the orientation of the eigenvectors (contrary to a single thermal noise measurement). The measurement vector, $_\beta$, for each data set is represented in the inset within the left and right panels, where the uncertainty on its norm and direction is illustrated by a translucent red ellipse.

Let us measure the reflected light from the nanowire with a measurement vector in a given direction, $\mathbf{e}_\beta$,

$$\delta r_\beta[\Omega] = \mathbf{e}_\beta \cdot \delta\mathbf{r}[\Omega], \tag{4.5}$$

where $\delta\mathbf{r}[\Omega] = \underline{\underline{\chi}}[\Omega] \cdot \left(\delta\mathbf{F}_{\text{ext}}[\Omega] + \frac{1}{M_{\text{eff}}}\,\delta\mathbf{F}_{\text{th}}\right)$, where $\delta\mathbf{F}_{\text{ext}}$ is an external force drive (in this case the pump laser radiation pressure).

To reconstruct the trajectory in the transverse plane, one must make use of two non-collinear direction of projective measurement channels, $\mathbf{e}_{\beta,1}$, $\mathbf{e}_{\beta,2}$. We denote the components of $\delta\mathbf{r} = (\delta r_x, \delta r_z)$ in the XZ coordinate system since the angle of the betas are defined w.r.t the XZ axis. We then have the two signals,

$$\begin{pmatrix} \delta r_{\beta,1} \\ \delta r_{\beta,2} \end{pmatrix} = \begin{pmatrix} \cos(\beta_1) & \sin(\beta_1) \\ \cos(\beta_2) & \sin(\beta_2) \end{pmatrix} \cdot \begin{pmatrix} \delta r_x \\ \delta r_z \end{pmatrix}, \tag{4.6}$$

$$= M_{\beta_1,\beta_2} \cdot \begin{pmatrix} \delta r_x \\ \delta r_z \end{pmatrix}, \tag{4.7}$$

and the nanowire position can be expressed as,

$$\begin{pmatrix} \delta r_x[\Omega] \\ \delta r_z[\Omega] \end{pmatrix} = M^{-1}_{\beta_1,\beta_2} \cdot \begin{pmatrix} \delta r_{\beta,1}[\Omega] \\ \delta r_{\beta,2}[\Omega] \end{pmatrix}, \tag{4.8}$$

the matrix being invertible as long as the measurement angles are not collinear. For a given frequency, the stationary driven trajectory is,

$$\delta\mathbf{r}(t) = \mathrm{Re}[\delta\mathbf{r}[\Omega]\, e^{-i\,\Omega\, t}], \tag{4.9}$$

$$= \mathrm{Re}[(\delta r_x[\Omega]\mathbf{e}_x + \delta r_z[\Omega]\mathbf{e}_z)\; e^{-i\,\Omega\, t}]. \tag{4.10}$$

One can plot such elliptical trajectories via a parametric plot on $\Omega\, t$ spanning from 0 to 2π. From the trajectories we can derive the parameters of the ellipse, and in particular the orientation it forms with the x-axis given by the angle,

$$\psi = \frac{\pi}{2} + \frac{1}{2}\arctan\left(\frac{2\,|\delta r_x\,\delta r_z|\,\cos(\phi_z - \phi_x)}{|\delta r_x|^2 - |\delta r_z|^2}\right) \tag{4.11}$$

However, in the optical setup of the cryostat, the nanowires tilt is not fully controlled. In Fig. 4.8, the eigenvectors are not observed orthogonal which would be partly explained with the tip vibration occurring in a tilted plane, but it is mostly due to the large uncertainty in the measurement vector direction for the response measurement presented in the left panel. Over all, in our cases the nanowires are prepared to have a small tilt, which should have no measurable impact in the ellipse measurement.

4.2.3 Response measurements

When considering the response measured when modulating the pump laser, it is no longer obvious that the modulated signal is a displacement. Indeed, as explained in previous section, other contributions can modulate the reflected photon flux. It is then interesting to display the data both as a displacement modulation and as a flux modulation in click-per-second (cps or Hz). Finally, in order to analyse the origin of the optical response of the nanowire, it is useful to normalize the response measured using the red laser by the strength of the optical modulation injected in the pump fibres. Similarly, the phase of the response is normalized with respect to the phase of the pump beam modulation, which is simultaneously measured.

A typical response measurement is shown in Fig. 4.9, on a large frequency span. We can identify the three first longitudinal resonant families of the nanowire. Here the pump laser is located at the nanowire extremity and those response signals correspond to a displacement generated by the radiation pressure of the pump laser. In green, we fitted the response while only accounting for the radiation. We observe that the fits are in good agreement with the data at high frequencies, but largely differ at low frequencies, where the photothermal effects come into play. At first approximation the broadband response is well modelled by the coherent sum of the radiation pressure and a low-pass like response, accounting for the photothermal effects. In the following sections we will investigate the different mechanisms at play for such thermal response.

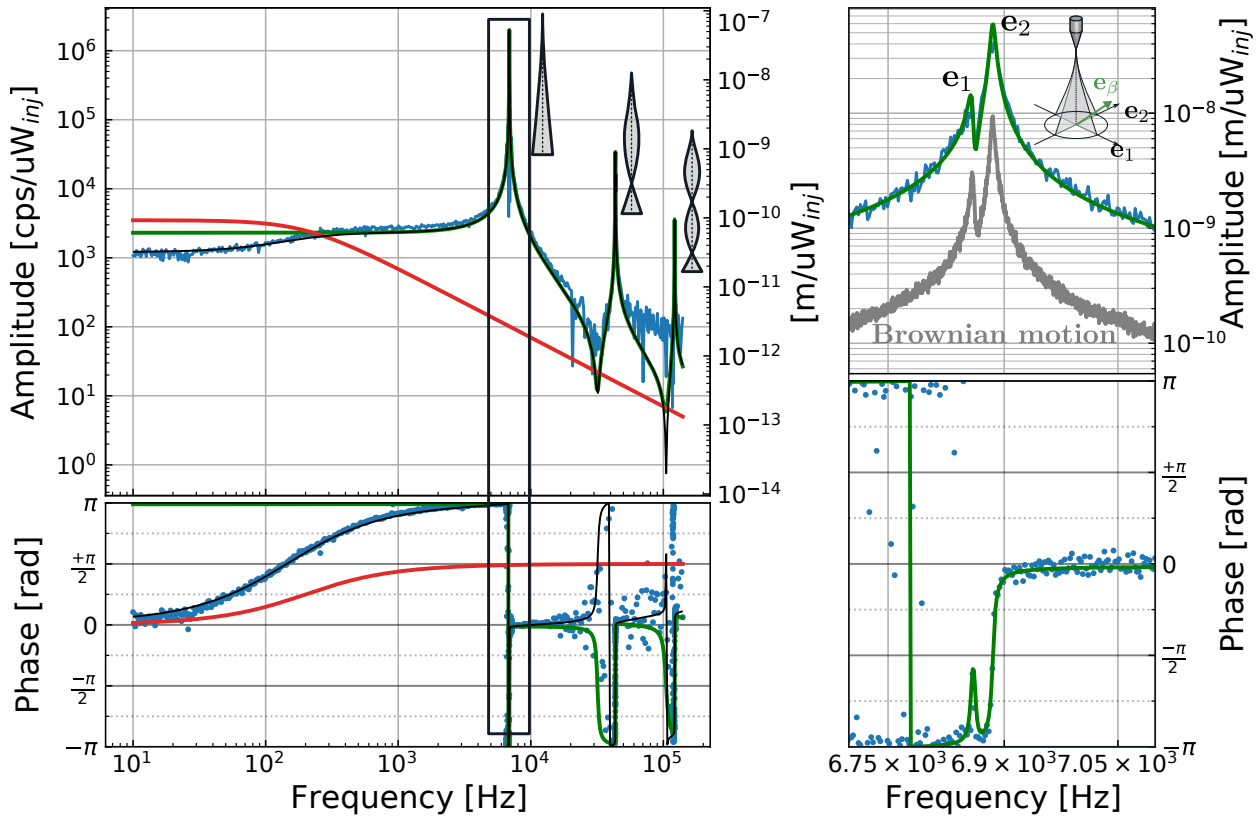

Figure 4.9: Typical result of a Pump-probe response measurement, plotting the ratio of the reflected flux per input power modulation strength and their dephasing (left labels of panels), or the corresponding driven displacement (right labels). The measurement sequence is composed of a broad frequency sweep, using a logarithmic progression and subsequent response measurements zoomed on each longitudinal eigenmodes' family. The response of the three first longitudinal families clearly emerges on top of a broader photothermal response. In the zoom we plot the projected driven response of the nanowire, projected on the measurement vector, and one can identify the two transverse mechanical polarisation. The measurement background measured separately on a spectrum analyser is added in grey, using the same demodulation bandwidth, 1.0 Hz here. The plain green line in the large frequency span response corresponds to the radiation pressure dominated response of the nanowire. The red line is a low-pass response which represent a first order approximation of the photothermal response of the nanowire, which coherently adds up to the radiation pressure response giving the full fit represented by the solid black line. The overall reduction in the response observed at low frequencies is due to the fact that both effects partially compensate each other.

4.3 Measurement channel

In this section we describe the signals that can be exploited via the interferometric optical readout of the nanowire.

4.3.1 Interferometric readout

As described in sec. 3.4, the measurement of the probe signal results from the interference between the light reflected by the fibre output in the objective and the light reflected by the nanowire which is then collected back into the injection fibre. We will focus here on the description of the information that can be obtained from such an interferometer as well as the relation to our experimental study.

Let us consider the case where the nanowire is positioned on the optical axis (Z) of the objective. In that case, the total reflected flux,

Φ_R, at the detector can be written in first approximation,

$$\Phi_R = \Phi_0 \left| r_{\text{fiber}} + t_{\text{fiber}}^2 \, e^{i(2kz)} \, \bar{r}_{\text{nw}} \right|^2 , \tag{4.12}$$

where Φ_0 is the photon flux injected in the fibre (assuming a lossless propagation), k is the light wave-vector, r_{fiber}, t_{fiber} are the reflection and transmission coefficient of the fibre output (which serves as a phase reference here), and $\bar{r}_{\text{nw}}$ is the complex reflection coefficient of the nanowire which models the partial reflection of the input light collected back into the fibre mode.

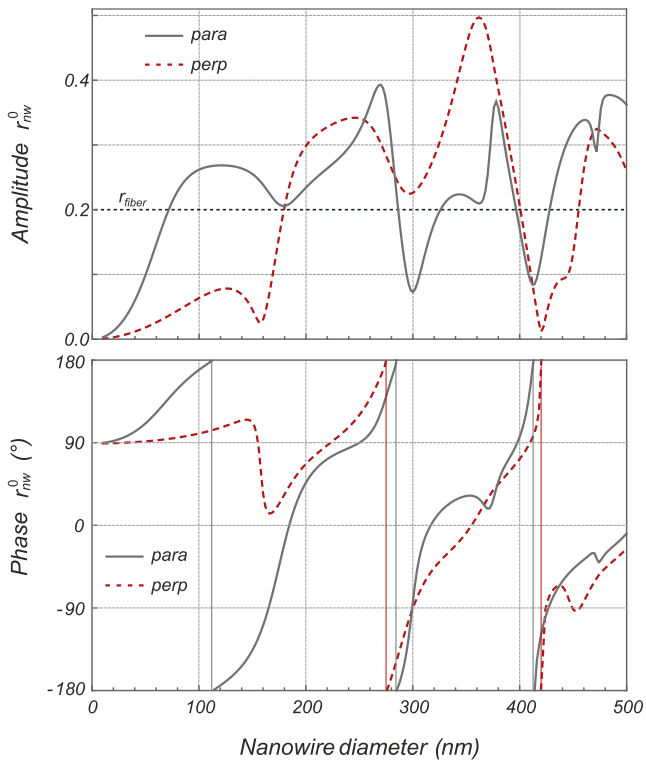

Figure 4.10: Dependence of the amplitude and phase of the reflection coefficient r_{nw} with the nanowire diameter for an incoming parallel and orthogonal laser polarisation. These calculations were realized for a numerical aperture of 0.7, and a wavelength of 633 nm. Adapted from [76, 91].

In the following we will denote the nanowire reflectivity, $\bar{r}_{\text{nw}} = r_{\text{nw}} \, e^{i \phi_{\text{nw}}}$, with r_{nw}, ϕ_{nw} the modulus and phase of the reflectivity coefficient. Those coefficients can be determined by measuring which fraction of the incident light is collected back into the fibre mode, which is subsequently transmitted into the fibre. As seen in sec. 2 the large refractive index of 3C-SiC (2.7 in the visible), allows the nanowires to sustain internal optical resonances in the visible range. Those Mie resonances strongly structure the reflectivity coefficients of the nanowires, and are at the origin of a strong dependence on their diameters. The scattering properties of an infinite cylinder can be solved analytically [89] under an incident plane wave illumination, one can then expand any incident light field onto the plane wave basis and thus compute the internal and scattered fields as well as the overlapping with the incident mode. A. Reigue developed numerical estimation of the quantities, r_{nw} and ϕ_{nw}, accounting for Mie resonances combined with the description of focused laser beam beyond the paraxial approximation, see Fig. 4.10. To do so, we inject a reference signal in the fibre, and one part is reflected by the fibre output

corresponding to a reflection coefficient (in power) of $r^2_{\text{fiber}} = 4\%$ of the injected light. We note this reference value was verified to match the reflectivity coefficient of the interferometric objectives, but an equivalent model could be used to account for any imperfection in the light propagation path (partial reflections, *etc...*). The remaining part of the field is subsequently focussed by the objective. We expand the incident Gaussian field on the plane wave basis while accounting for non-paraxial effects by adding an individual polarisation to each plane wave, following the principle exposed in Ref. [115]. We considered the limiting case of orthogonal and parallel polarisations with respect to the nanowire. To retrieve the reflectivity coefficient of the nanowire we computed the scattered field, being the sum of each plane wave contribution compositing the incident illumination, and projected back the resulting field onto the incoming Gaussian beam, thus isolating the part of the scattered field that is collected back into the fibre (we took advantages of the orthogonality of the Hermite-Gaussian modes). Those calculations allowed us to estimate the amplitude and phase of the nanowire reflectivity for varying diameters and wavelengths. It is greatly structured by the Mie resonances as shown in Fig. 4.10. One can note that for small diameters, the nanowire recover a dipole-like response, *i.e.* it is polarisable only for an incoming radiation parallel to its axis.

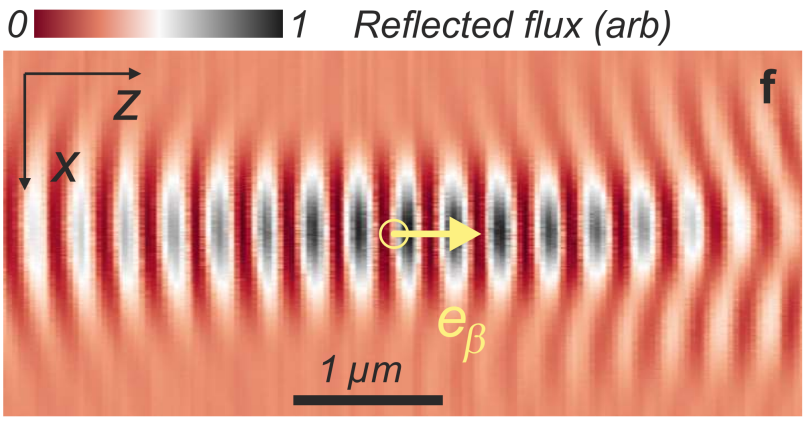

Figure 4.11: Horizontal XZ-maps of the reflected photon flux, and the beta measurement vector when the nanowire is positioned at a maximum slope in the interference pattern [66] along the optical axis.

Thus, the measured reflected flux is given by,

$$\Phi_R = \Phi_0 \left| r_{\text{fibre}} + t^2_{\text{fibre}}\, r_{\text{nw}}\, e^{i(2kz+\phi_{\text{nw}})} \right|^2, \tag{4.13}$$

$$= \Phi_0 \left[(r^2_{\text{fibre}} + t^4_{\text{fibre}}\, r^2_{\text{nw}}) + 2\, t^2_{\text{fibre}}\, r_{\text{fibre}}\, r_{\text{nw}}\, \cos(2kz + \phi_{\text{nw}}) \right]. \tag{4.14}$$

As such, a change in the reflected flux can occur not only from a displacement $(z_0 + \delta z(t))$, but also from a change in the nanowire reflectivity both in amplitude and phase $(r_{\text{nw}} + \delta r_{\text{nw}},\ \phi_{\text{nw}} + \delta\phi_{\text{nw}})$, see Fig. 4.12. It follows that the modulated photon flux arises from three contributions,

$$\delta\Phi_R = \partial_z \Phi_R\, \delta z + \partial_{r_1} \Phi_R\, \delta r_{\text{nw}} + \partial_{\phi_1} \Phi_R\, \delta\phi_{\text{nw}}. \tag{4.15}$$

In general, the flux modulation is greatly dominated by the nanowire displacements, especially when the nanowire position is chosen close to the maximum interference slope. However, when the nanowire temperature is modulated by the pump laser, it also modulates its radius and refractive index. The Mie resonances further amplify those changes in refractive index, as a cavity does and causes an enhanced reflectivity change compared to the one that could be observed on a bulk material. Although in practice the amplitude and phase of the nanowire reflectivity are intertwined by the Mie resonances, for study purposes we will consider them independent. We then must formally consider all three contributions. Their spatial dependence with respect to the nanowire resting position, z_0, are given,

$$\partial_z \Phi_R = -4\Phi_0\, k\, r_{\text{fibre}}\, r_{\text{nw}}\, t^2_{\text{fibre}}\, \sin(2\,k\,z_0 + \phi_{\text{nw}}), \tag{4.16}$$

$$\partial_{r_{\text{nw}}} \Phi_R = 2\,\Phi_0\, t^2_{\text{fibre}} \left[t^2_{\text{fibre}}\, r_{\text{nw}} + r_{\text{fibre}} \cos(2\,k\,z_0 + \phi_{\text{nw}}) \right], \tag{4.17}$$

$$\partial_{\phi_{\text{nw}}} \Phi_R = -2\Phi_0\, r_{\text{fibre}}\, r_{\text{nw}}\, t^2_{\text{fibre}}\, \sin(2\,k\,z_0 + \phi_{\text{nw}}). \tag{4.18}$$

Figure 4.13 shows the spatial sensitivity along the optical axis to those contributions in the modulation of the reflected flux along the interference pattern. Indeed, if we place the nanowire at an extremum of a peak or a crest of the interference pattern, then $\partial_z \Phi_R = \partial_{\phi_1} \Phi_R = 0$, and all the contribution we measure originates from a variation of the amplitude of the reflectivity coefficient. On the slopes of the interference pattern, we are maximally sensitive to the vibrations of the nanowire and to the modulation of the phase of the reflectivity coefficient.

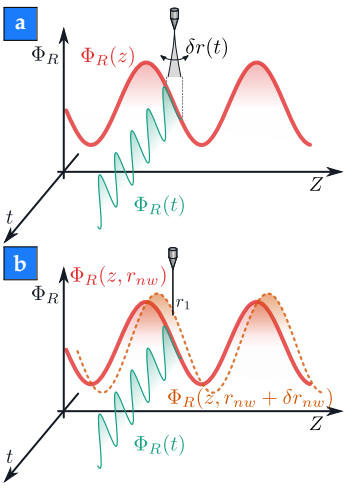

Figure 4.12: Illustration of the different mechanism generating a reflected light intensity modulation. (a) Modulation due to the nanowire displacement, (b) modulation due to a reflectivity change of the nanowire (amplitude and phase), thus deforming the measurement interference.

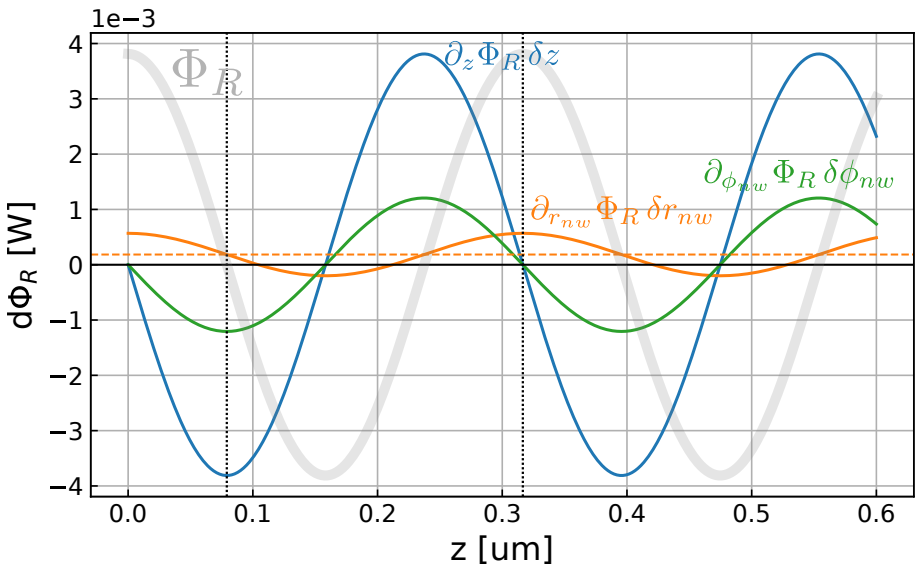

Figure 4.13: Dependence of the different contributions to the reflected flux modulation $\delta\Phi_R$ with the nanowire resting position along the interference pattern (normalised in grey). We consider realistically : $\delta z \simeq 5\,\text{nm}$, $\delta r_1 \simeq r_1 \times 1\%$, $\delta\phi_1 \simeq \pi/100$.

In practice, those reflectivity changes are relatively weak compared to the mechanical signals, they were however observed with a larger nanowire, see sec. 4.4. Indeed, while the nanowire mechanical response will be peaked around its mechanical frequencies, the thermally induced reflectivity modulation should have a low pass filter behaviour, thus visible outside mechanical resonance and most likely maximum at low frequency.

4.3.2 Vertical readout

When modulating the green laser (pump) we generate thermal waves within the nanowire due to absorption. Thermal expansion occurs, and the nanowire length varies according to the induced temperature change within the nanowire. The dynamical length change $\delta L_{\text{tot}}[\Omega]$ is connected to the internal dynamical temperature profile by :

$$\delta L_{\text{tot}}[\Omega] = \int_0^L \alpha_{\text{SiC}}\, \delta T[\Omega] \mathrm{d}y \tag{4.19}$$

where α_{SiC} is the thermal expansion coefficient of silicon carbide.

In general when considering the force sensing experiments, we are essentially interested in the lateral deformation of the nanowire and are not directly sensitive to this effect when the nanowire reflectivity is longitudinally homogeneous in the measurement area (so that a change in nanowire length does not result in a reflectivity change). Nonetheless, it can be efficiently detected by positioning half of the probe laser waist at the tip of the nanowire giving us a vertical projection of the displacement, see Fig. 4.14. We deal with the nanowire expansion response in greater details in sec. (5.1), the method being very sensitive to temperature changes in the nanowire.

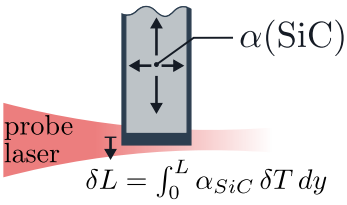

Figure 4.14: Measurement configuration used for nanowire elongation response. When the nanowire is subjected to an elevation of temperature of δT, it undergoes a total elongation of δL.

4.4 Reflectivity measurements

As seen in the previous section 4.3, our experimental setup is sensitive to reflectivity change in the nanowire. In this section we present pieces of evidence of thermally induced reflectivity change when modulating the pump laser intensity and probing at the nanowire vibrating tip.

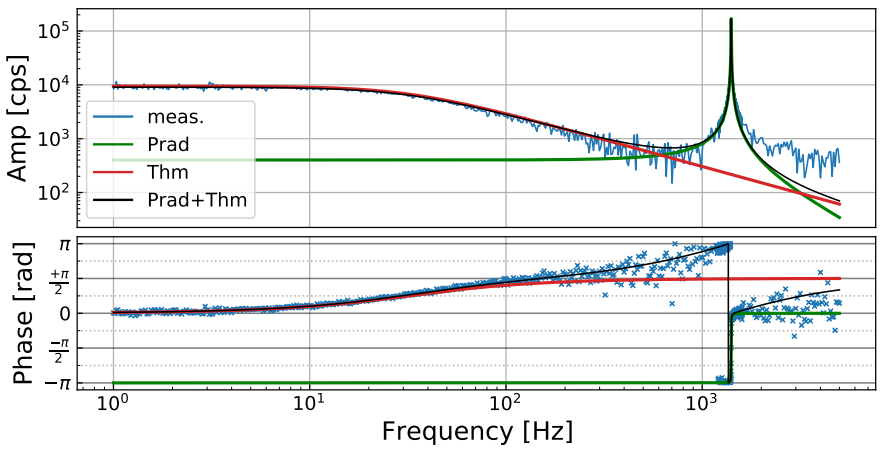

Figure 4.15: Broadband response measurement of the reflected photon flux when modulating the pump optical power. We fit the response using a simplified low pass filter model (red line) coherently sum to an instantaneous mechanical response (green line), which fully captures the low frequency and the resonant part of the response (black line).

For this set of measurements, we used a rather large nanowire of length $L = 650\,\mu$m and diameter of 400 nm. At room temperature, the mechanical quality factor is too low to resolve the two mechanical polarisations. Nonetheless, the low frequency photothermal response is well visible. It can be approximately fitted by a first-order Low Pass filter. The entire broadband response, $\delta\Phi_R[\Omega]$, is well-adjusted

in amplitude but most importantly in phase, by the coherent sum of a direct optical force contribution driving the nanowire displacement, $\delta\Phi_{\delta r_\beta} = \beta\,\mathbf{e}_\beta\left(\underline{\underline{\chi}}[\Omega]\,\delta\mathbf{F}_{\text{opt}}\right)$ (with β the conversion factor between the local change of photon flux and the nanowire displacement), and the photothermal response one, $\delta\Phi_{\text{thm}}[\Omega] = \text{LPod1}[\Omega]$, see Fig. 4.15.

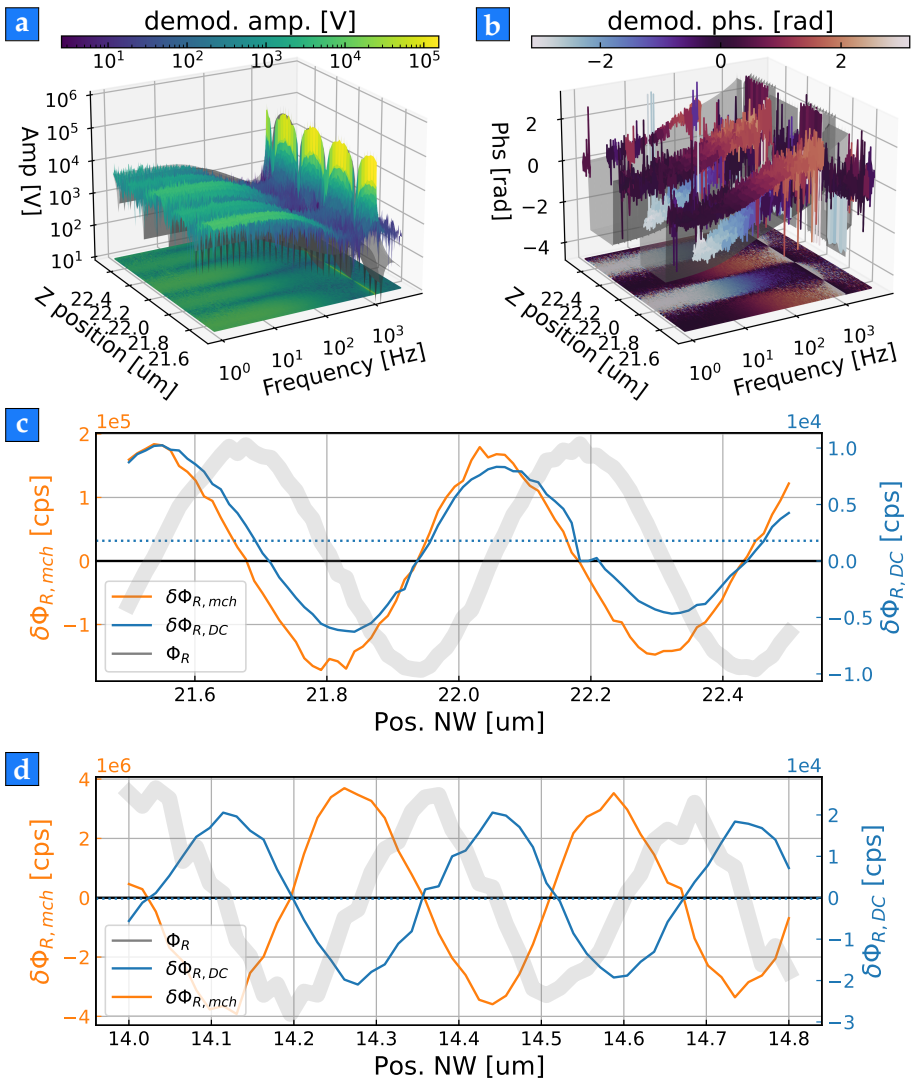

Figure 4.16: Broadband response measured at different positions within the readout interference pattern. Having placed the nanowire at the maximum intensity of the pump laser in the X-axis, we measure the broadband response while scanning the nanowire position along the Z-axis. Figure (a) shows the response in amplitude, and (b) in phase. In (c) we represent the evolution of the different response contribution along the Z-axis for a nanowire of length 650 μm and diameter 400 nm, within the interference pattern. The orange colour represents the reflected flux modulation evaluated at the mechanical resonance, $\delta\Phi_{R,\text{mch}}$, due to the direct optical force. In blue the modulation evaluated in the DC plateau, $\delta\Phi_{R,\text{DC}}$, due to the photothermal low pass contribution. We represented in grey the average reflected flux (spanning from 0.5 to 3 Mcps), in order to have the interference pattern reference position. Figure (d) shows a similar analysis carried out for a different nanowire, with length 200 μm and diameter 180 nm, while the average reflected flux spans from 2.7 to 4.6 Mcps. The position of the interference is thus different for (c).

We performed this measurement at different locations along the optical axis, after having placed the nanowire at the maximal intensity of the pump along the X-axis. The 3D plots of Figures 4.16a and 4.16b, show how the amplitude and phase of the response varies with the nanowire position within the readout interference pattern. In Fig. 4.16c, we show the evolution of the response at both the mechanical resonance (orange) and the low frequency plateau (blue) along the Z-axis. For this data set, we can observe the low frequency plateau oscillations are offsetted from the origin, contrary to the response at resonance. On top of that, we note a small spatial dephasing between the spatial oscillations of the two responses. The resonantly driven response represents here a reference for the deformation signal, it is extremum at positions of maximum slopes. This is not the case for the

low frequency response of the nanowire, meaning that we are not only sensitive to a low frequency displacement contribution, but also to a photothermal modulation of the nanowire local reflectivity. For this measurement, the reflectivity amplitude modulation of the nanowire is approximately 2% of the reflectivity.

As a comparison, we present in Fig. 4.16d the same measurement as in Fig. 4.16c but performed in a nanowire of length $L = 200\,\mu$m and diameter 180 nm. In this measurement we no longer see an amplitude offset of the demodulated response, nor a spatial dephasing different from 0 or π between the derivative of the interference pattern (orange) and the reflected flux modulation induced by the pump laser (blue). The main contribution to the modulation of the reflected flux is then either a photothermal deformation or a pure phase modulation of the nanowire reflectivity. We will detail this mechanism in more details in sec. 5.3.

4.5 Model for the thermal response

In this section, we want to derive a simple model for accessing the temperature evolution along the nanowire in presence of time-modulated laser heating in the diffusion regime, which is the dominant source of heat conduction for nanowires in vacuum. We will not go in the details of the heat diffusion equation, and more generally the heat conduction in materials, as it is an already well documented domain [116].

Furthermore, we will neglect the effect of black body radiation in the establishment of the temperature profile in the nanowire. Indeed, the irradiated power P_r, emitted by a surface dS, at temperature T, is given by the Stefan-Boltzmann law,

$$P_r = \epsilon\, \sigma_S\, T^4\, \mathrm{d}S, \tag{4.20}$$

where $\sigma_S = 5.67 \times 10^{-8}\,\mathrm{W.m^{-2}.K^{-4}}$ the Stefan-Boltzmann constant, and ϵ the emissivity of the system (with $\epsilon = 1$ for perfect black body, while $\epsilon = 0$ for perfect mirror). We now shall compare the For our nanowires of radius around 100 nm and length 200 μm, the amount of heat per temperature elevation due to radiation loss is around, $\partial_T P_r\, 2\pi\, L\, R \simeq 0.8\,\mathrm{nW.K^{-1}}$ at room temperature while $\simeq 30\,\mathrm{aW.K^{-1}}$ at 1 K. On the other hand, the power transported by conduction to the thermal bath per temperature elevation along the nanowire can be estimated by $\kappa\, \pi\, R^2/L$, and amounts to $\simeq 50\,\mathrm{nW.K^{-1}}$ at room temperature (we considered $\kappa = 320\,\mathrm{W.m^{-1}.K^{-1}}$), while in the order of $\mathrm{pW.K^{-1}}$ at 1 K if we extrapolate the SiC conductivity to $\kappa \simeq 10^{-2}\,\mathrm{W.m^{-1}.K^{-1}}$ from the data in Fig. 3.27b. By comparison, we thus consider the heat dissipation by radiation negligible with respect to dissipation of heat by conduction in our nanowires.

4.5.1 Diffusion model

Starting from general thermodynamic consideration, one can arrive to the volumetric heat diffusion equation. The Fourier law connects the

heat flux to the temperature gradient according to : $\mathbf{j}_{\text{th}} = \kappa \vec{\nabla} T$ [117], with κ the thermal conductivity of the material. Our SiC nanowires present a very high aspect ratio, and in the following we will be interested in relatively slow temporal dynamics compared to the characteristic time of the thermal waves to propagate across the nanowire cross-section. We can thus approximate the propagation problem to a 1D heat diffusion problem.

The general heat diffusion equation in the 1D framework along the nanowire axis $\mathbf{e}_y$ can be expressed such as,

$$\partial_t \left(\rho\, C_p\, T\right) - \partial_y \left(\kappa\, \partial_y T\right) = s, \tag{4.21}$$

where T is the temperature of the infinitesimal volume at position y and time t, s is a volumetric heat source in [W.m^{-3}], and ρ, C_p, κ are the density, the heat capacity, the heat conductivity of SiC respectively. In the above equation we omitted the different dependencies for clarity.

In our experimental conditions, the heat source comes from optical absorption and is localised under the laser spot assuming the nanowire is sufficiently homogeneous (we will see that when we position the laser on a nanowire defect, the absorption area can become more extended than the laser waist). The nanowire is illuminated by the pump laser and absorbs a fraction of the injected optical power, P_{abs}, over the nanowire cross-section, $S = \pi R^2$. This absorption occurs along a given section, set by the size of the laser waist w_0. We thus choose to express the heat source term such as,

$$s(y,t) = \frac{P_{\text{abs}}(t)}{S} \sqrt{\frac{2}{\pi\, w_0^2}} e^{-2\frac{(y-y_0)^2}{w_0^2}}, \tag{4.22}$$

$$s(y,t) = \frac{P_{\text{abs}}(t)}{S}\, \delta(y - y_0), \tag{4.23}$$

where y_0 is the pump laser position, whereas eq. (4.23) is the limit case where the laser waist can be considered point like with respect to the nanowire length as well as the thermal wavelengths (in the frequency range of the modulated pump signal, corresponding to 3 μm at 1 MHz). Note that the Dirac distribution is dimensioned in m^{-1}.

Since we study suspended nanowire in vacuum, there is thus no heat dissipation by conduction at the surface, and as discussed above we neglect the dissipation by radiation. We assume the support to be connected to a heat sink. Thus, the boundary condition are : 1) $j_{\text{th}} = 0$ at the free extremity, thus $\partial_y T(L,\, t) = 0$, 2) $T(0,t) = T_{\text{cryo}}$ where T_{cryo} is the temperature of the heat sink, the cryostat in our case.

Even though it is known that the heat conductivity and capacity vary with temperature, at room temperature the changes due to temperature elevation can be considered small with respect to the starting value. We thus continue assuming constant coefficient in the heat diffusion problem,

$$\rho\, C_p\, \partial_t T(y,t) - \kappa\, \partial_{yy} T(y,t) = s(y,t). \tag{4.24}$$

For the sake of clarity we will consider the source Dirac-like in the following, $s(y,t) = s_0(t)\,\delta(y-y_0)$, with $s_0(t) = P_{\text{abs}}(t)/S$. Indeed, in the case of constant coefficients, the overall physics does not change. Still, the more heavy but continuous expressions in the case of a gaussian-shaped heat source can be found in the appendix, sec. A.3.

4.5.2 Static profile

Considering a point-like heat source profile, we solve the diffusion equation by part. The solution by parts is given in the form,

$$T_s(y) = a_\pm\, y + b_\pm, \tag{4.25}$$

where $+$ and $-$ represent $y > y_0$ and $y < y_0$ respectively, with y_0 the pump laser position. Accounting for the boundary conditions, the continuity condition, and the step condition at crossing, one must solve,

$$\begin{bmatrix} 0 & 1 & 0 & 0 \\ 0 & 0 & 1 & 0 \\ y_0 & 1 & -y_0 & -1 \\ -1 & 0 & 1 & 0 \end{bmatrix} \cdot \begin{bmatrix} a_- \\ b_- \\ a_+ \\ b_+ \end{bmatrix} = \begin{bmatrix} T_{\text{cryo}} \\ 0 \\ 0 \\ -\frac{P_{\text{abs}}}{S\,\kappa} \end{bmatrix}. \tag{4.26}$$

The stationary temperature profile is then given by,

$$T_s(y) = T_{\text{cryo}} + \frac{P_{\text{abs}}}{S\,\kappa}\,\left(y - \Theta(y-y_0)\,(y-y_0)\right), \tag{4.27}$$

where Θ is the Heaviside distribution. In the limiting case where the pump laser is at the vibrating tip of the nanowire, the profile is linear, and we retrieve the thermal resistance of our system, R_{nw},

$$\Delta T = T_s(L) - T_{\text{cryo}} = P_{\text{abs}}\,R_{\text{nw}}, \tag{4.28}$$

where $R_{\text{nw}} = \frac{L}{\kappa\,S}$.

4.5.3 Periodic excitation

We now consider modulating the injected pump laser optical power around an average value, which leads to consider $P_{\text{abs}}(t) = P_{\text{abs},0} + \delta P_{\text{abs}}\,\cos(\Omega\,t)$ with Ω the modulation frequency. In frequency space, this results in solving,

$$(\partial_{yy} - \beta^2)\,\delta T[\Omega](y) = \frac{\delta P_{\text{abs}}}{S\,\kappa}\,\delta(y-y_0), \tag{4.29}$$

where we denoted $\beta^2 = i\,\Omega\,\frac{\rho\,Cp}{\kappa} = i\frac{\Omega}{D}$, with D the diffusion coefficient. Similarly to the stationary case, we solve the equation by parts, with the homogeneous solution,

$$\delta T[\Omega](y) = a_\pm\,e^{\beta\,y} + b_\pm\,e^{-\beta\,y}. \tag{4.30}$$

Considering the boundary conditions, the continuity and the step at crossing, we solve the equation for the coefficients,

$$\begin{bmatrix} 1 & 1 & 0 & 0 \\ 0 & 0 & e^{\beta L} & -e^{-\beta L} \\ e^{\beta y_0} & e^{-\beta y_0} & -e^{\beta y_0} & -e^{-\beta y_0} \\ -\beta e^{\beta y_0} & \beta e^{-\beta y_0} & \beta e^{\beta y_0} & -\beta e^{-\beta y_0} \end{bmatrix} \cdot \begin{bmatrix} a_- \\ b_- \\ a_+ \\ b_+ \end{bmatrix} = \begin{bmatrix} 0 \\ 0 \\ 0 \\ -\frac{\delta P_{\text{abs}}}{S\kappa} \end{bmatrix}. \tag{4.31}$$

In the end one gets the response temperature profile for an optical power modulation, such as,

$$\delta T[\Omega](y, y_0) = \frac{\delta P_{\text{abs}}}{S\kappa} \frac{1}{2\beta} \left[\frac{e^{\beta(L-y_0)} + e^{-\beta(L-y_0)})}{(e^{\beta L} + e^{-\beta L})} (e^{\beta y} - e^{-\beta y}) \right.$$
$$\left. - \Theta(y - y_0) \left(e^{\beta(y-y_0)} - e^{-\beta(y-y_0)}\right) \right]. \tag{4.32}$$

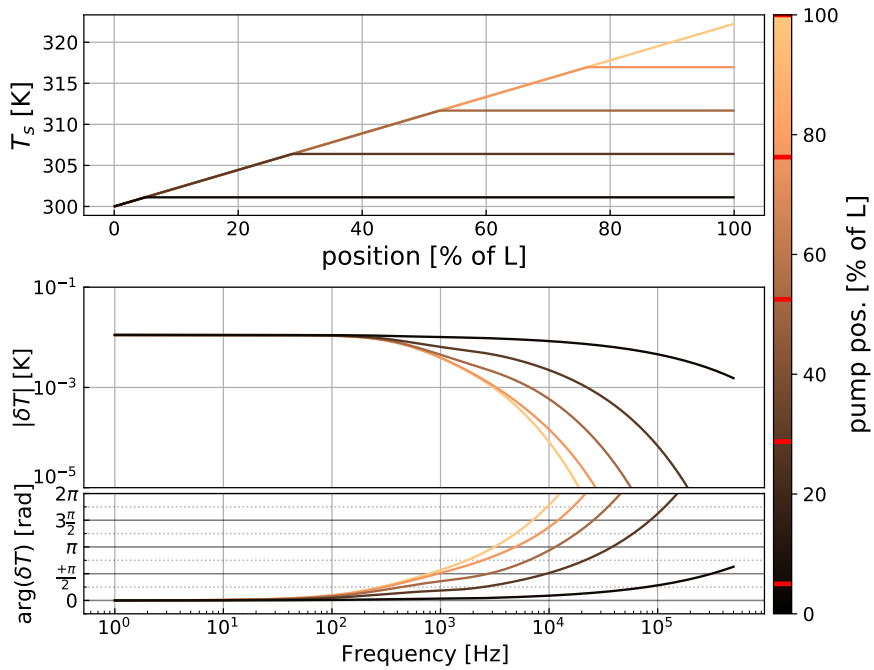

Figure 4.17: The top panel shows the static temperature profile along the nanowire for different position of the pump laser. The bottom panel shows the temperature response evaluated close to the clamping (at $y = 0.001\,L$) at different pump laser position, for a 3C-SiC nanowire of length $L = 200\,\mu$m and diameter $a = 180$ nm. The chosen heat source has a dirac-like profile, with absorbed power of $P_{\text{abs}} = 1\,\mu$W while the power modulation in the response plot is chosen to be $\delta P_{\text{abs}} = P_{\text{abs}}/2$. The red lines in the colorbar correspond to the chosen source positions in the plots in display.

Figure 4.17 shows the stationary temperature profile T_s, and the expected temperature response upon modulating the pump optical power for various pump position. The stationary temperature profile shows a steady increase of the temperature along the nanowire from the thermal bath at the clamp ($y = 0$) to the heat source, after which the temperature is constant. It means that positioning the laser pump close to the nanowire clamp, leaves a quasi-homogeneous temperature profile along the naowire, at the cost of a poor heating efficiency. Concerning the thermal response, in Fig. 4.17 we show the modulation of the temperature close to the clamping when modulating the absorbed optical power. The oscillating heat source will generate thermal waves that propagate along the nanowire with a wavelength given by,

$\lambda_{\text{thm}} = \sqrt{2\,\kappa/(\rho\, C_p\, \Omega)}$. Those waves are over damped, meaning the temperature modulation amplitude is strongly attenuated after only one wavelength. It relates to the low pass filter behaviour displayed in the response figure. The phase of the temperature response shows a cumulated delay related to how far is positioned the pump from the temperature measurement point. We note that the DC limit of the response profile is given by,

$$\delta T[\Omega \to 0](y,\, y_0) = \frac{1}{2}\frac{\delta P_{\text{abs}}}{S\,\kappa}\,(y - \Theta(y - y_0)\,(y - y_0)), \tag{4.33}$$

which follows the stationary profile. When the pump laser is placed at the tip, $y_0 = L$, the above linear profile gives us a direct estimation of the ration between the absorbed optical power and the conductivity.

4.6 Thermal noise under non-homogeneous temperature profile

Looking at the thermal model, we see that the temperature is no longer constant along the nanowire position, when the heat is generated by absorption of the pump laser optical power. A question that can arise is: How does it affect the measured noise temperature of the nanowire?

When we consider a non-homogeneous temperature profile throughout the nanowire, the fundamental assumption of thermal equilibrium needed to use the fluctuation-dissipation theorem does not hold any more. Indeed, even if we consider the system in a stationary state, under a gradient of temperature, there is necessary a heat flux. In our case, considering the timescale of the measurements and the characteristic time of the thermal propagation, one can assume the nanowire to be in **non-equilibrium steady state (NESS)**. Study of how the equipartition theorem is modified considering optomechanical system in NESS [118, 119] shows that one must account for the mode strain when internal damping mechanisms dominate the dissipation.

However, in the case of our resonators we have pieces of evidence that the quality factors are not intrinsically limited. In this case, we can consider the nanowire as a collection of oscillators coupled between them through the normal modes, as illustrated in Fig. 4.18. Moreover, we assume the dissipation in our nanowire to be homogeneous along the nanowire axis, otherwise one cannot assume decoupling between the modes [37]. In addition, we assume the mode profiles are not changed at first order, since the stiffness of the nanowire depends on the temperature and thus is no longer homogeneous. However, the change in stiffness is small compared to the value from the starting homogeneous temperature case.

In the following we consider an infinitesimal section of the nanowire at altitude y that undergoes a displacement δr due to thermal noise. To each section, we associate a temperature, $T(y)$, which is the thermal bath for the Langevin force, see Fig. 4.18. Starting from

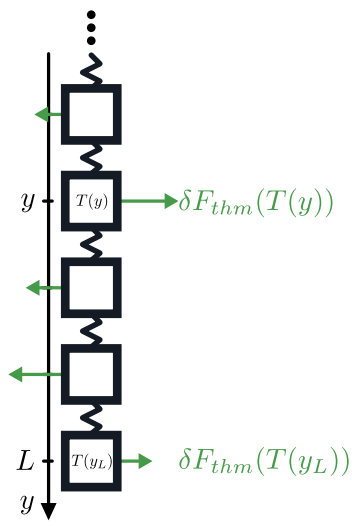

Figure 4.18: Illustration of the convolution mechanism we consider when estimating the noise motion of the nanowire generated by a non-homogeneous temperature profile. In our case we consider the nanowire as a succession of independent oscillators, each thermally driven by a Langevin force which amplitude is given by a local FDT related to the temperature of the oscillator.

the damped Euler-Bernoulli equation without external forces, the displacement dynamic of a given mode family is expressed by projecting the equation to the given normal mode. We get,

$$\partial_t^2 \delta r_n(t) + \Omega_n^2\, \delta r_n(t) \;+ \Gamma_n\, \partial_t \delta r_n(t) = \frac{1}{M_{\text{eff}}} \int_0^L \delta f_{\text{thm}}(y,t)\, u_n(y)\, \frac{\mathrm{d}y}{L} \tag{4.34}$$

where M_{eff} is the effective mass of the mode n. In frequency domain,

$$\delta r_n[\Omega] = \chi_n[\Omega] \int_0^L \delta f_{\text{thm}}[\Omega](y)\, u_n(y)\, \frac{\mathrm{d}y}{L}, \tag{4.35}$$

$$\equiv \chi_n[\Omega]\, \delta F_{\text{thm,n}}[\Omega], \tag{4.36}$$

where χ_n is the effective susceptibility associated to the n-th mode, and $\delta F_{\text{thm,n}}$ describes the effective Langevin force. Due to the statistical feature of the Langevin force, we assume an absence of coupling between the local Langevin forces δf_{thm}, and one can write the PSD of the displacement [120],

$$S_{\delta \mathbf{r}_n}[\Omega] = \left| \underline{\underline{\chi}}_n[\Omega] \right|^2 S_{F_{\text{thm,n}}}[\Omega]. \tag{4.37}$$

We now express the PSD of the n-th mode Langevin force as,

$$S_{F_{\text{thm,n}}}[\Omega] = \int_{-\infty}^{\infty} C_{F_{\text{thm,n}}}(\tau)\, e^{-i\Omega\tau}\, \mathrm{d}\tau, \tag{4.38}$$

$$= \int_{-\infty}^{\infty} \left[\int_{-\infty}^{\infty} \delta F_{\text{thm,n}}(t)\, \delta F_{\text{thm,n}}(t-\tau)\, \mathrm{d}t \right] e^{-i\Omega\tau}\, \mathrm{d}\tau, \tag{4.39}$$

$$= \iint_0^L \frac{\mathrm{d}y\, \mathrm{d}y'}{L^2}\, u_n(y)\, u_n(y') \int_{-\infty}^{\infty} C_{f_{\text{thm}}}(y,y',\tau)\, e^{-i\Omega\tau}\, \mathrm{d}\tau, \tag{4.40}$$

where $C_{f_{\text{thm}}}(y,y',\tau) = \langle \delta f_{\text{thm}}(y,\, t)\, \delta f_{\text{thm}}(y',\, t-\tau) \rangle$, by definition. Although there is a gradient of temperature along the nanowire, we assume there is no spatial correlation for the thermal noises between the different sections of the nanowire, such that we write, $C_{f_{\text{thm}}}(y,y',\tau) = C_{f_{\text{thm}}}(y,\tau)\, \delta(y-y')$. This assumption can be justified by considering the phonon mean free path, Λ_{ph}, to be infinitesimal over the nanowire length, which is true at room temperature but not likely the case at the lowest temperature achieved. The thermal noise power density of a given resonant mode is then given by,

$$S_{F_{\text{thm,n}}}[\Omega] = \int_0^L \frac{\mathrm{d}y}{L}\, u_n^2(y)\, S_{f_{\text{thm}}}[\Omega](y), \tag{4.41}$$

$$= 2\, M_n\, \Gamma_n\, k_B \int_0^L u_n^2(y)\, T(y)\, \frac{\mathrm{d}y}{L}. \tag{4.42}$$

One can introduce the noise temperature of the n-th mode, $T_{\text{noise, n}} = \int_0^L u_n^2(y)\, T(y)\, \frac{\mathrm{d}y}{L}$. This quantity can be measured by fitting the Brownian Motion of the nanowire at resonance.

When measuring the Brownian Motion of the nanowire vibrating tip for a given resonant mode, one can get the effective noise temperature of such mode,

$$T_{\text{noise, n}} = \frac{S_{F_{\text{thm,n}}}}{2\, M_n\, \Gamma_n\, k_B} = \int_0^L u_n^2(y)\, T(y)\, \frac{\mathrm{d}y}{L}, \tag{4.43}$$

which relate the temperature profile to the mode amplitude profile. In the homogeneous temperature case, we recover the nanowire temperature, while in the inhomogeneous case the noise temperature is the weight average of the lattice temperature profile with the mode amplitude.

We have to acknowledge our reasoning is based on a cumulative effect of the thermal drive, where each section of the nanowire undergoes a motion noise is described by a local fluctuation-dissipation theorem. This description does not rely on the description of the dissipation mechanism. Other approach account for the weighting of the temperature profile with the curvature profile of the oscillators [121], tackling the dissipation side of the FDT. To better understand if this approach applies in the case of our nanowires, we aim at measuring the optical heating profile for different mode families. This kind of measurement as been carried out for silicon cantilevers [121], and showed the dissipation profile is the main parameter that drive the thermal noise evolution under non-homogeneous temperature profile across the oscillator.

4.7 Chapter summary

In this chapter we started describing the measurement protocols we used in order to calibrate and characterise the mechanical properties of our nanowires. We then presented a standard pump-probe response across a wide frequency range, which serves as the fundamental measurement method enabling us to explore various photo-thermal effects that our interferometric measurement setup is sensitive to.

As such, since the cryostat experimental setup make use of an interferometric probing, we are not only sensitive to the nanowire deformation but also to the change of its reflectivity. For a given nanowire with a large diameter, we showed pieces of evidence we were able to detect thermally induced reflectivity change in the nanowire at the probe position.

We continued formalising the temperature dynamics inside our nanowire to better understand the low-pass behaviour of this photothermal effects. This model will constrain the response of the different thermal actuations the nanowire is subjected to, making it easier to describe and discriminate the photothermal effects we are observing.

The chapter concludes with the description of how the non-homogeneous temperature profile, generated by the local optical power absorption of the pump laser, affects the thermal noise of our

nanowire. Our approach differs from discussions found in the literature. It accounts for a cumulative thermal forcing by the Langevin force along the nanowire. It results the noise temperature of the nanowire is the renormalisation of the temperature profile with the normal mode profile of the considered mode family.

CHAPTER 5

A COMPILATION OF PHOTOTHERMAL MECHANISMS WITHIN THE SIC NANOWIRES

Contents

Introduction 99

5.1 Thermal elongation of the nanowire length 100

5.1.1 Measurement of the nanowire elongation response 101

5.1.2 Absorption inhomogeneities 104

5.1.3 Mie enhanced absorption 105

5.2 Heat diffusion coefficient of the nanowires and thermal contact resistance . 109

5.3 Thermal lateral deformation 113

5.4 Profile structure of the low frequency lateral deformation response 115

5.5 Modelling of the thermomechanical effect at the clamping 118

5.6 Thermal modulation of the optical cross-section 124

5.7 Electrostriction 127

5.8 Chapter summary 128

Introduction

This chapter presents several measurements that involve thermal effects within 3C-SiC nanowires. While discussing those measurements, we will refine the 'naive' 1D model of heat propagation in the nanowires described in sec. 4.5, such as the thermal contact resistance. Moreover, these measurements allow us to calibrate quantities that are not controlled in our sample preparation protocols.

Measuring the nanowire response to an optical intensity modulation allows us to be sensitive to several mechanisms coupling scattering and thermal effects. In Fig. 5.1, we illustrate the main contributions we have been sensitive to and that can be generated by a time-modulated laser intensity while detected with an optical readout. As addressed in sec. 5.6, the light can exert an optical force on the nanowire subsequently inducing a displacement of its vibrating tip. Furthermore, if part of the light is absorbed it will cause a temperature modulation and one has to take into account the propagation

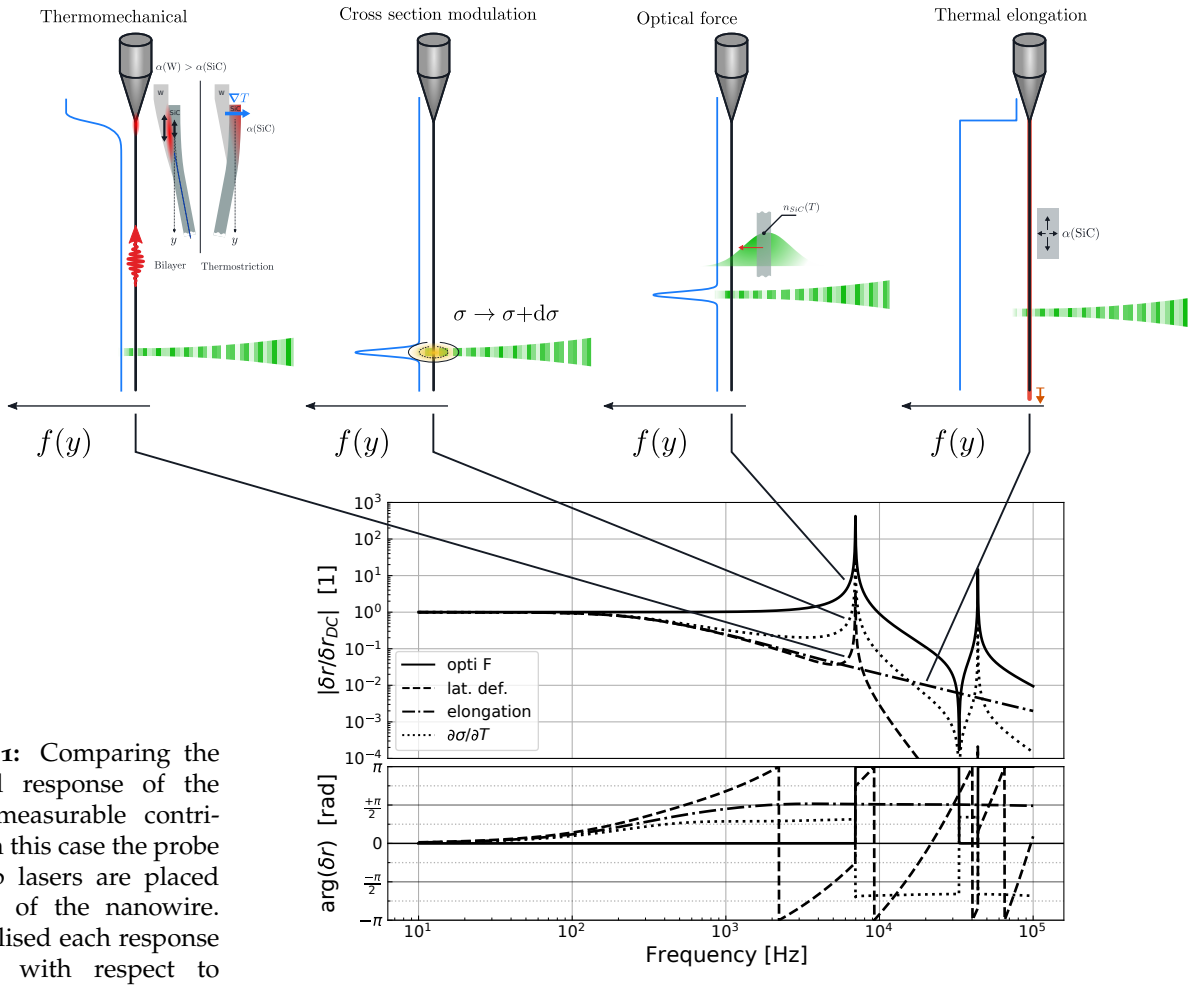

Figure 5.1: Comparing the broadband response of the different measurable contributions. In this case the probe and pump lasers are placed at the tip of the nanowire. We normalised each response amplitude with respect to their DC value.

of heat waves along the nanowire to understand their impact on the nanowire dynamics. This temperature modulation can in turn modify the optical as well as the mechanical properties of the nanowire. One can expect to detect a thermal expansion of the nanowire, as well as a change in its resonance frequencies. When the thermal wave reaches the clamping area, it generates a dynamical deformation of the nanowire, caused by either a bilayer effect between the nanowire and its tungsten support, or by a thermostrictive bending due to temperature gradient across the nanowire cross-section. We will also present measurements realised not in the cryostat optical setup, but instead in a vacuum chamber at room temperature where the optical readout and pump modulation are operated in a free space optical system, see Fig. 5.2. In the following, we review those different mechanisms and discuss their main phenomenological properties.

5.1 Thermal elongation of the nanowire length

In this section we measure and describe the effect of thermal elongation in nanowires when subjected to optical heating. From the mea-

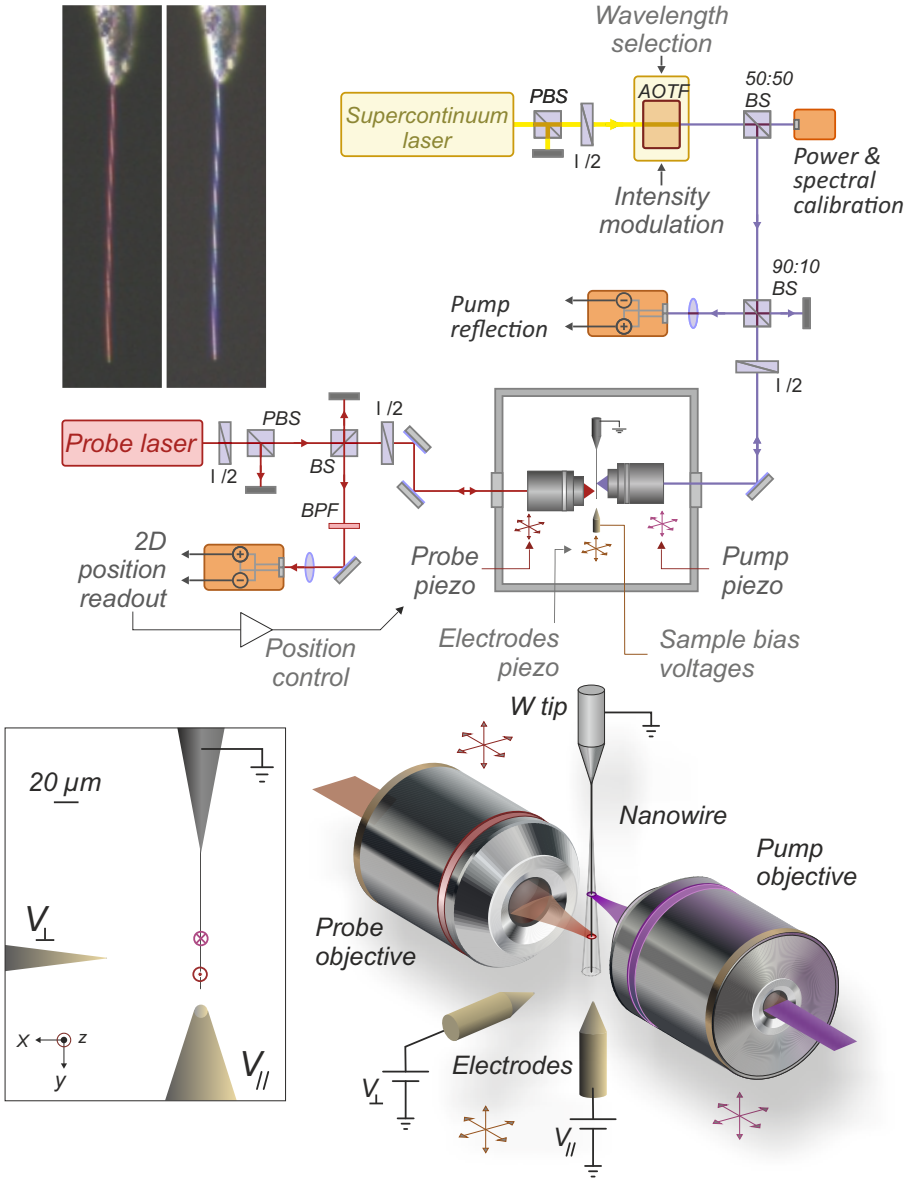

Figure 5.2: Scheme of the measurement setup used for the elongation and side-band modulation measurements. This setup makes use of a Super-Continuum whose colour is selected using an Acousto-Optic Tunable Filter (AOTF). The setup was initiated by postdoc A. Fontana, and further developed by C. Dousset during her internship.

surements of the elongation response to a modulation of the optical power, we demonstrate it can be used to retrieve the local absorption of the incident pump laser intensity.

5.1.1 Measurement of the nanowire elongation response

When we heat up a nanowire, the dominant deformation caused by the thermal expansion is an elongation of the nanowire length due to the high aspect ratio. In Figure 5.3 we present the measurement of the broadband response of the longitudinal deformation to an intensity modulation of the pump laser, when of the probe laser is placed at the tip of the nanowire, a position where we are most sensitive to thermal elongation. Note that we can also be sensitive to thermal elongation if the probe laser is placed at a defect of reflectivity, see sec. 5.1.2.

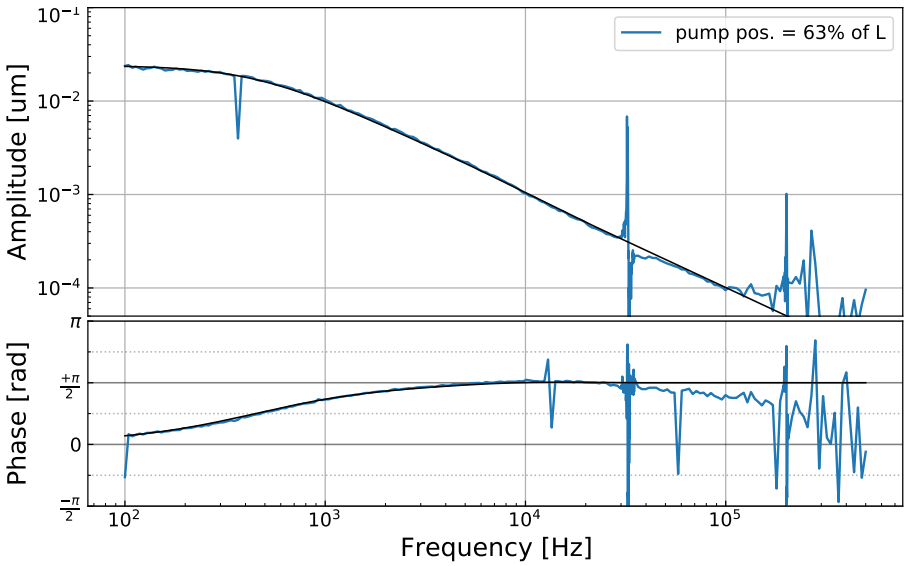

Figure 5.3: Measurement of the broadband elongation response to an intensity modulation of the pump laser, using a nanowire of length $L = 108\,\mu$m and radius $R = 130\,$nm. The measurement was carried out in the vacuum chamber setup at room temperature, setting the probe laser at the tip of the nanowire and the pump at 63% of the nanowire length on a maximum of absorption. In black line, the expected model for such elongation response with a fitted amplitude accounting for an unknown absorption.

This response displays a striking low-pass behaviour which is well modelled by the theory, see in the following. Contrary to measurements of the lateral response to the modulation of the pump optical power, the elongation response shows a global increase of the DC amplitude, although one needs to account for possible heterogeneities in the absorption between measurements, as shown in the following sections. Although we aim to measure the longitudinal deformation of the nanowire, the lateral mechanical resonant displacement is still visible (at 32.5 kHz) because there is a non-zeros component in the lateral direction for the measurement vector due to the nanowire tilt in the YZ-plane.

To model the thermal elongation response, we account for the thermal expansion that couples the nanowire deformation to its temperature. The linear thermal expansion coefficient, α, is defined as,

$$\alpha(T) = \frac{1}{l_0} \left.\frac{\partial l_0}{\partial T}\right|_P, \tag{5.1}$$

with T the temperature while considering a section l_0 undergoing an infinitesimal change of temperature at constant pressure P. If one measures the longitudinal expansion of the nanowire at a given position y, the elongation $\Delta L(y)$ relates to the internal temperature change from the resting temperature profile $\Delta T(y)$, such that,

$$\Delta L(y) = \int_0^y \alpha\, \Delta T(y')\, \mathrm{d}y'. \tag{5.2}$$

In our experimental setups, we induce the internal temperature change with a pump laser. The expression of the static elongation, ΔL_s, and the elongation response to a modulation of the pump optical power, $\delta L[\Omega]$, are given by integrating the temperature profiles

defined in the 1D diffusion model of sec. 4.5. In such case, we get,

$$\Delta L_s(y_{\text{probe}}, y_0) = \int_0^{y_{\text{probe}}} \alpha \, \left(T_s(y') - T_{\text{cryo}}\right) \, \mathrm{d}y', \tag{5.3}$$

$$= \alpha \left(\frac{1}{2} y_{\text{probe}}^2 + (y_{\text{probe}} - y_0)\, y_0\right) s_0, \tag{5.4}$$

$$\delta L[\Omega](y_{\text{probe}}, y_0) = \int_0^{y_{\text{probe}}} \alpha \, \delta T[\Omega](y', y_0) \, \mathrm{d}y', \tag{5.5}$$

$$= \alpha \frac{\delta s_0}{2\,\beta^2} \left[\frac{\cosh(\beta\,(y_L - y_0))}{\cosh(\beta\, y_L)} \left(e^{\beta\, y_{\text{probe}}} + e^{-\beta\, y_{\text{probe}}} - 2\right)\right.$$
$$\left. - \Theta(y_{\text{probe}} - y_0) \left(e^{\beta\,(y_{\text{probe}} - y_0)} + e^{-\beta\,(y_{\text{probe}} - y_0)} - 2\right)\right], \tag{5.6}$$

where y_{probe} is the position of the elongation measurement, y_0 the pump laser position, α the thermal expansion coefficient of 3C-SiC, $\beta = \sqrt{i\,\Omega/D}$ the thermal wave vector, $s_0 = P_{\text{abs}}/(\kappa\,\pi\,R^2)$ the heat source static amplitude, and $\delta s_0 = \delta P_{\text{abs}}/(\kappa\,\pi\,R^2)$ the heat source modulation amplitude. Figure 5.4 shows the static elongation as well as the broadband elongation response, when the pump laser is placed at different position along the nanowire.

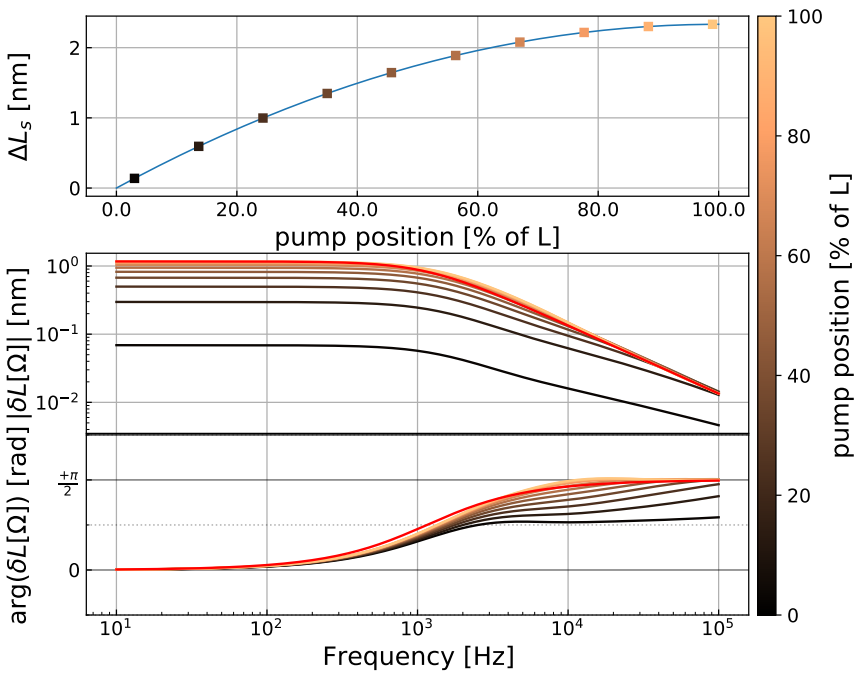

Figure 5.4: Calculation of the stationary profile as well as the response of the elongation of the nanowire tip with the pump position. We considered a nanowire of resting length 200 μm, and diameter 180 nm, under an average absorbed optical power of 1 μW, while a modulated optical power of 50 % of the average power for the response. We considered the bulk 3C-SiC conductivity at room temperature $\kappa = 320$ W.K^{-1}.m^{-1}, and the thermal expansion coefficient $\alpha = 3.8 \times 10^{-6}\,\text{K}^{-1}$. In red, the low-pass approximation of the elongation response when the probe and pump laser are at the tip of the nanowire.

For maximum sensitivity, it is best to set the probe laser at the tip of the nanowire. In this case the low frequency plateau relates directly the elongation to the absorbed pump optical power,

$$\lim_{\Omega \to 0} \delta L[\Omega](L, y_0) = \delta L_{\text{DC}}(L, y_0) = \frac{\alpha}{2} \frac{\delta P_{\text{abs}}}{\kappa\,\pi\,R^2}\, y_0\,(2\,L - y_0), \tag{5.7}$$

with L the nanowire resting length. In particular, when both the probe laser and the pump laser are at the tip of the nanowire, the relative

elongation in the DC limit gives a simple measure of the absorbed optical power, $\delta L_{\mathrm{DC}}/L = \frac{\alpha L}{2}\frac{\delta P_{\mathrm{abs}}}{\kappa \pi R^2}$. From such measurements and knowing the conductivity and the thermal expansion coefficient (which are well established at room temperature for bulk 3C-SiC), one can retrieve a measure of the local absorption of the nanowire under the pump laser waist. In addition, a second order approximation of the elongation response at low frequency is equivalent to a low-pass filter,

$$\delta L[\Omega](L,\, L) = \frac{\alpha\, L^2}{2}\,\frac{\delta P_{\mathrm{abs}}}{\kappa\, \pi\, R^2}\,\frac{1}{1 + i\,\frac{\Omega}{\Omega_c}}, \tag{5.8}$$

where we can define the low-pass cutoff frequency $\Omega_c = 2\,D/L^2$, with the diffusion coefficient $D = \kappa/(rho\, C_p)$.

One can also estimate the sensitivity of the elongation response measurement to temperature increase, especially in the cryostat experimental setup. Let us assume a homogeneous temperature increase of $T \to T + \delta T$, the relative elongation of the nanowire is $\frac{\delta L}{L} = \alpha\,\Delta T$. In the cryostat setup experiment, the shot noise of the laser limits our sensitivity to a measurable displacement. The measurement signal is the reflected flux and can be written, $\delta\Phi_R = C\,\delta L[\Omega] + \delta\Phi^{\mathrm{shot}}$, with C the conversion factor between the reflected flux and the actual displacement. At first approximation, see Fig. 5.5, C can be estimated to be $C = (\Phi_{R,max} - \Phi_{R,0})/4w_0$, which in the case of the interferometric readout gives,

$$C = \frac{\Phi_0\,(r_{\mathrm{nw}}^2 + 2\,r_{\mathrm{nw}}\,r_{\mathrm{fiber}})}{4\,w_0}, \tag{5.9}$$

with r_{fiber} the reflection of the fibre end in the cryostat objectives, and r_{nw} the reflectivity of the nanowire accounting for the objective transmission. The power spectrum density of the signal is then, $S_\Phi = C^2\,S_{\delta L} + S_\Phi^{\mathrm{shot}}$, with $S_\Phi^{\mathrm{shot}} = \Phi_{R,0}$.

In the end, the smallest detectable displacement is taken to be the value when the SNR is unity, and we get,

$$\delta T_{\mathrm{min}} = \frac{1}{\alpha\, L}\,\frac{4\,w_0}{\sqrt{\Phi_{R,0}}}\left(\frac{r_{\mathrm{fiber}}^2}{r_{\mathrm{nw}}^2 + 2\,r_{\mathrm{nw}}\,r_{\mathrm{fiber}}}\right). \tag{5.10}$$

If we put some number, one can expect to be sensitive to temperature change down to 10 mK. Although eq. (5.10) shows the temperature sensitivity increases with the probe laser intensity, one needs to keep in mind the probe laser power is also absorbed by the nanowire, thus limiting the minimum achievable temperature change, see Fig. 5.6.

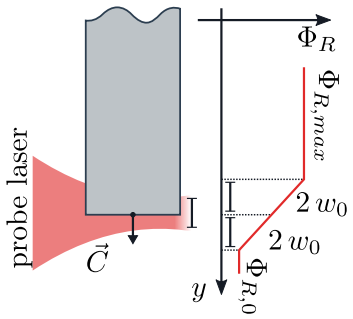

Figure 5.5: Schematic of the expected measurement vector amplitude at the tip of the nanowire when measuring the elongation in the cryostat setup.

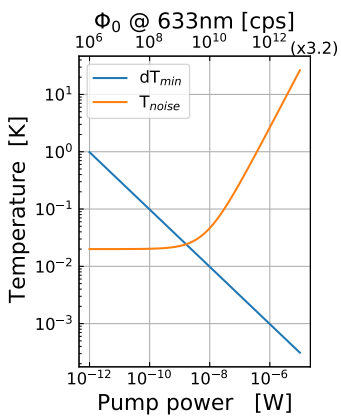

Figure 5.6: Minimal temperature change expected to be measured with the thermal elongation of the nanowire at different probe optical power for 1 Hz of RBW, compared to the noise temperature of the nanowire with the induced temperature profile by absorption of the probe optical intensity. We considered the cryostat temperature to be 1 mK, and the nanowire to absorb 3% of the injected optical power.

5.1.2 Absorption inhomogeneities

In this section we demonstrate the heterogeneity of the absorption along a nanowire. In Figure 5.7 we show concomitant measurements made by scanning the pump position in the XY-plane of the nanowire, with a pump wavelength of 576 nm. We plot the map of the pump laser reflected flux, Φ_R, and its associated mean profile along the Y-axis. The pump reflection map is compared to the XY map of

the amplitude and phase of the elongation response, that were measured at a fixed demodulation frequency Ω_d (in the case of Fig. 5.7, $\Omega_d/2\pi = 1.015\,\text{kHz}$, which corresponds to the end of plateau of the thermomechanical effect for this nanowire, see Fig. 5.3). The first striking feature is the granularity of the reflected flux and elongation amplitude along the nanowire. In the elongation response, the bright spots in the amplitude correspond to defects of high absorption and of increased nanowire temperature, thus the "**hot spots**" denomination. Those spots seem also correlated to lower reflection spots. On the other hand, the phase signal of the demodulation is much more homogeneous along the nanowire axis, demonstrating that the increase in absorption in the "hot spots", does not change the physics of the thermal effect and that the phase of the response is a reliable quantity when studying the profile of the thermal response.

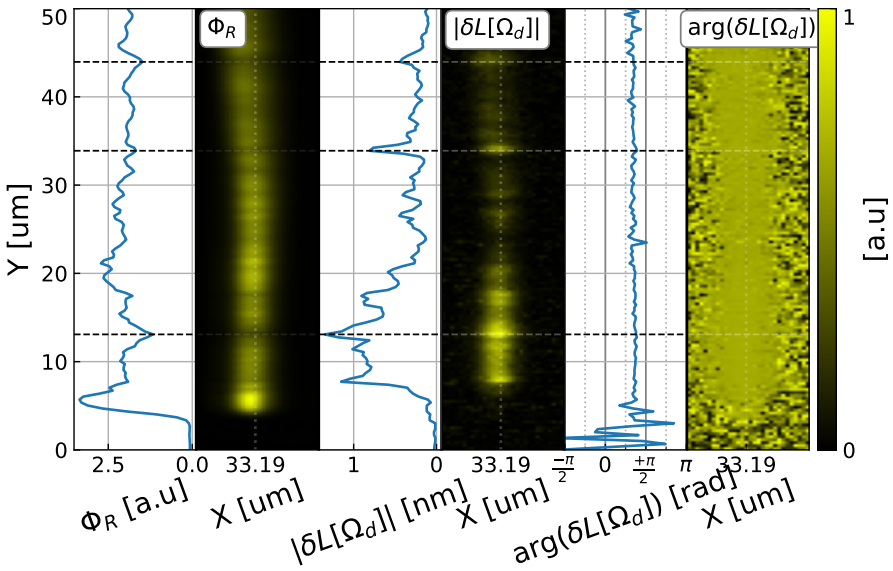

Figure 5.7: Measurement maps of the pump light reflection, as well as the elongation response at the tip of the nanowire demodulated at $\Omega_d = 1.015\,\text{kHz}$, while scanning in XY-plane, for a pump laser wavelength at 576 nm. The nanowire total length is $L = 108\,\mu\text{m}$ and has a radius of $R = 130\,\text{nm}$, with a resonant at 32.5 kHz. The colour maps show the relative evolution of the quantities, while their associated left line plot represents the evolution along Y of a slice taken at the centre of the nanowire diameter, around $X = 33.20\,\mu\text{m}$. The Y coordinates corresponds to the position of the pump laser scanner, and is thus inverted with respected to the Y-axis of the nanowire. The free end tip of the nanowire is close to $Y = 5\,\mu\text{m}$ in the maps, and is the most visible looking at the reflected flux.

The inhomogeneities in the absorption properties along the nanowires could originate from surface contaminants, internal defects in the crystalline structure, or diameter change. However, crystalline defects tend to be of the hexagonal polytype of SiC, which has a lower optical absorption rate due to its gap in the shorter wavelength range. This is why the observed hot spots might be more related to diameter changes.

5.1.3 Mie enhanced absorption

In this section we fix the position of the pump laser at the vibrating tip of a large diameter nanowire ($d = 555\,\text{nm}$), and we carry out an elongation response varying the incident wavelength of the pump laser using a Super-Continuum laser coupled with an AOTF filter. As described in the above section, the analysis of the DC plateau allows us to retrieve a measure of the local optical power absorption knowing the injected pump laser optical power. Figure 5.8 shows the converted DC value of the elongation response to an estimated absorption with

the wavelength of the pump laser at a fixed position. The local absorption presents well-defined peaks, related to the Mie resonances for the given nanowire diameter. On top of that, the background level starts a significant increase below the wavelength 515 nm. This is indeed expected, since the band gap of 3C-SiC is approximately 2.52 eV and the penetration depth (related to the imaginary part of the refractive index) follows the same trend when looking at the literature for bulk 3C-SiC, see Fig. 5.9.

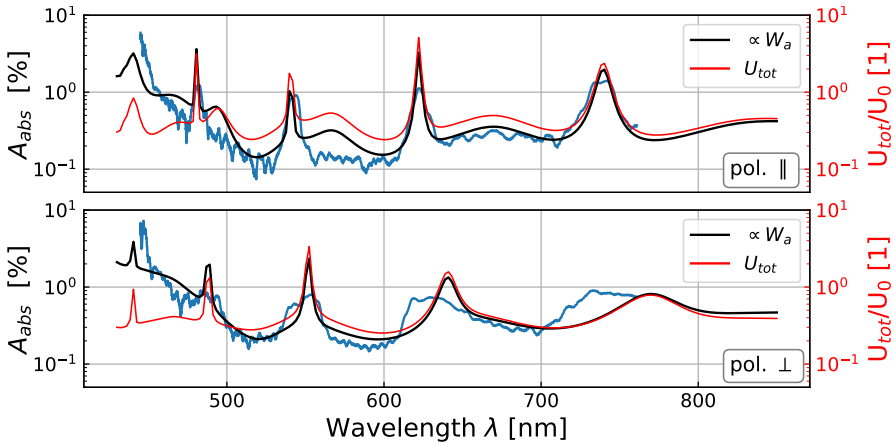

Figure 5.8: Evolution of the local absorption coefficient, computed from the DC plateau of the elongation response for a nanowire of length $L = 500\,\mu$m and diameter $d = 555$ nm.

As seen in chap. 2, the Mie resonances structure the interaction of our nanowires with the incident laser illumination. When we look at the total internal EM energy across a nanowire cross-section for a given diameter, see Fig. 5.8, the energy per unit length is enhanced with the Mie resonances and can reach multiple times the energy that the total energy of the incident radiation would have been in the same area.

The electromagnetic energy density in a dielectric medium (Chap-10, 80 - $ The field in dispersive media, of ref. [122]), is given by,

$$u_1^{\parallel,\perp}(r,\phi) = \frac{1}{8\pi}\left(\epsilon\,\|\mathbf{E}_1^{\parallel,\perp}\|^2 + \mu_0\,\|\mathbf{H}_1^{\parallel,\perp}\|^2\right), \tag{5.11}$$

where $u_1^{\parallel,\perp}$ denote the EM energy density inside the nanowire for an incident parallel and perpendicular plane wave polarisation respectively, while $\mathbf{E}_1$ and $\mathbf{H}_1$ are the electric and magnetic fields inside the nanowire with their expression given in chap. 2. We want to compute the total energy spanning the cross-section of the nanowire. We then compute the electromagnetic energy per unit length such as,

$$U_{\text{int}}^{\parallel,\perp} = \int_0^R \int_0^{2\pi} u_1^{\parallel,\perp}(r,\phi)\, r\, \mathrm{d}r\, \mathrm{d}\phi, \tag{5.12}$$

where R is the nanowire radius. Considering the average amplitude of the EM-field with, $\|\mathbf{E}\|^2 = \mathbf{E}\,\mathbf{E}^*$ and $\|\mathbf{H}\|^2 = \mathbf{H}\,\mathbf{H}^*$, we can write the terms in $u^{\parallel,\perp}$ and integrate it over the angles. Due to the orthogonality of the cylindrical harmonics, the cross order terms in the double sum

will vanish and only the product of same order will persist. In the end, one can show the expression to be,

$$U_{\text{int}}^{\parallel,\perp} = \frac{1}{4}\,\epsilon_0\,|n|^4\,k_0^2 \sum_{m=-\infty}^{+\infty} \|c_m^1\|^2 \int_0^a \left[\left(\frac{n^2}{|n|^2} + \frac{m^2}{|n|^2\,k_0^2\,r^2}\right)|Z_m^1(n\,k_0\,r)|^2 + |\partial_\rho Z_m^1(n\,k_0\,r)|^2\right] r\,\mathrm{d}r, \tag{5.13}$$

where the refractive index can be complex, and $c_m^1 = a_m^1$ for the parallel polarisation while $c_m^1 = b_m^1$ for the perpendicular one, and $k_0^2 = \omega^2\,\epsilon_0\,\mu_0$ the amplitude of the wave vector in vacuum. We kept k_0 in vacuum in order to explicitly write the dependence in the refractive index, n. For comparison, we compute the incident wave plane energy that would be present in the same surface without the nanowire,

$$U_0 = \int_0^R \int_0^{2\pi} u_i(r,\phi)\,r\,\mathrm{d}r\,\mathrm{d}\phi = \epsilon_0\,E_{i,0}^2\,(\pi\,a^2), \tag{5.14}$$

and plotted the relative energy in Fig. 5.8. One can note the measured enhanced absorption corresponds well to the spectral distribution of EM energy within the nanowire, as expected when considering the absorbed energy is proportional to the energy in the material.

Still a constant material absorption is not sufficient to explain the measurements. Indeed, the absorption coefficient of the cubic 3C-SiC is also wavelength dependent, see Fig. 5.9, which explains the global increase at smaller wavelength in the absorption measurement. Absorption in media are often described by their complex refractive index,

$$n(\lambda) = n_1 + i\,n_2, \tag{5.15}$$

where n_1 and n_2 are positive reals. One can relate the imaginary part of the refractive index such that it relates to the penetration depth, denoted a, with $n_2(\lambda) = a(\lambda)/k_0$.

In the case of Mie resonances, we compute the local absorbed power, W_a, by calculating the total flux passing through a closed surface around the scattering particle [89]. This gives,

$$W_a = \oint_A \mathbf{S}\,\mathrm{d}\sigma, \tag{5.16}$$

where $\mathbf{S}$ is the Poynting vector, A the closed surface and $\mathrm{d}\sigma$ the infinitesimal oriented surface unit. In the case of the nanowire, we define a close cylinder of radius R_{cyl} larger than the nanowire radius, and of height H. Since we look for the Poynting vector outside the nanowire, only the incident and scattered fields will come to play. The time averaged external Poynting vector can then be decomposed

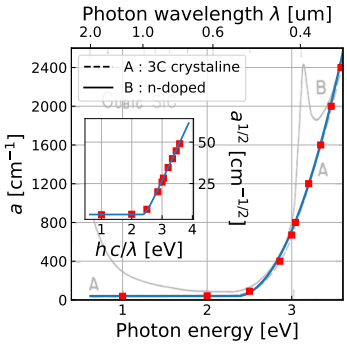

Figure 5.9: Evolution of the absorption coefficient (or penetration depth) with the photon energy. We model the A line (corresponding to the absorption of a quadratic SiC crystal) with a cubic function flatten to a constant value ($40\,\mathrm{cm}^{-1}$) before the threshold at 2.35 eV (corresponding to approximately 527 nm photon wavelength), see inset figure. Data figure from [123]

into three contributions: the incident Poynting vector $\mathbf{S}_i$, the scattered one $\mathbf{S}_s$, and the interaction of the fields denoted $\mathbf{S}_{\text{ext}}$. We write,

$$\mathbf{S} = \frac{1}{2}\,\text{Re}[(\mathbf{E}_i + \mathbf{E}_s) \times (\mathbf{H}_i + \mathbf{H}_s)^*], \tag{5.17}$$

$$= \mathbf{S}_i + \mathbf{S}_s + \mathbf{S}_{\text{ext}}. \tag{5.18}$$

It follows the absorption rate can also be developed into three contributions, such as,

$$W_a = W_i - W_s + W_{\text{ext}}, \tag{5.19}$$

where W_i vanishes at long distances (an order of magnitude larger than the nanowire diameter). Computing the Poynting vector, one can remark it has no component along the nanowire axis, $\mathbf{e}_y$, when the incident plane wave vector has an orthogonal incidence on the nanowire. We thus define the absorbed power per unit length such as, $w_a = W_a/H$,

$$w_a = \int_0^{2\pi} \mathbf{S}(R_{\text{cyl}},\, \phi,\, y)\, \mathbf{e}_r\, R_{\text{cyl}}\, \mathrm{d}\phi. \tag{5.20}$$

Moreover, considering the surrounding medium of the nanowire as non-absorbing, the above quantity should not depend on the integrating surface we defined. Thus, one can take R_{cyl} of asymptotically great radius and make use of the asymptotic behaviour of the Bessel's function, reducing the contribution to the absorption power computation to,

$$w_s^{\parallel,\perp} = \frac{2\,c\,\epsilon_0\,E_{i,0}^2}{k} \sum_{m=-\infty}^{\infty} |c_m^s|^2\,, \tag{5.21}$$

$$w_{\text{ext}} = \frac{2\,c\,\epsilon_0\,E_{i,0}^2}{k} \sum_{m=-\infty}^{\infty} \text{Re}(c_m^s), \tag{5.22}$$

where $c_m^s = a_m^s$ for incident parallel polarisation, while $c_m^s = b_m^s$ for perpendicular incident polarisation as defined in chap. 2, and we denoted in lower case w the power per unit length. We compare this absorbed power to the received power on the half section surface of the nanowire by the incident plane wave,

$$w_0 = \int_{-\pi/2}^{+\pi/2} \mathbf{S}_i\, \mathbf{e}_r\, R\, \mathrm{d}\phi = \epsilon_0\, c\, E_{i,0}^2\, R, \tag{5.23}$$

where R is the nanowire radius. We plotted the theoretical absorbed power in black in Fig. 5.8, where we adjusted the global amplitude to best fit the measurements. Indeed, in the experimental setup, we measure the ratio between the absorbed power P_{abs} and the injected laser power. The ratio, w_a/w_0 does not account for spurious losses, nor for the change of waist shape with the colour of the pump laser. Still, the measurements and the expected Mie enhanced absorption spectrum qualitatively match.

Not only the elongation response to a pump intensity modulation allows us to study the establishment of a temperature profile along

the nanowire, but those measurements give us access to the absorption properties of the nanowire as well as a method to calibrate the optical properties heterogeneities along a given nanowire. In the following section, we will compare the thermal properties between different nanowires.

5.2 Heat diffusion coefficient of the nanowires and thermal contact resistance

Over the years of this PhD, we accumulated numerous thermal measurements that are not all presented in this manuscript. Nevertheless, in Figure 5.10a we compare the measured effective diffusion coefficient parameter we use to fit the low frequency response over the different nanowires we used. The dispersion in the values of the diffusion coef-

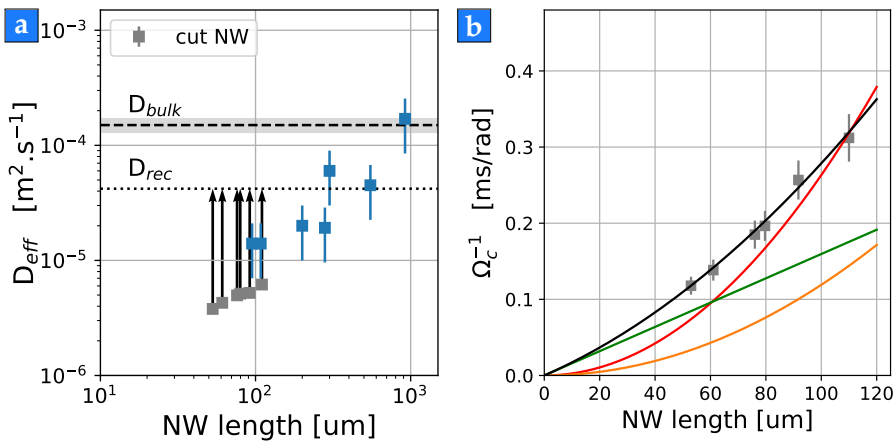

Figure 5.10: (a) Evolution of the measured effective diffusion coefficients used in fitting thermal model for various nanowires with various lengths (blue squares), and for the same nanowire that has been cut to change its total length (grey squares). The dotted black line is the value of the rectified diffusion coefficient, D_{rec}, when accounting for a thermal contact resistance. (b) Evolution of the effective thermal cutoff frequency Ω_c upon changing the length of the same nanowire by in situ laser cutting (grey squares, same data set as *cut NW* in (a)). We show the different models in solid line defined in the following by eq. (5.31), see discussion at the end of the section. We show the expected evolution of the thermal cutoff with the nanowire length when not accounting for a thermal contact resistance (red line), the linear evolution of the thermal cutoff due to the reduction of the nanowire thermal resistance (green line), the quadratic evolution due to the reduction of the propagation length (orange line), and the sum of the two latter (black line).

ficients is not explained by the variety of nanowires found in the powder sample from which the nanowire are chosen. Mostly the estimated diffusion coefficient is under-estimated with respect to the expected bulk at room temperature (see Fig. 3.27d in chap. 3). Nonetheless, the distribution seems to display a trend with the nanowire length. In addition, we proceeded to measure the low frequency thermal cutoff while reducing the length of the same nanowire, see Fig. 5.10b. In our simple 1D Fourier diffusion model, the thermal cutoff should follow $\Omega_c^{-1} \propto L^2$ (red line in Fig. 5.10b), which does not correspond to the measured trend.

Up to now, we considered the nanowire perfectly thermalised to the heat sink at its clamping, fixing a constant temperature of the nanowire at the clamping, which may not be the case for a non-perfect thermal contact. The clamping area is poorly controlled by our fabrication procedure: the quantity of carbon glue employed to fix the nanowire on the tungsten etched tip and the precise geometry of the clamping is varying a lot from sample to sample. More fundamentally, the interface contact resistance strongly depends on the material employed and on their respective phonon mode spectral densities. At

low temperature, the mismatch between the phonon modes of the 2 materials gives rise to a Kapitza resistance. In our diffusive model, we can model this imperfection by the addition of a boundary contact resistance, R_c (as illustrated in Fig. 5.11), which will be responsible for a temperature drop between the sink temperature and the nanowire temperature at the clamping,

$$\Delta T = T(y = 0^+) - T_{\text{cryo}} = R_c \, j_{\text{thm}} \, S, \tag{5.24}$$

with j_{thm} the heat flux at the clamping, T_{cryo} the temperature of the heat sink, and $S = \pi R^2$ the nanowire cross-section surface.

Figure 5.11: Scheme of the contact thermal resistance at the clamping in the 1D model.

This change of boundary condition leads to the new expressions for the stationary temperature profile along the nanowire, T_s, and for the temperature response profile, δT, such as,

$$T_s(y) = \frac{\delta P_{\text{abs}}}{S\,\kappa} \left[y - \Theta(y - y_0)\,(y - y_0) \right] + R_c \frac{\delta P_{\text{abs}}}{S} + T_{\text{cryo}}, \tag{5.25}$$

$$\delta T[\Omega](y) = \frac{\delta P_{\text{abs}}}{S\,\kappa} \frac{1}{2\,\beta} \left[\frac{\left(e^{\beta\,(y_L - y_0)} + e^{-\beta\,(y_L - y_0)}\right)}{\left((1+u)\,e^{\beta\,y_L} + (1-u)\,e^{-\beta\,y_L}\right)} \left((1+u)\,e^{\beta\,y} - (1-u)\,e^{-\beta\,y}\right) - \Theta(y - y_0)\left(e^{\beta\,(y - y_0)} - e^{-\beta\,(y - y_0)}\right)\right], \tag{5.26}$$

where y_0 is the pump laser position, we denoted $u = R_c\,S\,\kappa\,\beta = \frac{R_c}{R_{\text{nw}}}\,\beta\,L$, and where $\beta = \sqrt{i\,\Omega\,\frac{\rho\,C_p}{\kappa}}$. We denote $R_{\text{nw}} \equiv \frac{L}{\kappa\,S}$ the nanowire thermal resistance, which gives an order of comparison for the thermal contact resistance.

The thermal resistance of a 100 μm x 200 nm nanowire is of 20 K/μW at room temperature. Considering a thin layer of carbon glue between the nanowire and the tungsten tip, the contact resistance can be estimated using the out of plane conductivity of graphite and an interface length of 100 nm on a 10 μm x 200 nm surface, it amounts to 2.5^{-3} K/μW, which is largely negligible. The situation may not be identical at very low temperatures, where Kapitza effects may come into play.

In Figure 5.12a, we compare the linear responses for different contact thermal resistance. We evaluate the temperature close to the clamping area, while setting the pump laser at 90% of the nanowire

length. When the contact thermal resistance increases we gain in temperature sensitivity at the clamping upon heating using the pump laser. Higher contact resistance also shifts the thermal response cutoff to lower frequency. This effect is even more striking when calculating the expected elongation response when varying the thermal contact resistance, see Fig. 5.12b. In this case we observe a net shift of the low-pass like response to lower frequency, with a higher gain for the DC plateau. Consequently, not calibrating the contact thermal resistance can lead to underestimate the thermal cutoff and subsequently overestimate the diffusion coefficient inside the nanowire. We will address this issue in more detail in the following.

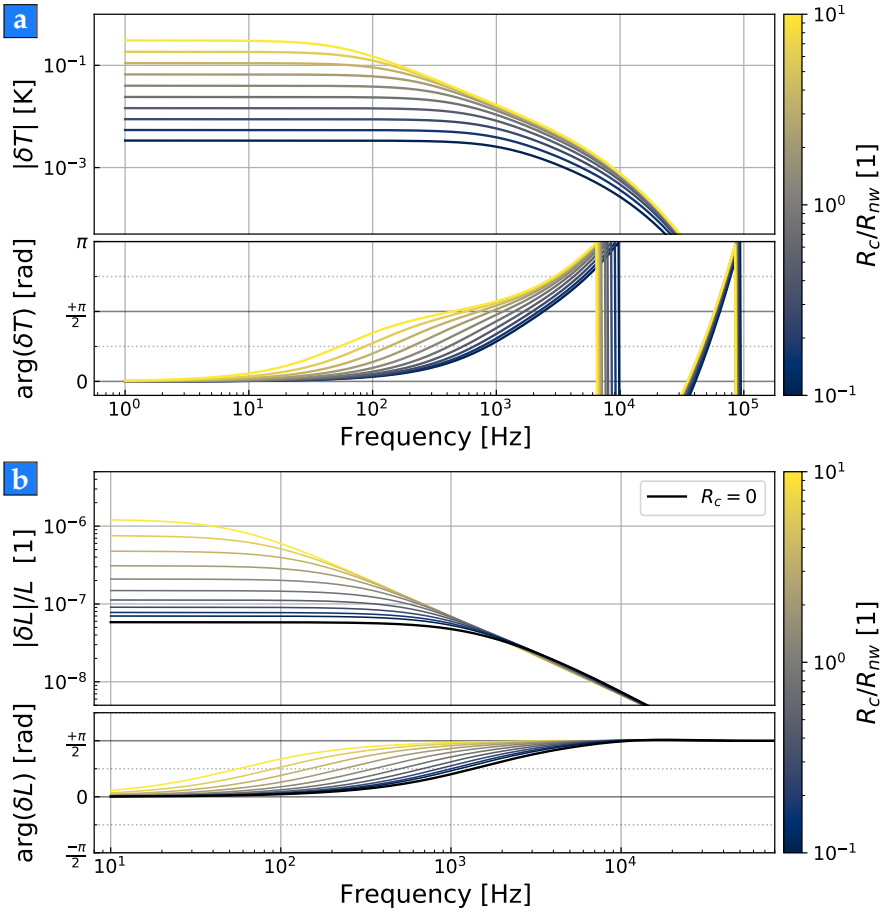

Figure 5.12: (a) Comparison of the static profile and the spectral responses for various contact resistance at the clamping. We computed those responses for an absorbed average pump optical power of $P_{\text{abs}} = 0.01\,\mu\text{W}$ while modulating at $\delta P_{\text{abs}} = 0.5\,P_{\text{abs}}$. The considered nanowire conductivity is $\kappa = 320\,\text{W.K}^{-1}.\text{m}^{-1}$, its length is $200\,\mu\text{m}$ and its diameter 180 nm. This gives $R_{\text{nw}} = 6\,\text{K}/\mu\text{W}$. (b) Evolution of the elongation response to an optical intensity modulation with varying contact thermal resistances.

Considering the effect of a thermal contact resistance on the nanowire elongation, the static and the modulated response are given by,

$$\Delta L(y_{\text{probe}}, y_0) = \frac{\alpha}{2}\, y_{\text{probe}}^2\, s_0 + \alpha (y_{\text{probe}} - y_0)\, y_0\, s_0 + \alpha\, R_c\, S\, s_0\, y_{\text{probe}}, \tag{5.27}$$

$$\delta L[\Omega](y_{\text{probe}}, y_0) = \alpha\, \frac{\delta s_0}{2\,\beta^2\,\kappa} \left[\frac{2\,\cosh(\beta\,(y_L - y_0))}{((1+u)\,e^{\beta\, y_L} + (1-u)\,e^{-\beta\, y_L})} \left((1+u)\,e^{\beta\, y_{\text{probe}}} + (1-u)\,e^{-\beta\, y_{\text{probe}}} - 2 \right) \right.$$
$$\left. - \Theta(y_{\text{probe}} - y_0) \left(e^{\beta\,(y_{\text{probe}} - y_0)} + e^{-\beta\,(y_{\text{probe}} - y_0)} - 2 \right) \right]. \tag{5.28}$$

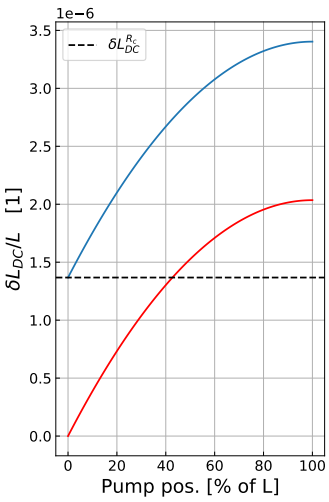

Figure 5.13: Evolution of the DC plateau of the elongation response to an optical intensity modulation while moving the pump position along the nanowire. We compare the cases when there is no thermal contact resistance (red line) contrary to when we consider a contact resistance (blue line). We chose $R_c = R_{\mathrm{nw}}/3$ in these simulations.

Proceeding similarly to the previous section 5.1, we express the response behaviour in the DC limit and get at first approximation,

$$\delta L[\Omega](L, y_0) = \frac{\delta L_{\mathrm{DC}}(y_0)}{1 + i\,\frac{\Omega}{\Omega_c}}, \tag{5.29}$$

with the new DC limit, $\delta L_{\mathrm{DC}}(y_0) = \frac{\alpha}{2}\,\frac{\delta s_0}{\kappa}\left(2\,L\,y_0 - y_0^2 + 2\,\frac{R_c}{R_{\mathrm{nw}}}\,L^2\right)$, and the reduced cutoff frequency $\Omega_c = \frac{\kappa}{\rho\,C_p}\,\frac{2}{L^2}\,\frac{1}{(1+2\,\frac{R_c}{R_{\mathrm{nw}}})}$. This DC limit profile when moving the pump position, is interesting as it can be a non-destructive measure of the thermal contact resistance between the nanowire clamping at the heat sink, see Fig. 5.13. However, as seen in sec. 5.1.2, the heterogeneity of the absorption along the nanowire makes such measurement unreliable.

On the other hand, the measurement of the cutoff frequency as an estimation of the heat diffusion coefficient, leads us to define the reduced diffusion coefficient,

$$D_{\mathrm{Rc}} = D/(1 + 2\,\frac{R_c}{R_{\mathrm{nw}}}), \tag{5.30}$$

where $D = \kappa/(\rho\,C_p)$ is the bulk value. This effective coefficient is indeed lower than the bulk one, which is in accordance with our measurements. Consequently, the expression of the effective thermal cutoff can be expressed as,

$$\Omega_c^{-1} = L^2/(2\,D) + L\,R_c\,\kappa/(D\,S), \tag{5.31}$$

which is the sum of two contributions as represented in Fig. 5.10b: a quadratic one corresponding to the expected trend without the contact resistance (orange line), and a linear contribution due to the poor thermal contact (green line), the sum (black line) fits well the measured data.

One can define the equivalent nanowire length, $L_c = R_c\,\kappa\,\pi\,R^2$, that would be the length of the nanowire so that its thermal resistance equates the contact resistance. The more the nanowire's length is larger than L_c, the less we are sensitive to the thermal contact. Assuming the quality of the contact is roughly the same across our nanowires, this explains the increase of the measured effective diffusion coefficient with the length of the nanowire. Still, the impact of the thermal contact is important. If one wonders what would be the length of the nanowire such that the direct measurement of the thermal cutoff makes an ϵ relative error to the cutoff without thermal contact resistance, this length would be, $L_\epsilon = 2\,L_c\,\left(\frac{1-\epsilon}{\epsilon}\right)$. Meaning that considering the thermal resistance found for the nanowire presented in Fig. 5.10b, to achieve a maximum of 10% error of the internal diffusion coefficient, we would require a nanowire that is 1.2 mm long.

5.3 Thermal lateral deformation

In this section we study the thermal effect responsible for the observed lateral deformation of the nanowire, when modulating the pump intensity. Up to now we measured the longitudinal expansion of the nanowires with temperature. However, when measuring force fields at nanoscales, we measure the lateral displacement of the nanowire tip.

In the cryostat experimental setup, we implemented an interferometric readout. We already observed that the low frequency response can be attributed to a modulation of the local nanowire reflectivity, see sec. 4.4. However, this is not always the case. The following measurements present the broadband response of the lateral displacement of a nanowire of length 200 μm and diameter 180 nm. Upon measuring the low frequency response along the readout interference pattern, we observed no offset of the DC responses with respect to the radiation pressure one. To further discriminate if the low frequency signal corresponds to a photothermal deformation or to a reflectivity phase change, we conducted an experiment where we switched the green and red lasers on each objective as illustrated in Fig. 5.14a. In that situation, the reflectivity phase changes should remain identical from the probe laser perspective while the deformations, if due to a photothermal deformation, should remain in the same direction, defined by the clamping geometry. The radiation pressure drive should also be inverted, upon switching the laser injection. Thus, when considering the nanowire position on the same interference pattern slope, with respect to the piezo axis, the sign of the response should follow as depicted in Fig. 5.14a depending on the contribution at play.

Figure 5.14b shows the broadband responses measurements taken in the two configurations of the lasers, for positive and negative interference slopes in each configuration. It shows that for configuration 2, the low frequency and the resonant responses are in phase opposition (one can compare the low frequency phase response and the phase response just on the left of the mechanical resonance). This explains why the total signal gets reduced at low frequencies. On the other hand, in configuration 1, the two contributions are in phase, thus leading to a coherent increase of the response at low frequency.

As a conclusion, the low frequency response is thus dominated by the photothermal effect whose direction does not depend on the pump laser orientation, as expected for a deformation mechanism dominated by the clamping geometry, being due to a bilayer or to a thermostriction effect. This mechanism thus allows to indirectly probe the temperature modulation at the nanowire clamping point. We will use this feature to obtain pieces of information on the heat propagation within the nanowire.

Thermomechanical deformations are a consequence of the interplay between the temperature field and the material deformations. The relation between temperature changes and deformations is determined by the constitutive equation of continuous material [50],

$$\sigma_{ij} = -\frac{E}{1-2\nu}\,\alpha_{\mathrm{SiC}}\,\Delta T\,\delta_{ij} + \lambda\,\epsilon_{ll}\,\delta_{ij} + 2\mu\,\epsilon_{ij}, \tag{5.32}$$

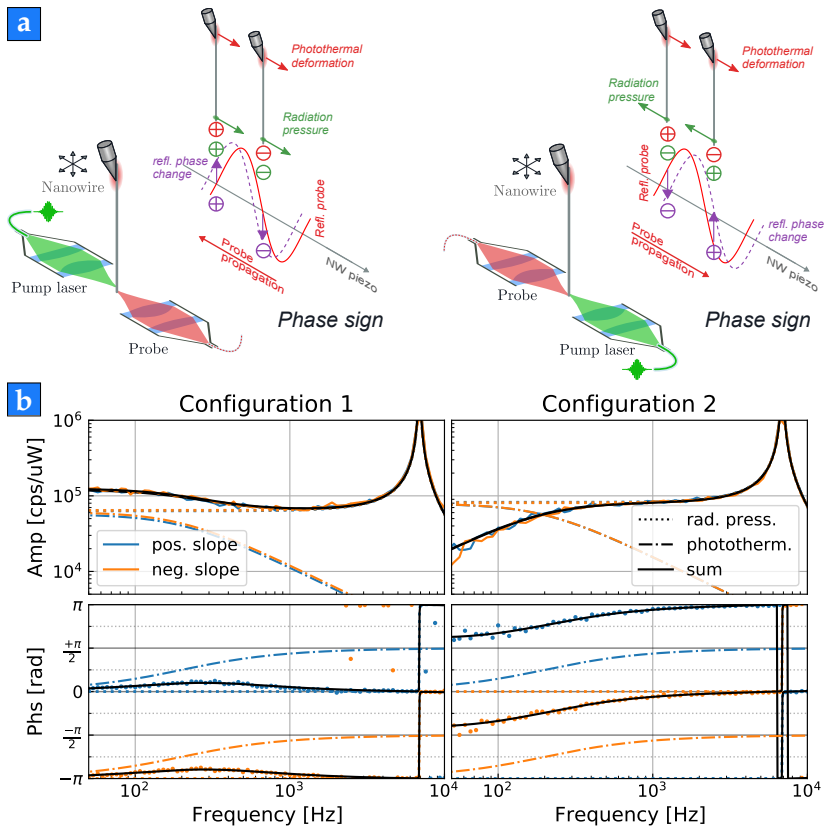

Figure 5.14: (a) Experimental scheme employed to discriminate thermally induced reflectivity phase changes and photothermal deformations. (b) Response measurements realised in the two configurations of the pump-probe setup : the resonant response is dominated by the radiation pressure and serves as a reference. The low frequency photothermal response changes its response sign with respect to the radiation pressure.

where σ is the stress tensor, $\epsilon_{ij} = \frac{1}{2}(\partial_j u_i + \partial_i u_j)$ is the strain tensor associated by the displacement vector field $\mathbf{u}$, λ and μ refer to the Lamé coefficients, E and ν are the Young modulus and the Poisson coefficient respectively, while α is the thermal expansion coefficient of the material. This equation couples to the heat diffusion equation that establishes the temperature profile inside the material,

$$\rho\, C_p\, \partial_t T - \boldsymbol{\nabla}\,(\kappa\, \boldsymbol{\nabla} T) = \frac{E}{1-2\nu}\, \alpha_{\mathrm{SiC}}\, \Delta T\, \partial_t \epsilon_{ij}. \tag{5.33}$$

It results in a system of coupled differential equations that are not in general analytically solvable for complex geometries. In the following we choose to implement numerical simulations in order to model and better understand the deformation at the clamping.

Considering our experimental configuration, a thermal wave propagating inside the nanowire and reaching its support will be able to generate a deformation of the nanowire through two mechanisms : a bilayer effect (since the nanowire and the tungsten tip do not present the same thermal expansion mechanism) and a thermostrictive one (originating from temperature lateral inhomogeneities in the nanowire and in the support). In view of the clamping area shown in the SEM image of Fig. 5.20a one understands that the correct description of the photothermal effects may be complex. We will nonetheless try to further precise the origins of the photothermal lateral actuation in the following section.

5.4 Profile structure of the low frequency lateral deformation response

We continue the analysis of the thermal deformation observed in the above section, sec. 5.3. This deformation can be understood as an equivalent forcing drive acting along the nanowire. We denote $\mathbf{F}_{\text{th,n}}$ the resulting apparent force that drives the considered mechanical mode family n. At room temperature, the main contribution to the nanowire lateral displacement upon modulating the intensity of a green laser at 515 nm, are the radiation pressure and such thermo-mechanical force. Considering the modal development, the total dis-

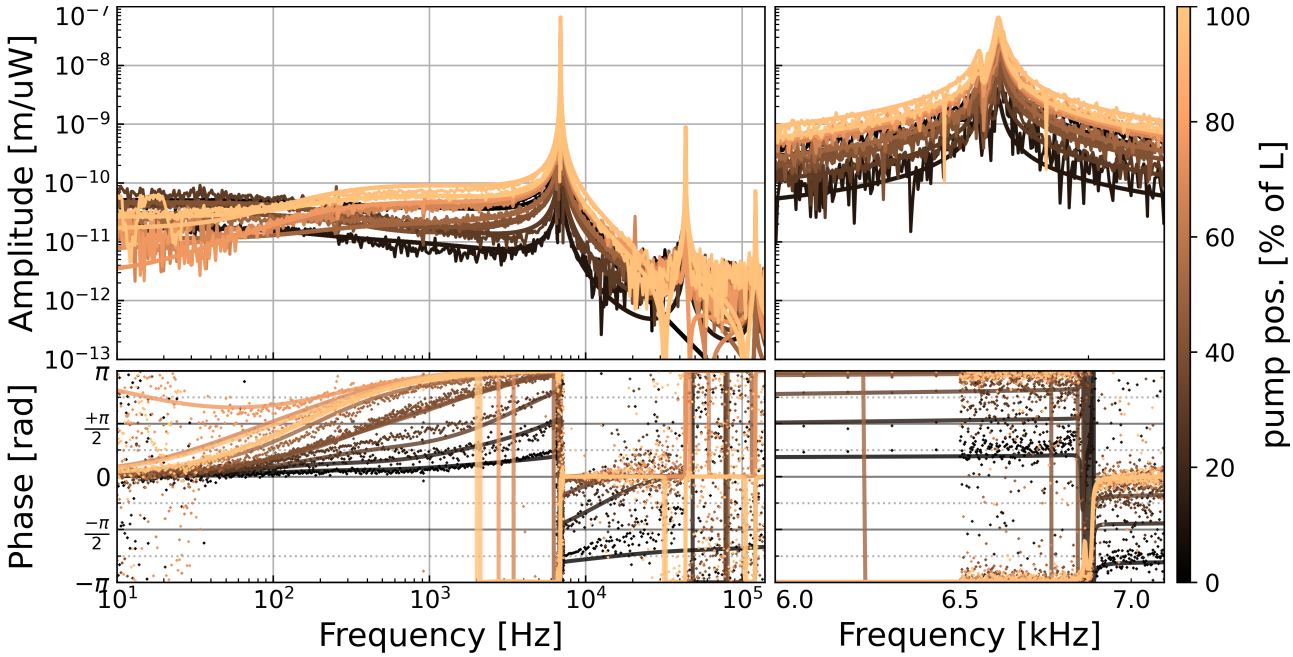

Figure 5.15: Broadband response measurements of the lateral deformation of the vibrating tip of the nanowire, at different pump laser position (left panels). (Right panels) Response measurement zoomed around the first resonance family of the nanowire. In solid lines are the fitted model of the data, using the model described in the present section. On the broadband measurements, one can identify the three first resonant mode families. The amplitude measurements are expressed in displacement per unit of μW injected pumping optical power.

placement measured along the measurement vector, $\mathbf{e}_\beta$, is modelled with,

$$\delta r_\beta[\Omega] = \mathbf{e}_\beta \cdot \sum_n u_n(y_{\text{probe}})\, \underline{\underline{\chi}}_n[\Omega] \cdot \big[F_{\text{rad}}\, u_n(y_{\text{pump}})\, \mathbf{e}_F + F_{\text{th,n}}[\Omega](y_{\text{pump}})\, \mathbf{e}_{\text{th,n}}\big] \tag{5.34}$$

where u_n is the normal mechanical modes, F_{rad}, $F_{\text{th,n}}$ are the amplitude of the radiation pressure and the thermomechanical effective force associated to the mode n respectively, and $\underline{\underline{\chi}}_n$ is the n-th mode effective susceptibility such as,

$$\underline{\underline{\chi}}_n[\Omega] = \frac{1}{M_{\text{eff}}} \left[\frac{\mathbf{e}_1}{(\Omega_{n,1}^2 - \Omega^2) - i\,\Omega\,\Gamma_{n,1}} + \frac{\mathbf{e}_2}{(\Omega_{n,2}^2 - \Omega^2) - i\,\Omega\,\Gamma_{n,2}} \right], \tag{5.35}$$

where $\Omega_{n,i}$, $\Gamma_{n,i}$ are the mechanical polarisation resonant frequency and damping of the n-th mode, respectively.

In Figure 5.15 we show the broadband and the zoomed responses of the tip lateral displacement with the modulation of the optical pump power, at different pump positions along the nanowire. When the pump position is close to the nanowire tip, the low frequency part the response shows the coherent subtraction of the DC response of the radiation pressure with the contribution of the thermomechanical deformation. On the other hand, close to the clamping, the thermal actuation becomes the dominant contribution at low frequency as well as at resonance, since the phase at resonance is no longer aligned with an instantaneous force. Still, the radiation pressure is the dominant drive at the different resonant family for most of the nanowire length. This allows us to calibrate the pump position, by comparing the driving efficient of the radiation pressure between the mode families at resonances which depends on the position of the pump along the normal modes. The positioning with radiation pressure compensate the unreliability of the attoCube steppers.

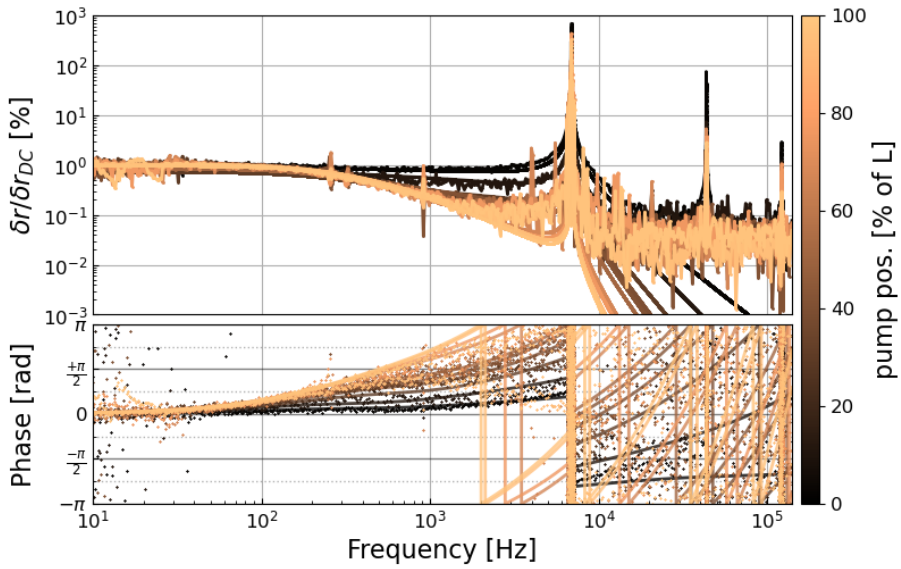

Figure 5.16: Broadband response measurement of the lateral deformation of the nanowire vibrating tip, with the radiation pressure removed. We normalised the responses amplitude to their DC value.

The resonant mode families allow us to fit the radiation pressure contribution to the broadband response. We then remove this contribution to reveal the spectral profile of the thermal actuation. The DC level of the thermal responses has been set to unity, because the amplitude value of the DC response is dependent on the local absorption under the pump, which was not calibrated for this nanowire. Figure 5.16 shows the broadband response profile of the thermal contribution in the lateral displacement of the nanowire tip. It was obtained by the deconvolution of the radiation pressure response contribution from the measured response. The amplitude and phase evolution with the pump position is similar to the phase of the temperature response close to the clamping. This behaviour is coherent with the assumption that the thermal deformation take place at the clamping of the nanowire. In the following section, we will present how strains and thermal gradients can generate the measured responses.

In Figure 5.17 we show the fitting method of the broadband response when the pump is placed at the tip. The resulting displacement response (black line) is the sum of the response to an optical drive (due to the radiation pressure) with the response to a thermal deformation acting as a force drive due to the temperature modulation at the clamping. The thermal drive is then modelled as an effective force proportional to the temperature modulation at the clamping,

$$\mathbf{F}_{\text{th,n}} = C_n \, \delta T[\Omega](y_{\text{th}}, y_0) \, \mathbf{e}_{\text{th,n}}, \tag{5.36}$$

where $\delta T[\Omega]$ is the temperature response described by a 1D diffusion model (see sec. 4.5), y_0 is the pump position, y_{th} is the position where we evaluate the temperature (in this case close to zero), C_n the actuation coefficient in [N/K], and $\mathbf{e}_{\text{th,n}}$ the direction of the effective force. This fitting model captures well the spectral phase structure when moving the heat source position. While the radiation pressure dominates the nanowire driving mechanism at resonance, at low frequency the thermal actuation catches up to the DC plateau of the radiation pressure. Note that between 10 and 50 Hz, there is an additional coherent response. We attribute this response to a dynamic of the tungsten that adds to the low frequency dynamic of the nanowire lateral deformation. At those frequencies, the thermal waves are large enough to penetrate the tungsten tip.

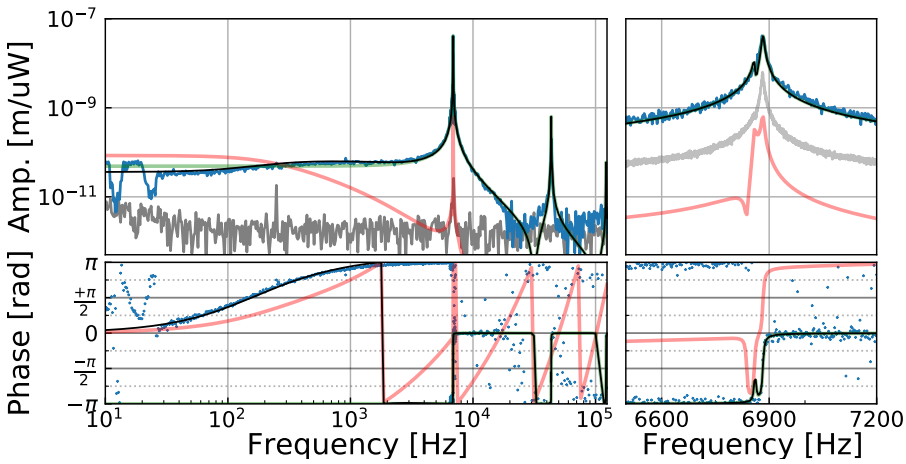

Figure 5.17: Fitting of the broadband response (left panels) and the zoomed response around the first mode family (right panels), when the pump laser is at the tip. In this measurement, the driving contribution at the first resonant mode families is the radiation pressure (see zoomed panel), which allows fixing the amplitude of the radiation pressure (green line). We then adjust the contribution of the thermal effective force (red line) so that the total response (black line) best fits the broadband data. The light grey data in the zoom panels, is the motion noise measured with the SA.

In Figure 5.18, we show the evolution of the response fitting parameters with the pump position. Regarding the equivalent forces at the first resonance, the amplitude of the radiation pressure force follows the expected behaviours for a constant pressure acting along the amplitude profile of the resonant normal mode. The fitted value is $F_{\text{rad}} = 5 \times 10^{-17}\,\text{N}/\mu\text{W}$, which in a naive model of the radiation pressure against a mirror of reflectivity r_{nw}, gives an equivalent reflectivity value of $r_{\text{nw}} \simeq 0.13$ with $F_{\text{rad}} = r_{\text{nw}}^2 \, 1\mu\text{W}/c$, c being the light celerity. This value is in accordance with the expected one for our nanowires. The thermal contribution amplitude of the thermal drive increases as the heat source gets closer to the clamping, and becomes dominant below a third of the nanowire length. Still the dispersion in the absolute value of the thermal actuation is most likely to be caused by the heterogeneity in the local absorption.

The global diffusion coefficient is relatively at $D \simeq 22 \pm 1 \times 10^{-6}\,\mathrm{m}^2.\mathrm{s}^{-1}$, which is lower than the bulk value, but consistent with the fact we did not account for a thermal contact resistance. The DC value of the displacement is roughly constant and is of the same order of magnitude than the DC displacement of the radiation pressure modulation.

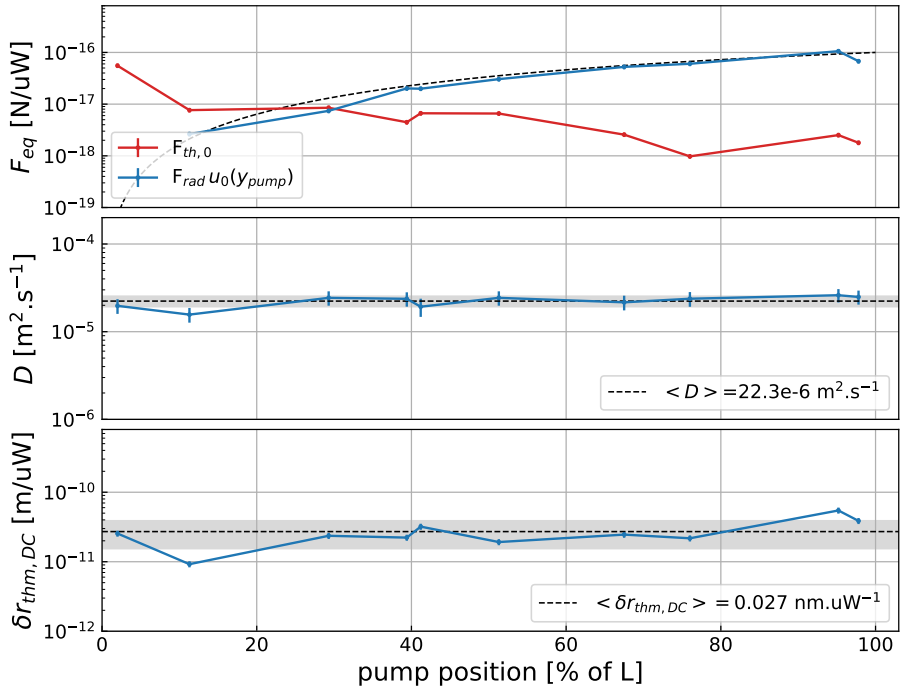

Figure 5.18: Evolution of the fitting parameters in the displacement response model showed in eq. (5.34), upon scanning the pump position. We fitted the data showed in Fig. 5.15, where the dominant contribution are the thermally induced deformation at the clamping area and the radiation pressure, at room temperature.

In the following section we will model and simulate the thermal effects that can generate such lateral deformation when the heat generated by the pump optical power absorption is modulated.

5.5 Modelling of the thermomechanical effect at the clamping

In this section we make use of numerical simulation in order to understand the mechanisms at play that generate a thermal displacement of the nanowire tip when modulating the heat source placed under the pump laser waist. The thermomechanical deformation is localised at the clamping area, and one can attribute this effect to two main contributions: a bilayer effect and a thermostrictive one.

Bilayer effect

Bilayer effect appears when two materials with different thermal expansion coefficients are clamped together. One can observe a lateral deformation consecutive to a temperature change. This effect, first studied by Stoney [124] in a phenomenological way, has been useful to build thermostats [125], converting a temperature change into a measurable deformation. This effect is well known in the cantilever AFM

(Atomic Force Microscopy) community and is at the base of several actuation mechanisms for such systems [126, 127, 128].

In the case of our suspended nanowires the bilayer mechanism arises at the clamping point, where only one side of the nanowire is connected to the tungsten tip. Unfortunately, it strongly depends on the nanowire-tungsten tip clamping geometry, which is not perfectly controlled in our preparation method and its magnitude must be calibrated for each nanowire. We also note that the lateral deformation caused by the bilayer effect is typically 10 times smaller than the elongation effect. In order to separate the different effects, it will be important to operate with rather straight nanowires and by trying to adjust the measurement vectors to be perpendicular or aligned with their axis. To estimate the magnitude of the bilayer effect as well as its sensitivity to the clamping geometry, we developed COMSOL simulations [129], as shown in Fig. 5.20.

At the interface between the tungsten tip and the 3C-SiC nanowire, the stress generated by the difference of thermal expansion coefficient (typically $\alpha_{SiC} = 3.8 \times 10^{-6}\,K^{-1}$ and $\alpha_W = 4.5 \times 10^{-6}\,K^{-1}$) will accumulate to generate a moment that will bend the base of the nanowire. This results in a static deformation profile, which linearly increases with the distance to the clamping point. Furthermore, the numerical simulations confirm the temperature profile inside the nanowire corresponds well to a 1D diffusion profile with no heat dissipation, except at the clamping area playing the role of a heat sink.

Thermostriction

When the temperature within the nanowire cross-section is non-homogeneous, this will cause a lateral mechanical deformation of the nanowire. The regions where this mechanism may occur are:

- under the pump laser spot because the optical intensity profile within the nanowire is not homogeneous,
- at the clamping point because one side of the nanowire is directly connected to the tip and thus more efficiently cooled,
- if there are defects on the nanowire surface, which may modify the temperature profile across the cross-section.

In other areas, the temperature profile across the nanowire cross-section can be assumed being quasi homogeneous. Indeed, the characteristic time of the thermal propagation across our 3C-SiC nanowire is $\tau_{thm} = \frac{R^2}{D} \simeq 10\,ns$ at room temperature, with $D \simeq 4 \times 10^{-5}\,m^2.s^{-1}$ the diffusion coefficient and R the nanowire radius. This corresponds to response in the 100 MHz range, which falls beyond the detection bandwidth of our detectors. In the clamping area, a small temperature gradient appears as the base of the nanowire thermalises to the temperature of the tungsten tip, see Fig. 5.20b. This generates an internal thermal stress inside the nanowire, causing a static deformation in the same direction to the temperature gradient. In addition, the tungsten support may also contribute to the photothermal response of the nanowire via internal temperature gradients. However, the heat conductance of the tip is way larger than the one of the nanowire,

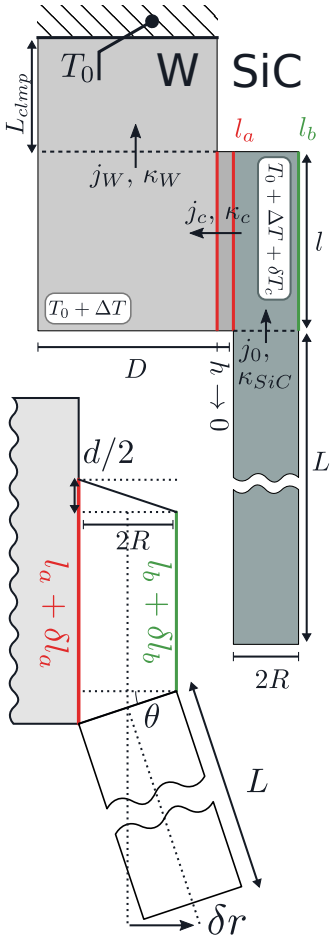

Figure 5.19: Geometrical model for thermomechanical deformation. We introduce a thin layer of thermal resistive material that models the contact resistance between the nanowire and the tungsten support. In this scheme, L_{clmp} is the distance between the fixed bath temperature, T_0, and the clamping area, D the clamp diameter, h the infinitesimal thickness of the resistive layer, κ_W, κ_c, κ_{SiC} the tungsten, contact layer and nanowire conductivity and j_W, j_c, j_{SiC} their respective heat flux, L the length of the nanowire and R its radius. We also introduced d as the length expansion difference between the face of the nanowire clamped to the tungsten and the free one.

meaning that it will not be possible to generate significant temperature gradients within the support. Also, this response is expected to play a role only at very low frequencies, when the thermal wave has time to reach the nanowire support, which does not fall in the measurement frequency span we employed.

Simplified model

In a simplified deformation model, as shown in Fig. 5.19, the nanowire tip lateral displacement stems from the length expansion difference due to thermal deformation between the length of the nanowire surface in contact with the clamp, l_a, and the length of the opposite free surface, l_b. Considering the approximation that the temperature is homogeneous in sections close to the clamping area, one can relate the nanowire tip displacement to the temperatures at the clamping with the expression,

$$\delta r = \frac{L}{4\,R}\, l\, \left[(\alpha_{\text{W}} - \alpha_{\text{SiC}})\,\Delta T - \alpha_{\text{SiC}}\,\delta T_c\right], \tag{5.37}$$

where α_{W} and α_{SiC} are the thermal expansion coefficients of the tungsten and nanowire respectively, ΔT the temperature difference between the cryostat temperature T_0 and the tungsten at the clamping area, L and R are the length and radius of the nanowire respectively, $\delta T_c = R_c\, j_c\, S$ is the temperature offset between the tungsten support and the nanowire resulting from a thermal contact resistance with R_c the thermal resistance in [K.W^{-1}], j_c the heat flux across the contact and S the surface of the contact. By neglecting the heat loss by radiation, one can link the different temperatures offset with the conservation of the heat rate, such that we have $\delta T_c = R_c/R_W\,\Delta T$, where $R_W = L_{\text{clmp}}/(\kappa_W\,\pi\,D^2/4)$ and $R_c = h/(\kappa_c\, l_a\, 2R)$ are the thermal resistance of the tungsten tip and the contact respectively. In the end, the tip displacement can be expressed only in terms of the temperature increase ΔT, such as $\delta r = C\,\Delta T$, with C the actuation coefficient in [m.K^{-1}].

Although very simplistic, we can draw some conclusions from the model. If the contact resistance is null, only the difference between the thermal expansion coefficient of the nanowire and the tungsten will generate a displacement, this is a pure bilayer effect that generates a bending of the nanowire toward the opposite side of the nanowire-tungsten interface (the direction of deformation being determined by the sign of the thermal expansion difference). On the other hand, if the two expansion coefficients are equal, it is the temperature gradient between the nanowire and the tungsten (here due to a thermal contact resistance) that will generate a displacement, this is a pure thermostrictive effect that generates a bending in the direction of the thermal gradient, *i.e* toward the interface.

When cumulating both, one can wonder for which thermal contact resistance the two effects compensate. One can estimate the thermal contact resistance for which the displacement is null, R_c^{eq}. Considering the energy conservation in the stationary case, we get,

$$R_c^{\text{eq}} = \frac{(\alpha_{\text{W}} - \alpha_{\text{SiC}})}{\alpha_{\text{SiC}}}\,\frac{R_W}{\kappa_W}. \tag{5.38}$$

By comparison the thermal resistance of the full nanowire is given by $R_{\mathrm{nw}} = L/(\kappa_{\mathrm{SiC}}\,\pi\,R^2)$, which is typically in the order of several K.μW^{-1}. The ratio gives,

$$\frac{R_c^{\mathrm{eq}}}{R_{\mathrm{nw}}} = 4\,\frac{(\alpha_{\mathrm{W}} - \alpha_{\mathrm{SiC}})}{\alpha_{\mathrm{SiC}}}\,\frac{\kappa_{\mathrm{SiC}}}{\kappa_{\mathrm{W}}}\,\frac{L_{\mathrm{clmp}}}{L}\,\frac{R^2}{D^2}. \tag{5.39}$$

Putting some number as in Table. 5.1, we get $R_c^{\mathrm{eq}} \simeq 0.018$ K.μW^{-1}, which corresponds to 0.3% of R_{nw}.

Notation	Value
α_{SiC}	3.8×10^{-6} [K^{-1}]
α_{W}	4.5×10^{-6} [K^{-1}]
κ_{SiC}	320 [W.m^{-1}.K^{-1}]
κ_{W}	164 [W.m^{-1}.K^{-1}]
L	200 [μm]
L_{clmp}	50 [μm]
R	180 [nm]
D	2 [μm]

Table 5.1: Expect order of magnitude of the parameters involved in the simplified model.

ComSol simulations

We implemented a numerical simulation using ComSol software [129], defining a simple 2D model as shown in Fig. 5.20a. The 2D simulation accounts for a square nanowire of length 200 μm and height 180 nm, corresponding to the dimensions of the nanowire used in the lateral deformation response measurements. The clamping area is modelled by a square for simplification, without changing the physics. We also

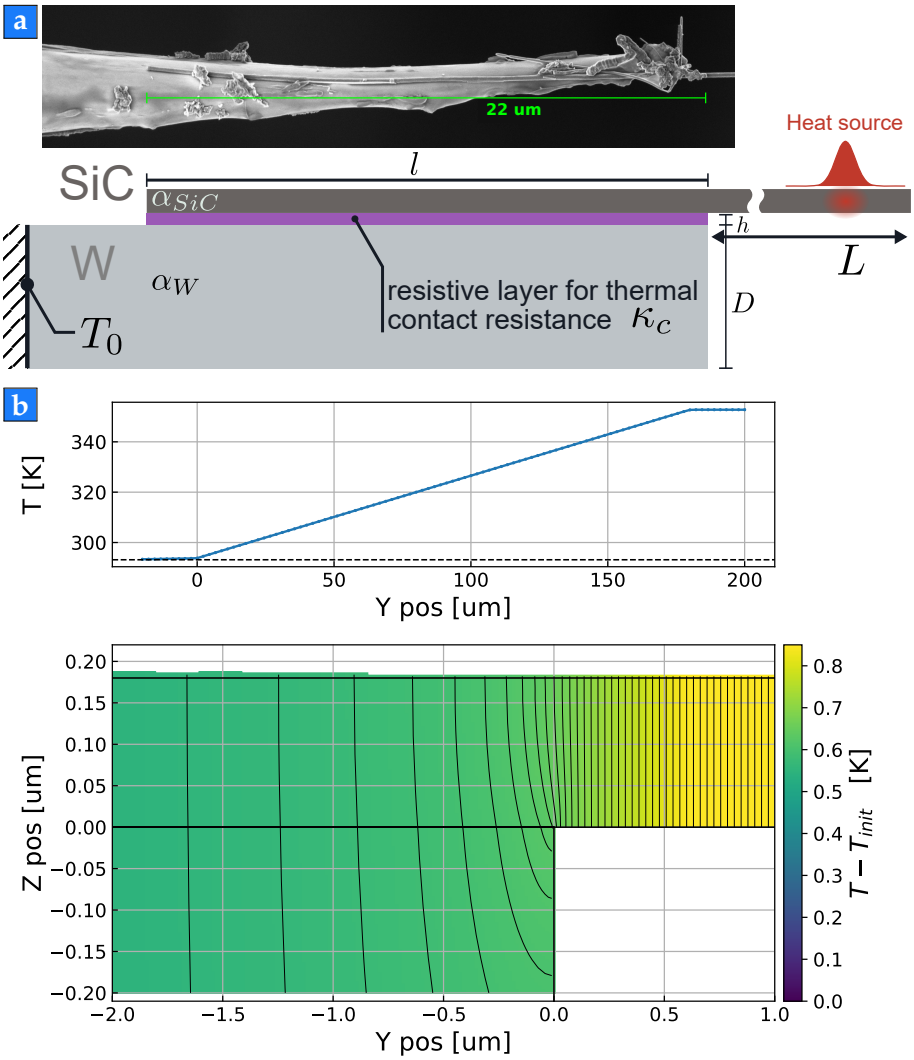

Figure 5.20: COMSOL simulation of the static deformation caused by a Bilayer effect at the clamping. (a) SEM picture of the clamping area and of its simplified modelling (lower panel). (b) Temperature profile when applying a heat source at 50% of the nanowire length, as well as the temperature gradient near the clamping.

implemented a contact thermal resistance layer between the nanowire

and the tungsten to account for several contributions in the low controlled clamping of the nanowire. To avoid additional complexity, the resistive layer has the same properties than the tungsten (especially for the thermal expansion coefficient), except for the conductivity which is our control parameter to set the wanted thermal resistance. In order to render thermally induced deformation, we used the thermal physics coupled to the elastic deformation physics module in the software. The tungsten left boundary is fixed in position as well as in temperature T_{bath}, which plays the role of the temperature sink. We set the reference temperature to be the room temperature, which defines the resting position of the nanowire and the tungsten support without any deformation. The heating by a pump laser is implemented with an internal heat source with a gaussian profile along the nanowire axis. The heat source amplitude in taken to be $q_{\text{source}} = P_{\text{abs}}/(\pi R^2)$, where P_{abs} is the absorbed pump optical power taken to be 1 μW.

Running a simulation in the static case, see Fig. 5.20b, the temperature along the nanowire is as expected from a 1D heat diffusion, and we observe small temperature gradient across the clamping area throughout small regions compared to the nanowire radius.

Response to a heat modulation

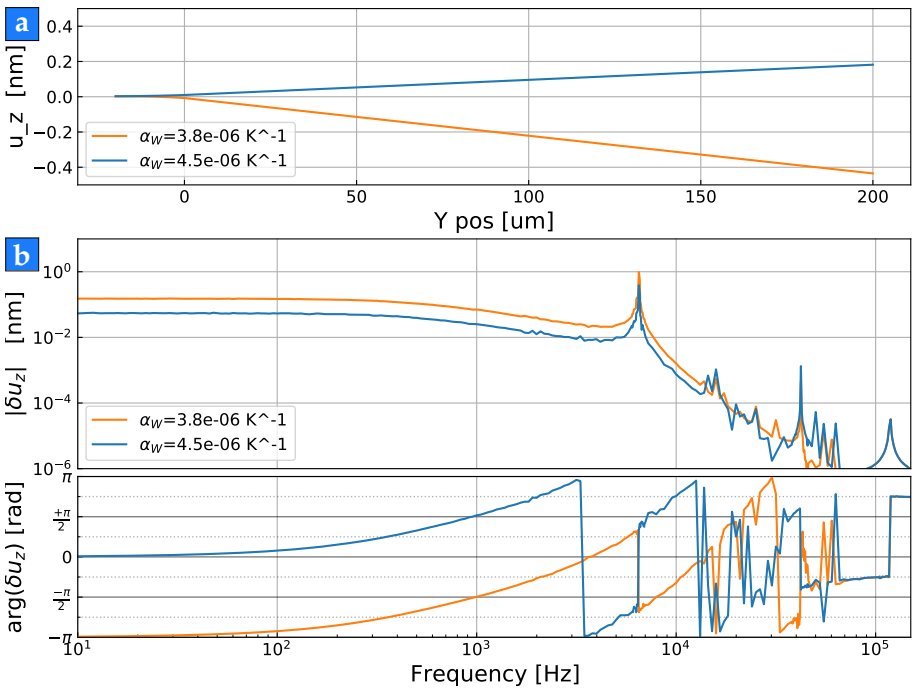

Figure 5.21: (a) Stationary deformation profile in the case where we equate the tungsten thermal expansion coefficient to the nanowire one (orange solid line), and when the two thermal expansion coefficients are not equal (blue solid line). (b) Broadband response to a heat power modulation for two values of the tungsten thermal expansion coefficient, where $\alpha_W \neq \alpha_{SiC}$ (blue line) and $\alpha_W = \alpha_{SiC}$ (orange line).

We want to reproduce the broadband response measurements, we thus make use of the harmonic perturbation module of the COMSOL software. To evaluate the relative strength of the bilayer and thermostriction mechanisms, we ran several numerical simulations as shown in Fig. 5.21. Changing the value of the thermal expansion coefficient of the tungsten we can change the dominant mechanism between two contributions. When no contact resistance is accounted,

the bilayer deformation dominates when both effects are present in the simulation (blue curve in Fig. 5.21).

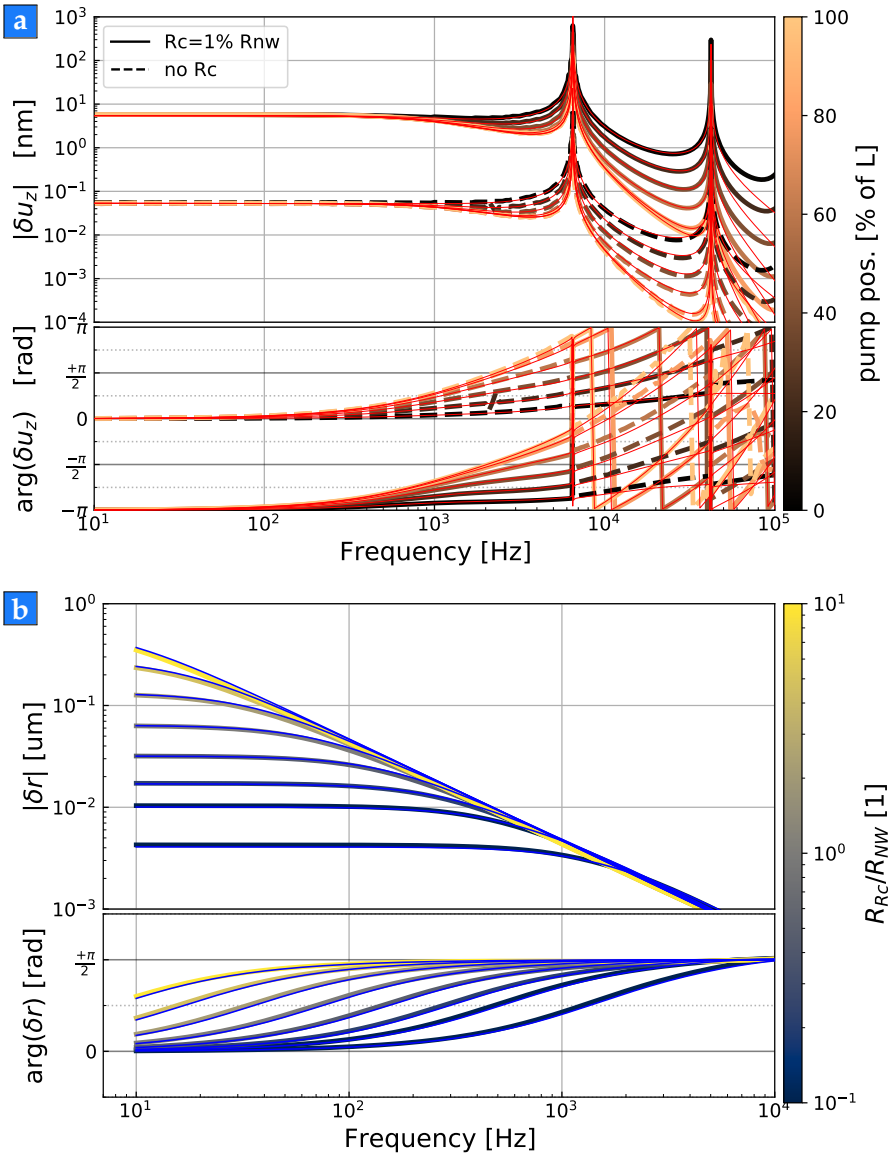

Figure 5.22: COMSOL simulation of the static deformation caused by a Bilayer effect at the clamping. (a) Broadband response ComSol simulation of the tip lateral displacement when scanning the heat source position. The red lines are the models of such response by convoluting the time response of the temperature at the clamping area to the mechanical response of the nanowire. (b) Elongation response profile when varying the contact resistance of the layer between the tungsten and the nanowire. In blue the theoretical elongation response in the 1D model, when accounting for the same contact resistance at the clamping.

However, when setting a thermal contact resistance, the deformation due to the relative expansion between the nanowire and the tungsten tip caused by the resistive temperature offset, dominates even for low value of R_c, see Fig. 5.22a. Still in both case (with and without a resistive layer between the nanowire and the tungsten), the tip lateral displacement response to a heat source modulation is well-fitted by convoluting the temperature response at the clamping ($Y \simeq 0$) with the mechanical susceptibility of the nanowire. Meaning the measurement of the lateral thermal deformation at the tip of the nanowire gives a good estimation of the temperature response at the base of the nanowire. On top of that, the effect of placing a thin layer between the nanowire and the tungsten, is equivalent to set a thermal contact resistance in the 1D diffusion model. Indeed, in Fig. 5.22b we show the simulated longitudinal displacement response for varying thermal resistance of the resistive layer, while superimposing the

theoretical elongation response with the same thermal resistance (in blue). Those simulations, that account for the geometrical complexity of thermomechanical deformation problems, validate the simple 1D diffusion model we used up to now in the description of the nanowire thermal dynamics at room temperature.

5.6 Thermal modulation of the optical cross-section

For a small nanowire behaving as an optical dipole, the optical forces are in general separated between dipolar and radiation pressures forces [90]. All optical forces linearly depend on the optical power seen by the nanowire, and on the nanowire optical response function, as well as its polarizability. In our system the optical response time constants are extremely fast with respect to the mechanical timescales, the direct optical forces are thus expected to instantaneously follow the optical modulation. A simple model to describe the radiation pressure force, $\mathbf{F}_{\text{opt}}$, applied on the nanowire consists in introducing an optical cross-section, σ_{opt}, which will depend on the nanowire refractive coefficient, on its diameter and on the Mie resonances which strongly structure the light-nanowire interaction as discussed in chap. 2. The optical force acting on a nanowire by a focused laser beam propagating along the z-axis is thus expressed as,

$$\mathbf{F}_{\text{opt}} = \sigma_{\text{opt}}(y)\,\Pi\,\mathbf{e}_z, \tag{5.40}$$

with $\Pi\,\mathbf{e}_z$ being the Poynting vector.

The optical force is localised at the waist of the pump laser, and since the laser waist is small compared to the nanowire length, the force profile can be assimilated to a point-like force, $f(y) = \delta(y - y_{\text{pump}})$, where y_{pump} is the position of the pump laser along the nanowire axis. In the modal development framework, the measured displacement for a given mechanical resonance mode generated by the optical force at a fixed probe position y_{probe} is expressed as,

$$\delta r_{n,\beta} = \mathbf{e}_\beta \cdot \chi_n \cdot \delta\mathbf{F}_{\text{opt}}\,\langle f, u_n\rangle\, u_n(y_{\text{probe}}) \tag{5.41}$$

$$= \mathbf{e}_\beta \cdot \chi_n \cdot \delta\mathbf{F}_{\text{opt}}\, u_n(y_{\text{pump}})\, u_n(y_{\text{probe}}), \tag{5.42}$$

with u_n the normal mode amplitude. The above expression shows that at a given mechanical resonance, the spectral response of such a force is convoluted with the amplitude of the eigenmode of interest. Figure 5.23 shows the expected tip displacement response to an optical drive as the sum of the resonant mode responses, when the pump laser is placed at the tip of the nanowire. One understands that the optical force is inefficient when positioned at a node of a mechanical mode or close to the clamping (as see in the measurement of the optical drive in the lateral displacement response measurements sec. 5.4).

Moreover, when the pump laser intensity is modulated, it can also induce a modulation of the optical cross-section of the nanowire through the local temperature change (the non-linear optical response

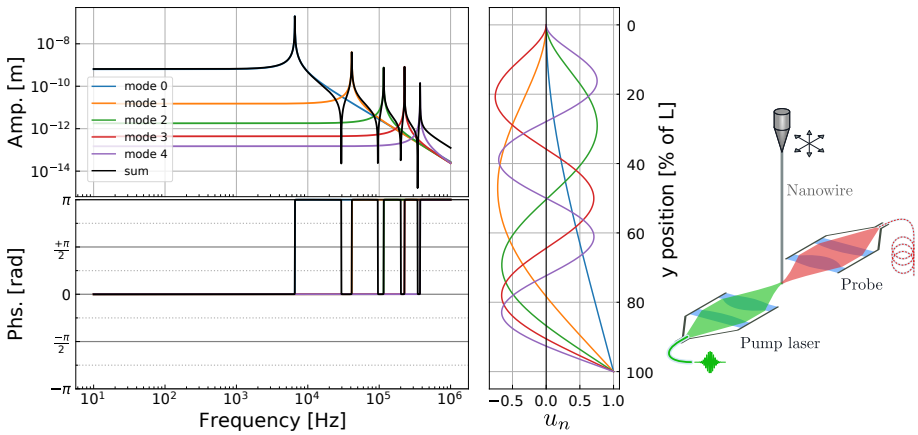

Figure 5.23: Spectral response of the nanowire to an optical force (in absence of thermally induced changes of the optical cross-section). The pump laser as well as the probe laser are located here at the vibrating tip of the nanowire. From the modal expansion, the total response is the coherent sum of the individual response of each mechanical mode, which are responsible for the cancellations in the response at certain frequencies. Here both modes are still driven, but their measured response perfectly cancels at the measurement position.

of the material, such as the Kerr effect, is in general rather weak compared to the thermally induced changes). As such the modulated optical force will be separated in two contributions: one arising from the direct modulation of the light field around the nanowire (corresponding here to a modulation of the Poynting vector, $\mathbf{\Pi}$), and one originating from the photothermal modulation of the nanowire optical cross-section, $\delta\sigma_{\text{opt}}$,

$$\delta\mathbf{F}_{\text{opt}} = \sigma_{\text{opt}}\delta\mathbf{\Pi} + \frac{\partial\sigma_{\text{opt}}}{\partial T}\frac{\partial T}{\partial P}\mathbf{\Pi}, \tag{5.43}$$

with P the optical power. The first contribution, the usual optical force without thermal effects, is oriented along the Poynting vector and is instantaneous. The second term is also oriented along the laser axis but will be delayed due to the thermalisation processes. Finally, both components of the optical force can be computed numerically, but one needs to carefully take into account the Mie resonances, which will strongly structure the light nanowire interaction. In addition, one can expect the modulation of the optical cross-section to be greatly depend on the pump wavelength, because of the Mie resonances as well as the wavelength dependence of the light absorption.

We realised several broadband responses to a modulation of the pump optical power while varying the pump laser wavelength, see Fig. 5.24. In this series of measurements we use a nanowire of length $L = 110\,\mu$m and diameter $d = 250\,$nm, placed in the vacuum measurement setup at room temperature. The low frequency response is associated to the lateral thermal deformation, and the amplitude evolution is given by the absorption colour dependency. The phase of the thermal response is consistent between the measurements. On the other hand, we observed a change of behaviour in the periphery of the first mechanical resonances, which undergo a π phase shift with the pump laser colour. While at resonance the direct optical response is always the dominant drive, at lower frequencies we shift from a highly effective thermomechanical stress at the clamping (due to efficient optical power absorption) to a cross-section modulation dominated response (due to local heating at the source). This particular transition is related to the interplay between thermal actuation and the Mie scattering that structures the cross-section modulation around a particular

optical resonance (in the case of the nanowire presented in Fig. 5.24 a resonance appears around $\lambda = 540\,\text{nm}$).

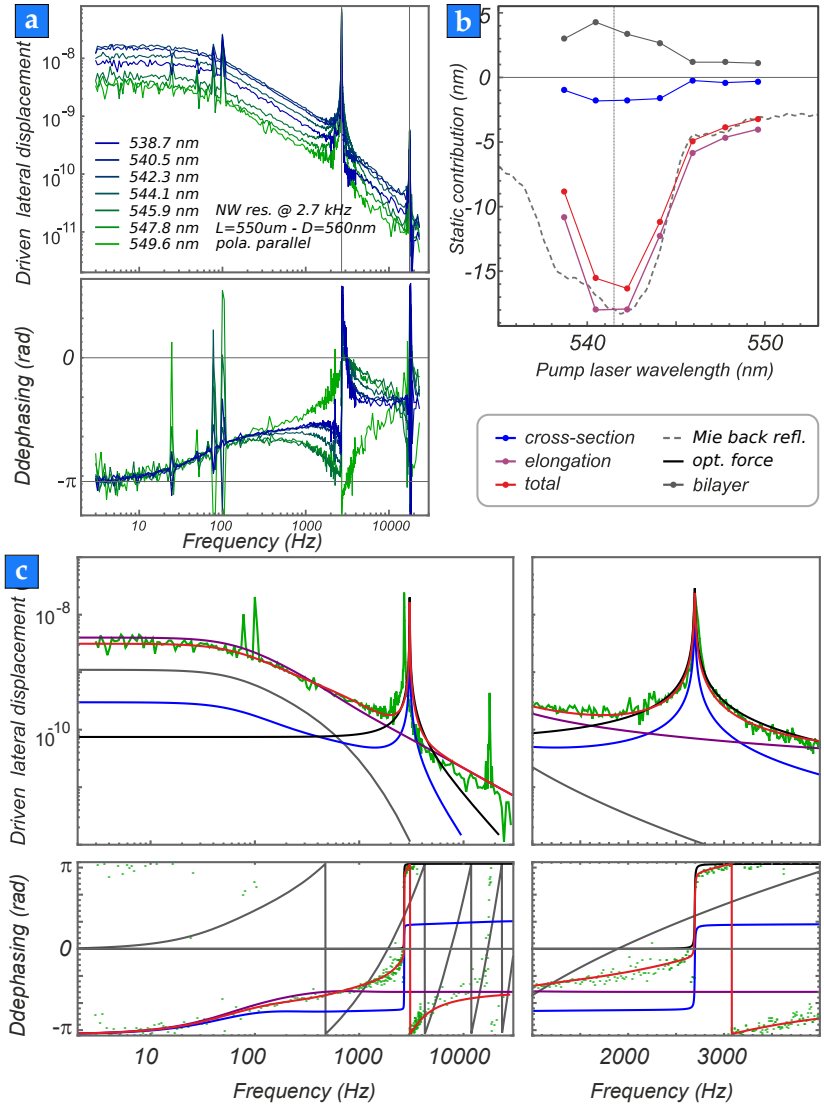

Figure 5.24: Cross-section modulation measurements. (a) Multiple response measurements of the lateral deformation of a nanowire at room temperature under a pump intensity modulation when varying the pump wavelength close to a Mie resonance. Figures (c) show examples of fitting the responses with the sum of the three contributions with the pump wavelength at 542.3 nm. (b) Analysis of the different amplitude contributions with the pump wavelength. Although the total response is dominated by the elongation response, one needs to account for a non-negligible contribution of the cross-section modulation to best fit the phase at resonance.

From our elongation measurements, see sec. 5.1, we know the local temperature increase can reach up to 10 K at room temperature for a 100 μm long nanowire illuminated at 532 nm with a 10 μW laser beam. We note that we are still sensitive to the elongation of the nanowire, although we measure the lateral deformation, because the relative position of the probe laser to a local reflectivity variation can be modulated by the dynamical expansion of the nanowire with the modulation of its temperature profile. For 3C-SiC one can find in the literature a thermo-optic coefficient, $\alpha_n(T) = \frac{1}{n(T)} \left.\frac{\partial n}{\partial T}\right|_T$, which can vary around $2.9 - 5.7 \times 10^{-5}\,\text{K}^{-1}$ [80, 81], from room temperature to 500 K. With a taken value of approximately $4 \times 10^{-5}\,\text{K}^{-1}$, this will cause a relative change of the SiC refractive index of 1.5×10^{-4}, and thus a spectral displacement of the Mie resonance by $\mathrm{d}\lambda = \lambda \left(\frac{1}{n}\frac{\partial n}{\partial T}\right) \mathrm{d}T$, of about 0.07 nm, because they linearly evolve with the optical path length coefficient $n\,R$ (with R the nanowire radius). Since the Mie resonances typ-

ically spread over 10 nm for large nanowires in the green, this means that the relative change in optical cross-section can be evaluated at the level of $\frac{d\sigma}{\sigma} = 0.07/10$, assuming that the pump laser seats on the side of the Mie resonance. As such the ratio between the pure optical force (10 fN/10 μW) and its modification due to the temperature induced cross-section modification will be approximately of 0.007%, thus causing an approximately 0.1 fN force change on the nanowire for the 10 μW optical pump power. The phase of this additional force will be different from the phase of the direct optical force, which will help its discrimination. This cross-section modulation force will be oriented along the laser propagation axis, and will be proportional to the induced temperature modulation below the laser spot. To isolate this effect, we should conduct response measurements at different wavelengths across a Mie resonance, which will be further explored in future investigations.

5.7 Electrostriction

In response measurements carried out at low temperature (which will be more detailed in the following chapter), we observed that to fit the global response of the lateral displacement when modulating the pump intensity close to the nanowire clamping, we had to introduce an instantaneous effective force of high amplitude compared to a pure optical force (radiation pressure or cross-section modulation). This instantaneous contribution is aligned with the laser axis and increases when getting close to the clamp, which lead us to consider a strain effect not thermally induced (because instantaneous).

When the nanowire is illuminated by the pump laser, the intra-nanowire intensity profile is non-homogeneous and structured by the Mie resonances. As a consequence, the electrostriction mechanism (the deformation of a material in presence of an electro-magnetic field) [130, 131] should not be homogeneous across the nanowire cross-section and could thus induce a bending moment. This local drive mechanism, is quasi-instantaneous with respect to the timescale of mechanical oscillation. One expects the direction of the electrostriction drive is aligned with the laser propagation axis to preserve the symmetry. Also, this effect will efficiently drive one eigenmode when the pump laser is located at positions of large dynamical strain modulation for the considered mode, meaning close to the clamping area or the nodes of a longitudinal mode.

In the experiments, at a few occasions, we noticed that the instantaneous force vector, was notably increasing when bringing the pump laser close to the clamping area. We believe this could be a signature of such an electrostriction mechanism. The phenomenon has been largely evaluated in other optomechanical systems, especially in microspheres, where it is known to significantly contribute (10th %) to the total optomechanical coupling strength, [132].

5.8 Chapter summary

This chapter focuses on room temperature thermomechanical response measurements. We demonstrated how we could use the broadband dynamical response to an optical power modulation in order to characterise previously unknown important parameters concerning the light-nanowires interaction, such as the local absorption or the thermal contact resistance at the clamping.

The thermal elongation response to the modulation of the pump laser optical power, provides a measure of the cumulated effects of the temperature response profile that establishes along the nanowire. Constrained by the heat propagation model, we can retrieve the temperature elevation our nanowires undergo under these conditions. We still need to accounting for a thermal contact resistance that was made evident when cutting a nanowire, but which can ultimately be measured non-destructively by probing the spatial evolution of the elongation response. Doing so, we were able to characterise the spatial variation of the local absorption coefficient of ours nanowires, as well as the spectral structure of the absorption which involves the Mie resonances. All in all, the thermal elongation response measurement provides a robust tool that gives us access to global parameters that drive the heat diffusion in our nanowires

We also provided a throughout analysis on a thermomechanical effect acting at the clamping area, were the thermal expansion due to local temperature variation give rise to an appreciable lateral deformation of the nanowire free-end tip. The dynamic of this deformation with respect to the modulation of the pump laser optical power, gives us information on the propagation properties of heat from the pump laser position to the clamping area of the nanowire. In other conditions, we were able to measure the effect of a more local photothermal mechanism, where the optical forces gain an additional modulation term due to a thermally induced change of the local optical cross-section, at the pump laser waist.

All in all, this chapter presented the new tools we developed in order to better characterise, but also probe, the thermal properties of our SiC nanowires. We demonstrated we can indirectly have access to local temperature indicators depending on the dominant thermal actuation mechanism.

CHAPTER 6

THERMAL RESPONSE FROM ROOM TO CRYOGENIC TEMPERATURE

Contents

Introduction **129**

6.1 Photothermal responses at low temperature **130**

6.2 Thermal waves in a non-linear regime **137**

6.2.1 Heat diffusion when C_p, κ, vary with temperature 137

6.2.2 Stationary temperature profile 138

6.2.3 Dynamical heat diffusion in the non-linear regime 140

6.3 Frequency shift with temperature **150**

6.3.1 Two level system (TLS) contribution 151

6.3.2 Non-homogeneous temperature profile 153

6.4 Dynamical investigation of the photothermal modulation of the mechanical resonance **156**

6.5 Chapter summary **161**

Introduction

In this chapter we present the measurements of the thermal response realised on a single nanowire (identified as nanowire-20200910). We present techniques and pieces of evidence of exotic heat diffusion effects at low temperatures and how it impacts the mechanical properties of the nanowire.

At first, we compare the broadband responses measured between room temperature and low temperature (10 K), showing a global increase of the thermomechanical actuation efficiency in driving the lateral deformations of the nanowire. We then show that the thermal response of the material rapidly vary with the temperature at low temperatures, thus inducing a modification of the nanowire dynamical response due to variations in the stationary temperature profile inside the nanowire. This feature can be observed in the measured evolution of the dynamical thermal response at different working noise temperature. While scanning the pump laser position, the static properties of

the nanowire also evolve, and we inspect the evolution of the mechanical frequency as well as the noise temperature shift with the optical pump power. We observe a global shift of the relative frequency shift figure when the pump laser position is scanned along the nanowire, which we phenomenologically explain. To obtain a better insight on the dynamics of photo-induced mechanical frequency shifts, we finish by proposing a measurement method that allows to retrieve the photothermal response by investigating the dynamics of the mechanical frequency modulation created by a photothermal wave, in the non-adiabatic regime, with a high signal-to-noise. A measurement method that would have interesting applications in low temperature measurements.

6.1 Photothermal responses at low temperature

In this section we compare the thermal response of the same nanowire (with length $L = 200\,\mu$m and diameter $d = 180\,$nm) between room temperature and a state where the nanowire presents a noise temperature of 10 K, obtained via laser heating. At such temperatures and in our measurement configuration the thermal response of the nanowire is believed to be still in the diffusion regime. In the cryostat setup we are more sensitive to lateral deformations, and thus proceed to measure how the thermal lateral deformation dynamics evolves at lower temperature.

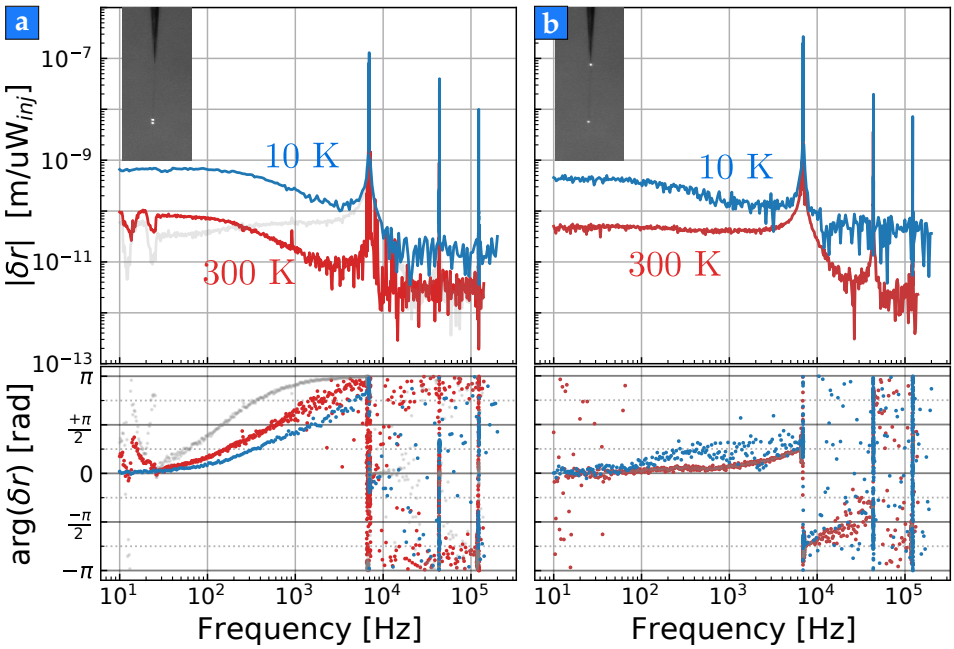

Figure 6.1: Comparison of broadband response measurements normalised by the injected pump power modulation amplitude. For the represented response at 300 K (in red) we have removed the fitted contribution of the radiation pressure. In light grey is the measured response with all the contributions at 300 K. (a) Responses measured when the pump laser is positioned at the vibrating tip, while in (b) the pump laser is positioned close to the clamping.

After cooling down the sample stage and aligning the pump and probe objective, we realised a set of characterisation measurements. The measurement of the Brownian motion gave us the nanowire resonant frequency shifts and the changes in the quality factor, compared

to the room temperature. In those low temperature measurements, where we measured the nanowire response to the pump intensity modulation, we used a rather large optical power in the order of μW, so as to keep a SNR larger than one even on the low frequency part of the photothermal response (on the plateau). For such large powers, the noise of the nanowire is around 10 K, although the sample holder is measured at 27 mK. This suggests that a large temperature gradient is built within the nanowire, but as we already discussed, the temperature gradients are expected to be mainly localised at the nanowire clamping point due to the rapid increase of their heat conductance with the temperature (see also below). For those measurements, the probe power was maintained around 1 pW, so that its contribution to the temperature increase is negligible here.

We already discussed [66] that the noise temperature gives a good indication of the nanowire lattice temperature. Indeed, the noise temperature follows the cryostat temperature when the pump is turned off, while heating the sample holder temperature using a resistor.

Figure 6.1 shows the comparison between the responses taken at room temperature and 10 K of noise temperature. At first sight, the overall response shape remains similar to what has been observed at room temperature, which indicates that the diffusion regime seems to be still relevant in describing our observations. Then the resonant photothermal response increases due to an increase of the quality factor of the clamped nanowire. On top of that, when the pump laser is located at the vibrating tip of the nanowire, Fig. 6.1a, we observe an increase by one order of magnitude of the low frequency response. This can be a consequence of several mechanisms: an increase of the contact resistance at the clamping, a decrease of the conductivity κ of the nanowire, or an increase of the optical absorption coefficient. Then the phase of the response presents a slight acceleration visible as an increase of the thermal cutoff frequency, which suggests the heat diffusion coefficient, $D = \kappa/(\rho C_p)$, has increased at 10 K. This increase could be caused by a stronger reduction of the heat capacity compared to the heat conductivity. This would be expected if the nanowire was only made of crystalline 3C-SiC material, but we know that it also supports a thin amorphous layer (see Fig. 3.24c of the quality factor evolution with the nanowire temperature), whose thermal coefficients present anomalous variations with temperature. We also note that the driving mechanism at resonance is no longer fully dominated by the radiation pressure even when the pump laser is positioned at the nanowire extremity, because the phase at resonance is no longer pinned to 0 or π.

In Figure 6.1b we realised a broadband photothermal response when the pump laser is located close to the clamp (within approximately 5 μm). Although we still observe a large increase of the low frequency response compared to room temperature measurements, the phase signal is not any more in accordance with a global increase of the diffusion coefficient (while the nanowire average temperature is supposedly reduced at that pump position). Instead, the behaviour of the dephasing is similar to the prediction expected when accounting for a non-negligible thermal contact response, sec. 5.2.

We carried out similar broadband response measurements for vary-

ing pump laser positions along the nanowire. For each measurement we also recorded the resonantly driven response of the three first mode families, as well as the spectrum when the pump laser modulation is turned off. We kept the mean power unchanged so as not to change the mean temperature profile within the nanowire. At this temperature, the line width of the resonances is small (typically below 100 mHz), and the resolution bandwidth (RBW) must be lowered as well. All in all, each set of measurements takes up to 14 h to gather well resolved responses. It is to be remarked that after aligning the objectives to the nanowire, the optical setup positioning stability is noteworthy when the cryostat is at base temperature, and the misalignment drifting is less than a nm/h. Still we could not complete a set of measurements with the pump position varied all along the nanowire length at that time, because of hydrogen corking which progressively locks the mixture circulation after 1-2 weeks. When this happens, one must heat up the cryostat to 4 K and condense again the mixture (which approximately takes 1 hour) but then one cannot fully guaranty to come back to the same position with respect to the "hot spots" since we did not have fine scanners on the pump objective at that time.

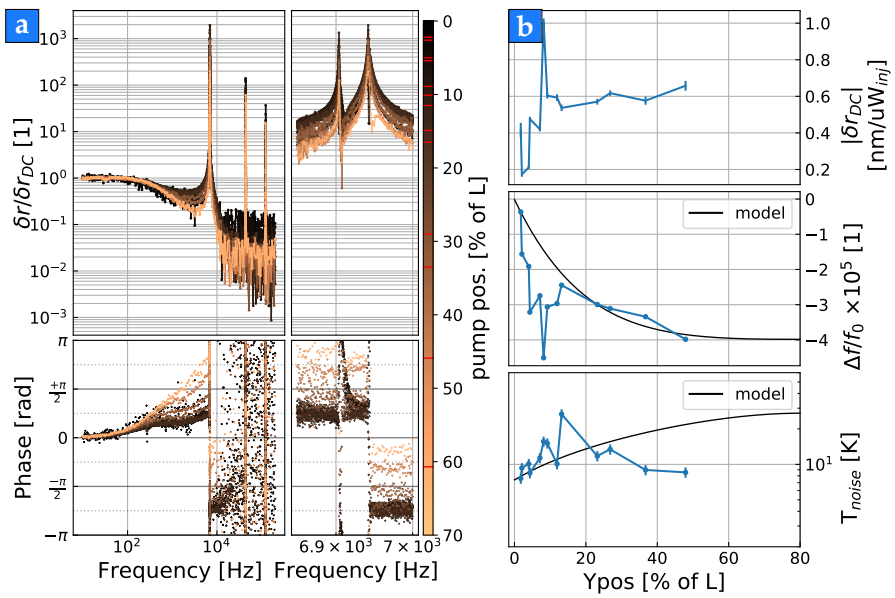

Figure 6.2: Broadband lateral responses of the nanowire to a modulation of the optical pump power at different pump laser positions along the nanowire. The noise temperature of the nanowire is of 10 K for this measurement set (with an average of 1 μW optical power). (a) Superimposed broadband responses measured at different pump laser positions. The entirety of the nanowire has not been scanned, because the cryostat started to heat up, which happens regularly when cold for more than ten days, and each sequence of measurement at a given pump position takes around 14 h. (b) (top panel) Evolution of the DC response with the pump laser position. This level reflects the thermal actuation response plateau, and thus gives a mean to account for the local absorption. The middle and bottom panels are the relative frequency shift and the noise temperature of the nanowire when the pump optical modulation is turned off.

Figure 6.2 shows the evolution of the broadband responses when the pump is located at different positions along the nanowire. Because the absorption is not homogeneous all along the nanowire, the responses' amplitude can vary significantly along the nanowire, see Fig. 6.2b. In Fig. 6.2b we show the DC plateau amplitude variation with the pump position along the nanowire, as well as the relative frequency shift and the noise temperature of the first mode family when the optical modulation is turned off. We compare those measurements with a model of the frequency shift induced by non-homogeneous temperature profile [41], that will be detailed in sec. 6.3, while for the noise temperature we use the model described in sec. 4.6. We thus prefer comparing the broadband responses when normalised rel-

atively to their DC plateau amplitude, see Fig. 6.2a. The evolution of the phase response with the pump laser position differs greatly from similar measurements realised at 300 K see Fig. 5.15. Indeed at room temperature, the more the pump is positioned close to the clamping area, the slower is the phase accumulation due to delay. At 10 K we observe the phase to reach an intermediary plateau at $\pi/8$ around 300 Hz, even though the pup laser is positioned very close to the nanowire clamping (close to the expected thermal actuation area). This behaviour which suggests a strong relative increase of the thermal contact resistance with respect to the nanowire thermal resistance.

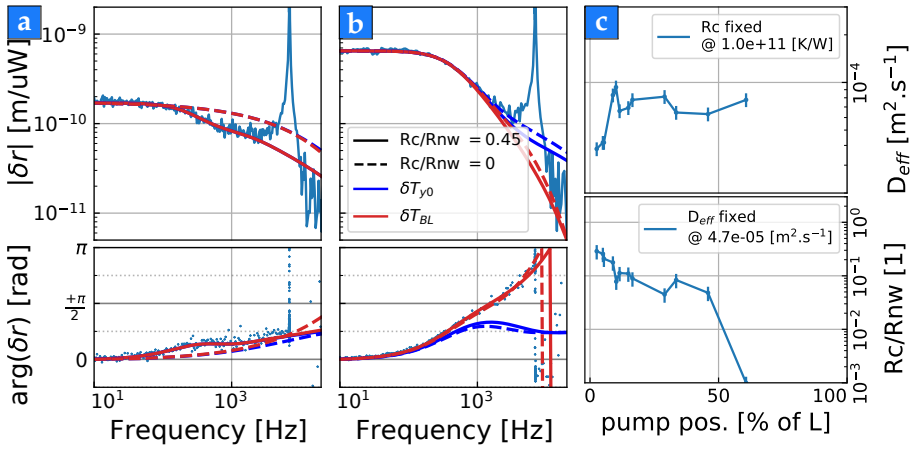

Figure 6.3: Evolution of the effective diffusion coefficient and the relative thermal contact resistance with the pump position. (a) Comparison between the broadband response of the lateral displacement to the temperature response of the bilayer actuation model (red) and an actuation below the pump (blue). We considered two limiting cases for our models: when no thermal resistance is accounted for (dotted lines), and when we account for the thermal contact resistance (plain line). In the left panel the pump location is close to the clamp and the two models corresponds to (R_c/R_{nw}=0, D_{eff} =0.1e-5 $\text{m}^2.\text{s}^{-1}$), (R_c/R_{nw}=0.45, D_{eff} =4.7e-5 $\text{m}^2.\text{s}^{-1}$). In (b) the right panel the pump is located far from the clamp and the parameters for the two models are (R_c/R_{nw}=0, D_{eff} =4e-5 $\text{m}^2.\text{s}^{-1}$), (R_c/R_{nw}=0.45, D_{eff} =8e-5 $\text{m}^2.\text{s}^{-1}$). (c) Evolution of the model parameters when fitting the low frequency part of the broadband response at different pump position.

In figure 6.3a and 6.3b we adjust the thermal part of our measurements with our 1D diffusion model and highlight the difference between the temperature responses when considering thermal contact resistance or not. Since we are only interested in the low frequency part of the response, we compare directly the deformation response to the temperature response of the nanowire close to the clamping point using a prefactor to match the low frequency response level. Indeed, from the previous chapter, see sec. 5.5, the mechanical response to the heat propagation can be approximately modelled by the weighted convolution of the mode families mechanical susceptibility with the temperature response of the point of actuation. In this case, we accounted for two different photothermal mechanisms: first an actuation at the clamping, δT_{BL} (bilayer effect, represented in red in Fig. 6.3), and an actuation located under the pump laser waist, δT_{y_0} (optical cross-section modulation or thermostrictive stress due to non-homogeneous heating, represented in blue in Fig. 6.3). One may note that when the pump laser is close to the clamping area, both temperature responses are similar at low frequency, since at those frequencies the heat wavelength is too large to resolve the distance between the clamping and the pump positions.

In both figures, we adjust the low frequency part of the responses changing the effective diffusion coefficient and the thermal contact resistance to best fit the data. The introduction of a thermal contact resistance (rather large compared to the nanowire one), allows us to correctly adjust the amplitude and phase of the responses, and in particular the model reproduces well the intermediary plateau of the

phase observed between 200 Hz and 2 kHz. To illustrate the necessity of introducing a thermal contact resistance in order to fit the measurement when the pump is located close to the nanowire clamping, see Fig. 6.3a, we plot two models: one in plain line that best fits the low frequency part of the response, and one in dotted line that does not account for a thermal contact resistance, but instead we reduced the effective diffusion coefficient in order to match the phase measured at resonance. On the other hand, when doing the same analysis with the pump located away from the clamping area, see Fig. 6.3b, whether we account for a thermal contact or not, we can find a reduced effective diffusion coefficient that fits the measurements. Still the value of the effective diffusion coefficient is affected by the chosen ratio R_c/R_{nw}. Moreover, when moving the pump position away from the clamping, there is no single value of the relative thermal contact resistance or the effective diffusion coefficient that best-fit all the responses. Figure 6.3c

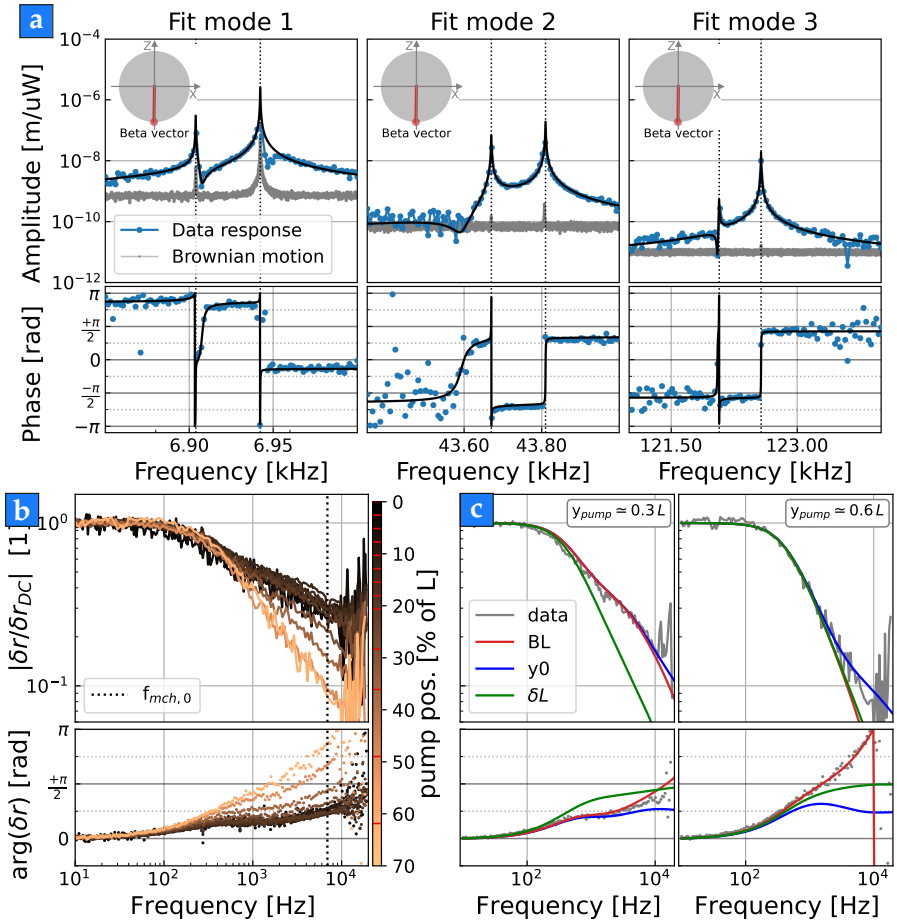

Figure 6.4: (a) Zoomed response measurement of the three first mode families, to a modulation of the pump intensity (blue). In black : the fitting with two complex Lorentzian functions for each mode family. (b) We deconvolved the resonantly driven response of the fundamental modes from the broadband response in order to better visualise the thermal response evolution with the pump position along the nanowire. The responses' amplitudes are normalised at their DC value. (c) We superimposed the spectral profile of the thermal response of the three main model: the bilayer effect (red), a thermomechanical drive at the laser focal point (blue), and an elongation effect (green). This method can give hints on which contribution dominates.

shows the evolution with the pump position of the effective diffusion coefficient used in the 1D diffusion model when the thermal contact resistance value is fixed at its clamping value. Alternatively we show the evolution of the thermal contact resistance which best fits the data, when the effective diffusion coefficient is fixed at the pump position away from the clamping area. This variation of those thermal quantities with the pump laser position, points out that at low temperature it becomes necessary to take into account the non-linearity of the ther-

mal coefficients. We will explore the non-linearity arising from the temperature dependence of the thermal coefficients in more details in the next section.

As mentioned above, the thermomechanical lateral deformations are the dominant contributions in driving the nanowire resonant response at low temperatures. However, it is still not clear if there is only one thermal mechanism that contributes to the nanowire deformations. To obtain a better understanding of the photothermal responses, we will now inspect the resonantly driven response in greater details. We fit each resonant mode family with the coherent sum of two complex Lorentzian functions (one for each mechanical polarisation), see Fig. 6.4a. In Figure 6.4b, we retrieved the mechanical contribution of the first mode family, in order to compare the thermal response profile to temperature responses associated to specific thermomechanical contributions, see Fig. 6.4c. This will be helpful later on in discriminating the dominant thermomechanical effect at different pump position.

For a given longitudinal mode family, the measured response associated to the measurement vector, $\boldsymbol{\beta}$, is given by,

$$\delta\Phi_R = \frac{|\boldsymbol{\beta}|\,(\mathbf{e}_1\cdot\mathbf{e}_\beta)\,(\mathbf{e}_1\cdot\delta\mathbf{F}_{\text{tot}})}{M_{\text{eff}}\,\left(\Omega_1^2-\Omega^2-i\,\Omega\,\Gamma_1\right)} + \frac{|\boldsymbol{\beta}|\,(\mathbf{e}_2\cdot\mathbf{e}_\beta)\,(\mathbf{e}_2\cdot\delta\mathbf{F}_{\text{tot}})}{M_{\text{eff}}\,\left(\Omega_2^2-\Omega^2-i\,\Omega\,\Gamma_2\right)}, \tag{6.1}$$

$$= A_0\,e^{i\,\phi_0}\,\frac{(-i\,f_0\,G_0)}{\left(f_0^2-f^2-i\,f\,G_0\right)} + A_1\,e^{i\,\phi_1}\,\frac{(-i\,f_1\,G_1)}{\left(f_1^2-f^2-i\,f\,G_1\right)}, \tag{6.2}$$

where A_i, ϕ_i, f_i and G_i are the amplitude, phase, frequency and line width for each mechanical polarisation i, while M_{eff}, $\mathbf{e}_i$, $\mathbf{e}_\beta$ are the effective mass of the mode, the orientation of the mechanical polarisation modes i, the orientation of the measurement vector, and we have $\Omega_i = 2\pi\,f_i$, $\Gamma_i = 2\pi\,G_i$. The projected driven deformation is given by $\delta r_\beta[\Omega] = \delta\Phi_R[\Omega]/|\boldsymbol{\beta}|$, with $|\boldsymbol{\beta}|$ in [m/cps]. In eq. (6.2) we present the fitting parameters used in our python optimisation code, using the non-linear fitting module LMFIT [133]. On the other hand, one can model the resonantly driven response by a force vector with complex component, $\delta\mathbf{F}_{\text{tot}}$. This effective 4 dimensional quantity encapsulates the different thermal actuation contributions in phase, amplitude and orientations.

In our case, we are not sensitive to the thermal elongation response as the nanowire reflectivity is locally homogeneous at the probe position. We thus assume the effective complex force to be only composed of two contributions : a thermomechanical drive from an actuation at the clamping area, and a thermostrictive drive caused by the temperature modulation at the pump position,

$$\delta\mathbf{F}_{\text{tot}} = \delta\mathbf{F}_{\text{clmp}} + \delta\mathbf{F}_{y_0}, \tag{6.3}$$

where $\delta\mathbf{F}_{\text{clmp}}$ and $\delta\mathbf{F}_{y_0}$ are contributions in the form, $\delta\mathbf{F}_i = F_i\,e^{i\,\phi_i}\,\mathbf{e_i}$, with $i = \text{clmp}, y_0$. Assuming a slowly varying phase for the temperature response across the mechanical frequency span, we can fix the

phases of the force modulation to,

$$\phi_{\text{clmp}} = \arg\left(\delta T[\Omega_{\text{m}}](y_{\text{clmp}}, y_0)\right), \tag{6.4}$$

$$\phi_{y_0} = \arg\left(\delta T[\Omega_{\text{m}}](y_0, y_0)\right), \tag{6.5}$$

Solving the four equations derived from (6.1), (6.2), which connect the vector to the fit parameters, one can retrieve the amplitude and direction of the driving force.

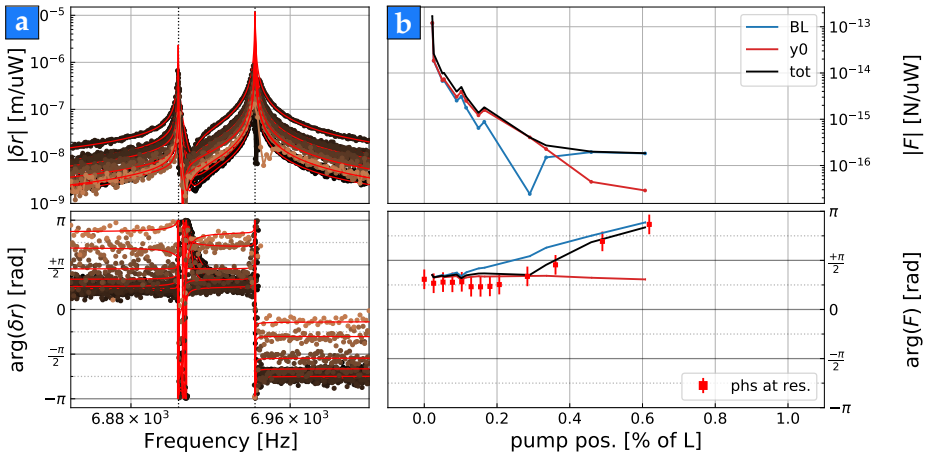

Figure 6.5: (a) Fitted resonantly driven responses at different pump position. We normalised the lateral deformation modulation by the optical power modulation amplitude. (b) Profile of the extracted contributions from the fitted responses. We converted the amplitude of the contributions to the equivalent force that would generate the measured displacement.

Figure 6.5 shows the evolution of the two contributions amplitudes. In Fig. 6.5b we see a switch in the dominant contribution, from a bilayer effect at large distances from the clamp to a local effect at closer distances. This transition is associated to a change in the resonant phase response, which is transiting from a delay like evolution to a pi/4 delay as observed under the pump laser at frequencies above the thermal cutoff. This behaviour is expected since the thermostrictive drive under the pump laser focal point must be convolved by the strain profile of the driven mode (the fundamental one here), which is maximal at the clamping of the nanowire. On the other hand, the thermomechanical effect at the clamping is only attenuated by the decreasing heating efficiency as the pump moves further from the clamping.

Those measurements around 10 K of nanowire noise temperature (measured using the noise spectra when the modulation is turned off, and with a fixed average power) allowed us to highlight the increased contribution of the thermomechanical effects in the resonantly driven mechanical response of the nanowire. It is interesting to evaluate those effects at low temperature as they directly affect the behaviour of the nanowires. We also showed the increase importance of the thermal contact resistance in the temperature response. Moreover, we observed first signatures of the rapid variations of the stationary or mean field state of the system with the pump laser position, as the fitting of the low frequency thermal response suggests adapting the effective diffusion coefficient when the pump position is moving. This will lead to consider the direct effect of the temperature dependency of the thermal quantities, κ and C_p in the 1D heat diffusion.

6.2 Thermal waves in a non-linear regime

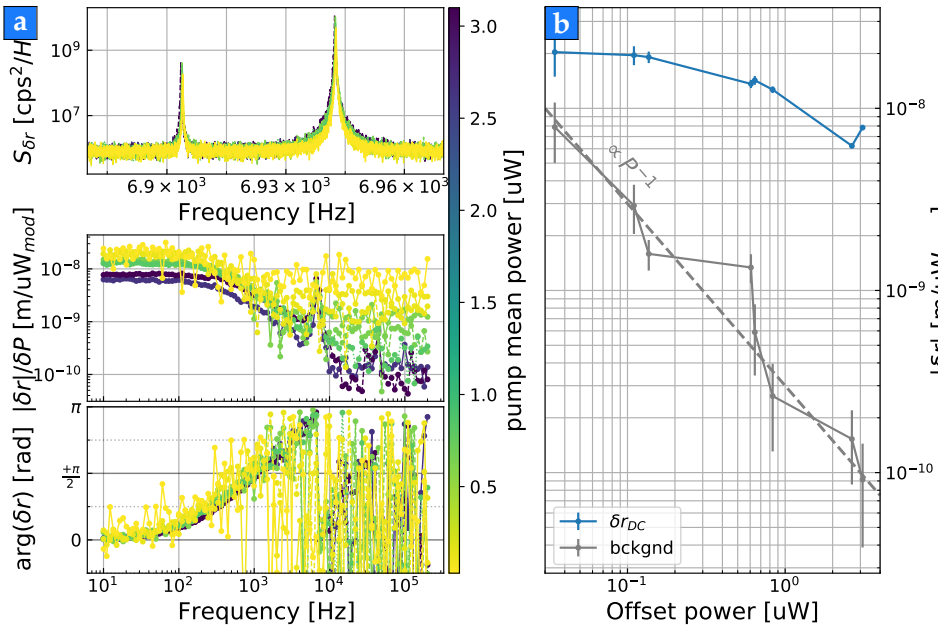

Figure 6.6: (a) Photothermal response measurements and thermal noise spectra measured with the pump laser located at the tip of the nanowire, while varying the mean pump power. The Brownian motion is measured at constant power when the modulation is off (top panel), and the broadband responses are normalised by the injected optical modulated (bottom panel). (b) Comparison of the DC plateau amplitude with the background of the signal.

The thermomechanical actuation measured in the above section presents pieces of evidence of some non-linearity in the heat diffusion properties (variation of the heat conductivity and contact resistance with the laser position). In order to test this observation, we realised photothermal responses at different average power, see Fig. 6.6. To do so, we vary the offset sent on the AOM, and normalise our deformations measurements to the modulation strength.

Although we fixed the pump laser position, the low frequency plateau of the lateral photothermal response varies with the mean optical power. This evolution can be understood as such: with lower optical power the nanowire temperature increase due to laser heating is reduced, thus causing a decrease of the average conductance experienced by the thermal waves, which consequently increases the thermal heating efficiency. On the other hand, the background increases because the readout sensitivity stays the same when varying the modulation power.

6.2.1 Heat diffusion when C_p, κ, vary with temperature

In the following we present the evolution of the heat diffusion in the case where the thermal coefficients of the Fourier equation become temperature dependent. Since the temperature profile is non-homogeneous, this dependence will include an additional spatial dependence in the equation, which in turn becomes non-linear. We focus our attention in the special case where C_p and κ present a dependency in the temperature. This modification leads to a non-linearity in the heat diffusion equation, and we will analyse its impact here. To ex-

plore those modifications, we first assume that the conductivity and the heat capacity of the nanowire can be modelled as,

$$\rho \simeq Cst; \qquad \kappa = K_0 \left(\frac{T}{T_0}\right)^{\mu}; \qquad C_p = C_0 \left(\frac{T}{T_0}\right)^{\alpha}, \tag{6.6}$$

where $K_0 = \kappa(T_0)$, and $C_0 = C_p(T_0)$, μ and α are real numbers, which are expected to be positive at low temperature. This power law behaviour is expected from various heat transport models [39, 104, 134] (see sec. 3.5.3). Measurements found in the literature of the material properties of 3C-SiC, see sec. 1.3, allow us to fix some coefficients. Concerning the heat capacity of the nanowire, the bulk contribution is expected to follow the Debye model, but we are lacking measurements to fully characterize the nanowire properties at low temperatures. In particular, the oxide crust contribution should be taken into account. Nevertheless, this sections aims at describing the generic behaviour of the temperature profile in the system and its impact on our measurements.

6.2.2 Stationary temperature profile

As briefly discussed in the end of chap. 3, when approaching dilution temperatures we can no longer neglect the significant variations of the conductance with temperature. This modifies the temperature profile along the nanowire in the diffusive regime, and impacts the noise temperatures depending on where the optical heat source is positioned.

Let's first consider the static temperature profile caused by a constant laser illumination at a position y_0. Likewise, sec. 4.5, we assimilate the heat source profile to a Dirac distribution. The heat flux $j_{\text{thm}} = -\kappa \partial_y T$ is still constant in each section of the nanowire, and considering eq. (6.6) the static equation becomes,

$$\frac{K_0}{(\mu+1)\, T_0^{\alpha}}\, \partial_{yy}\left(T^{\mu+1}\right) = -s_0\, \delta(y - y_0), \tag{6.7}$$

where y_0 is the pump position, $s_0 = P_{\text{abs}}/S$ the surface heat source amplitude with P_{abs} the absorbed optical power and S the nanowire cross-section.

Assuming the existence of a thermal contact resistance at the clamping, the solution is given by,

$$T_{\text{s}}(y) = \left[\left(T_{\text{cryo}} + R_c\, P_{\text{abs}}\right)^{\mu+1} + \frac{P_{\text{abs}}}{S}\, \frac{\mu+1}{K_0\, T_0^{-\mu}}\, \left(y - \Theta(y - y_0)\,(y - y_0)\right)\right]^{1/(\mu+1)}, \tag{6.8}$$

for $\mu \neq -1$ (but one expects μ to be positive), and R_c the thermal contact resistance in [K.W^{-1}]. Note that the solution without accounting for a thermal contact resistance is the same expression as eq. (6.8)

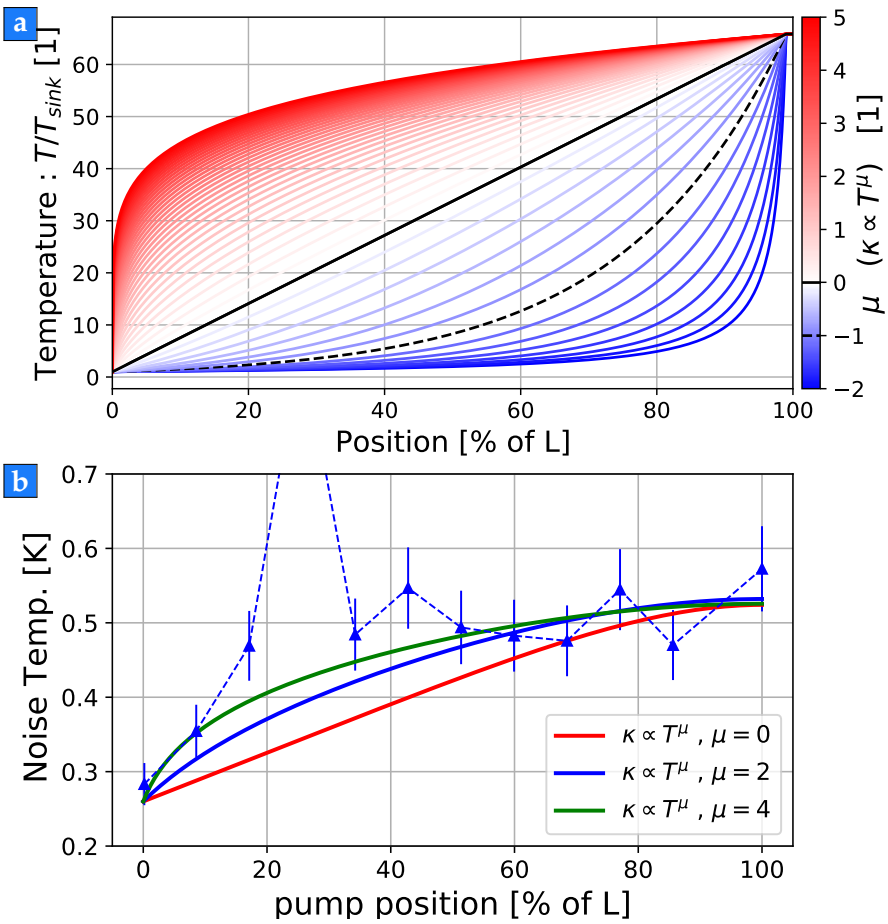

Figure 6.7: (a) Stationary profile tendency with respect to the conductivity power law dependence on the temperature with $R_c = 0\,\mathrm{K.W^{-1}}$ and $T_{\mathrm{sink}} = 20\,\mathrm{mK}$, when the pump is set at the vibrating tip of the nanowire. For each profile, we adapt T_0 so that every maximal temperature for each profile equated the value of the linear profile at the tip (here $T_{\mathrm{max}} \simeq 1.3\,\mathrm{K}$ where $P_{\mathrm{abs}} = 10\,\mathrm{nW}$ and $K_0 = 60\,\mathrm{W.m^{-1}.K^{-1}}$). (b) Noise temperature profile when the lowest offset pump optical power is used, with some modelled profiles expected from discussion in sec. 4.6. We see the maximal temperature is only twice the minimal temperature, which does not correspond to the above models where we assume $R_c = 0\,\mathrm{K.W^{-1}}$. Those models are qualitative and compare the different trends.

with $Rc = 0$ K.W^{-1}. Indeed, since we assumed an absence of lateral radiation loss, the heat flux between the source and the heat sink must remain constant, thus the contact resistance only adds an offset proportional to the deposited heat power in the static case.

In Figure 6.7a we show the different static temperature profiles with varying μ when we set the reference temperature, T_0, such that the tip temperature remains the same. We see that for the positive values of μ, which are expected at low temperature, the temperature gradients are largely concentrated at the clamping area, where the conductance is smaller. However, the static regime does not allow us to have insight on the heat propagation inside the nanowire. We thus aim to study the dynamical response of the heat propagation when modulating the amplitude of the heat source, using optical absorption of a laser.

Figure 6.7b shows the measured noise temperature profile when varying the pump position, at the lowest pump average power. The observed dispersion of the value is most likely due to the non calibration of the local absorption, which echoes the δr_{DC} amplitude profile in Fig. 6.2b. Nonetheless, we compared this partial profile with the expected noise temperature profile computed from eq. (4.43) in sec. 4.6, when considering the non-linear temperature distribution in eq. (6.8) for some value of μ. It is difficult to assert any conclusion besides the qualitative agreement with the noise temperature profile when considering the nanowire conductance varies in T^4 at low temperatures.

6.2.3 Dynamical heat diffusion in the non-linear regime

In order to reach truly cryogenic temperatures, we need to reduce the optical power of the pump and of the probing laser as well, to several pW. At those optical powers, the low frequency response of the lateral deformation is not accessible and buried in the readout shot noise. In this case, we can take advantage of the large quality factor of the first mode family ($Q \simeq 10^5$) to investigate the nanowire resonant photothermal response. If the response is dominated by the bilayer effect or by the cross-section modulation, we will furthermore have access to local temperature estimators. Indeed, from previous measurements and considerations, we concluded the main photothermal effects driving the nanowire deformation up to the first mode family were : the bilayer effect (actuation proportional to the temperature modulation at the clamping area), and either a thermostriction effect at the pump laser waist or the optical cross-section modulation (both being actuation proportional to the temperature modulation under the pump laser).

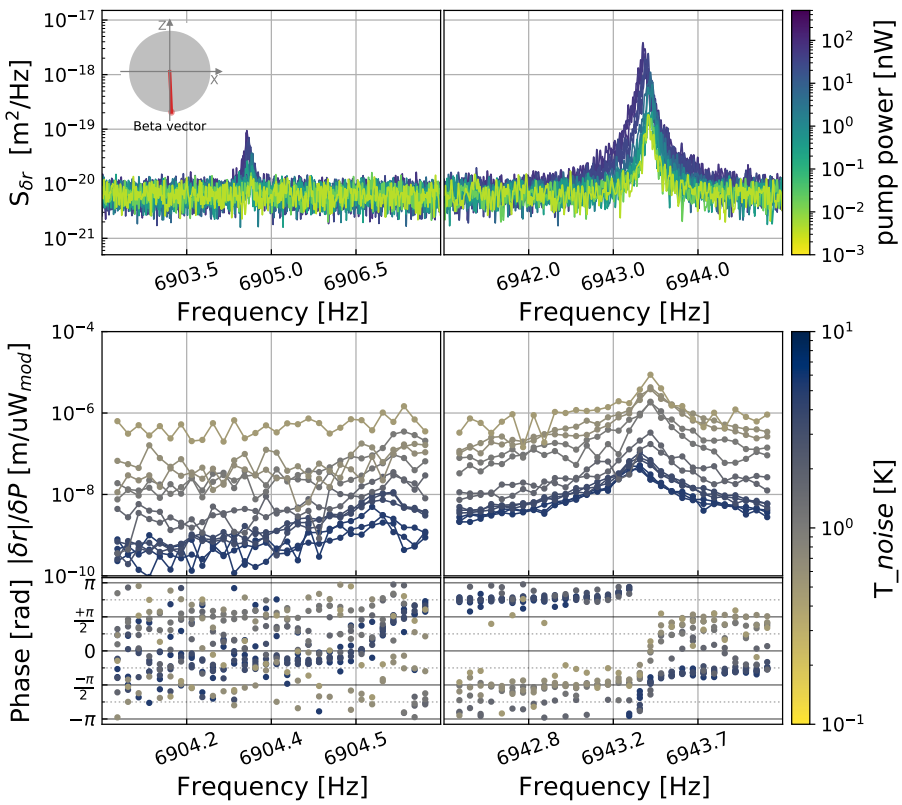

Figure 6.8: Brownian motion (top panel) and resonantly driven response (bottom panel) at different average pump optical power and noise temperature. We measure the Brownian temperature when not-modulating, and then we measure the response. In this set of measurements we placed the pump at the tip of the nanowire close to the probe laser position.

In Figure 6.8 we show the resonant response measured at various average pump optical powers. For this measurement, we pumped and probed the nanowire response with both lasers located at the vibrating tip of the nanowire. The measurement of the Brownian Motion (top panel) allows us to retrieve the noise temperature and analyse its evolution at different average pump powers. We can then compare the resonantly driven lateral displacement responses, normalised by

the modulation amplitude of the pump optical intensity, at different working temperature. Doing so, we observe a striking phase shift at resonance from 10 K to several 100 mK (most visible for the high frequency mechanical polarisation mode best aligned with the measurement vector) as well as an increase by two orders of magnitude of the normalised response amplitude. It is most likely to be attributed to a change of the diffusion coefficient, or to a change in the dominant actuation mechanism. However, since we do not change the laser positions, we believe this behaviour transition is indeed due to the change of the diffusion coefficient subsequent to a change of the heat capacity as well as the heat conductance within the nanowire. Independently of the origin of the actuation mechanism, we are in presence of a very non-linear response, which dramatically increases in efficiency at low temperatures.

At those noise temperature (ranging from 0.8-10 K), we have already observed a change in the heat conduction regime in previous work, see sec. 3.5.3. Still it can also stem from a shift in the dominant contributing mechanism.

We repeat the resonantly driven response at different optical powers for several positions of the pump laser in order to analyse the position dependence of the observed non-linear thermomechanical response. Figure 6.9a shows four significant resonant responses at different pump positions along the nanowire in use. Due to the extreme duration of the measurements, we were not able to scan all the nanowire, and decided to focus on the responses of the area close to the clamping, since it is where we expect the largest variations of the thermal response. Moreover, the temperature response at the clamping and below the pump laser are very similar when the pump position is close to the clamping area. This would reduce the complexity of the response transition in case of a change of the dominant thermomechanical contribution.

In Fig. 6.9b is shown the noise temperature deduced from Brownian motion for different average optical power and at different positions of the pump laser along the nanowire. Its general trend confirms that the efficiency of the optical heating of the nanowire increases when going away from the clamping point, which is expected, but it also reveals the non homogeneity of the absorption as observed in the analysis of chap. 5. This means that it will not be possible to directly compare the absolute amplitudes of the response between the different locations of the pump laser.

We can nonetheless compare the variations of the amplitude and phase with respect to the effective noise temperature for increasing mean optical pump power, see Fig. 6.9c. On the bottom panel of Fig. 6.9c, we show the relative frequency shifts with the nanowire noise temperature. Except for the red line, where pump position is located at the vibrating tip of the nanowire (where one expects a global shift of the resonant frequency due to the sensitivity of the pump laser force field gradients), the frequency shift with the noise temperature follows the "universal" tendency observed in nanowires at those temperatures, with a typical inversion around 500 mK. The inversion of the frequency shifts is a good indicator of a given temperature state within the nanowire, even if the temperature profiles within the nanowire

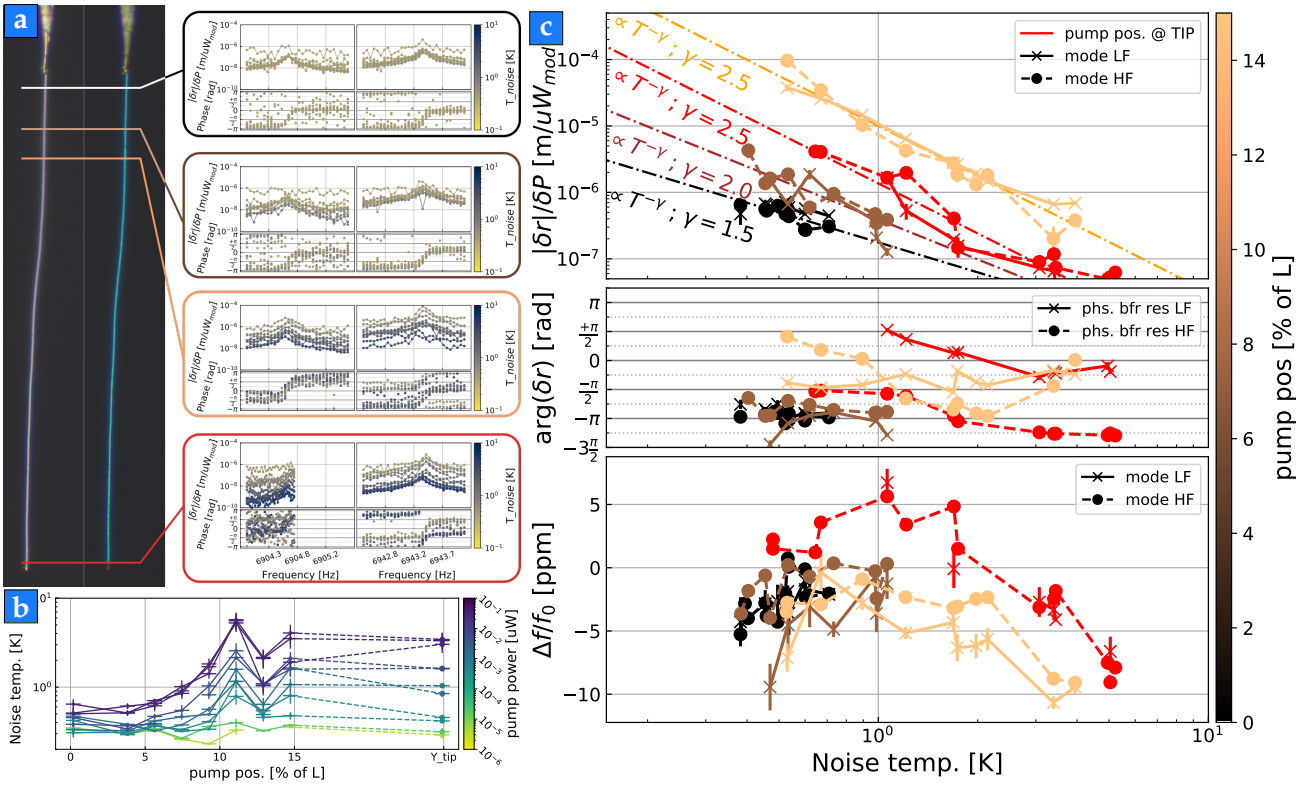

Figure 6.9: Resonantly driven response amplitude and phase, when pumping at different average power. (a) Representation of the response associated to the pump position while measuring the lateral displacement at the tip. Note that for the response of the low frequency mechanical polarisation at the tip (red squared data), we miss a part of the data which is due to an error in the frequency range. Since each measurement set last at least 14h, and this resonance is not the most visible we proceeded to measured for the next position. (b) The noise temperature profile with the average pump optical power. (c) Evolution of the lateral displacement modulation per μW of modulation amplitude $|\delta r|$, the phase before and after the resonance, the relative frequency shift, with the average noise temperature of the nanowire when scanning the working point of the pump optical offset.

6

are expected to be significantly dependent on the pump laser position. This reference temperature is also located in a temperature range where the dominant conduction mechanisms are expected to rapidly change. Looking at the amplitudes normalised by the optical modulation depth (top panel), we observe a systemic decreasing efficiency of the photothermal driving mechanism at resonance for both mechanical polarisation modes, when the mean optical power, and thus the noise temperature increases. The rate of this decrease seems to stay stable (around $T^{-\gamma}$ with γ = 2-2.5) with the pump position, for positions sufficiently far from the clamping area. Also, concerning the measurement taken close to the vibrating tip of the nanowire, we also get an average power law of about 2.5 above 1 K, while both phases identically slowly evolve (modulo π due to projection effects) with the mean optical power. For the measurements taken close to the clamping area (in brown and black) phases before resonance are relatively stable and identical for the two mechanical polarisations. They are almost instantaneous, indicating that the thermal cutoff is higher than the mechanical frequency. Although the rate of decrease seems lower than for the data with the pump positioned further from the clamping area, the plotted slope are guidelines that have some variability. On the contrary, the phase evolutions of the resonantly driven response

measured far from the clamping are not trivial to interpret, and the observed evolutions might be related to the non-linear regime of the heat diffusion at those temperatures, as we will discuss below.

Static limit considerations

A first step to interpret these data is to consider the evolution of the response in the static limit, which can be relevant when the heat source is located close to the clamping area. In this case, the responses were observed to remain instantaneous, meaning that the photothermal cutoffs are found at higher frequencies than the mechanical resonances. The noise temperature of the first mode family, T_{noise}, at a given pump position y_0 is given by,

$$T_{\text{noise}} = \frac{1}{L} \int_0^L T_s(y)\, u_0^2(y)\, \mathrm{d}y \simeq T_s(y_0), \tag{6.9}$$

where the approximation holds when y_0 is located close to the clamping, since the mode profile u_0 vanishes at the clamping and T_s is stable after y_0. The variation of the noise temperature with the average optical absorbed power has been shown to scale either as $T_{\text{noise}} \propto P_{\text{abs}}^{1/(\mu+1)}$ if the nanowire effective resistance is higher than the thermal contact resistance, or as $T_{\text{noise}} \propto P_{\text{abs}}$ in the opposite case. In other words, if the temperature elevation at the pump position is dominated by the nanowire internal temperature gradients, or by the step increase due to the contact resistance. We note that the first power law is in general smaller than 1, but this assumes that the contact resistance does not depend on the injected power, which is unlikely. More precisely, when one increases the injected optical power, the temperature at the clamping point increases, which is likely to induce a decrease in the contact resistance (on the example of a Kapitza interfacial resistance).

On the other hand, one can analyse the amplitude evolution around the stationary temperature profile, $T_s(y)$ when introducing a perturbative heat source elevation, $P_{\text{abs}} \to P_{\text{abs}} + \delta P_{\text{abs}}$ that generates a perturbation in the stationary temperature profile denoted δT_s. At first order in δP_{abs}, the static perturbation to the stationary profile for $y \leq y_0$ is found to be,

$$\frac{\delta T_s(y)}{\delta P_{\text{abs}}} = \left[\frac{\mu+1}{K_0\, T_\kappa^{-\mu}\, S}\, P_{\text{abs}}\, y + \left(T_{\text{cryo}} + R_c\, P_{\text{abs}}\right)^{\mu+1} \right]^{\frac{-\mu}{\mu+1}} \left(\frac{y}{K_0\, T_\kappa^{-\mu}\, S} + \left(T_{\text{cryo}} + R_c\, P_{\text{abs}}\right)^{\mu}\, R_c \right). \tag{6.10}$$

Note that when $y \geq y_0$, the above expression is simply evaluated at y_0. One must distinguish several limit cases:

- the observed displacement is generated by the temperature modulation at the clamping, $y \to 0$ (as in the case of a bilayer effect),

thus only the thermal contact resistance is involved in the temperature change and $\delta T_s(y)/\delta P_{\text{abs}} \approx R_c$, and the relation between the normalised amplitude of the response and the noise temperature is $\delta T_s(y)/\delta P_{\text{abs}} \propto T_{\text{noise}}^{\mu+1}$ or T_{noise}^{-1} whether the temperature elevation is dominated by the nanowire thermal resistance or not;

- if the lateral displacement is generated by the temperature modulation under the pump laser, one can consider the case where the contact resistance is negligible and $\delta T_s(y_0)/\delta P_{\text{abs}} \propto P_{\text{abs}}^{-\mu/(\mu+1)}$ and thus $\delta T_s(y_0)/\delta P_{\text{abs}} \propto T_{\text{noise}}^{-\mu}$ or $T_{\text{noise}}^{-\mu/(\mu+1)}$.

Concerning the measurement in Fig. 6.9c, the working point of those measurements would fall into the optical heating regime where the noise temperature evolves as $P^{1/2}$, corresponding to $\mu = 1$. However, our dynamical results are not consistent with this stationary discussion, which is not surprising since the phase of the responses is not instantaneous, except for the measurements set taken close to the clamping point where the slope is compatible with the above coefficients in the case of an instantaneous photothermal response. A more complete description of the dynamical heat propagation is needed to understand the evolution of the responses at lower positions along the nanowire.

The amplitude and phase evolutions of the resonantly driven lateral displacements induced by thermomechanical effects are difficult to interpret without further characterising measurements (such as elongation measurements to estimate frequency cutoff, or coloured responses to evaluate the Mie resonances contributions to the local response). Nonetheless, in the following, we will further investigate the expected behaviour of the heat diffusion dynamics under temperature dependent thermal coefficients. It will give us insights on how to interpret the measured resonantly driven thermomechanical responses.

Non-linear heat diffusion with temperature dependent heat capacity and conductivity

When considering the time variation of the heat diffusion with thermal coefficients varying with the local temperature, one can derive the **degenerate non-linear diffusion equation**,

$$\rho\, C_0\, T_{C_p}^{-\alpha}\, \partial_t \left(T^{\alpha+1}\right) - \frac{K_0\, T_\kappa^{-\alpha}}{\mu+1}\, \partial_{yy} \left(T^{\mu+1}\right) = s(y,t), \tag{6.11}$$

$$\partial_t \theta - a_0\, \partial_{yy} \theta^m = \tilde{s}, \tag{6.12}$$

where we rewrote eq. (6.11) into eq. (6.12), introducing $\theta = T^{\alpha+1}$, $m = \frac{\mu+1}{\alpha+1}$, $a_0 = \frac{K_0}{\rho\, C_0} \frac{T_{C_p}^{\alpha}}{T_\kappa^{\mu}} \frac{1}{\mu+1}$ and $\tilde{s} = s/(\rho\, C_0\, T_{C_p}^{-\alpha})$. Equation (6.12) is also known as the **Porous Medium Equation (PME)** [135, 136, 137]. This form allows to parametrize the non-linearity with only one variable, m. On the other hand it partially hides the roles played by the temperature dependencies of the heat capacity and the conductivity. Solving the PME equation for various problems is not trivial and does

not always have analytical solutions. In the following we will implement a perturbative method and will numerically solve the temperature response to a modulation of the heat source.

On the Porous Medium Equation (PME)

Besides the non-linear heat transfer, *"there are a number of physical applications where this simple model appears in a natural way, mainly to describe processes involving fluid flow, heat transfer or diffusion. Maybe the best known of them is the description of the flow of an isentropic gas through a porous medium, modelled independently by Leibenzon [367] and Muskat [394] around 1930. An earlier application is found in the study of groundwater infiltration by Boussisnesq in 1903 [123]. Another important application refers to heat radiation in plasmas, developed by Zel'dovich and coworkers around 1950 [533]. Indeed, this application was at the base of the rigorous mathematical development of the theory. Other applications have been proposed in mathematical biology, spread of viscous fluids, boundary layer theory, and other fields."* [...]*"In spite of the simplicity of the equation and of having some important applications, a mathematical theory for the PME has been developed at a slow pace over several decades, due most probably to the fact that it is a nonlinear equation, and also a degenerate one. Though the techniques depart strongly from the linear methods used in treating the heat equation, it is interesting to remark that some of the basic techniques are not very difficult nor need a heavy machinery. What is even more interesting, they can be applied in, or adapted to, the study of many other nonlinear PDEs of parabolic type. The study of the PME can provide the reader with an introduction to, and practice of some interesting concepts and methods of nonlinear science, like the existence of free boundaries, the occurrence of limited regularity, and interesting asymptotic behaviour."* Citations from [136].

Linearization of the temperature response in the non-linear case

In the case of our experimental setup, we modulate the heat source harmonically. We now look for the dynamical response for small perturbation around a stationary profile in the case of temperature dependent thermal conductance and capacitance in the 1D case. Let us consider the temperature solution to be in the form $T(y,t) = T_s(y) + \delta T(y,t)$, where T_s is the stationary temperature profile. The source term is considered to be a monochromatic excitation on top of a stationary source profile, $s(y,t) = s_s(y) + \delta s(y)\,\cos(\Omega\, t)$, where s_s is the stationary source profile for which T_s is the solution. The thermal coefficients become,

$$C_p(T_s + \delta T)(t,y) = C_p(T_s)(y) + \partial_T C_p(T_s)(y)\,\delta T(t,y) \tag{6.13}$$

$$= C_{p,s}(y) + C'_{p,s}(y)\delta T(y,t), \tag{6.14}$$

$$\kappa(T_s + \delta T)(t,y) = \kappa(T_s)(y) + \partial_T \kappa(T_s)(y)\,\delta T(t,y) \tag{6.15}$$

$$= \kappa_s(y) + \kappa'_s(y)\delta T(y,t), \tag{6.16}$$

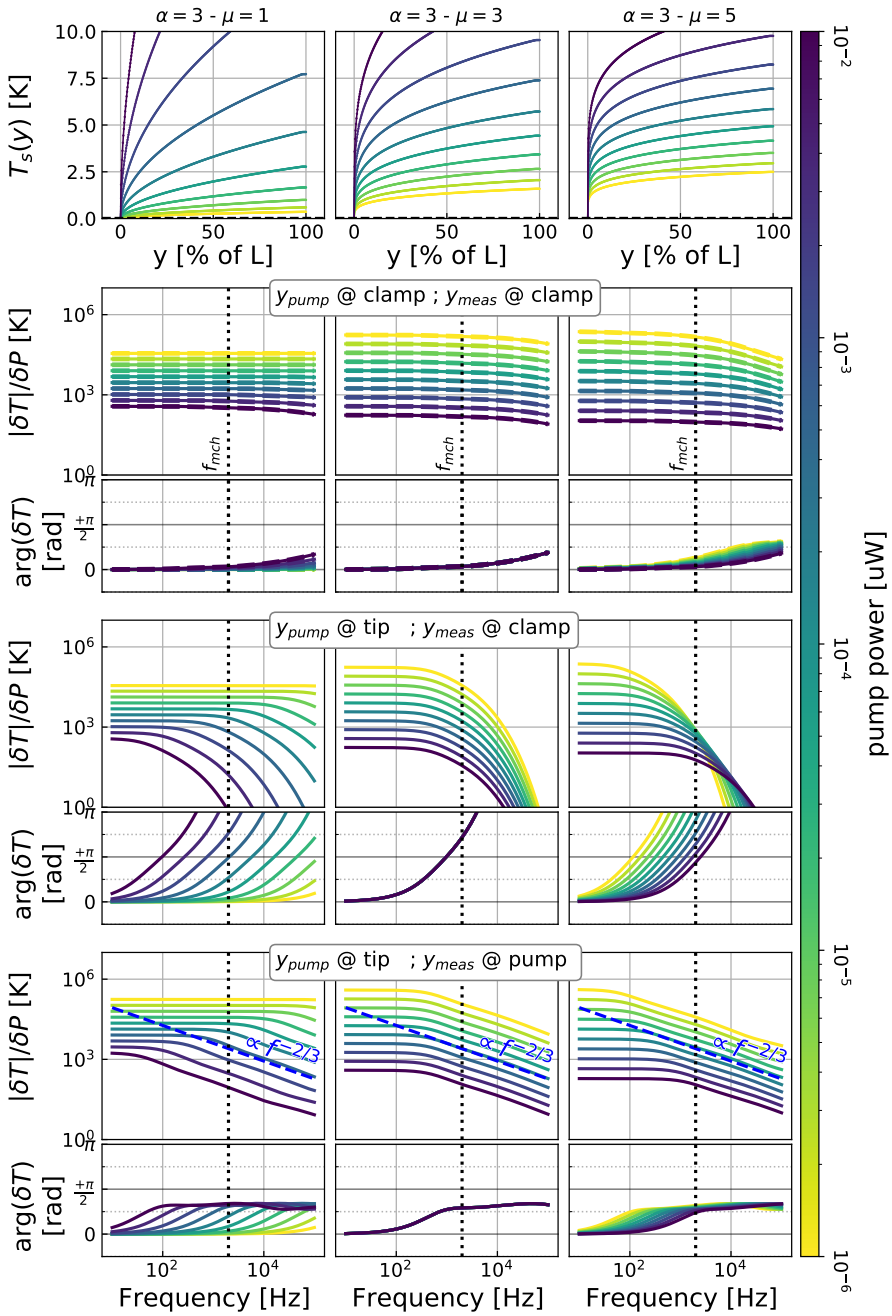

Figure 6.10: Multiple figures of the non-linear 1D heat diffusion for the case of our nanowires, shown for three sets of conductance power law of the temperature. The top panels show the static temperature profiles at different pump power when the pump is fixed at the tip of the nanowire. The following panels show the temperature response for different pump position and probe position when varying the pump power. In our model we adapted C_0 so that the thermal cutoff is comparable at different μ, and as been set between 0.1 and $0.5\,\mathrm{J.K^{-1}.kg^{-1}}$. On the other hand, K_0 is fixed at $0.15\,\mathrm{W.m^{-1}.K^{-1}}$. In this configuration, $T_{cp} = T_\kappa = 5\,\mathrm{K}$ around the working point of the nanowire noise temperature. We considered the dynamic for a nanowire of diameter 180 nm and length 200 μm.

where we denoted $C_{p,s} = C_p(T_s)$ and $\kappa_s = \kappa(T_s)$. Substituting in the 1D heat diffusion equation we develop to first order in δT the equation and get,

$$\partial_t \left[\rho\, C_p(T)\, T\right] - \partial_y \left[\kappa(T)\, \partial_y T\right] = s, \tag{6.17}$$

$$a(y)\, \partial_{yy}\delta T + b(y)\, \partial_y \delta T + c(y)\, \delta T = -\delta s(y), \tag{6.18}$$

where we used $-\nabla\left(\kappa_s\, \nabla T_s\right) = s_s(y)$, and we denoted,

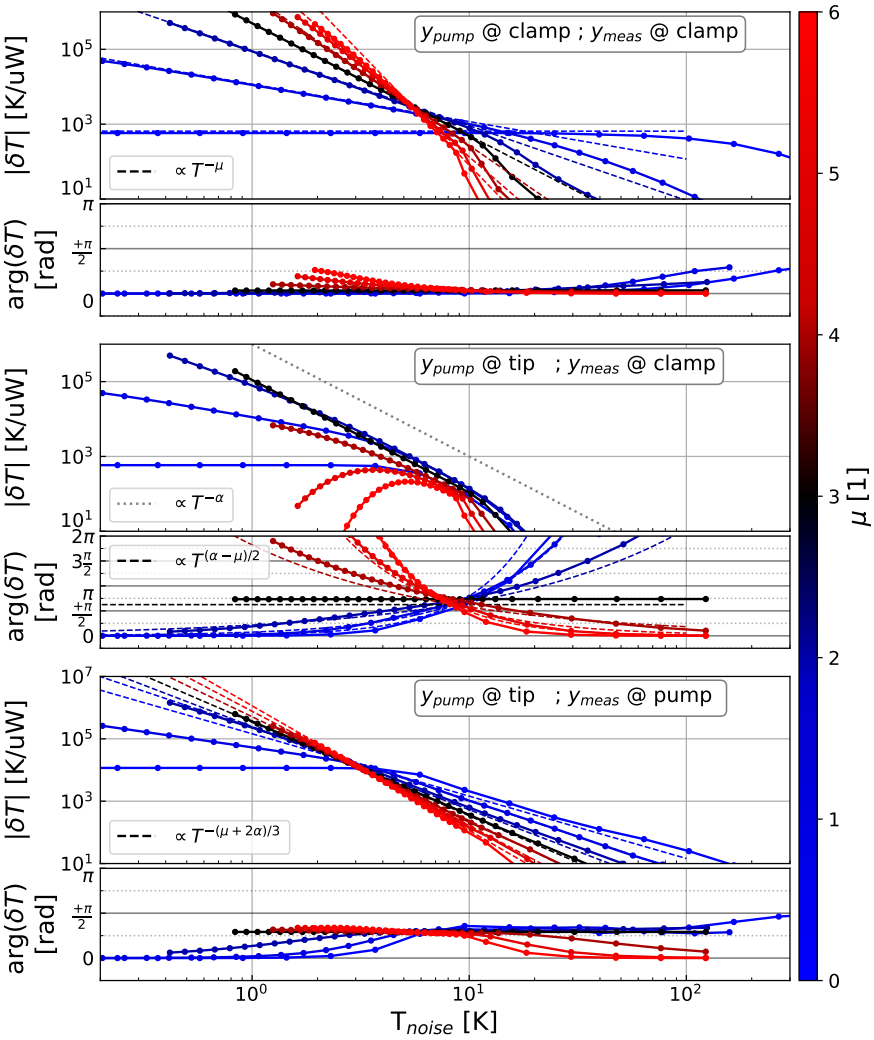

Figure 6.11: Amplitude and phase evolution of the photothermal responses evaluated at the mechanical resonant frequency of the first mode family as a function of the computed noise temperature for varying coefficients μ of the temperature dependence of the conductance. For each measurement set, the mean optical power is varied from 10^{-6} to 10^{-2} μW. In the three row panels we implemented different pump-probe position configurations where "tip" corresponds to 95% of the nanowire length and "clamp" corresponds to 5%.

$$a(y) = \kappa_s, \tag{6.19}$$

$$b(y) = \left[\partial_y \kappa_s + (\kappa_s' \, \partial_y T_s)\right] = 2\,\partial_y \kappa_s = 2\,\partial_T \kappa_s \, \partial_y T_s, \tag{6.20}$$

$$c(y) = \left[\partial_y (\kappa_s' \, \partial_y T_s) + i\,\Omega\,\rho\,\left(C_{p,s} + C_{p,s}' \, T_s\right)\right]. \tag{6.21}$$

We expressed the coefficients in terms of temperature derivative of κ and C_p for easier numerical implementation. Concerning the bound-

ary conditions, we have,

$$\delta T(0) = T(0) - T_s(0) \qquad = R_c\, S\, \kappa(T)\, \partial_y \delta T(0), \tag{6.22}$$

$$\partial_y \delta T(L) = \partial_y T(L) - \partial_y T_s(L) \qquad = 0. \tag{6.23}$$

In the particular case where the heat capacity and the conductance have a power law dependency in the temperature (eq. 6.6), the ODE coefficients simplify to,

$$a(y) = K_0 (\frac{T_s}{T_\kappa})^\mu, \tag{6.24}$$

$$b(y) = 2\,\mu\, K_0\, T_\kappa^{-\mu}\, T_s^{\mu-1}\, \partial_y T_s, \tag{6.25}$$

$$c(y) = \mu\,(\mu-1) T_s^{-2}\,(\partial_y T_s)^2 + \mu\, T_s^{-1}\, \partial_{yy} T_s + i\,\Omega\, \frac{K_0}{\rho\, C_0}\, \frac{T_{C_p}^\alpha}{T_\kappa^\mu}\,(\alpha+1)\, T_s^{\alpha-\mu}. \tag{6.26}$$

Since the stationary temperature profile and its derivative can be rather complex, we did not find an analytical solution of the above PDE. We thus implemented a numerical integration method in order to solve the temperature response at different modulation frequencies. In figure 6.10, we present several temperature response functions with varying average pump powers, while normalizing the amplitude of the modulated response by the amplitude of the pump modulation. To simplify the analysis, we did not account for a thermal contact resistance ($R_c = 0$), so that the change in dynamic is only due to the temperature dependencies of the heat capacity and conductivity. We compare those responses for different power laws of the temperature dependence of the conductance ($\mu = 1$, 3 and 5). The power law temperature dependency of the heat capacity is fixed to $\alpha = 3$, assuming a Debye like behaviour. We chose to test those three values of μ so that we expect to see the thermal cutoff decrease/being stable/increase with the optical power in each case. Indeed the diffusion coefficient, which defines the frequency cutoff of the response, scales as $\kappa/C_p \propto T^{\mu-\alpha}$. We set the constants, K_0 and C_0, so that the variation of the thermal cutoff in the tested pump power range is close to the kHz.

Once the simulation performed, we analyse the static and dynamical temperature profiles. In order to better understand our measurements, for each set of parameters, we compute the noise temperature of the nanowire from the static temperature profile, and evaluate the temperature response at the mechanical frequency.

Figure 6.11 shows the local evaluation of the resonantly driven temperature response, normalised by the amplitude of the source modulation with respect to the noise temperature working point, at multiple pump and probe position configurations. When the pump is close to the clamping area (upper plots), the thermal cutoff is generally pushed toward higher frequencies, as we already observed in our room temperature and 10 K measurement sequences. Upon changing the pump optical average power, the resonant phase does not significantly evolve, and the behaviour of the amplitude follows the one of

the DC plateau, and $\delta T/\delta P_{\text{abs}} \propto T^{-\mu}$, as discussed above in absence of contact resistance. On the other hand when the pump is positioned close to the vibrating tip of the nanowire while the temperature is probed at the clamping (bilayer configuration), we are sensitive to the shift of the thermal cutoff and the phase change follows a $T^{(\alpha-\mu)/2}$, where $\alpha - \mu$ comes from the diffusion coefficient. The amplitude behaviour gives less clear information, as the cutoff frequency passes through the mechanical frequency. Finally, if the thermal actuation is due to the temperature modulation at the pump position (bottom panel in Fig. 6.11), the behaviour of the amplitude presents a transition between a $T^{-\mu}$ to a $T^{-(\mu+2\alpha)/3}$ power law, where the latter one can be understood considering the slope of the $\delta T/\delta P$ amplitude response to be $f^{-2/3}$ after the cutoff (see bottom panels in Fig. 6.10).

Concerning the measurement presented in Fig. 6.9, the slopes of the amplitude response measured when the pump is the closest to the clamping, would suggest the conductance regime to be $\mu \simeq$1-2, which is in agreement with the $P^{1/2}$ - $P^{1/3}$ power laws observed on the heating rates from previous work.

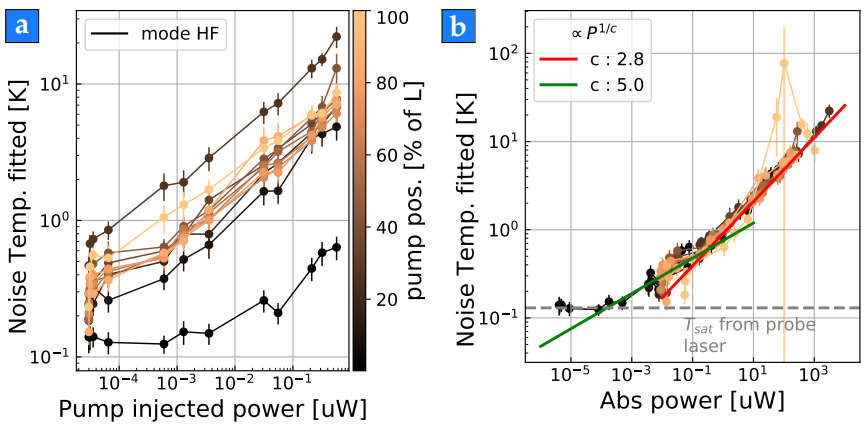

Figure 6.12: (a) Evolution of the noise temperature measured on the most visible polarisation mode with the injected optical power of the pump laser. (b) Noise temperature of the nanowire, accounting for the absorption inhomogeneities. In red line the power law for the high temperature measurements, in green the power law for the non-linear regime.

In Figure 6.12a we present the optical heating curves measured at different pump position along the nanowire. Except for the data taken when the pump is positioned the closest to the clamping area (0 % of L), we observe the heating curve to have a similar evolution with a different offset. This is most likely due to absorption inhomogeneities. For the same injected optical power, the absorbed power $P_{\text{abs}} = A_{\text{abs}} P_{\text{inj}}$ (with A_{abs} the local absorption coefficient) can vary from position to position of the pump laser along the nanowire, leading to different minimal noise temperature at the lowest optical power. In the case we assume the power dependence $T_{\text{noise}} \propto P_{\text{abs}}^{1/(\mu+1)}$ (see sec. 3.5.3), using a linear regression in log-space one can retrieve the power law coefficient and the constant part related to the absorption. For each optical heating curve, $\log(T_{\text{noise}}) = 1/c \log(P_{\text{inj}}) + B$, where c is a fitting parameter, and B an unknown constant including the local absorption. Figure 6.12b shows the corrected optical heating curves, assuming $T_{\text{noise}} = P_{\text{abs}}^{1/c}$, where we corrected the power axis by the fitted local absorption coefficient retrieved from B. The red line power coefficient was obtained with a linear regression of the point with temperature above 1 K. The optical heating measurement presented

in Fig. 6.12b seems to indicate the regimes of conductance in this temperature range follow a power law where $\mu = 1.8 \pm 0.2$, which is close to the observed value in the resonantly driven thermal response measurements.

All in all, upon observing the resonantly driven responses when the pump laser is positioned close to the clamping area, the dynamics of the thermal effects becomes quasi-instantaneous for the coldest temperatures, and the reasoning in the static limit gives a good approximation for analysing the evolution of the responses. Looking back at the data taken when the pump is positioned at the vibrating tip of the nanowire, if we consider the dominant effect to be a cross-section modulation, the slope of the resonantly driven response amplitude evolution with the noise temperature would indicate $\mu \approx 1.5$, which is also in agreement with the expected regime of conduction at those temperatures.

However, in the discussion concerning the thermal response with temperature dependent thermal coefficients (see sec. 6.2.3), one must note we have not yet taken into account the possible variation of the thermal contact resistance with temperature in our model. Indeed, in those regimes of temperature, one expects the thermal contact to change and the heat transfer to be reduced with a decreasing temperature. Kapitza resistance vary in T^{-4} of the material temperature at the contact and is expected to become dominant at low temperatures. As discussed, this is likely the origin of the plateau in $P^{1/5}$ observed in the heating curves, where the effective conductance of the nanowire is not limited by the internal conduction but by the heat transfer at the contact. Further investigations to account for such possible dynamics will soon be carried out.

6

6.3 Frequency shift with temperature

High quality factors and stable oscillators are essential for the detection of weak frequency shifts used in force sensing and mass detection purposes. Moreover, the frequency is very sensitive to external and internal changes in the experiment, with sensitivities to force gradients approaching the fN/m level in 40 s at the coldest temperatures employed. Also, the oscillator frequency varies with temperature (see Fig. 6.13a and 6.13b), due to temperature dependent quantities such as the Young modulus E, the contribution from amorphous defects, *etc.*..., and it can thus also provide interesting thermometric information at the condition to characterise this evolution. In the following, we will denote the relative frequency shift of a mechanical mode n by,

$$\frac{\delta f}{f_{0,n}} = \frac{f_n - f_{0,n}}{f_{0,n}} = \frac{\Omega_n - \Omega_{0,n}}{\Omega_{0,n}}, \tag{6.27}$$

with $f_{0,n}$ the resonant frequency of the mode taken at a given reference point.

In parallel to those frequency shifts, on can also observe modifications of the mechanical oscillator damping rates, see Fig. 6.13c. Damping mechanism at low temperature limits the intrinsic quality factor of nano-resonators. Those mechanisms can have multiple

origins : clamping losses, acoustic emission in the surrounding gas, phonon-phonon interaction ("higher order phonon process" more generally), thermoelastic damping, Akhiezer damping [138, 139]. For amorphous or partly amorphous nanomaterials (produced from micro and nanofabrication techniques), the dominant damping contribution is a coupling between the deformation strain due to mechanical oscillation and low energy excitations in the medium [140], often associated to atomic conformation changes in the material. Those low energy excitations can be modelled as an assembly of Two Levels Systems (**TLS**).

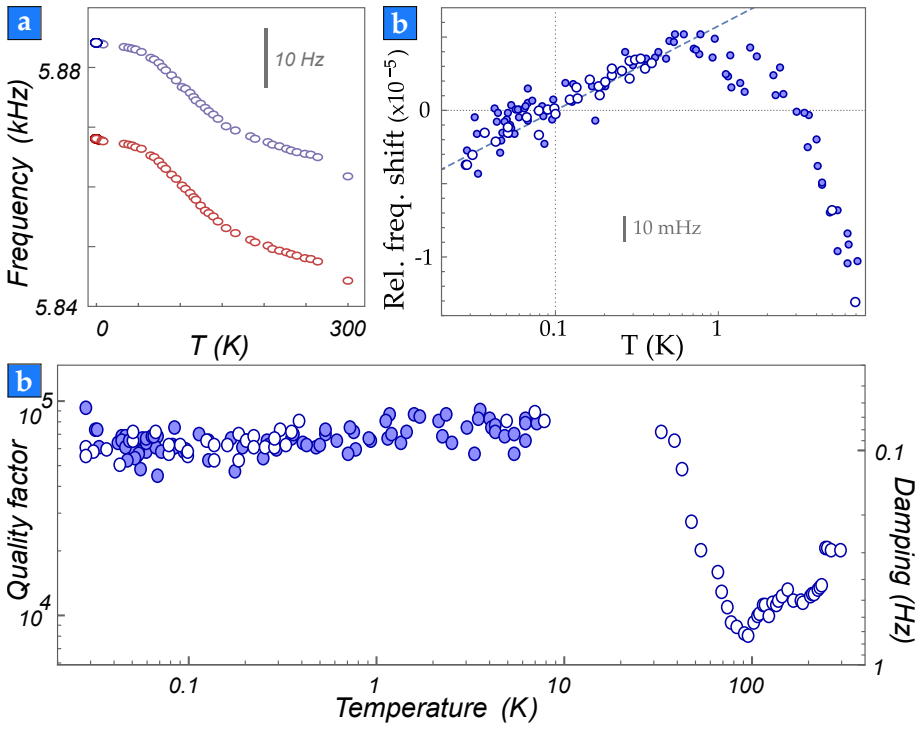

Figure 6.13: (a) Frequency shifts of the mechanical modes of the first longitudinal family from room temperature to kelvin one, and zoom for sub-kelvin temperature in (b). (c) Evolution of the mechanical quality factor with the cryostat temperature. (figures adapted from F. Fogliano [91])

6.3.1 Two level system (TLS) contribution

The interaction between the phonons associated to the mode of interest and the internal dynamics of the amorphous material, is modelled by a strain wave interacting with an assembly of TLS, which was originally intended to describe the internal conformational changes, but remains valid for many other internal degrees of freedom. When the strain wave interacts with the TLSs it may lose a bit of energy, and this interaction is also responsible for a modification of the speed of sound in the material. One can distinguish the relaxation regime which arises when the phonon frequency is very different from the TLS frequency splitting, and the resonant regime when both frequencies are identical and where the interaction takes a Jaynes-Cummings like form [141].

Tunnelling Two-Level System (**TTLS**) damping occurs because the energy levels of the TTLS couple to the vibrational motion of the mechanical oscillator through the local strain field. This coupling is quantified by a coupling constant, γ, which depends on the dimensionality, the structure and various other parameters. Thus, γ is often measured

instead of being predicted. There are two main mechanisms that have been developed in the literature [101, 102, 142, 143] to account for such damping : the **relaxation absorption** through the modulation of the TTLS energy levels by the modulation of the strain field, and the **resonant absorption** when the equivalent frequency of the TTLS absorption energy $\epsilon_0 = \hbar\,\omega_0$ is close to the mechanical mode frequency.

In the Low Temperature regime, it is the resonant interaction that dominates the frequency shifts, leading to the theoretical logarithmic trend, which has been largely observed in numerous experiments [144],

$$\frac{\delta f}{f_0} = C\,\ln\left(\frac{T}{T_0}\right), \tag{6.28}$$

where C and T_0 are constants. The constant C was found to be quasi universal for many kinds of glass types, and is directly proportional to the density of TLS in the material. Looking at the low temperature relative frequency shifts of our nanowires, see Fig. 6.13b and 6.14, we recognize the logarithmic trend, but with a constant being only 1% of the values found in the literature [144]. Our 3C-SiC nanowires are known to present an oxide crust at their periphery, as observed in TEM measurements, with a thickness of up to 10 nm. The reduction in the constant could thus be attributed to this partially amorphous character of our otherwise crystalline resonators.

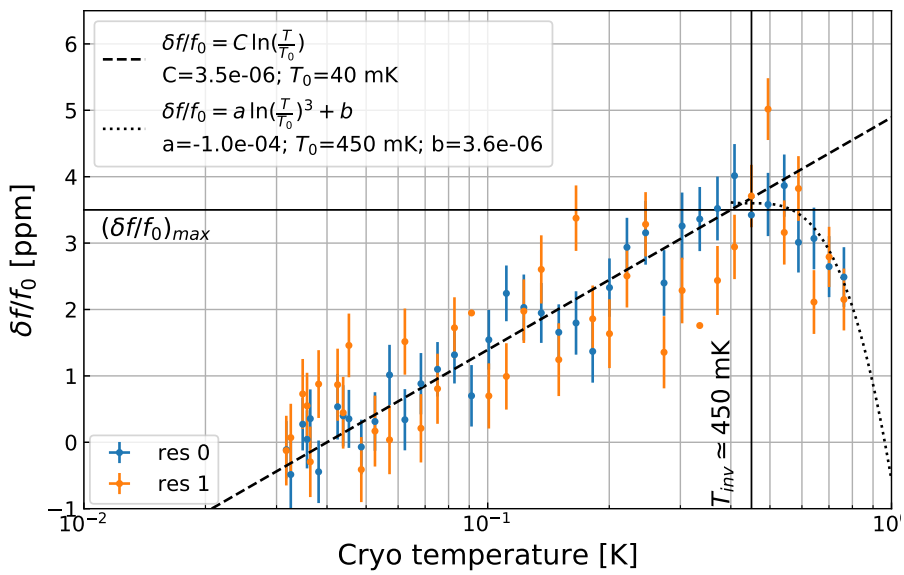

Figure 6.14: Relative frequency shifts of the two mechanical polarisation modes of the fundamental mode family of a nanowire of diameter 180 nm and length 200 μm. We swept the cryostat temperature and measured the relative frequency shift. The dashed line represents the TLS model with a constant $C = 3.5 \times 10^{-6}$. The dotted line is a phenomenological model.

The interaction to the TLSs is also responsible for a characteristic evolution of the Q factor with temperature [144], whose analysis could also be of interest to investigate the internal temperature properties of the nanowires. However, we observed that at temperatures below 10 K, the damping rate of the nanowires remains unchanged, suggesting a possible limitation by clamping losses (to $Q \simeq 10^5$). If such losses are the dominant source of damping, it would suggest the noise temperature to be fixed at the clamping area, as in the FDT the damping provide the weighting of the temperature profile for the position fluctuation [145]. As such there is not much information to

obtain from the dissipation of the nanowires, and we will mainly focus on the analysis of their frequency shifts.

6.3.2 Non-homogeneous temperature profile

It has been observed that the frequency shifts induced by thermal heating can be mode dependent in mechanical oscillators [41, 145]. Those observations led to an investigation on how the temperature profiles inside the resonator impacts their resonant frequencies, in the case of simple geometries. The effect of the inhomogeneous temperature profile to the frequency shift has been well studied in ref. [41], and we will thus briefly adapt their findings to our nanowire resonators.

We denote the thermal coefficients of the Young modulus, α_E, and of the expansion, α_l for the material,

$$\alpha_E(T_0) = \frac{1}{E_0}\frac{\mathrm{d}E}{\mathrm{d}T}\bigg|_{T=T_0}, \qquad \alpha_l(T_0) = \frac{1}{l_0}\frac{\mathrm{d}l}{\mathrm{d}T}\bigg|_{T=T_0}, \tag{6.29}$$

where E_0, l_0 are the reference quantity at T_0. Those intrinsic quantities appear in the Euler-Bernoulli equation, through the Young modulus E, the mass distribution ρ, and the second moment of inertia, $I = \frac{\pi r^4}{4}$. The Young modulus temperature dependency for SiC nano-resonators has been scarcely studied [146]. The difficulty for reliable experimental setup is a limiting factor: the measured values are strongly defect depend, the difficult estimation of the effective cross-section within the measurement method, and a good thermomechanical control over the experiment. Nonetheless, from 200 K to $R.T$ the temperature coefficient of the Young modulus is in the range $\alpha_E \in [-79, -40] \times 10^{-6}\,\mathrm{K}^{-1}$ [146, 147].

Let us consider a small temperature elevation profile along the nanowire denoted such as,

$$T(y) = T_0 + \delta T(y). \tag{6.30}$$

The resonator properties undergo a change expressed by,

$$E(y) = E_0\,(1 + \alpha_E\,\delta T(y)), \tag{6.31}$$
$$I(y) = I_0\,(1 + 4\,\alpha_l\,\delta T(y)), \tag{6.32}$$
$$(\rho\,S)(y) = \rho_0\,S\,(1 - \alpha_l\,\delta T(y)), \tag{6.33}$$

with $S = \pi R^2$ the nanowire cross-section. The new nanowire length is extended due to thermal expansion and becomes $L = L_0 + \alpha_l \int_0^{L_0} \delta T(y)\,\mathrm{d}y$. Without going into the details of the calculation, see ref. [41], when the perturbations are sufficiently small ($\alpha_E\,\delta T \ll 1$ and $\alpha_l\,\delta T \ll 1$) one can express the induced frequency shift at first order:

$$\frac{\delta f}{f_{0,n}} = \frac{1}{2}\int_0^L \left[A_E(\delta T(y))\, s_n(y) + A_l(\delta T(y))\ \left(4\, s_n(y) + c_n(y) - 4\right)\right] \mathrm{d}y, \tag{6.34}$$

$$A_E(\delta T) = \int_{T_0}^{T_0+\delta T(y)} \alpha_E(T)\, \mathrm{d}T, \qquad A_l(\delta T) = \int_{T_0}^{T_0+\delta T(y)} \alpha_l(T)\, \mathrm{d}T, \tag{6.35}$$

$$s_n(y) = \frac{(\partial_y^2 u_n(y))^2}{\frac{1}{L}\int_0^L (\partial_y^2 u_n(y))^2\, \mathrm{d}y}, \qquad c_n(y) = \frac{u_n(y)^2}{\frac{1}{L}\int_0^L u_n(y)^2\, \mathrm{d}y}, \tag{6.36}$$

where u_n are the unperturbed normal modes of the oscillator and s_n, c_n their normalised squared curvature and deformation profiles, while A_E, A_l are the cumulated perturbations when α_E, α_l are temperature dependent. The appearance of the curvature profile can be understood considering that a change in elasticity will affect the potential strain energy. Region of low strain, *i.e.* low curvature, will not contribute as much in the total potential energy. Likewise, the dimension modulation modifies the momentum of inertia and the local mass density, which plays a role in the kinetic energy, leading to this weighting by the squared deformation amplitude. Lastly, a change in the nanowire length will directly affect the resonant frequency mode as it is involved in the boundary conditions that gives the resonant frequencies, $k_n L$.

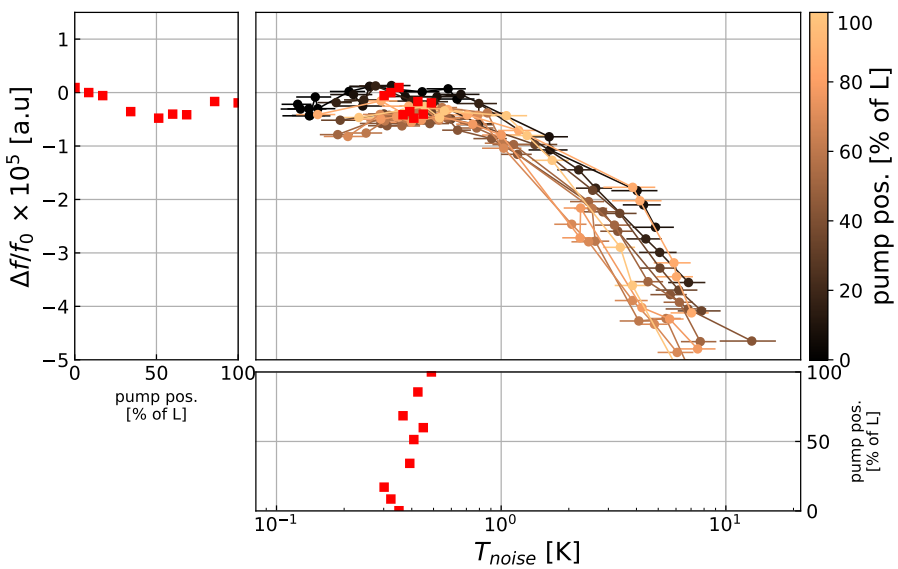

Figure 6.15: Relative frequency shift of the first resonant mode with temperature at different pumping positions along the nanowire length. We change the noise temperature by increasing the mean optical power of the pump laser, from 30 pW to 0.8 μW. The local maxima of each measurement is shown with red squares, and are plotted with respect to the pump laser position.

In the case of our SiC nanowires, the thermal expansion is 10 times smaller than the relative Young modulus temperature change, and the dominant contribution in the oscillator frequency shift is the softening of the material. This is confirmed by having the nanowires resonant frequencies decreasing when the temperature increases, which relate to the sign of the thermal coefficients. Thus, the eq. 6.34 can be re-

duced to,

$$\frac{\delta f}{f_{0,n}} = \frac{1}{2} \int_0^L A_E(\delta T(y))\, s_n(y)\, \mathrm{d}y. \tag{6.37}$$

In Figure 6.15 we present the measurement of the relative frequency shifts as a function of the noise temperature (nanowire-20200910) while increasing the pump power and this for different pump positions along the nanowire length. The frequency shifts as well as the noise temperature are extracted from the thermal noise measurements. Here we chose to compare the frequency shift with the noise temperature so as not to be sensitive to the absorption non-homogeneity along the nanowire. At all positions, we observe a characteristic frequency shift inversion but with a systematic trend: the curves taken with the laser far from the clamping position present a smaller inversion frequency, which are attained at larger optical powers. The global translation of each frequency shift measurement when moving the pump laser can be attributed to the non-linear temperature profile inside the nanowire.

One can note that the maximal frequency shift is obtained when the laser is positioned close to the clamping point: in that situation, the temperature within the nanowire is supposedly homogeneous, so that when the noise temperature reaches the temperature of the frequency shift trend inversion, almost the entire nanowire is found at that same temperature, so we are in a similar configuration of Fig. 6.14, when the cryostat temperature is raised to that precise temperature. The situation is different when the heating laser is positioned further apart from the nanowire: in that situation we are not any more in the quasi homogeneous temperature profile, and when the frequency shift reaches its maximal value, it is only a little fraction of the nanowire that is found at the extremum temperature, in all other areas the temperature is different, leading to a smaller frequency shift in the weighted integral. The same reasoning explains the apparent displacement at higher temperatures of the extremum point: when the laser is not located at the clamping point, the situation where the frequency shift is extremum corresponds to a warmer temperature at the nanowire vibrating extremity, which increases more the noise temperature than when the temperature profile is more homogeneous.

As discussed, we can have a qualitative understanding of the measurements. The ingredients for a more quantitative interpretation have been introduced, but it is important to keep in mind that the optical force gradients, even if very small at those optical powers, are still largely detectable by our nanowires: the demonstrated force gradient sensitivity of a few fN/m in 40 s [91] achieved when using PLLs, is indeed comparable to the radiation pressure force gradients caused by a $P = 1\,\mathrm{pW}$ laser beam focussed on a waist w_0 of 500 nm ($P/c/w_0 \simeq 6\,\mathrm{fN/m}$). As such, such an analysis should always be completed by a precise estimation of the surrounding force gradients.

6.4 Dynamical investigation of the photothermal modulation of the mechanical resonance

In this section, we present a different characterisation measurement exploiting the dynamical response of the oscillator frequency shift to the laser-induced temperature modulation. To do so, we first drive our nanowire with a reference force (an electrostatic force here produced by applying a voltage modulation on a nearby electrode) and read the induced vibrations with a red probe laser positioned at its vibrating extremity. This reference drive can be used to turn a PLL on to get rid of slow frequency shifts, but most of the measurements were carried out without frequency feedback. Then we position the pump laser close to the nanowire extremity, and add a power modulation tone. Those measurements are carried on at room temperature, on the historical experiment of PhD P. Heringlake, where the mechanical frequency is known to decrease with temperature. The

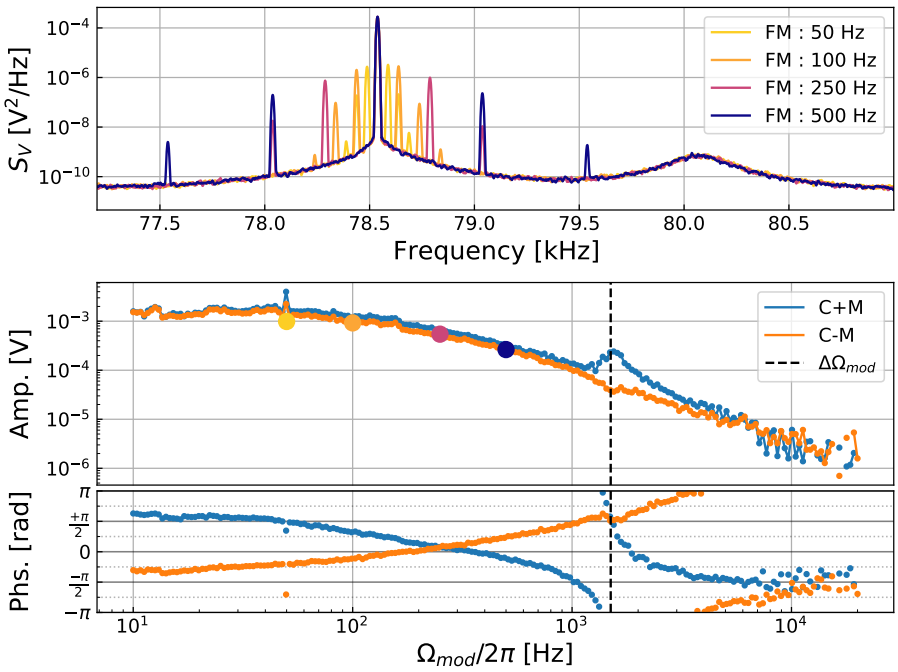

Figure 6.16: Measurement (at room temperature) of the thermally induced frequency modulation sidebands. On the top panel is the PSD of the lateral displacement measured with the red probe laser for different optical intensity modulation frequencies of the pump laser, at fixed modulation depth. The frequency modulation is responsible for the apparition of sidebands. In addition, the nanowire is driven by a fixed electrostatic force, the carrier tone. The amplitude of the first sidebands measured in the PSD is reported in the bottom panel (dot markers), where we also present the demodulation of the upper and lower (C+M and C-M) thermally induced sidebands. The dotted line indicates the frequency splitting between both mechanical polarisations, which only affects the upper sideband demodulation.

temperature modulation induced by the pump beam will thus create a frequency modulation which, if the modulation frequency is slow enough compared to the thermalisation time (ms here), will generate a modulation of the mechanical resonance. On the contrary, when the optical modulation frequency becomes larger than this thermal frequency cutoff, the effect is expected to become less and less efficient. In our experiment, the mechanical line width is around 10-20 Hz, so the induced frequency modulation will be faster than the mechanical response time, meaning that it will become visible as sidebands to the central driving tone. In this section we analyse how those sidebands can be exploited to reconstruct the photothermal response of

the nanowire.

Sideband modulations

In sec. 6.3 we showed measurement of our nanowires relative frequency shifts. Between room and low temperature (1 K), this frequency is determined by the temperature profile that establishes inside the nanowire. Upon driving our nanowire at resonance with an external source such as an electrostatic tip, while modulating the pump optical power in order to induce thermal waves inside the nanowire, we observed sidebands to the central peak, separated by the optical power modulation frequency. Figure 6.16 presents the analysis of the sidebands, in amplitude and in phase (with respect to the pump power modulation) for varying modulation frequencies.

The sidebands strengths are directly correlated to the frequency shift caused by the photothermal modulation. Modulating the pump power intensity generates a stationary temperature profile, $\delta T[\Omega](y)$. Using eq. 6.34, one can retrieve the expected frequency shift, $\delta\Omega_{m,n}[\Omega]$, in response to the temperature modulation. It depends on the pump position along the nanowire, on the temperature profile and on the modulation frequency. Assuming that the effects of the thermal softening are dominant in the frequency shift at room temperature compared to the dimensional changes, one can estimate the relative frequency shift induced by thermal modulation with,

$$\frac{\delta\Omega_m}{\Omega_m}[\Omega] = \frac{1}{2}\int_0^L \alpha_E\, \delta T[\Omega](y)\, \frac{(\partial_{yy} u_n(y))^2}{\frac{1}{L}\int_0^L (\partial_{yy} u_n(y))^2\, \mathrm{d}y}\, \mathrm{d}y, \tag{6.38}$$

where u_n the mode amplitude, and α_E the Young modulus temperature coefficient. Figure 6.17 shows the demodulated dynamical frequency shift measured in response to a temperature modulation when the pump position is scanned along the nanowire length. The strain profile being maximal at the clamping point, the response curves are very similar to the bilayer effect which samples the temperature profile close to the clamping point: one observe the characteristic plateau arising at intermediate frequencies in the phase response when the pump laser is approaching the clamping area. The inflexions observed

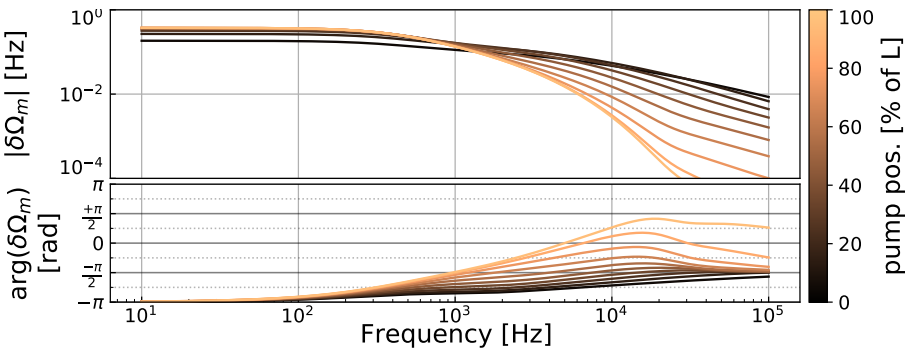

Figure 6.17: Theoretical Bode diagram of the dynamical relative frequency shift undergone by a nanowire under photothermal induced temperature modulation for varying pump laser positions along the nanowire.

at higher frequencies differ from the previous curves and are due to the non-local character of the strain weighting of eq. (6.38).

We will now present how one can retrieve the frequency shift modulation strength from the sideband modulation experiment, via a numerical simulation of the system.

Externally driven mechanical oscillator subjected to a frequency modulation

Frequency modulation has a wide spectrum of application, especially in engineering physics and further. It has been used in laser stabilisation [148], spectroscopy [149], communication [150], electronic music generation [151]. However, in most cases, frequency modulated signals are generated by a phase modulation of the carrier, and methods of analysis are not adapted to our system.

In this section, we investigate the dynamics of a 1D mechanical oscillator, subjected to a thermally induced frequency modulation while resonantly driven by an external force (whose frequency is chosen close to the unmodulated resonant frequency). We will analyse how the generated sidebands depend on the frequency modulation strength and on the modulation frequency

The dynamics of the system can be described by the differential equation,

$$\partial_t^2 x + \Gamma\, \partial_t x + (\Omega_\mathrm{m} + \delta\Omega_\mathrm{m}[\Omega_\mathrm{mod}]\, \cos(\Omega_\mathrm{mod}\, t + \phi_\mathrm{m}[\Omega_\mathrm{mod}]))^2\, x = \frac{\delta F}{M_\mathrm{eff}}\, \cos(\Omega_\mathrm{d}\, t). \tag{6.39}$$

where x is the observable (in our case the lateral displacement of the nanowire tip), $\Gamma/2\pi$, $\Omega_\mathrm{m}/2\pi$, M_eff are the damping rate, the natural frequency and the effective mass of the oscillator respectively, δF is the external drive acting on the oscillator observable modulated at Ω_d. The other parameters appear when we consider the oscillator frequency modulated at a frequency $\Omega_\mathrm{mod}/2\pi$ with amplitude $\delta\Omega_\mathrm{m}/2\pi$ and ϕ_m are both the amplitude and phase of the thermally induced frequency modulation, when the pump optical power is modulated at Ω_mod. In the particular case where we resonantly drive the oscillator with an external force ($\Omega_\mathrm{d} = \Omega_\mathrm{m}$), the drive is periodically in and out of resonance with the oscillator, and we generate sidebands in the PSD, see Fig. 6.18.

In our case, we want to compute the demodulated signal recorded by the Zurich Instrument demodulator, which formally demodulates the projected position $\delta r_\beta(t)$ ($\delta x(t)$ here) at the frequencies $\Omega_d \pm \Omega_\mathrm{mod}$, with a phase reference being the one of the output used to modulate the optical power. After having numerically solved the above equation, we thus compute the demodulated quantities,

$$\mathrm{Re}\,(\mathrm{SB}[\pm\Omega_\mathrm{mod}]) = \frac{1}{T}\int_0^T \delta x(t)\cos((\Omega_\mathrm{d} \pm \Omega_\mathrm{mod})\, t)dt, \tag{6.40}$$

$$\mathrm{Im}\,(\mathrm{SB}[\pm\Omega_\mathrm{mod}]) = \frac{1}{T}\int_0^T \delta x(t)\sin((\Omega_\mathrm{d} \pm \Omega_\mathrm{mod})\, t)dt, \tag{6.41}$$

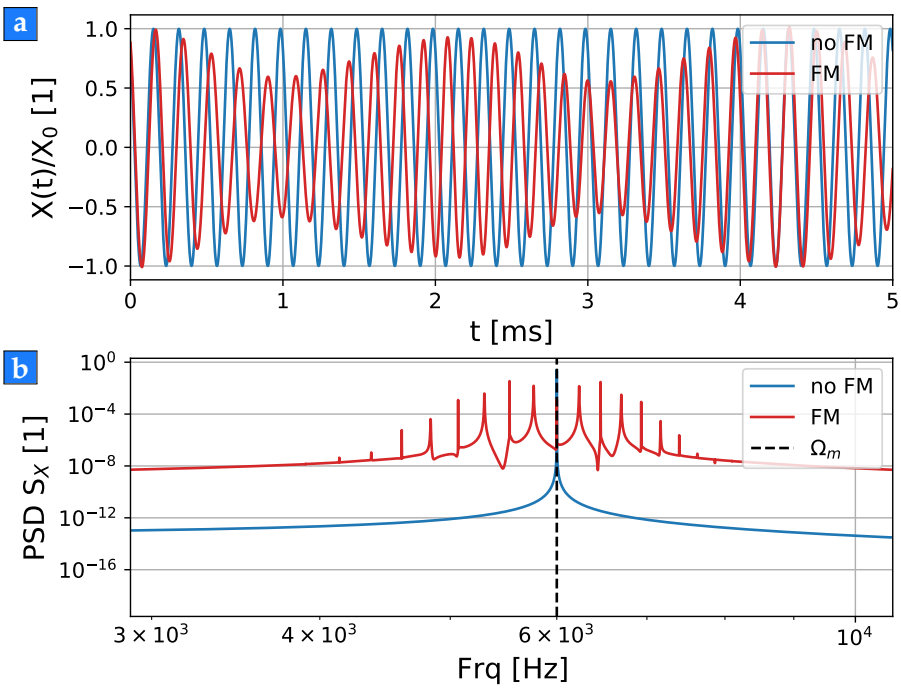

Figure 6.18: Numerical integration of equation 6.39. (a) Comparison of the time oscillations when the FM is on (red line) or off (blue line). (b) Computed PSD of the time signal for the two cases.

with T the sample duration (preferably an integer number of the oscillation period), SB the complex quadrature of the demodulated signal. We subsequently evaluate the amplitude and phase of both demodulated signals.

Figure 6.19 shows the evolution of the demodulated signals of the first sidebands when scanning the frequency $\Omega_{\text{mod}}/2\pi$ of the FM. For the sake of clarity we only show the C+M sideband demodulation, since its counterpart C-M is its complex conjugate. In the upper panel, we vary the damping rate Γ, while we vary the modulation strength $\delta\Omega_{\text{m}}$ in the bottom panel. When varying $\delta\Omega_{\text{m}}$, we observe that the sideband strength increases at low frequencies for smaller damping rates, which is a consequence of the increased mechanical response to the driving tone. In parallel, the bandwidth of the response behaves as a first order low pass filter, as long as $\delta\Omega_{\text{m}}$ remains smaller than Γ, otherwise the modulation strength becomes too large, and we observe folding due to the Bessel function cancellations. One can thus discriminate two regimes whether the damping rate Γ is larger or smaller than the amplitude of the modulated frequency shift. In the former case, the demodulated signal behaves as a first order low pass filter. When the frequency modulation is larger than the damping rate, one needs to account for cancellations that involves Bessel's functions, a recurrent feature of FM. On the other hand the phase of the sideband demodulation shows a similar first order low pass behaviour, still in the case where $\delta\Omega_{\text{m}} < \Gamma$.

As long as the modulation strength remains sufficiently small to avoid the unfolding of the Bessel functions, we found that the sideband strength can be well described by the expression,

$$\text{SB}_n[\Omega_{\text{mod}}] = \frac{\delta F}{2\,M_{\text{eff}}}\,\frac{1}{\Omega_{\text{m}}\,\Gamma}\left|\left(J_0\left(\frac{\delta\Omega_{\text{m}}}{\Omega_{\text{mod}}+i\Gamma/2}\right)J_n\left(\frac{\delta\Omega_{\text{m}}}{\Omega_{\text{mod}}+i\Gamma/2}\right)\right)\right|, \tag{6.42}$$

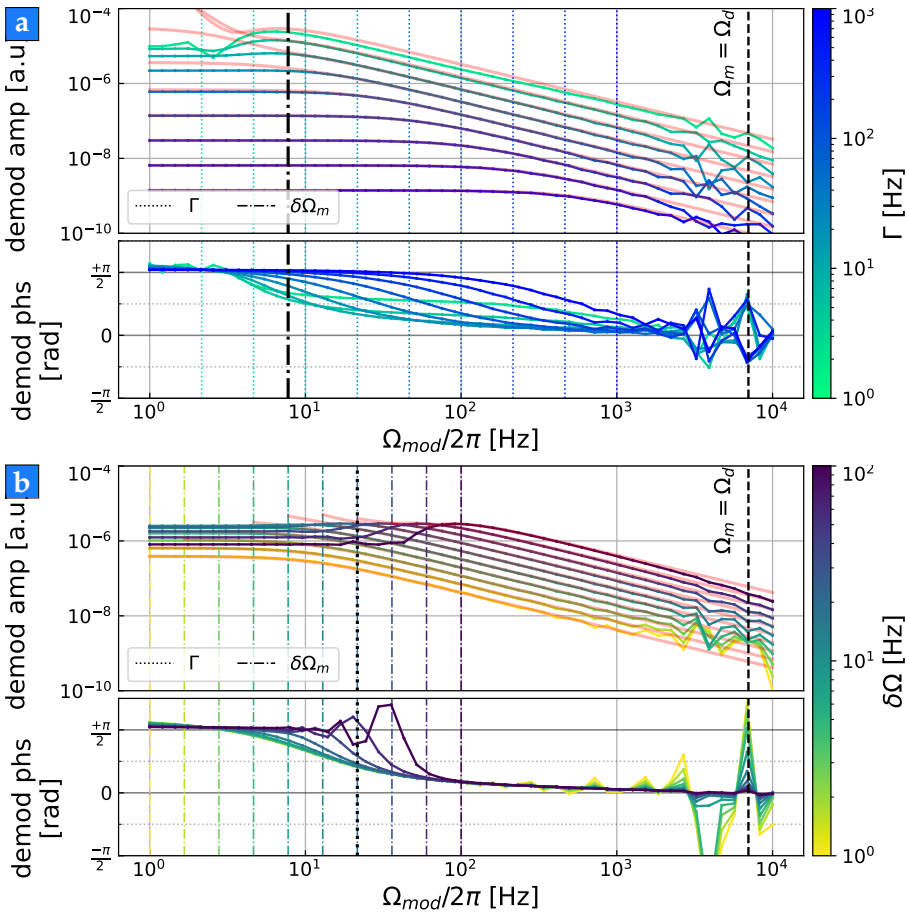

Figure 6.19: Numerical computation of the quadratures (amplitude and phase) of the demodulated C±M sideband at $\Omega_d \pm \Omega_{mod}$ computed from the numerical resolution of eq. (6.39), while varying some parameters: (a) we vary Γ (for each curve, the value of Γ is indicated by a dashed coloured line), (b) we vary $\delta\Omega_m$ which are taken as a constant of the FM frequency (for each curve, the value of $\delta\Omega_m$ is indicated by a dot-dashed coloured line). In both cases, the external drive modulation strength is kept identical for all modulation frequencies. The red curves represent the simplified expression of eq. (6.42), which provides a good agreement with the numerical results as long as the modulation strength is not too large.

6

with δF the driving force, n the number of the considered sideband. The red lines in Fig. 6.19 correspond to that expression. This expression can be inverted (as long as we remain far from the unfolding of the Bessel functions) and thus allowing us to retrieve the frequency shift $\delta\Omega_m[\Omega_{mod}]$ at each modulation frequency, knowing the damping rate of our nanowires. In Figure 6.20a, we show the difference between the measured sideband strength, and the expression 6.42 (vertically adjusted to match the low frequency response). The latter assumes that the modulation strength is constant with the modulation frequency, we see that this is the case up to a few hundred Hertz, but beyond that, the demodulated amplitude gets reduced, before reaching a frequency range, above 1 kHz, where both curves do present identical evolutions. We reconstructed the modulation strength, and is shown in Figure 6.20b, which presents the extracted normalised amplitude of the frequency modulation depth. For comparison, we also show the expected modulation depth $\delta\Omega_m[\Omega_{mod}]$ deduced from the simulations shown in Fig. 6.17.

The extracted amplitude frequency modulation shows a good qualitative agreement with the expected photothermal response at low frequencies, but presents a plateau at larger modulation frequencies. We have some reasons to believe that the latter could be the contribution of the optical force field gradients, which modulate the nanowire frequency with a flat response, on mechanical time scales. However, we

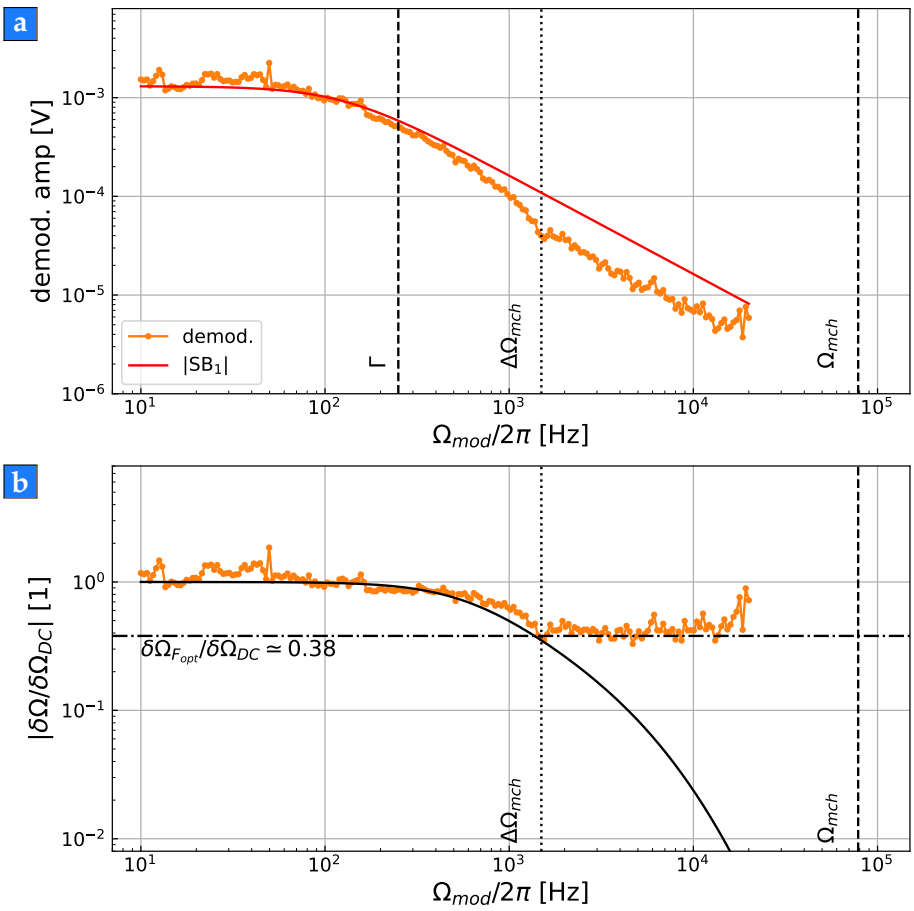

Figure 6.20: (a) Amplitude of the measured sideband C-M response. The red line is the conjectured model for a constant modulation depth $\delta\Omega_m$. (b) Extraction of the frequency modulation depth as a function of the modulation frequency. The black curve represents the expected frequency modulation depth, when positioning the laser close to the nanowire vibrating extremity and adapting the thermal parameters in the simulation of the temperature profile. The damping rate $\Gamma/2\pi$ is independently determined from the noise spectrum measurements. We denoted $\delta\Omega_{F_{opt}}$ the frequency shift generated by the optical forces, which are expected to be flat in frequency.

will need other measurements to confirm this point and further exploit this measurement technique. Still, the measurement of the thermally induced frequency modulation seems to provide another method to probe the temperature dynamics inside our nanowires. Already, static measurements of the frequency shift profile induced by optical heating, led to a valuable imaging of the nano-resonators internal properties at high temperatures [37, 41]. This technique will be subjected to further investigation at dilution temperatures, since the nanowires do present a systematic frequency shift with the temperature, while we have shown that one can drive them mechanically to very large amplitudes, without suffering from an increase of their noise temperatures [91], due to the very low dissipation rates.

6.5 Chapter summary

In this chapter we investigated how the photothermal effects evolve at low temperature, using the same nanowire and pump-probe technique used in the study described in sec. 5.4. We first observed a remarkable increase of the photothermal effects efficiency at driving the nanowire lateral deformation. We also show that, at medium noise temperatures, we become much more sensitive to the thermal contact resistance. This demonstrates the increasing sensitivity to the optical

absorption at lower temperature. In the future, we would greatly benefit from implementing elongation response measurements in order to better characterise the contact resistance temperature evolution.

Indeed, although the measurements at low temperature are presented last in the manuscript, they were performed first in chronological order. Only latter on, we improved and developed tools at room temperature to better characterise and calibrate several thermal mechanisms that would explain the photothermal effects observed at low temperatures. In addition, the contribution of the different photothermal mechanisms can vary greatly from room to low temperature. We also showed pieces of evidence that the main photothermal mechanisms driving the resonance of the nanowire, can change while scanning the pump position.

On top of that, the photothermal response evolves greatly with the mean pump optical power at fixed pump position, suggesting we are sensitive to non-linear effects. At low temperatures, we expect the temperature dependence of the heat capacity and heat conductivity to be noticeable when modulating the temperature around a cold averaged static temperature profile. We changed the linear heat propagation to a non-linear diffusion problem, laying the ground to better understand the evolution of the responses with the noise temperature of the nanowire.

At last, we conclude the chapter introducing a new measurement method using the thermally induced frequency shift of our nanowires resonant families. We explored this method at room temperature making use of an electrostatic tip driving the mechanical resonance while modulating the resonant frequency using the absorbed light from the pump laser. The study of the frequency shift response is then carried out through the response behaviour of the subsequent generated sidebands, when scanning the optical power modulation frequency. Doing so we take advantage of the nanowires quality factor increasing the SNR, which is expected to greatly improved at low temperatures. This technique allows to probe a different coupling between the temperature response and the nanowire thermal properties, and allows probing the material response to the temperature change.

CONCLUSION AND PERSPECTIVES

In this thesis work we investigated several aspects involved in the photothermal responses of our SiC nanowires consecutive to light illumination. The understanding of the optical interaction and light absorption on the nanowire properties is essential to properly operate the nanowires as ultrasensitive force field sensors at dilution temperatures. In that view, we made use of pump-probe response measurements, to separate the readout and the actuation channels and obtain a better understanding of the thermal waves produced upon absorption of a dynamically modulated pump laser beam. We also investigated how the different mechanical properties of the nanowires (resonant frequencies, noise temperature, *etc*) were affected by the light, and in particular investigated the role of internal optical resonances that strongly structure their photothermal and optomechanical responses.

Optical interaction of the nanowire

The optical interaction of our SiC nanowire with the pump and probe light fields is strongly structured by internal optical resonances, called the Mie resonances, which in turn impact their photothermal response. We designed a new experimental setup that allows the measurement of the far field angular scattering diagrams of a nanowire illuminated by focused gaussian beam at different colours. This allowed to clearly identify the role of the internal optical resonances in the light-nanowire interaction. This setup along with the data analysis process, offers a colorimetric independent method to measure optically the subwavelength-sized diameter of our nanowires.

Perspectives

The improved determination of the light-nanowire interaction should help us in the observation of exotic optical forces, such as optical pulling forces which are anticipated when exploiting higher order Mie resonances [92]. A. Reigue (post doctorate) already began the numerical simulations' implementation of the scattering properties under a gaussian illumination, where the gaussian beam is projected on the plane wave basis. He could simulate advanced phenomenological observations measured in our cavity nano-optomechanical experiment based on fibre microcavities [76]. He could also compute the effec-

tive reflection coefficient of the nanowires in the interferometric readout measurement setup, in order to determine the nanowire diameters that optimize the readout efficiencies. Further development will help better understanding the light-nanowire interaction in strongly focussed light field that deviate from the paraxial approximation [115].

In addition, this refined understanding and the developed characterisation capacity of the light-nanowire interaction will also serve in other projects in the group, such as the one aiming at coupling a Nitrogen-vacancy (NV) defect hosted in a diamond nano-crystal to a nanowire. Indeed, one needs to understand how the quantum emitter emission diagram couples to the optical resonances of the SiC nanowires, and how the pumping efficiency will be affected by the nanowire close by. Such an investigation would help reduce the optical pump powers employed in the experiments as well as increasing the collection efficiency. This study would gain from improving the radial conical mirror to a parabolical one, in order to increase the collection of the camera sensor.

Heat transport in nanowires

In a second time, we upgraded the optomechanical experimental setup installed on the cold plate of the SIONLUDI cryostat, which provides fast cooldown, large working cold platform and low functioning noise. We were able to perform optical pump-probe measurement on nanowires from 300 K to 100 mK of noise temperatures.

We successfully used this contactless readout technique for probing thermal transport, using several actuation mechanisms. At room temperature, we performed broadband response measurements of the thermal elongation and thermomechanical deformation at the clamping (also referred as bilayer mechanism), where both effects were found to be in good agreement with a model based on a Fourier heat diffusion in a 1D geometry. Measurements of the thermal elongation responses were used in order to probe the evolution of the nanowires' absorption with the pump laser wavelength. We showed that it relates well to the absorption spectra derived from the Mie theory, combined with the material absorption, which increases when hitting the semiconductor bandgap of 3C-SiC. By scanning the pump laser position along the nanowire, we could also image the absorption profile of the nanowire, which revealed the existence of so-called "hot spots", where the absorption is typically increased by a factor of 10. The underlying mechanism can be due to a local contaminant, but also to a more efficient injection of light inside the nanowire at the locations where the nanowire diameter is non-homogeneous.

The description of the clamping area between the nanowire and its metallic support is delicate in view of the used functionalisation process. However, the finite element simulations in COMSOL helped us understand the interplay of strain and thermal waves in the area and provided results in good agreement with our broadband measurements up to the second resonant mode family. This confirmed that the measurement of the modulation of the nanowire lateral deformation due to thermomechanical effects at the clamping provides an indirect measurement of the temperature modulation in that region.

We also observed a signature of thermally induced optical cross-section modulation by measuring the evolution of the thermal responses upon scanning the pump wavelength across a Mie resonance, which was well identified by colour-dependent elongation measurements. We managed to fully interpret the measurements with the coherent sum of the three main photothermal mechanisms (bilayer, elongation and cross-section modulation) where the modulation of the cross-section was found to be essential to correctly adjust the measurements. Now, we will aim at implementing a more direct observation of the modulation of the optical forces due to thermally induced cross-section modulation. Using the real time force field imaging techniques, developed during the work of P. Heringlake [79], should lead to better investigation of the vectorial structure of the optical and photothermal forces within the optical waist and at different positions along the nanowire.

We also investigated the impact of a non-perfect thermal contact on the nanowire photothermal responses, and were able to evaluate the contact resistance quantitatively, in a proof of principle experiment which was however destructive for the nanowire. This investigation showed us that the contact resistance can be comparable to the thermal resistance of shorter nanowires already at room temperatures, and gave us the possibility to identify direct signatures of the effect, which were subsequently used to interpret the nanowire response at lower temperatures.

At low temperatures, we further improved the measurement apparatus developed during the PhD of F. Fogliano. Doing so, we were able to investigate the thermal properties of our nanowires down to 100 mK of noise temperature. We found that photothermal mechanisms can largely dominate the optical response of the nanowires at low frequencies for temperatures below 10 K. They also present a large variability depending on the laser position and on the sample temperature, and they feature a strong non-linearity with the optical power originating from the temperature dependence of the thermal coefficients of the nanowire. We aimed at investigating the non-trivial heat conduction regimes that would relate to the observations made when measuring the noise temperature whilst increasing the optical heating power. To do so, we scanned the position of the pump laser to investigate the spatial sensitivity of the light induced heating of the nanowire, as well as to probe their broadband and resonantly driven responses to the modulation of the laser intensity. To better understand the strong non-linearity observed in our measurements (varying by several orders of magnitude with the mean optical power), we formalised and solved the diffusion equation considering temperature dependent coefficients. This allowed us identifying limiting cases which could be used to better interpret the large non-linearity observed in our coldest response measurements.

We also analysed the evolution of the resonant vibration frequency shift with temperature, optical powers and laser positions, in the 0.1-2 K range. These measurements showed a clear variability in the laser position, which is in qualitative agreement with the non-homogeneous temperature profiles expected inside the nanowire at those temperatures and will be further analysed in the following. To help us in this

task, we tried to go beyond this static measurement of the frequency dependence with the temperature and investigated the dynamics of the frequency modulation induced by a time-modulated external perturbation, a heat wave here. Preliminary results obtained at room temperature are encouraging and could be directly implemented at dilution temperatures, providing information with a very large signal-to-noise ratio compared to other measurement channels.

Perspectives

In parallel, we designed a new optomechanical setup for dilution temperatures that will soon be implemented in the cryostat. In this new setup, we no longer scan the position of the nanowire in order to better decouple the nanowire support from spurious vibrational and electronic noise brought to the supporting piezo scanner. Instead, we will move the interferometric objectives and operate with a fixed nanowire. We will also add another scanner stage so as to approach a sample of interest below the nanowire, and thus realize force measurements at dilution temperatures. The great sensitivity of the nanowires to electric field should help to investigate nano-electronic samples where single electrons can be manipulated at dilution temperatures.

This movable support will thus be used to host future samples for 2D force microscopy at dilution temperature. Fast measurement protocols, developed by P. Heringlake [79], will be used in that perspective. Moreover, the charge waves dynamics within the nanowire created upon laser absorption in the semiconductor, were investigated during the PhD of H. Weltz and the internship of C. Dousset. They helped us understand how to control the charge state at the extremity of the nanowire. This knowledge will be used to investigate the stray fields above nano-electronic sample of interest, such as single electron transistor islands for example, that can only host a finite number of charges. In view of the extreme sensitivity of the nanowire, the imaging of the stray field produced by a single electron is in principle largely achievable.

On the optical part we also aim to improve the interferometric objectives, using a set of three lenses in order to operate with higher numerical aperture, allowing us to retrieve larger signals, while better compensating for chromatic aberrations.

Concerning the measurement of force field gradients, the frequency stability of our nanowires sets a limit to the sensitivity of the force field gradients which are dressing the nanowire eigenmodes [54], and was measured at the level of 1 fN/m in 40 s, which is rather small. Further investigations of the Allan variance should be conducted to determine the most optimised measurement configuration, which may not always be to operate at the coolest temperature in view of the overall stability of the system.

A collaboration with R. Braive and T. Martel (C2N - Centre de Nanosciences et de Nanotechnologies) gave us access to photonic crystals microcavity, see Fig. 6.21b, where the coupling between a nanowire and such a system are currently investigated during the PhD work of C. Zhang. Those photonic crystals can be injected with lensed fibres, which offers an attractive platform in order to imple-

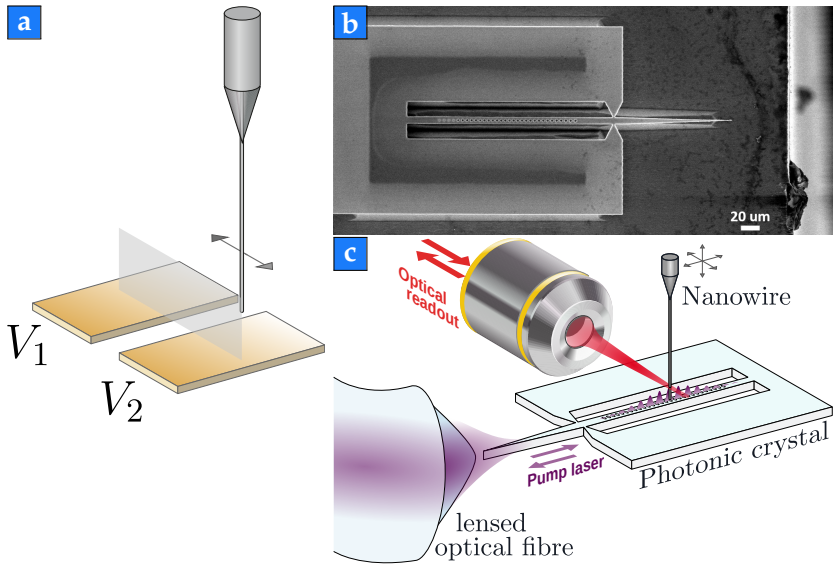

Figure 6.21: (a) Field compensation scheme in one direction, in order to compensate spurious electrostatic contribution from unperfect sample surface, from H. Weltz. (b) SEM image of the suspended photonic crystal designed and build by T. Martel in the group of R. Braive. (c) Experimental setup scheme for observing the coupling of a nanowire to the optical mode of the photonic crystal developed in the group of R. Braive.

ment cavity nano-optomechanics experiments in a cryostat. It was already demonstrated, during the work of F. Fogliano [66], that introducing a nanowire in the small mode volume of a fibre microcavity, the optomechanical coupling strength was large enough to enter the single photon regime of cavity optomechanics. He could measure the force field induced by a mean intra cavity photon number smaller than unity. At room temperature, the dynamics of the nanowire was still dominated by their thermal noise, but should be only dominated by the quantum fluctuations of the light field below 4 K [76].

APPENDIX A

ANNEXE : ADDITIONAL HEAT DIFFUSION PROBLEMS

Contents

A.1 Static temperature profile with a transition regime of the heat conductivity temperature dependence 169

A.2 Thermal response accounting for the thermal contact resistance inertia 172

A.3 Heat diffusion under Gaussian-shaped heat sources 176

A.3.1 Static profile with constant heat capacity and conductivity 176

A.3.2 Periodic excitation with constant diffusion coefficient 177

A.3.3 Stationary temperature profile with the heat capacity and conductivity varying with the temperature 178

A.1 Static temperature profile with a transition regime of the heat conductivity temperature dependence

We saw at the end of chap. 3 we expect the temperature dependence of our nanowire conductance to transition between different regimes of heat conduction. In this section we derive the expressions of the static temperature profile along the nanowire, in the case where the temperature within the nanowire crosses the transition temperature, T_{trans}, of the conductance regimes.

Without loss of generality, let us consider the conductivity of the nanowire switching continuously from one power law of the temperature $\kappa \propto T^{\mu_1}$ to another $\kappa \propto T^{\mu_2}$, where μ_1, μ_2 are real numbers. The static diffusion equation reads,

$$-\partial_y \left(\kappa(T)\, \partial_y T\right) = s(y), \tag{A.1}$$

where s is the heat source term. Introducing Λ the antiderivative of the conductivity with respect to the temperature, $\partial_T \Lambda = \kappa$, we can express eq. (A.1) into,

$$\partial_{yy} \Lambda[T(y)] = -s(y). \tag{A.2}$$

Annexes

Considering the usual boundary condition for our nanowires, without losses by radiation, one arrives to the general solution,

$$\Lambda[T(y)] - \Lambda[T(y=0)] = \int_0^y \int_{y'}^L s(y'')\,\mathrm{d}y'', \tag{A.3}$$

with the initial temperature given by the heat sink temperature and a possible thermal contact resistance, $T(y=0) = T_{\text{cryo}} + R_c\,P_{\text{abs}}$, where P_{abs} is the absorbed optical power and R_c the thermal contact resistance in $\mathrm{K/W^{-1}}$.

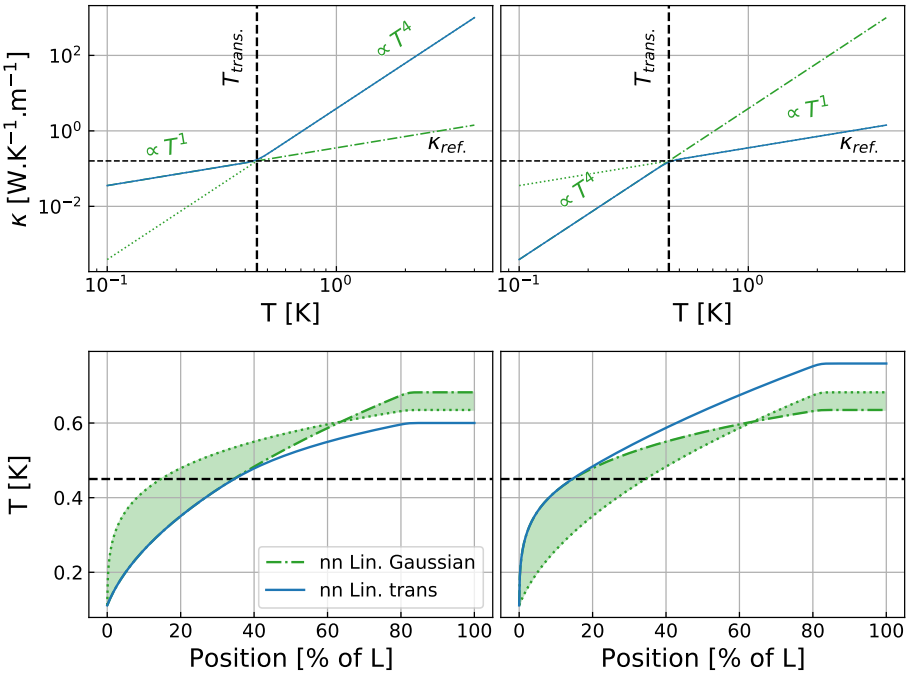

Figure A.1: Static temperature profile along a nanowire when a conductance regime transition occurs within the temperature establishment. We present two cases: when the power law transitions from smaller to higher power coefficient ($\mu_1 < \mu_2$) corresponding to the left panels, and from higher to smaller coefficient ($\mu_1 > \mu_2$) corresponding to the right panels. The top panels show the conductivity regimes, while the bottom panels show the static temperature profiles in the two limit cases (green lines) and when accounting for the transition (blue line).

We investigate this regime using a simple model for the regime transition of the conductivity such that Λ is well-defined, and we solved numerically eq. (A.3) to retrieve the temperature profiles. Depending on the case (μ_1 is greater or lower than μ_2), we chose the expression for the conductivity such as,

$$\kappa(T) = \kappa_0\,\left[(T/T_{\text{trans}})^{\mu_1} + (T/T_{\text{trans}})^{\mu_2}\right]; \qquad \text{when } \mu_1 \leq \mu_2, \tag{A.4}$$

$$\kappa(T) = \kappa_0\,\left[(T/T_{\text{trans}})^{-\mu_1} + (T/T_{\text{trans}})^{-\mu_2}\right]^{-1}; \qquad \text{when } \mu_1 > \mu_2, \tag{A.5}$$

plotted in Fig. A.1 for the particular cases of $\mu_1, \mu_2 \in \{1, 4\}$.

In Figure A.1 we show the static temperature profile along the nanowire when accounting for a regime transition in the temperature dependence of the nanowire conductance. The reference conductivity κ_{ref} has been evaluated considering the diffusion coefficient

$D = \kappa/(\rho\, C_p)$ close to values we encountered in our various response measurements, while fixing the heat capacity to $C_p = 1.0\,\mathrm{J.K^{-1}.kg^{-1}}$ (taken from the literature at 1 K). The transition temperature is set to 450 mK, which is close to the temperature where we observe a change of regime in the optical heating measurements presented in chap. 3.

The new temperature profile shows we can easily overestimate the temperature at the tip of the nanowire when we transition from a slowly varying conductance regime with temperature to a quickly varying one. On the other hand, one can underestimate the tip temperature for the other case.

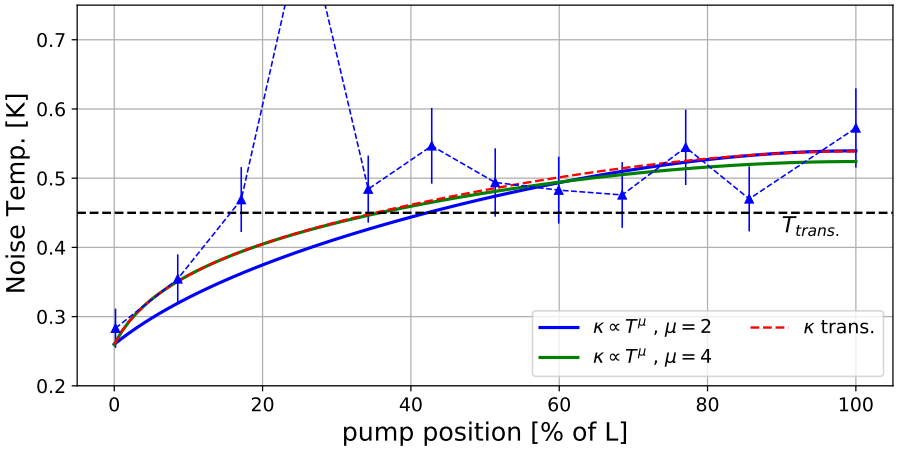

Figure A.2: Measurement of the noise temperature profile at low pump optical power. In coloured solid lines the models in the limit cases where the conductance vary with T^2 and T^4, as well as when accounting for a regime transition (red dashed line).

Using this new temperature profile, we can estimate the measured noise temperature when scanning the position of the pump laser, likewise in sec. 6.2.2. Figure A.2 shows the noise temperature profile measurement realised at low temperatures, fitted by the noise temperature model when considering two conduction regimes (blue and green lines) as well as the transition from one to the other (red dotted line). This allows to fit more realistically the data close to the clamping area, which are colder and in the regime of high temperature gradient, while accounting for a steady increase on the noise temperature when moving the pump laser close to the vibrating end of the nanowire. Still the data are noisy and the lack of calibration of the local absorption render the discussion only qualitative.

A.2 Thermal response accounting for the thermal contact resistance inertia

In this section we want to derive the temperature response to a heat source intensity modulation while accounting for the inertia of the thermal contact resistance. To do so, we assume the thermal contact resistance is a layer a thermally resistive material, having a given length L_c, which separates the nanowire from the tungsten clamping (considered in thermodynamic equilibrium with a heat sink). The thermal contact resistance inertia is given by its diffusion coefficient D_c, while its total resistance value can be linked to the material conductivity κ_c, such that $R_c = L_c/(\kappa_c S)$ with S the nanowire cross-section. Figure A.3 illustrates the system parameters.

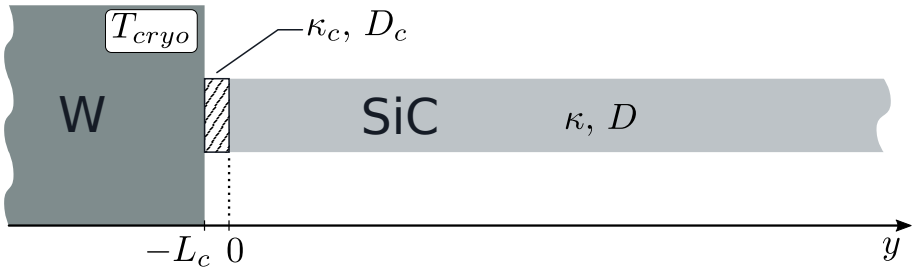

Figure A.3: Scheme of the contact thermal resistance at the clamping in the 1D model, where the thermal contact resistance is modelled by a layer of resistive material.

The diffusion problem will be split in two parts: the diffusion inside the thermal contact resistance material, and the diffusion in the nanowire, while accounting for the boundary conditions defined in previous chapters. We look for the temperature response to a time modulated heat source with profile modelled by a punctual source,

$$\delta s(y) = \frac{\delta P_{\text{abs}}}{S}\,\delta(y - y_0), \tag{A.6}$$

with δP_{abs} is the modulated absorbed optical power, and y_0 is the laser position along the nanowire. In Fourier space we solve the equations,

$$\left(\partial_{yy} - \beta^2\right)\,\delta T[\Omega](y) = -\frac{\delta P_{\text{abs}}}{S\,\kappa}\,\delta(y - y_0), \tag{A.7}$$

$$\left(\partial_{yy} - \beta_c^2\right)\,\delta T_c[\Omega](y) = 0, \tag{A.8}$$

where δT refers to the temperature response within the nanowire while δT_c refers to the one inside the contact resistance material, and we denoted $\beta = \sqrt{i\,\Omega/D}$, as well as $\beta_c = \sqrt{i\,\Omega/D_c}$. The solutions are in the form,

$$\delta T(y) = a_\pm\, e^{\beta\, y} + b_\pm\, e^{-\beta\, y}, \tag{A.9}$$

$$\delta T_c(y) = a_c\, e^{\beta_c\, y} + b_c\, e^{-\beta_c\, y}, \tag{A.10}$$

with $\pm$ refers to the left/right side of the heat source position y_0. The

boundary conditions are given by,

$$\delta T_c(-L_c) = 0, \tag{A.11}$$
$$\partial_y \delta T(L) = 0, \tag{A.12}$$
$$\delta T_c(0^-) = \delta T(0^+), \tag{A.13}$$
$$\kappa_c\, \partial_y \delta T_c(0^-) = \kappa\, \partial_y \delta T(0^+), \tag{A.14}$$
$$\delta T(y_0^-) = \delta T(y_0^+), \tag{A.15}$$
$$\partial_y T(y_0^+) - \partial_y T(y_0^-) = -\frac{\delta P_{\text{abs}}}{S\,\kappa}, \tag{A.16}$$

where eq. (A.13, A.14) translate the continuity of temperature and heat flux at the contact. In matrix form, this reads,

$$\begin{bmatrix} 0 & 0 & 0 & 0 & e^{-Lc\beta_c} & e^{Lc\beta_c} \\ 0 & 0 & e^{L\beta} & -e^{-L\beta} & 0 & 0 \\ 1 & 1 & 0 & 0 & -1 & -1 \\ e^{\beta y_0} & e^{-\beta y_0} & -e^{\beta y_0} & -e^{-\beta y_0} & 0 & 0 \\ \beta\kappa & -\beta\kappa & 0 & 0 & -\beta_c\kappa_c & \beta_c\kappa_c \\ -\beta e^{\beta y_0} & \beta e^{-\beta y_0} & \beta e^{\beta y_0} & -\beta e^{-\beta y_0} & 0 & 0 \end{bmatrix} \cdot \begin{bmatrix} a_- \\ b_- \\ a_+ \\ b_+ \\ a_c \\ b_c \end{bmatrix} = \begin{bmatrix} 0 \\ 0 \\ 0 \\ 0 \\ 0 \\ -\frac{\delta P_{\text{abs}}}{S\,\kappa} \end{bmatrix}. \tag{A.17}$$

Checking the solvability of the system, we obtain the coefficients for the expression of the temperature response within the nanowire. Making use of the Heaviside distribution in order to write compactly the solutions, we express the temperature response within the nanowire such as,

$$\delta T[\Omega](y) = (1 - \Theta(y - y_0)) \left[a_-\, e^{\beta\, y} + b_-\, e^{-\beta\, y}\right] + \Theta(y - y_0) \left[a_+\, e^{\beta\, y} + b_+\, e^{-\beta\, y}\right], \tag{A.18}$$

$$= \frac{\delta P_{\text{abs}}}{S\,\kappa} \frac{1}{2\,\beta} \left[\frac{\left(e^{\beta\,(y_L - y_0)} + e^{-\beta\,(y_L - y_0)}\right)}{\left((1+u_c)\, e^{\beta\, y_L} + (1-u_c)\, e^{-\beta\, y_L}\right)} \left((1+u_c)\, e^{\beta\, y} - (1-u_c)\, e^{-\beta\, y}\right) \right.$$
$$\left. - \Theta(y - y_0) \left(e^{\beta\,(y - y_0)} - e^{-\beta\,(y - y_0)}\right) \right], \tag{A.19}$$

where we introduced the parameters $u_c = \beta\,\kappa/(\beta_c\,\kappa_c)\,\tanh(\beta_c\,L_c)$, related to the contact resistance thermal properties. The above expression (A.19) is very similar to eq. (5.26) in sec. 5.2, where we did not account for the thermal contact inertia. However, in this case the coefficient u_c depends on the modulation frequency through β_c instead of β in the latter case. One can also express u_c as,

$$u_c = \sqrt{\frac{D_c}{D}}\, \frac{R_c}{R_{\text{nw}}}\, \frac{L}{L_c}\, \tanh(\beta_c\, L_c), \tag{A.20}$$

where the thermal resistances are defined as, $R_{\mathrm{nw}} = L/(\kappa\, S)$ and $R_c = L_c/(\kappa_c\, S)$. This expression gives a more explicit view of the relation between the thermal quantities at play.

Finally, the temperature response inside the thermal contact can be expressed as,

$$\delta T_c(y) = \frac{\delta P_{\mathrm{abs}}}{S\,\kappa}\,\frac{1}{2\beta}\,\frac{\left(e^{\beta\,(y_L-y_0)} + e^{-\beta\,(y_L-y_0)}\right)\left[e^{\beta_c\,(y+L_c)} - e^{-\beta_c\,(y+L_c)}\right]}{\left((1+u_c)\,e^{\beta\,y_L} + (1-u_c)\,e^{-\beta\,y_L}\right)}\,\frac{u_c}{\sinh(\beta_c\,L_c)}. \tag{A.21}$$

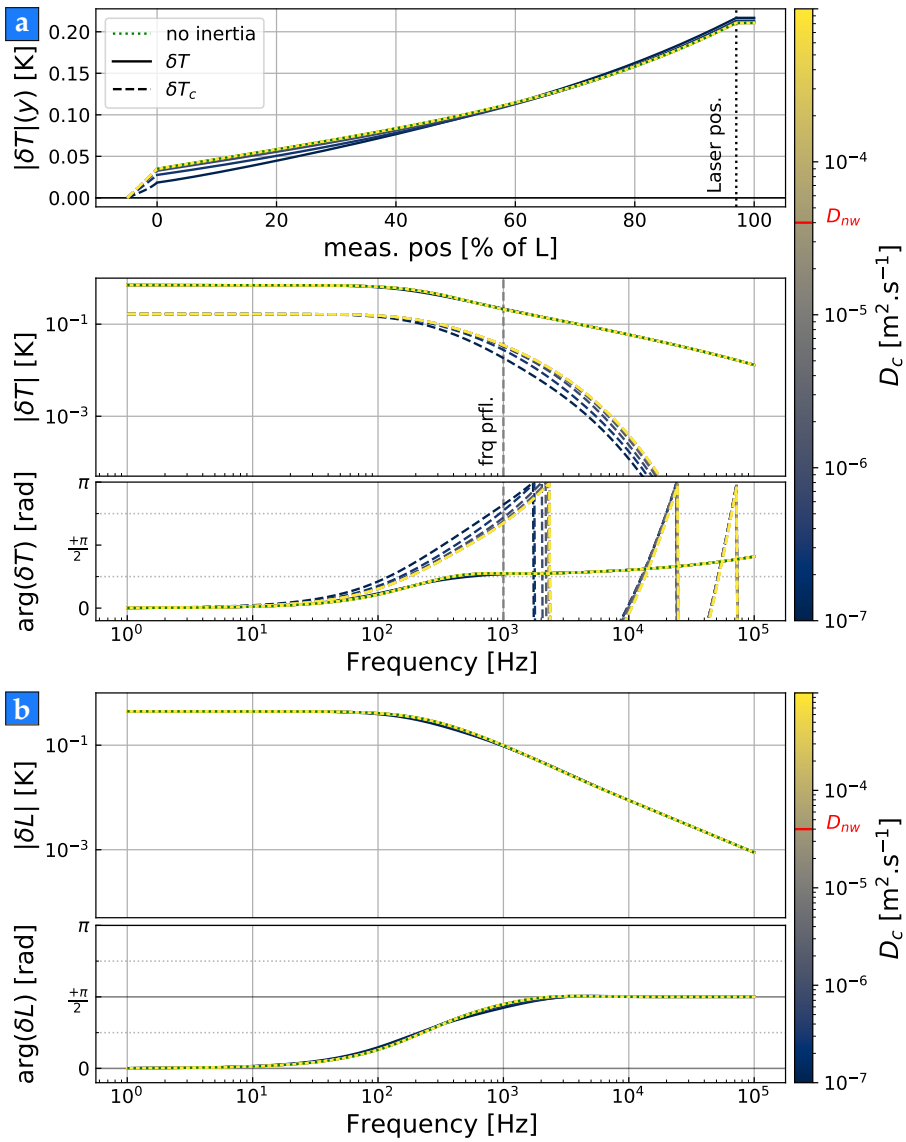

Figure A.4: (a) Temperature response profile along the nanowire (solid lines) and inside the thermal contact resistive material (dotted lines), measured at a given frequency while varying the thermal resistance inertia (top panel). We show the Bode diagram of the temperature response to an absorbed optical power modulation (bottom panel), measured at the tip of the nanowire (plain line), as well as measured at the interface between the nanowire and the thermal resistance (dotted lines). The green dotted line represents the limit when we do not account for the resistance inertia. The red line in the colorbar indicates the nanowire diffusion coefficient, considered for those simulations. (b) Elongation response of the nanowire measured at the nanowire tip, with the pump laser located at the vibrating tip, for varying thermal resistance inertia.

Figure A.4a shows the temperature response to a modulation of the heat source amplitude, for varying thermal contact inertia. In this simulation, we considered the thermal contact resistance extension to

be 5% of the nanowire length, and the pump laser positioned close to the vibrating tip of the nanowire. We observe the inertia of the thermal contact resistance has a minor effect on the temperature response measured at the tip of the nanowire. The elongation responses, shown Fig. A.4b, are also weakly affected by the contact resistance inertia.

A.3 Heat diffusion under Gaussian-shaped heat sources

In this section we present the expressions of the 1D heat diffusion analysis when the source term has a gaussian shape, as well as some important steps to obtain those expressions. Indeed, when integrating numerically certain expressions, it helps to deal with continuous functions and quantities, this was especially the case concerning the numerical integration of the PME.

A.3.1 Static profile with constant heat capacity and conductivity

The nanowire heating happens subsequently to the absorption of light at the waist of a focused laser beam. Assuming a homogeneous distribution of heat across the nanowire cross-section, we consider the heat source profile to be gaussian shaped along the nanowire axis, and write,

$$s(y) = \frac{P_{\text{abs}}}{S}\sqrt{\frac{2}{\pi\, w_0^2}}\, e^{-2\frac{(y-y_0)^2}{w_0^2}}, \tag{A.22}$$

where y_0 is the pump laser position, P_{abs} is the absorbed optical power of the pump laser over the nanowire cross-section $S = \pi\, R^2$, and w_0 is the laser waist. To proceed, we apply a change of coordinate, such as $y = z\, w_0/\sqrt{2}$, $y_0 = z_0\, w_0/\sqrt{2}$ and $L = z_L\, w_0/\sqrt{2}$. The static diffusion equation becomes,

$$\kappa\, \partial_{zz} T(z) = -S_0 e^{-(z-z_0)^2}, \tag{A.23}$$

where we denoted $S_0 = \frac{P_{\text{abs}}}{S}\frac{w_0}{\sqrt{2\,\pi}}$ in W.m^{-1}. The boundary conditions are chosen as usual considering a thermal contact resistance: $T(y = 0) = T_{\text{cryo}} + R_c\, S\, j_{\text{thm}}(y = 0)$ with j_{thm} the heat flux, and at the free end of the nanowire $\partial_y T(y = L) = 0$. Integrating successively eq. (A.23) first between a given position and the tip, $y_{\text{tip}} = L$, then from the clamping to a given position, $y_{\text{clamp}} = 0$, one can get,

$$T(y) = T(0) - \frac{1}{\kappa}\, S_0\, P_s(y), \tag{A.24}$$

$$\tag{A.25}$$

where the temperature at the clamping is fixed accounting for a thermal contact resistance R_c such as $T(0) = T_{\text{cryo}} + R_c\, S\, S_0\, \sqrt{\pi}/2\, (\text{erf}(z_L - z_0) - \text{erf}(-z_0))$, and we defined,

$$P_s(z) = \frac{\sqrt{\pi}}{2}\left[(z - z_0)\,\text{erf}(z - z_0) + \frac{e^{-(z-z_0)^2}}{\sqrt{\pi}} - z\,\text{erf}(z_L - z_0) + z_0\,\text{erf}(-z_0) - \frac{e^{-(z_0)^2}}{\sqrt{\pi}}\right]. \tag{A.26}$$

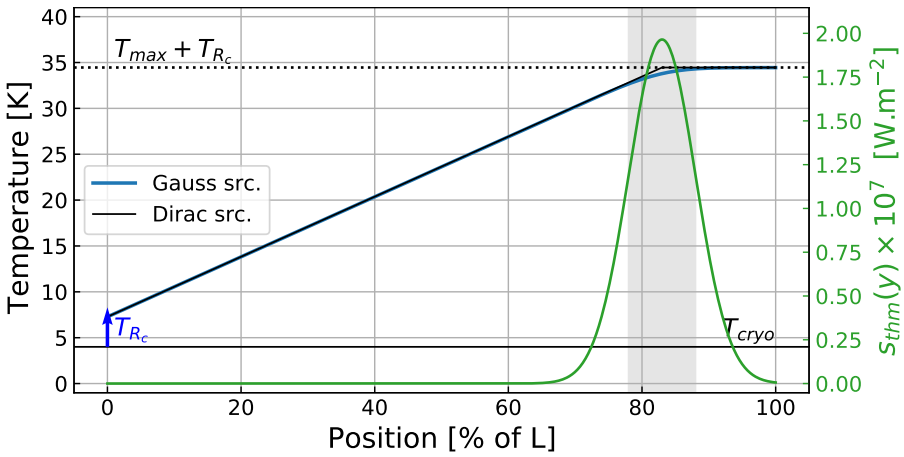

Figure A.5: Steady temperature profile along a SiC nanowire when the heat source profile is has a gaussian shape.

Figure A.5 presents the steady temperature profile inside a nanowire upon heating with a gaussian shaped heat source.

A.3.2 Periodic excitation with constant diffusion coefficient

We now consider a modulation of the pump laser intensity. This will generate a modulation of the heat source amplitude around its average value : $P_{\text{abs}} \to P_{\text{abs}} + \delta\,\P_{\text{abs}}$, and the source term can be expressed as,

$$s(y) = \frac{P_{\text{abs}}}{S}\sqrt{\frac{2}{\pi\, w_0^2}}\, e^{-2\frac{(y-y_0)^2}{w_0^2}}\,\left(1+\delta\cos(\Omega\, t)\right), \tag{A.27}$$

where Ω is the modulation frequency.

Due to the linearity of the differential equation, the solution can be decomposed into two contributions: the stationary solution T_s (see above section), and a forced perturbation around the equilibrium, δT. The total solution is then, $T(y,t) = T_s(y) + \delta T(y,t)$. The differential equation on the perturbation becomes,

$$\partial_t(\rho\, C_p\, \delta T) - \frac{1}{D_0}\,\partial_y(\kappa \partial_y \delta T) = \frac{P_{\text{abs}}}{S}\sqrt{\frac{2}{\pi\, w_0^2}}\, e^{-2\frac{(y-y_0)^2}{w_0^2}}\,\delta\,\cos(\Omega_0 t). \tag{A.28}$$

Proceeding similarly as for the static case, we introduce the same change of variables. Solving the above equation in the complex plane using the anzats, $\delta T(y,t) = \delta T(y)\, e^{-i\Omega\, t}$, eq. (A.28) transforms into,

$$\left(\partial_{zz} - \beta^2\right)\delta T(z) = -\delta S_0\, e^{-(z-z_0)^2}, \tag{A.29}$$

where we denote $\beta = \sqrt{i\frac{\Omega\, w_0^2}{2\,D}}$, with $D = \kappa/(\rho\, C_p)$ the diffusion coefficient in [m^2.s^{-1}].

The general solution is of the form,

$$\delta T(z) = A\, e^{-\beta z} + B\, e^{+\beta z} + \delta T^{(p)}(z), \tag{A.30}$$

with $e^{\pm\beta z}$ the linearly independent solution of the homogeneous equation, and $\delta T^{(p)}$ a particular solution taken in the form $T^{(p)}(z) = F(z)\, e^{\beta z}$, which gives,

$$\delta T^{(p)}(z) = \frac{\Gamma}{2\beta} e^{-\beta z} \left[-\mathrm{erf}(z - z_0 - \frac{\beta}{2}) + \mathrm{erf}(-z_0 - \frac{\beta}{2}) + e^{2\beta\,(z-z_0)}\, \mathrm{erf}(z - z_0 + \frac{\beta}{2}) \right]. \tag{A.31}$$

with $\Gamma = \delta S_0\, \frac{\sqrt{\pi}}{2}\, e^{+\beta z_0 + \frac{\beta^2}{4}}$.

Accounting for the boundary condition where the nanowire is connected to the heat sink via a thermal contact resistance R_c in [K.W^{-1}], the temperature modulation at the clamping is then,

$$\delta T(0,t) = (T(y=0,t) - T_s(0)) = R_c\, S\, \kappa\ \partial_y \delta T\big|_{y=0}. \tag{A.32}$$

In addition, at the tip of the wire, $y = L$, we have that $\partial_y T(L) = 0 = \partial_y T_s(L) + \partial_y \delta T(L)$, for all t. Likewise to sec. 5.2, we denote here $u_{w_0} = R_c\, S\, \kappa\, \beta\, \sqrt{2}/w_0 = R_c/R_{\mathrm{nw}}\, \beta\, L\, \sqrt{2}/w_0$, where we defined the nanowire thermal resistance $R_{\mathrm{nw}} = L/(\kappa\, S)$. All in all, the solution of the oscillating response can be expressed as,

$$A = \frac{-(1-u_{w_0})\, \beta\, e^{-\beta z_L}\, \delta T^{(p)}(0) - (1+u_{w_0})\, \partial_z \delta T^{(p)}(z_L)}{\left((1+u_{w_0})\, e^{+\beta z_L} + (1-u_{w_0})\, e^{-\beta z_L}\right)}, \tag{A.33}$$

$$B = \frac{-(1-u_{w_0})\, \beta\, e^{+\beta z_L}\, \delta T^{(p)}(0) + (1-u_{w_0})\, \partial_z \delta T^{(p)}(z_L)}{\left((1+u_{w_0})\, e^{+\beta z_L} + (1-u_{w_0})\, e^{-\beta z_L}\right)}. \tag{A.34}$$

A.3.3 Stationary temperature profile with the heat capacity and conductivity varying with the temperature

In this case, with consider the heat capacity and heat conductivity of the nanowire to vary with temperature, following the power laws,

$$\kappa = K_0 \left(\frac{T}{T_0}\right)^{\mu}; \qquad C_p = C_0 \left(\frac{T}{T_0}\right)^{\alpha}. \tag{A.35}$$

with K_0 and C_0 constants of the temperature. The stationary equation for the degenerate non-linear diffusion equation can then be expressed such as,

$$\frac{K_0}{(\mu+1)\, T_0^{\alpha}}\, \partial_{yy}\left(T_s^{\mu+1}\right) = -\frac{P_{\mathrm{abs}}}{S} \sqrt{\frac{2}{\pi\, w_0^2}}\, e^{-2\frac{(y-y_0)^2}{w_0^2}}, \tag{A.36}$$

where T_s is the stationary temperature profile. We proceed similarly to the linear case, and integrate the above equation twice, choosing the integration boundaries accordingly to the boundary conditions of our system. In our case, we account for the contact thermal resistance, $T_s(0) = T_{\text{cryo}} + R_c\, S\, \partial_y T_s\big|_{y=0}$, with $S = \pi R^2$ the nanowire cross-section and T_{cryo} the heat sink temperature (the cryostat in our case). Doing so, we get the expression for the static temperature profile with a heat conductivity varying with the temperature, for $\mu \neq 1$, such as,

$$T(y) = \left[-\frac{(\mu+1)}{K_0\, T_0^{-\mu}} \frac{P_{\text{abs}}}{S} \frac{w_0}{\sqrt{2}} P_s(y) + \left(T_{\text{cryo}} + T_{R_c}\right)^{\mu+1} \right]^{\frac{1}{\mu+1}} \tag{A.37}$$

where $T_{R_c} = R_c\, P_{\text{abs}} \left(\text{erf}(\sqrt{2}/w_0\,(L - y_0)) - \text{erf}(-\sqrt{2}/w_0\, y_0)\right)/2$, and P_s is defined by eq. (A.26). Concerning the special case where $\mu = 1$, there is still an analytical solution, that take the form,

$$T(y) = \left(T_{\text{cryo}} + T_{R_c}\right)\, e^{-\frac{P_{\text{abs}}}{S\, K_0\, T_0} \frac{w_0}{\sqrt{2}} P_s(y)}. \tag{A.38}$$

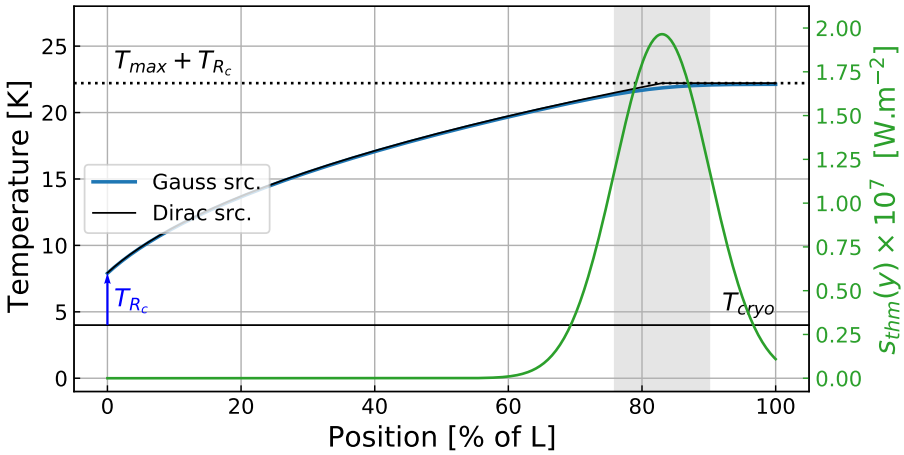

Figure A.6: Steady temperature profile along a SiC nanowire when accounting for the temperature dependence of the heat conductivity, under a gaussian shaped heat source term.

APPENDIX B

ANNEXE : ELLIPSE ON A TILTED PLANE

In this section we want to compute the transformation one need to account in order to retrieve the ellipse trajectories when the nanowire is tilted from the vertical. Indeed, in practice the nanowire and the vertical axis of the measurement setup may not be completely aligned. The measurement setup coordinate system is defined by the piezo displacement axis (X,Y,Z), while the transverse vibrations of the nanowire are governed by its two transverse eigenvectors, $\mathbf{e}_1$, $\mathbf{e}_2$, perpendicular to the nanowire axis denoted $\mathbf{n}_{\text{nw}}$, see Fig. B.1. In the following, we assume that the nanowire tip moves exclusively in the plane formed by the vectors $(\mathbf{e}_1, \mathbf{e}_2)$, denoted P_{nw}.

The measure of $\mathbf{n}_{\text{nw}}$, gives the tilt of P_{nw}, *w.r.t* the measurement plane (X, Z), denoted P_{XZ}. Assuming our measurement vectors are in the plane P_{XZ}, we will denote, $\delta\mathbf{r}_{\text{XZ}}$, the nanowire measured displacement projected onto P_{XZ}. On the other hand, we want to get the deformation of the nanowire in the plane P_{nw}, denoted $\delta\mathbf{r}_{\text{nw}}$, which relates to the real nanowire tip trajectories in the 3D space.

In order to measure the tilt angles, we measure 2D maps of the reflected photon flux on the nanowire. From a single XY-map measurement in the interferometric readout implemented in the cryostat setup, one can get the angle that the nanowire have *w.r.t* to the Y-axis, θ_y, using the interference pattern to also retrieve the tilt in the Z-direction, see Fig. B.2. It is more convenient to retrieve $\mathbf{n}_{\text{nw}}$ from its projection on the XY-plane, and on the ZY-plane. We denote $\mathbf{n}_{\text{nw}}^{(XY)}$ the projection of $\mathbf{n}_{\text{nw}}$ in the XY-plane, and α_{XY} the angle the vector makes *w.r.t* the Y-axis. Likewise concerning the projection onto the ZY-plane.

From those angles, the direction vector of the nanowire axis is given by,

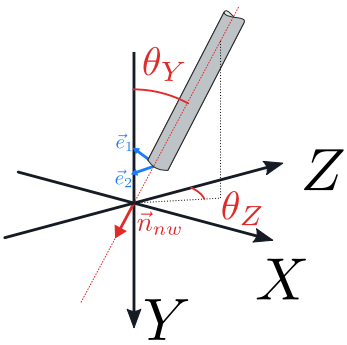

Figure B.1: Schematic and notations used in the tilting of a nanowire.

$$\mathbf{n}_{\text{nw}} = \begin{pmatrix} n_x \\ n_y \\ n_z \end{pmatrix}, \tag{B.1}$$

$$\mathbf{n}_{\text{nw}}^{(XY)} = \begin{pmatrix} n_x \\ n_y \end{pmatrix} = C_{XY} \begin{pmatrix} \sin(\alpha_{XY}) \\ \cos(\alpha_{XY}) \end{pmatrix}, \tag{B.2}$$

$$\mathbf{n}_{\text{nw}}^{(ZY)} = \begin{pmatrix} n_y \\ n_z \end{pmatrix} = C_{ZY} \begin{pmatrix} \cos(\alpha_{ZY}) \\ \sin(\alpha_{ZY}) \end{pmatrix}, \tag{B.3}$$

where we introduced, the constants C_{XY} and C_{ZY}. Satisfying the normalisation of $\mathbf{n}_{\text{nw}}$ to unity ($\|\mathbf{n}_{\text{nw}}\| = 1$), one gets,

$$\mathbf{n}_{\text{nw}} = \frac{\cos(\alpha_{XY})}{\sqrt{1+\cos^2(\alpha_{XY})\,\tan^2(\alpha_{ZY})}} \begin{pmatrix} \tan(\alpha_{XY}) \\ 1 \\ \tan(\alpha_{ZY}) \end{pmatrix}. \tag{B.4}$$

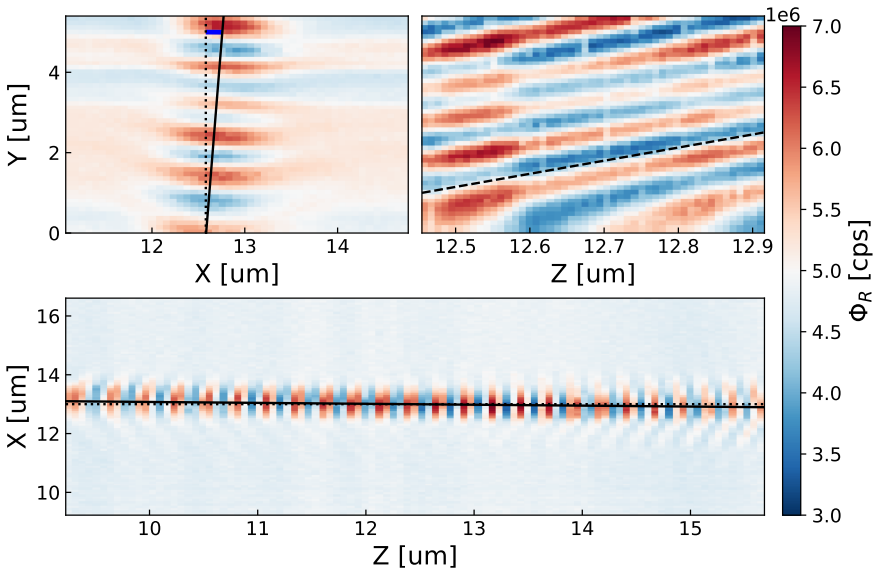

Figure B.2: 2D maps of the reflected photon flux by the nanowire and collected back to be measured with an APD detector. We present the three maps taken in the different planes, but in the interferometric readout scheme only the XY-map would have been sufficient to measure the nanowire axis tilt. The tilt from the Y-axis in the XY plane is measured to be 2.0 ± 0.1 deg, while in the ZY plane 17.0 ± 0.1 deg.

To express the displacement $\delta\mathbf{r}_{\text{nw}}$, defined in P_{nw}, we make use of the projection identities. Indeed, $\delta\mathbf{r}_{\text{XZ}}$ is a projection of the real displacement onto P_{XZ} with a normal vector $\mathbf{e}_y$. We can write,

$$\delta\mathbf{r}_{\text{XZ}} = \delta\mathbf{r}_{\text{nw}} - \mathbf{e}_y\,\left(\mathbf{e}_y \cdot \delta\mathbf{r}_{\text{nw}}\right), \tag{B.5}$$

while we have by assumption,

$$\delta\mathbf{r}_{\text{XZ}} \cdot \mathbf{e}_y = 0,\ \delta\mathbf{r}_{\text{nw}} \cdot \mathbf{n}_{\text{nw}} = 0. \tag{B.6}$$

It follows we can express directly $\delta\mathbf{r}_{\text{nw}}$ in terms of scalar and vector product with $\mathbf{e}_y$ and $\delta\mathbf{r}_{\text{XZ}}$, such that,

$$\delta\mathbf{r}_{\text{XZ}} \cdot \mathbf{n}_{\text{nw}} = -\left(\mathbf{e}_y \cdot \mathbf{n}_{\text{nw}}\right)\,\left(\mathbf{e}_y \cdot \delta\mathbf{r}_{\text{nw}}\right), \tag{B.7}$$

$$\delta\mathbf{r}_{\text{nw}} = \delta\mathbf{r}_{\text{XZ}} - \frac{\mathbf{e}_y\,\left(\delta\mathbf{r}_{\text{XZ}} \cdot \mathbf{n}_{\text{nw}}\right)}{\left(\mathbf{e}_y \cdot \mathbf{n}_{\text{nw}}\right)}, \tag{B.8}$$

$$\delta\mathbf{r}_{\text{nw}} = \delta\mathbf{r}_{\text{XZ}} - \frac{\left(\mathbf{e}_y \times \mathbf{n}_{\text{nw}}\right)}{\left(\mathbf{e}_y \cdot \mathbf{n}_{\text{nw}}\right)} \times \delta\mathbf{r}_{\text{XZ}}, \tag{B.9}$$

where we made use of the identity $\mathbf{a} \times \mathbf{b} \times \mathbf{c} = \mathbf{b}\,(\mathbf{a} \cdot \mathbf{c}) - \mathbf{c}\,(\mathbf{a} \cdot \mathbf{b})$.

All in all, we recovered the displacement vector $\delta\mathbf{r}_{\text{nw}}$ in P_{nw}, expressed in the (XYZ) coordinate system. For completeness, to have the 2D vector projected onto P_{nw}, one must define a basis in P_{nw}. Since in

practice the tilt is small, we consider using the projected $\mathbf{e}_x$ and $\mathbf{e}_z$ to define the P_{nw} basis:

$$\mathbf{e}_z^{(\mathrm{nw})} = \left[\mathbf{e}_z - \mathbf{n}_{\mathrm{nw}}\ (\mathbf{n}_{\mathrm{nw}} \cdot \mathbf{e}_z)\right] / \sqrt{1 - (\mathbf{n}_{\mathrm{nw}} \cdot \mathbf{e}_z)^2}, \tag{B.10}$$

$$\mathbf{e}_x^{(\mathrm{nw})} = \mathbf{n}_{\mathrm{nw}} \times \mathbf{e}_z. \tag{B.11}$$

APPENDIX C

ANNEXE : SOME MATHEMATICAL DEMONSTRATIONS

Contents

C.1 Getting T_{noise} from integrating Nanowire PSD Brownian motion 185

C.2 Demonstration of the limiting value of Mie coeff $C_{m,l}^{\parallel,\perp}$ 187

C.1 Getting T_{noise} from integrating Nanowire PSD Brownian motion

In this section we aim at demonstrating the relation between the integration of the Power Spectral Density (PSD) of a nanowire noise motion, and the noise temperature defined in the fluctuation dissipation theorem.

When considering a single mode of the nanowire in equilibrium with a thermal bath at a temperature T, as dealt in sec. 1.2.2, we introduce a Langevin force that relates the position fluctuation of the oscillator with the thermal bath. Without loss of generality, we consider only the 1D dynamic. In frequency space, one can write for a given mode family,

$$\delta r_{\text{thm}}[\Omega] = \chi[\Omega]\, F_{\text{thm}}[\Omega], \tag{C.1}$$

where δr_{thm} is the nanowire vibrating tip position, χ the susceptibility of the considered mode family, F_{thm} the Langevin force. The nanowire position PSD is given by,

$$S_{\delta r_{\text{tm}}}[\Omega] = \|\chi[\Omega]\|^2\, S_{F_{\text{thm}}}, \tag{C.2}$$

$$= \frac{2\, k_B\, T\, \Gamma}{M_{\text{eff}}\, [(\Omega_m^2 - \Omega^2)^2 + \Omega^2\, \Gamma^2]}, \tag{C.3}$$

where $\Omega_m/2\pi$ is the mechanical resonance, $\Gamma/2\pi$ the damping rate, M_{eff} the effective mass of the oscillator, and k_B the Boltzmann constant.

Annexes

If we integrate the PSD over all frequencies, we get,

$$I_{\text{B.M}} = \int_0^{\infty} S_{\delta r_{\text{tm}}}[\Omega]\mathrm{d}\Omega, \tag{C.4}$$

$$= \frac{2\,k_B\,T\,\Gamma}{M_{\text{eff}}} \int_0^{\infty} \frac{1}{|(\Omega-\Omega_+)\,(\Omega-\Omega_-)|^2}\mathrm{d}\Omega, \tag{C.5}$$

$$= \frac{2\,k_B\,T\,\Gamma}{M_{\text{eff}}} \int_0^{\infty} L[\Omega]\mathrm{d}\Omega \tag{C.6}$$

where $\Omega_\pm = \frac{1}{2}(-i\,\Gamma \pm \sqrt{4\Omega_m^2 - \Gamma^2})$. We denoted $L[\Omega]$ the integrand, which has four complex poles (since we integrate the norm, we have the complex conjugates $\overline{\Omega_\pm} = -\Omega_\mp$). From the **Residual theorem**, and the **Jordan's lemma**, we get that,

$$\int_{-\infty}^{+\infty} L[\Omega]\mathrm{d}\Omega = \sum_{\Omega_r=-\Omega_+,-\Omega_-} 2\,i\,\pi\,\mathrm{Res}[L](\Omega_r), \tag{C.7}$$

where we used the upper half-complex plain for the integration path, see Fig. C.1b, and $\mathrm{Res}[L]$ is the residual of the integrand. The residual of a function F for a pole z_0 of order k, is defined has,

$$\mathrm{Res}[F](z_0) = \frac{1}{(k-1)!}\,\frac{\mathrm{d}^{k-1}}{\mathrm{d}z^{k-1}}\left((z-z_0)^k\,F(z)\right)\Big|_{z_0}. \tag{C.8}$$

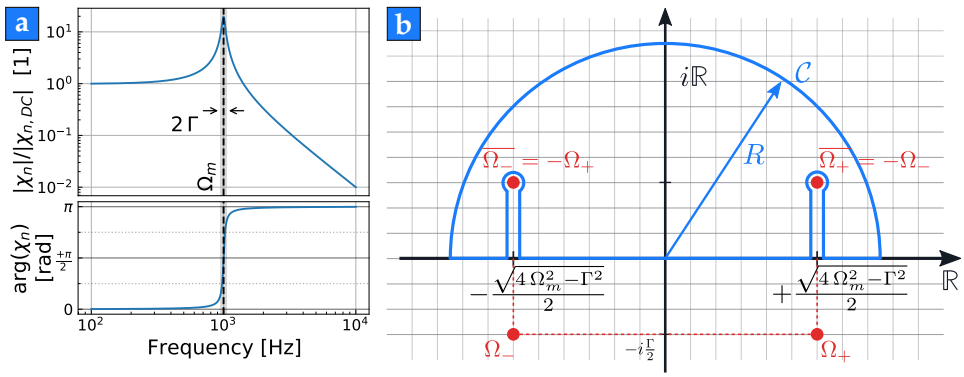

Figure C.1: (a) Nanowire mechanical 1D susceptibility χ for a given resonant mode. (b) Poles of the mechanical susceptibility and integration path illustration of the residual theorem when integrating complex function.

All in all, the integrated PSD of the noise motion of a nanowire at equilibrium with a temperature bath at T around its mechanical resonance Ω_{m} can be expressed such as,

$$I_{\text{B.M}} = \frac{2\,k_B\,T\,\Gamma}{M_{\text{eff}}}\left(\frac{1}{\Omega_m^2\,\Gamma^2}\right)\left(\pi\,\frac{\Gamma}{2}\right) = \frac{\pi\,k_B\,T}{M_{\text{eff}}\,\Omega_m s^2} \tag{C.9}$$

One can then directly evaluate the noise temperature from the noise motion integration with,

$$T = \frac{M_{\text{eff}}\,\Omega_m^2}{\pi\,k_B}\,I_{\text{B.M}}. \tag{C.10}$$

C.2 Demonstration of the limiting value of Mie coeff $C_{m,l}^{\parallel,\perp}$

In this section we aim at computing the asymptotic limit of $C_{m,l}^{\parallel,\perp}$, which is defined in chap. 2 within the framed text of sec. 2.2.2. The functions $C_{m,l}^{\parallel,\perp}$ includes Bessel's functions and their asymptotic behaviour is,

$$C_{m,l}^{\parallel} = +Z_m^{(3)}(k\,r)\,(\dot{Z}_l^{(3)}(k\,r))^* \underset{r\to\infty}{\sim} -i\,(-i)^{m-l}\,\frac{2}{\pi\,k\,r}, \tag{C.11}$$

$$C_{m,l}^{\perp} = -(Z_l^{(3)}(k\,r))^*\dot{Z}_m^{(3)}(k\,r) \underset{r\to\infty}{\sim} -i\,(-i)^{m-l}\,\frac{2}{\pi\,k\,r}, \tag{C.12}$$

where we denoted $Z_m^{(3)} = H_m^{(1)}$ the Hankel function of the first kind, k is the wave vector of the considered incident light, and r the distance to the nanowire axis. To arrive at the above asymptotic expression, one can use the asymptotic behaviour of the Bessel's function, in particular the for the first Hankel's function,

$$Z_m^{(3)}(x) = H_m^{(1)}(x) \underset{x\to\infty}{\sim} \sqrt{\frac{2}{\pi\,x}}\,e^{i\,(x-m\frac{\pi}{2}-\frac{\pi}{4})}. \tag{C.13}$$

Using the derivation recursion relation, true for the Bessel and Hankel's function,

$$2\,\partial_x Z_m^{(i)}(x) = Z_{m-1}^{(i)}(x) - Z_{m+1}^{(i)}(x), \tag{C.14}$$

with $Z_m^{(i)}$ as defined in sec. 2.2.1, one can combine the above expression using asymptotic analysis and find,

$$C_{m,l}^{\parallel} = +Z_m^{(3)}(k\,r)\,(\dot{Z}_l^{(3)}(k\,r))^*, \tag{C.15}$$

$$= \frac{1}{2}Z_m^{(3)}(k\,r)\,\left(Z_{l-1}^{(3)}(k\,r) - Z_{l+1}^{(3)}(k\,r)\right), \tag{C.16}$$

$$\underset{r\to\infty}{\sim} \frac{2}{\pi\,k\,r}\,(-i)^{(m-l+1)}. \tag{C.17}$$

Likewise for $C_{m,l}^{\perp}$.

Annexes

APPENDIX D

ANNEXE : UNSOLVED PROBLEMS

Contents

D.1 Convergence speed of Z-configuration mirror alignment 189

D.2 Mueller's matrices and wave plates 190

During one's PhD thesis work, it is current to encounter problems that go beyond the scope of the defined project. Due to limitation of time and skills, not all questions I met could be answered nor all problems I found could be solved. In the present annexe we report some enigma I found interesting to expose, and which could be an entertaining challenge to solve.

D.1 Convergence speed of Z-configuration mirror alignment

In order to align a laser with the optical elements present in our experimental setup, we used a well known alignment technique consisting of using two mirrors that are iteratively oriented, and two targets that define the path to be aligned with. There exists two configurations for this kind of alignment, see Fig. D.1, but the protocol remains the same.

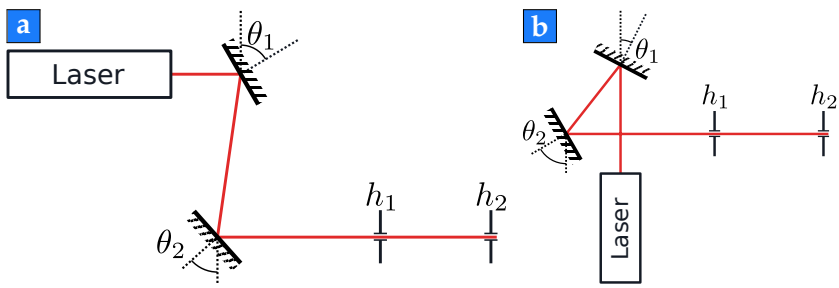

Figure D.1: (a) Z-fold configuration for laser beam alignment, while in (b) shows the 4-fold configuration.

The goal is to align the laser beam so that it passes through the wanted targets, h_1, h_2. To do so, we proceed by iteration. For each iteration, one must:

1. change the angle of the mirror the closest to the laser (from the laser path), in this case θ_1, so that the laser passes through the target the closest to the laser source, in this case, h_1,

2. change the angle of the mirror the farthest from the source, θ_2, so the laser passes through the farthest target, h_2.

We repeat this two steps stage several times, and the laser path after the mirrors will progressively be aligned with the two targets.

The problem is then: **What is the rate of convergence with the iteration number when aligning a laser beam using two mirrors in the Z-configuration ?** Is it the same rate of convergence than for the 4-fold configuration ?

D.2 Mueller's matrices and wave plates

When a laser beam passes through an optical system, it can undergo a transformation of its optical state. Especially concerning the polarisation state of the beam. In optical physics the optical state is often represented by a Stokes vector and the optical system is modelled by a Mueller matrix that acts on the optical sates of the radiation passing through, see Fig. D.2.

In the experiment presented in this thesis, we used fibred objectives to probe our nanowires, see chap. 3. However, the polarisation state in optical fibres are not always conserved due to birefringence that can occur along the fibre path. In order to better control the output polarisation state after the objectives, we proceeded by measuring the Mueller matrix of the system. We then wondered if we could compensate the polarisation changes using only wave plates.

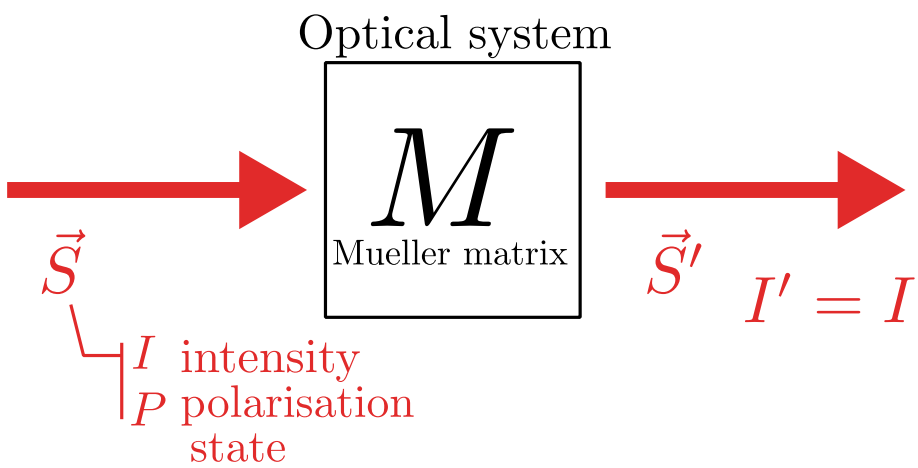

Figure D.2: Schematic representation of an optical system represented by a Mueller matrix, in the special case where there is no attenuation.

The problem is then: **Is it always possible to expand a unitary Mueller matrix into a product of HWP/QWP matrices ?** We consider only unitary Mueller matrices for energy conservation since, by definition, the wave plate matrix presentations do not act on the light intensity.

BIBLIOGRAPHY

[1] Benjamin P Abbott, Richard Abbott, TD Abbott, MR Abernathy, Fausto Acernese, Kendall Ackley, Carl Adams, Thomas Adams, Paolo Addesso, RX Adhikari, et al. Observation of gravitational waves from a binary black hole merger. *Physical review letters*, 116(6):061102, 2016. (page 2)

[2] Carlton M Caves. Quantum-mechanical radiation-pressure fluctuations in an interferometer. *Physical Review Letters*, 45(2):75, 1980. (page 2)

[3] V. B. Braginskii and A. B. Manukin. Measurement of weak forces in physics experiments. *Chicago*, 1977. (page 2)

[4] Shabir Barzanjeh, André Xuereb, Simon Gröblacher, Mauro Paternostro, Cindy A Regal, and Eva M Weig. Optomechanics for quantum technologies. *Nature Physics*, 18(1):15–24, 2022. (page 2)

[5] Aashish A Clerk, Michel H Devoret, Steven M Girvin, Florian Marquardt, and Robert J Schoelkopf. Introduction to quantum noise, measurement, and amplification. *Reviews of Modern Physics*, 82(2):1155, 2010. (page 2)

[6] Serge Reynaud. Introduction à la réduction du bruit quantique. In *Annales de Physique*, volume 15, pages 63–162. EDP Sciences, 1990. (page 2, 63)

[7] MD LaHaye, J Suh, PM Echternach, Keith C Schwab, and Michael L Roukes. Nanomechanical measurements of a superconducting qubit. *Nature*, 459(7249):960–964, 2009. (page 2)

[8] Daniel Rugar, Raffi Budakian, HJ Mamin, and BW Chui. Single spin detection by magnetic resonance force microscopy. *Nature*, 430(6997):329–332, 2004. (page 2)

[9] Joel Moser, J Güttinger, Alexander Eichler, María J Esplandiu, DE Liu, MI Dykman, and Adrian Bachtold. Ultrasensitive force detection with a nanotube mechanical resonator. *Nature nanotechnology*, 8(7):493–496, 2013. (page 2)

[10] Julien Chaste, A Eichler, J Moser, G Ceballos, R Rurali, and A Bachtold. A nanomechanical mass sensor with yoctogram resolution. *Nature nanotechnology*, 7(5):301–304, 2012. (page 2)

[11] Peter Weber, Johannes Güttinger, Adrien Noury, Jorge Vergara-Cruz, and Adrian Bachtold. Force sensitivity of multilayer graphene optomechanical devices. *Nature Communications*, 7(1): 12496, 2016. (page 2)

[12] Tongcang Li and Tongcang Li. Millikelvin cooling of an optically trapped microsphere in vacuum. *Fundamental Tests of Physics with Optically Trapped Microspheres*, pages 81–110, 2013. (page 2)

[13] Nikolai Kiesel, Florian Blaser, Uroš Delić, David Grass, Rainer Kaltenbaek, and Markus Aspelmeyer. Cavity cooling of an optically levitated submicron particle. *Proceedings of the National Academy of Sciences*, 110(35):14180–14185, 2013. (page 2)

[14] Jan Gieseler, Bradley Deutsch, Romain Quidant, and Lukas Novotny. Subkelvin parametric feedback cooling of a laser-trapped nanoparticle. *Physical review letters*, 109(10):103603, 2012. (page 2)

[15] Gambhir Ranjit, Mark Cunningham, Kirsten Casey, and Andrew A Geraci. Zeptonewton force sensing with nanospheres in an optical lattice. *Physical Review A*, 93(5):053801, 2016. (page 2)

[16] Ewold Verhagen, Samuel Deléglise, Stefan Weis, Albert Schliesser, and Tobias J Kippenberg. Quantum-coherent coupling of a mechanical oscillator to an optical cavity mode. *Nature*, 482(7383):63–67, 2012. (page 3)

[17] Jasper Chan, TP Mayer Alegre, Amir H Safavi-Naeini, Jeff T Hill, Alex Krause, Simon Gröblacher, Markus Aspelmeyer, and Oskar Painter. Laser cooling of a nanomechanical oscillator into its quantum ground state. *Nature*, 478(7367):89–92, 2011. (page 2, 3)

[18] D Cattiaux, I Golokolenov, S Kumar, M Sillanpää, L Mercier de Lépinay, RR Gazizulin, Xin Zhou, AD Armour, Olivier Bourgeois, A Fefferman, et al. A macroscopic object passively cooled into its quantum ground state of motion beyond single-mode cooling. *Nature communications*, 12(1):6182, 2021. (page 2, 3)

[19] E Collin. Mesoscopic quantum thermo-mechanics: a new frontier of experimental physics. *AVS Quantum Science*, 4(2):020501, 2022. (page 2)

[20] Olivier Arcizet, P-F Cohadon, Tristan Briant, Michel Pinard, and Antoine Heidmann. Radiation-pressure cooling and optomechanical instability of a micromirror. *Nature*, 444(7115):71–74, 2006. (page 2)

[21] Pierre-François Cohadon, Antoine Heidmann, and Michel Pinard. Cooling of a mirror by radiation pressure. *Physical Review Letters*, 83(16):3174, 1999. (page 2)

[22] John D Teufel, Tobias Donner, Dale Li, Jennifer W Harlow, MS Allman, Katarina Cicak, Adam J Sirois, Jed D Whittaker, Konrad W Lehnert, and Raymond W Simmonds. Sideband cooling of micromechanical motion to the quantum ground state. *Nature*, 475(7356):359–363, 2011. (page 2)

[23] Markus Aspelmeyer, Tobias J Kippenberg, and Florian Marquardt. Cavity optomechanics. *Reviews of Modern Physics*, 86 (4):1391, 2014. (page 2)

[24] Igor Pikovski, Michael R Vanner, Markus Aspelmeyer, MS Kim, and Časlav Brukner. Probing planck-scale physics with quantum optics. *Nature Physics*, 8(5):393–397, 2012. (page 2)

[25] AG Kuhn, M Bahriz, O Ducloux, Claude Chartier, O Le Traon, T Briant, P-F Cohadon, A Heidmann, Christine Michel, L Pinard, et al. A micropillar for cavity optomechanics. *Applied Physics Letters*, 99(12), 2011. (page 2)

[26] MD LaHaye, Olivier Buu, Benedetta Camarota, and KC Schwab. Approaching the quantum limit of a nanomechanical resonator. *Science*, 304(5667):74–77, 2004. (page 3)

[27] Benjamin Lassagne, Yury Tarakanov, Jari Kinaret, Daniel Garcia-Sanchez, and Adrian Bachtold. Coupling mechanics to charge transport in carbon nanotube mechanical resonators. *Science*, 325(5944):1107–1110, 2009. (page 3)

[28] S Etaki, M Poot, I Mahboob, K Onomitsu, H Yamaguchi, and HSJ Van der Zant. Motion detection of a micromechanical resonator embedded in a dc squid. *Nature Physics*, 4(10):785–788, 2008. (page 3)

[29] Xin Zhou, D Cattiaux, RR Gazizulin, A Luck, O Maillet, T Crozes, J-F Motte, Olivier Bourgeois, A Fefferman, and E Collin. On-chip thermometry for microwave optomechanics implemented in a nuclear demagnetization cryostat. *Physical Review Applied*, 12(4):044066, 2019. (page 3, 5)

[30] HJ Mamin and D Rugar. Sub-attonewton force detection at millikelvin temperatures. *Applied Physics Letters*, 79(20):3358–3360, 2001. (page 3)

[31] AC Bleszynski-Jayich, WE Shanks, and JGE Harris. Noise thermometry and electron thermometry of a sample-on-cantilever system below 1 kelvin. *Applied Physics Letters*, 92(1):013123, 2008. (page 3)

[32] Ye Tao, Alexander Eichler, Tim Holzherr, and Christian L Degen. Ultrasensitive mechanical detection of magnetic moment using a commercial disk drive write head. *Nature communications*, 7(1): 12714, 2016. (page 3)

[33] Martin Héritier, Alexander Eichler, Y Pan, Urs Grob, Ivan Shorubalko, Marc D Krass, Ye Tao, and Christian L Degen.

Nanoladder cantilevers made from diamond and silicon. *Nano letters*, 18(3):1814–1818, 2018. (page 3)

[34] Bai Song, Anthony Fiorino, Edgar Meyhofer, and Pramod Reddy. Near-field radiative thermal transport: From theory to experiment. *AIP advances*, 5(5):053503, 2015. (page 4, 5)

[35] Adib Tavakoli, Kunal Lulla, Thierry Crozes, Natalio Mingo, Eddy Collin, and Olivier Bourgeois. Heat conduction measurements in ballistic 1d phonon waveguides indicate breakdown of the thermal conductance quantization. *Nature communications*, 9 (1):4287, 2018. (page 4, 5)

[36] Anne Louchet-Chauvet, Pierre Verlot, Jean-Philippe Poizat, and Thierry Chanelière. Optomechanical backaction processes in a bulk rare-earth doped crystal. *arXiv preprint arXiv:2109.06577*, 2021. (page 4, 5)

[37] Cornelia Schwarz. *Optomechanical, vibrational and thermal properties of suspended graphene membranes*. PhD thesis, Université Grenoble Alpes, 2016. (page 4, 5, 77, 95, 161)

[38] Sebin Varghese, Jake Dudley Mehew, Alexander Block, David Saleta Reig, Paweł Woźniak, Roberta Farris, Zeila Zanolli, Pablo Ordejón, Matthieu J Verstraete, Niek F Van Hulst, et al. A pre-time-zero spatiotemporal microscopy technique for the ultrasensitive determination of the thermal diffusivity of thin films. *Review of Scientific Instruments*, 94(3), 2023. (page 4, 5)

[39] Olivier Bourgeois. *Thermique et thermodynamique des nanosystèmes*. Habilitation à diriger des recherches, Université Joseph-Fourier-Grenoble I, 2008. (page 3, 70, 138)

[40] Tristan Briant, Stephan Krenek, Andrea Cupertino, Ferhat Loubar, Rémy Braive, Lukas Weituschat, Daniel Ramos, Maria Jose Martin, Pablo A Postigo, Alberto Casas, et al. Photonic and optomechanical thermometry. *Optics*, 3(2):159–176, 2022. (page 5)

[41] Basile Pottier, Felipe Aguilar Sandoval, Mickaël Geitner, Francisco Esteban Melo, and Ludovic Bellon. Silicon cantilevers locally heated from 300 k up to the melting point: Temperature profile measurement from their resonances frequency shift. *Journal of Applied Physics*, 129(18):184503, 2021. (page 5, 132, 153, 161)

[42] Gregory S Doerk, Carlo Carraro, and Roya Maboudian. Single nanowire thermal conductivity measurements by raman thermography. *ACS nano*, 4(8):4908–4914, 2010. (page 5)

[43] Jungchul Lee, Thomas Beechem, Tanya L Wright, Brent A Nelson, Samuel Graham, and William P King. Electrical, thermal, and mechanical characterization of silicon microcantilever heaters. *Journal of Microelectromechanical Systems*, 15(6):1644–1655, 2006. (page 5)

[44] Mark R Abel, Tanya L Wright, William P King, and Samuel Graham. Thermal metrology of silicon microstructures using raman spectroscopy. *IEEE Transactions on components and packaging technologies*, 30(2):200–208, 2007. (page 5)

[45] Oliver Braun, Roman Furrer, Pascal Butti, Kishan Thodkar, Ivan Shorubalko, Ilaria Zardo, Michel Calame, and Mickael L Perrin. Spatially mapping thermal transport in graphene by an opto-thermal method. *npj 2D Materials and Applications*, 6(1):6, 2022. (page 5)

[46] Annu Majumdar. Scanning thermal microscopy. *Annual review of materials science*, 29(1):505–585, 1999. (page 5)

[47] Séverine Gomès, Ali Assy, and Pierre-Olivier Chapuis. Scanning thermal microscopy: A review. *physica status solidi (a)*, 212(3): 477–494, 2015. (page 5)

[48] Cornelia Schwarz, Benjamin Pigeau, Laure Mercier De Lépinay, Aurélien G Kuhn, Dipankar Kalita, Nedjma Bendiab, Laëtitia Marty, Vincent Bouchiat, and Olivier Arcizet. Deviation from the normal mode expansion in a coupled graphene-nanomechanical system. *Physical Review Applied*, 6(6):064021, 2016. (page 5)

[49] M De Rosa, F Marin, F Marino, O Arcizet, A Heidmann, and M Pinard. Experimental investigation of dynamic photothermal effect. *Classical and Quantum Gravity*, 23(8):S259, 2006. (page 5)

[50] DMA Leggett. Theory of elasticity. ld landau and em lifshitz, translated from russian by jb sykes and wh reid. pergamon press, london, 1959. 134 pp. illustrated. 40s. *The Aeronautical Journal*, 64(591):176–177, 1960. (page 5, 113)

[51] MH Kahrobaiyan, Mohammad Rahaeifard, SA Tajalli, and MT Ahmadian. A strain gradient functionally graded euler–bernoulli beam formulation. *International Journal of Engineering Science*, 52:65–76, 2012. (page 6)

[52] Singiresu S Rao. *Vibration of continuous systems*. John Wiley & Sons, 2019. (page 6)

[53] Silvan Schmid, Luis Guillermo Villanueva, and Michael Lee Roukes. *Fundamentals of nanomechanical resonators*, volume 49. Springer, 2016. (page 7)

[54] Laure Mercier de Lépinay. *Habillage mécanique d'un nanofil par un champ de force: de la mesure vectorielle ultrasensible aux systèmes quantiques hybrides*. PhD thesis, Université Grenoble Alpes, 2017. (page 9, 11, 12, 18, 19, 34, 35, 65, 166)

[55] Michel Pinard, Y Hadjar, and Antoine Heidmann. Effective mass in quantum effects of radiation pressure. *The European Physical Journal D-Atomic, Molecular, Optical and Plasma Physics*, 7(1):107–116, 1999. (page 9, 10, 13)

[56] Gregory M Harry, Helena Armandula, Eric Black, DRM Crooks, Gianpietro Cagnoli, Jim Hough, Peter Murray, Stuart Reid, Sheila Rowan, Peter Sneddon, et al. Thermal noise from optical coatings in gravitational wave detectors. *Applied optics*, 45 (7):1569–1574, 2006. (page 12)

[57] Herbert B Callen and Richard F Greene. On a theorem of irreversible thermodynamics. *Physical Review*, 86(5):702, 1952. (page 12, 13)

[58] Rep Kubo. The fluctuation-dissipation theorem. *Reports on progress in physics*, 29(1):255, 1966. (page 12, 13)

[59] VP Mitrofanov, VB Braginsky, and VI Panov. Systems with small dissipation, 1985. (page 12)

[60] Kevin Y Yasumura, Timothy D Stowe, Eugene M Chow, Timothy Pfafman, Thomas W Kenny, Barry C Stipe, and Daniel Rugar. Quality factors in micron-and submicron-thick cantilevers. *Journal of microelectromechanical systems*, 9(1):117–125, 2000. (page 12)

[61] Clarence Zener. Internal friction in solids. *Proceedings of the Physical Society (1926-1948)*, 52(1):152, 1940. (page 12)

[62] Pierdomenico Paolino and Ludovic Bellon. Frequency dependence of viscous and viscoelastic dissipation in coated microcantilevers from noise measurement. *Nanotechnology*, 20(40): 405705, 2009. (page 12)

[63] Ignacio Wilson-Rae. Intrinsic dissipation in nanomechanical resonators due to phonon tunneling. *Physical Review B*, 77(24): 245418, 2008. (page 12)

[64] Kyozi Kawasaki. Simple derivations of generalized linear and nonlinear langevin equations. *Journal of Physics A: Mathematical, Nuclear and General*, 6(9):1289, 1973. (page 12)

[65] Lev Davidovich Landau and Evgenii Mikhailovich Lifshitz. *Course of theoretical physics*. Elsevier, 2013. (page 13)

[66] Francesco Fogliano. *Ultrasensitive nanowire force sensors in extreme conditions: from dilution temperature to ultra-strong coupling in cavity nano-optomechanics*. PhD thesis, Université Grenoble Alpes (ComUE), 2019. (page 13, 18, 19, 20, 57, 69, 70, 87, 131, 167)

[67] Silicon carbide. Silicon carbide — Wikipedia, the free encyclopedia, 2022. URL https://en.wikipedia.org/wiki/Silicon_carbide. [Online; accessed 08-December-2022]. (page 14)

[68] John S Johnson, Kevin D Grobsky, and Don Bray. Rapid fabrication of lightweight silicon-carbide mirrors. In *Optomechanical Design and Engineering 2002*, volume 4771, pages 243–253. SPIE, 2002. (page 14)

[69] Joseph Robichaud, Deepak Sampath, Chris Wainer, Jay Schwartz, Craig Peton, Steve Mix, et al. Silicon carbide optics for

space and ground based astronomical telescopes. *Modern Technologies in Space-and Ground-based Telescopes and Instrumentation II*, 8450:31–38, 2012. (page 14)

[70] V Bougrov, ME Levinshtein, Sergey L Rumyantsev, and A Zubrilov. Properties of advanced semiconductor materials gan, aln, inn, bn, sic, sige. *Bougrov, ME Levinshtein, SL Rumyantsev, A. Zubrilov.- NY: Wiley*, pages 1–50, 2001. (page 14)

[71] Mikhael Bechelany, Arnaud Brioude, David Cornu, Gabriel Ferro, and Philippe Miele. A raman spectroscopy study of individual sic nanowires. *Advanced Functional Materials*, 17(6):939–943, 2007. (page 14)

[72] Peter TB Shaffer. Refractive index, dispersion, and birefringence of silicon carbide polytypes. *Applied optics*, 10(5):1034–1036, 1971. (page 15, 24)

[73] RefractiveIndex.info. Refractive index database, 2022. URL https://refractiveindex.info/?shelf=main&book=SiC&page=Shaffer. (page 15)

[74] Gustav Mie. Beiträge zur optik trüber medien, speziell kolloidaler metallösungen. *Annalen der physik*, 330(3):377–445, 1908. (page 15, 25)

[75] Arnaud Gloppe, Pierre Verlot, Eva Dupont-Ferrier, Alessandro Siria, Philippe Poncharal, Guillaume Bachelier, Pascal Vincent, and Olivier Arcizet. Bidimensional nano-optomechanics and topological backaction in a non-conservative radiation force field. *Nature nanotechnology*, 9(11):920–926, 2014. (page 18, 19, 77)

[76] Antoine Reigue, Francesco Fogliano, Philip Heringlake, Laure Mercier de Lépinay, Benjamin Besga, Jakob Reichel, Benjamin Pigeau, and Olivier Arcizet. Cavity nano-optomechanics with suspended subwavelength-sized nanowires. *Physical Review Applied*, 20(1):014025, 2023. (page 19, 20, 44, 86, 163, 167)

[77] Olivier Arcizet, Vincent Jacques, Alessandro Siria, Philippe Poncharal, Pascal Vincent, and Signe Seidelin. A single nitrogen-vacancy defect coupled to a nanomechanical oscillator. *Nature Physics*, 7(11):879–883, 2011. (page 20)

[78] Benjamin Pigeau, Sven Rohr, L Mercier de Lépinay, Arnaud Gloppe, Vincent Jacques, and Olivier Arcizet. Observation of a phononic mollow triplet in a multimode hybrid spin-nanomechanical system. *Nature Communications*, 6(1):8603, 2015. (page 20)

[79] Philip Heringlake. *Realtime imaging of force fields at the nanoscale with a 2D nano-mechanical probe*. PhD thesis, Université Grenoble Alpes, 2021. (page 20, 165, 166)

[80] Xiyuan Lu, Jonathan Y Lee, Philip X-L Feng, and Qiang Lin. Silicon carbide microdisk resonator. *Optics letters*, 38(8):1304–1306, 2013. (page 24, 126)

[81] Keith Powell, Amirhassan Shams-Ansari, Smit Desai, Mitchell Austin, Jiangdong Deng, Neil Sinclair, Marko Lončar, and Xiaoke Yi. High-q suspended optical resonators in 3c silicon carbide obtained by thermal annealing. *Optics express*, 28(4):4938–4949, 2020. (page 24, 126)

[82] Murat Onen and Marco Turchetti. Calculating the band structure of 3c-sic using sp3d5s*+delta model. *Journal of Theoretical and Applied Physics*, 13(1):1–6, 2019. (page 24)

[83] Krystian Karch, P Pavone, W Windl, O Schütt, and D Strauch. Ab initio calculation of structural and lattice-dynamical properties of silicon carbide. *Physical Review B*, 50(23):17054, 1994. (page 24)

[84] WJ Choyke. Optical properties of polytypes of sic: interband absorption, and luminescence of nitrogen-exciton complexes. In *Silicon Carbide–1968*, pages S141–S152. Elsevier, 1969. (page 25)

[85] Alfred Clebsch. Ueber die reflexion an einer kugelfläche. *Journal für die reine und angewandte Mathematik*, 1863(61):195–262, 1863. (page 25)

[86] Louis Lorenz. *Lysbevægelsen i og uden for en af plane Lysbølger belyst Kugle*. na, 1890. (page 25)

[87] Ludvig Lorenz. Sur la lumière réfléchie et réfractée par une sphère transparente. *Oeuvres Scientifiques*, pages 405–529, 1898. (page 25)

[88] Peter Josef William Debye. Der lichtdruck auf kugeln von beliebigem material. *Livres*, 2014. (page 25)

[89] Craig F Bohren and Donald R Huffman. *Absorption and scattering of light by small particles*. John Wiley & Sons, 2008. (page 25, 86, 107)

[90] Lukas Novotny and Bert Hecht. *Principles of nano-optics*. Cambridge university press, 2012. Chapter 14. (page 43, 124)

[91] Francesco Fogliano, Benjamin Besga, Antoine Reigue, Laure Mercier de Lépinay, Philip Heringlake, Clement Gouriou, Eric Eyraud, Wolfgang Wernsdorfer, Benjamin Pigeau, and Olivier Arcizet. Ultrasensitive nano-optomechanical force sensor operated at dilution temperatures. *Nature Communications*, 12(1): 4124, 2021. (page 44, 63, 66, 67, 68, 70, 86, 151, 155, 161)

[92] Jun Chen, Jack Ng, Zhifang Lin, and Che Ting Chan. Optical pulling force. *Nature photonics*, 5(9):531–534, 2011. (page 44, 163)

[93] PA Maia Neto and HM Nussenzveig. Theory of optical tweezers. *Europhysics Letters*, 50(5):702, 2000. (page 44)

[94] Alexander B Stilgoe, Timo A Nieminen, Gregor Knöner, Norman R Heckenberg, and Halina Rubinsztein-Dunlop. The effect of mie resonances on trapping in optical tweezers. *Optics express*, 16(19):15039–15051, 2008. (page 44)

[95] Martin de Wit, Gesa Welker, Kier Heeck, Frank M Buters, Hedwig J Eerkens, Gert Koning, Harmen van der Meer, Dirk Bouwmeester, and Tjerk H Oosterkamp. Vibration isolation with high thermal conductance for a cryogen-free dilution refrigerator. *Review of Scientific Instruments*, 90(1):015112, 2019. (page 48)

[96] ATAM De Waele. Basic operation of cryocoolers and related thermal machines. *Journal of Low Temperature Physics*, 164(5):179–236, 2011. (page 49)

[97] R Clark Jones. A new calculus for the treatment of optical systems v. a more general formulation, and description of another calculus. *JOSA*, 37(2):107–110, 1947. (page 58)

[98] R Clark Jones. A new calculus for the treatment of optical systems vi. experimental determination of the matrix. *JOSA*, 37(2): 110–112, 1947. (page 58)

[99] George Gabriel Stokes. Xxx. on the change of refrangibility of light. *Philosophical transactions of the Royal Society of London*, (142): 463–562, 1852. (page 58)

[100] Beth Schaefer, Edward Collett, Robert Smyth, Daniel Barrett, and Beth Fraher. Measuring the stokes polarization parameters. *American Journal of Physics*, 75(2):163–168, 2007. (page 58)

[101] William A Phillips. Two-level states in glasses. *Reports on Progress in Physics*, 50(12):1657, 1987. (page 67, 152)

[102] P W Anderson, Bertrand I Halperin, and C M Varma. Anomalous low-temperature thermal properties of glasses and spin glasses. *Philosophical Magazine*, 25(1):1–9, 1972. (page 67, 152)

[103] Supriyo Datta. *Electronic transport in mesoscopic systems*. Cambridge university press, 1997. (page 70, 73)

[104] Adib Tavakoli-Ghinani. *Phonon transport in the quantum regime*. PhD thesis, Université Grenoble Alpes, 2017. (page 70, 71, 138)

[105] A Zywietz, K Karch, and F Bechstedt. Influence of polytypism on thermal properties of silicon carbide. *Physical Review B*, 54 (3):1791, 1996. (page 71)

[106] D Morelli, J Heremans, C Beetz, WS Woo, G Harris, and C Taylor. Carrier concentration dependence of the thermal conductivity of silicon carbide. In *Institute of Physics Conference Series*, volume 137, pages 313–316. Bristol [England]; Boston: Adam Hilger, Ltd., c1985-, 1994. (page 71)

[107] Ju Li, Lisa Porter, and Sidney Yip. Atomistic modeling of finite-temperature properties of crystalline β-sic: Ii. thermal conductivity and effects of point defects. *Journal of Nuclear Materials*, 255(2-3):139–152, 1998. (page 71)

[108] Michael Shur, Sergey L Rumyantsev, et al. *SiC materials and devices*, volume 1. World Scientific, 2006. (page 71)

[109] Gary Lynn Harris. *Properties of silicon carbide*. Number 13. Iet, 1995. (page 72)

[110] HBG Casimir. Note on the conduction of heat in crystals. *Physica*, 5(6):495–500, 1938. (page 72)

[111] JS Heron, T Fournier, N Mingo, and O Bourgeois. Mesoscopic size effects on the thermal conductance of silicon nanowire. *Nano letters*, 9(5):1861–1865, 2009. (page 73)

[112] Robert Landauer. Spatial variation of currents and fields due to localized scatterers in metallic conduction. *IBM Journal of Research and Development*, 32(3):306–316, 1988. (page 73)

[113] Luis GC Rego and George Kirczenow. Quantized thermal conductance of dielectric quantum wires. *Physical Review Letters*, 81 (1):232, 1998. (page 73)

[114] Martin Maldovan. Transition between ballistic and diffusive heat transport regimes in silicon materials. *Applied Physics Letters*, 101(11):113110, 2012. (page 74)

[115] Ignacio Iglesias and Juan José Sáenz. Scattering forces in the focal volume of high numerical aperture microscope objectives. *Optics Communications*, 284(10-11):2430–2436, 2011. (page 87, 164)

[116] David Vernon Widder. *The heat equation*, volume 67. Academic Press, 1976. (page 91)

[117] Jean Baptiste Joseph baron Fourier. *Théorie analytique de la chaleur*. Chez Firmin Didot, père et fils, 1822. (page 92)

[118] Alex Fontana, Richard Pedurand, and Ludovic Bellon. Extended equipartition in a mechanical system subject to a heat flow: the case of localised dissipation. *Journal of Statistical Mechanics: Theory and Experiment*, 2020(7):073206, 2020. (page 95)

[119] Yu Levin. Internal thermal noise in the ligo test masses: A direct approach. *Physical Review D*, 57(2):659, 1998. (page 95)

[120] Petre Stoica, Randolph L Moses, et al. *Spectral analysis of signals*, volume 452. Pearson Prentice Hall Upper Saddle River, NJ, 2005. (page 96)

[121] Mickael Geitner, Felipe Aguilar Sandoval, Eric Bertin, and Ludovic Bellon. Low thermal fluctuations in a system heated out of equilibrium. *Physical Review E*, 95(3):032138, 2017. (page 97)

[122] Lev Davidovich Landau, John Stewart Bell, MJ Kearsley, LP Pitaevskii, EM Lifshitz, and JB Sykes. *Electrodynamics of continuous media*, volume 8. elsevier, 2013. (page 106)

[123] Lyle Patrick and WJ Choyke. Optical absorption in n-type cubic sic. *Physical Review*, 186(3):775, 1969. (page 107)

[124] George Gerald Stoney. The tension of metallic films deposited by electrolysis. *Proceedings of the Royal Society of London. Series A, Containing Papers of a Mathematical and Physical Character*, 82 (553):172–175, 1909. (page 118)

[125] Stephen Timoshenko. Analysis of bi-metal thermostats. *Josa*, 11 (3):233–255, 1925. (page 118)

[126] Daniel Ramos, Johann Mertens, Montserrat Calleja, and Javier Tamayo. Study of the origin of bending induced by bimetallic effect on microcantilever. *Sensors*, 7(9):1757–1765, 2007. (page 119)

[127] Chun-Hway Hsueh. Modeling of elastic deformation of multilayers due to residual stresses and external bending. *Journal of Applied physics*, 91(12):9652–9656, 2002. (page 119)

[128] Longfei Yang, Pu Li, Yuming Fang, and Xiao Ge. Thermoelastic damping in partially covered bilayer microbeam resonators with two-dimensional heat conduction. *Journal of Sound and Vibration*, 494:115863, 2021. (page 119)

[129] Sweden COMSOL AB, Stockholm. Comsol multiphysics® v. 5.0, 2022. URL http://www.comsol.com/. (page 119, 121)

[130] RE Newnham, V Sundar, R Yimnirun, J Su, and QM Zhang. Electrostriction: nonlinear electromechanical coupling in solid dielectrics. *The Journal of Physical Chemistry B*, 101(48):10141–10150, 1997. (page 127)

[131] Xuanhe Zhao and Zhigang Suo. Electrostriction in elastic dielectrics undergoing large deformation. *Journal of Applied Physics*, 104(12):123530, 2008. (page 127)

[132] Albert Schließer. *Cavity optomechanics and optical frequency comb generation with silica whispering-gallery-mode microresonators*. PhD thesis, lmu, 2009. (page 127)

[133] Matthew Newville, Till Stensitzki, Daniel B. Allen, and Antonino Ingargiola. LMFIT: Non-Linear Least-Square Minimization and Curve-Fitting for Python, September 2014. URL https://doi.org/10.5281/zenodo.11813. (page 135)

[134] Erode Gopal. *Specific heats at low temperatures*. Springer Science & Business Media, 2012. (page 138)

[135] Donald G Aronson. The porous medium equation. *Nonlinear diffusion problems*, pages 1–46, 1986. (page 144)

[136] Juan Luis Vázquez. *The porous medium equation: mathematical theory*. Oxford University Press on Demand, 2007. (page 144, 145)

[137] Juan Luis Vázquez. The mathematical theories of diffusion: Nonlinear and fractional diffusion. In *Nonlocal and nonlinear diffusions and interactions: new methods and directions*, pages 205–278. Springer, 2017. (page 144)

[138] Quirin P Unterreithmeier, Thomas Faust, and Jörg P Kotthaus. Damping of nanomechanical resonators. *Physical review letters*, 105(2):027205, 2010. (page 151)

[139] Andrew N Cleland. *Foundations of nanomechanics: from solid-state theory to device applications*. Springer Science & Business Media, 2013. (page 151)

[140] Olivier Maillet, Dylan Cattiaux, Xin Zhou, Rasul R Gazizulin, Olivier Bourgeois, Andrew D Fefferman, and Eddy Collin. Nanomechanical damping via electron-assisted relaxation of two-level systems. *arXiv preprint arXiv:2009.03804*, 2020. (page 151)

[141] Edwin T Jaynes and Frederick W Cummings. Comparison of quantum and semiclassical radiation theories with application to the beam maser. *Proceedings of the IEEE*, 51(1):89–109, 1963. (page 151)

[142] William A Phillips. Tunneling states in amorphous solids. *Journal of low temperature physics*, 7(3):351–360, 1972. (page 152)

[143] T Kamppinen, JT Mäkinen, and VB Eltsov. Dimensional control of tunneling two-level systems in nanoelectromechanical resonators. *Physical Review B*, 105(3):035409, 2022. (page 152)

[144] Christian Enss and Siegfried Hunklinger. *Low-temperature physics*. Springer Science & Business Media, 2005. (page 152)

[145] Felipe Aguilar Sandoval, Mickael Geitner, Éric Bertin, and Ludovic Bellon. Resonance frequency shift of strongly heated micro-cantilevers. *Journal of Applied Physics*, 117(23):234503, 2015. (page 152, 153)

[146] Tursunay Yibibulla, Yijun Jiang, Shiliang Wang, and Han Huang. Size-and temperature-dependent young's modulus of sic nanowires determined by a laser-doppler vibration measurement. *Applied Physics Letters*, 118(4):043103, 2021. (page 153)

[147] Euan J Boyd, Li Li, Robert Blue, and Deepak Uttamchandani. Measurement of the temperature coefficient of young's modulus of single crystal silicon and 3c silicon carbide below 273 k using micro-cantilevers. *Sensors and Actuators A: Physical*, 198:75–80, 2013. (page 153)

[148] Eric D Black. An introduction to pound–drever–hall laser frequency stabilization. *American journal of physics*, 69(1):79–87, 2001. (page 158)

[149] Gary C Bjorklund. Frequency-modulation spectroscopy: a new method for measuring weak absorptions and dispersions. *Optics letters*, 5(1):15–17, 1980. (page 158)

[150] A Michael Noll. *Principles of modern communications technology*. Artech House, 2001. (page 158)

[151] Curtis Roads. *The computer music tutorial*. MIT press, 1996. (page 158)

SUMMARIES

Résumé de la thèse en français

Le refroidissement des sondes de force nano-mécaniques vise à améliorer leur sensibilité grâce à la réduction concomitante de leur bruit thermique et de leur dissipation mécanique. Cependant, les mécanismes de conduction thermique deviennent moins efficaces à basse température, et il est de plus en plus difficile d'assurer mais aussi de vérifier leur bonne thermalisation.

Pour réaliser des mesures avec un minimum de perturbation, nous avons mis en œuvre des techniques de lecture opto-mécanique fonctionnant dans le régime de comptage de photons afin de sonder la dynamique des nanofils de carbure de silicium suspendus, dans un cryostat à dilution.

Afin de comprendre les effets de chauffage statique non triviaux (chauffage induit par la lumière et observées sur la température du bruit de mouvement du nanofil) nous avons mis en œuvre des mesures de réponse photo-thermique dynamique basées sur des techniques pompe-sondes utilisant deux lasers, qui peuvent être piézo-positionnés à différentes altitudes le long du nanofil. La modulation de l'intensité du laser de pompe génère des ondes thermiques qui se propagent le long du nanofil, tandis que leur impact sur les propriétés mécaniques, optiques et photo-thermiques du nanofil est étudié à l'aide du laser sonde. Nous examinons les différents mécanismes en jeu, notamment les changements de réflectivité des nanofils induits par la température, la réponse photo-thermique, l'élongation thermique, les changements de fréquence et les forces de pression de radiation.

Dans ce travail, nous présentons d'abord l'étude de l'interaction de nos nanofils avec la lumière, qui est fortement structurée par les résonances de Mie internes aux nanofils et qui gourvernent leurs réponses optiques et photo-thermiques. Nous avons conçu un dispositif expérimental permettant de mesurer la distribution ortho-radiale du champ lumineux diffusé par nos nanofils pour différentes couleurs dans le domaine du visible, grâce à un laser blanc supercontinuum suivi d'un filtre accordable. Nous ajustons les diagrammes mesurés aux prédictions théoriques basées sur la théorie de Mie, fournissant ainsi

une estimation quantitative des diamètres de nos nanofils de taille pourtant inférieure à la longueur d'onde. Des mesures complémentaires d'élongation induite ont également permis de mesurer directement la forte contribution de ces résonances de Mie dans l'efficacité d'absorption de la lumière.

Dans un deuxième temps, nous décrivons le dispositif expérimental conçu pour mesurer les propriétés mécaniques et thermiques des nanofils, partant de la température ambiante jusqu'à des températures cryogéniques. Nous présentons les différents mécanismes photothermiques en jeu dans le système et les techniques de caractérisation utilisées dans la configuration pompe-sonde. Ces mesures ont permis d'étudier la propagation des ondes de chaleur à l'intérieur des nanofils et de distinguer les différents régimes qui contribuent à leur réponse photo-thermique à des températures ambiantes et cryogéniques.

Ce travail ouvre la voie vers une meilleure caractérisation des propriétés photo-thermiques des nanofils, qu'il est important de contrôler afin d'optimiser la perturbation induite par la lumière dans des mesures de force ultrasensibles à basse température.

Résumé de la thèse en anglais

Cooling down nanomechanical force probes is a generic strategy to enhance their sensitivities through the concomitant reduction of their thermal noise and mechanical damping rates. However, heat conduction mechanisms become less efficient at low temperatures, which renders difficult to ensure and verify their proper thermalization.

To operate with minimally perturbing measurements, we implemented optomechanical readout techniques operating in the photon counting regime to probe the dynamics of suspended silicon carbide nanowires in a dilution refrigerator.

In order to understand the non-trivial light-induced static heating curves observed on the nanowire motional noise temperature, we implemented dynamical photo-thermal response measurements based on a pump-probe scheme making use of two lasers, which can be piezo-positioned at different positions along the nanowire. The intensity-modulated pump laser generates thermal waves which propagate along the nanowire, while their impact on the nanowire mechanical, optical and photothermal properties is investigated with the second probe laser. We discuss the different mechanisms at play which include in particular temperature induced nanowire reactivity changes, lateral photothermal response due to bilayer effects at their clamping point, thermal elongation, frequency shifts and radiation pressure forces.

In this work we first present the study of the interaction of our 3C-SiC nanowires with the incident light, where internal Mie resonances strongly govern and enhance their optical and photo-thermal properties. We designed an experimental setup to directly image the orthoradial distribution of the light field scattered by our nanowires in visible domain thanks to the use of a supercontinuum laser filtered by a tuneable filter. We adjust the measured diagrams to theoretical predictions based on the Mie scattering by cylindrical particles, thus providing a

quantitative estimation of the diameters of our subwavelength-sized nanowires. Separate measurements also allowed to directly measure the contribution of those internal Mie resonances in the structuration of the light absorption efficiency.

In a second time we describe the experimental setup designed for measuring the mechanical and thermal properties of nanowires from room to cryogenic temperatures. We present the different photo-thermal mechanism at play in the system and the characterisation techniques used in the pump-probe configuration. Measurements allowed to investigate the propagation of heat waves within the nanowires and discriminate between the different regimes dominating their photothermal response at room and cryogenic temperatures.

This work opens the road for a better characterisation of the nanowires' photo-thermal properties which are important to control before operating the nanowires as ultrasensitive vectoral force field sensors of faint forces at dilution temperatures.

Résumé de thèse vulgarisé pour le grand public en français

Afin de mesurer des forces infimes à l'échelle nanométrique, on peut utiliser des nanofils suspendus qui agissent comme un pendule. Ces nanofils, fabriqués en carbure de silicium ont une largeur de plusieurs centaines de nanomètres, mais une longueur mille fois supérieure. Ce rapport d'aspect très élevé permet d'être sensible aux forces à petite échelle, ainsi qu'avoir une résolution 2D des forces. Cependant, afin d'augmenter la sensibilité des nanofils à des températures froides, il est nécessaire de bien caractériser les propriétés thermiques de ces sondes mécaniques. C'est le travail de cette thèse. Nous avons mis en œuvre plusieurs techniques afin de mieux comprendre comment la chaleur se propage dans nos nanofils, ainsi que de comprendre comment elle modifie leurs propriétés mécaniques. Pour ce faire, nous avons également observé l'interaction subtile des nanofils avec la lumière visible qui les éclaire.

Nous présentons donc nos résultats et notre travail exploratoire concernant la façon dont les nanofils que nous utilisons pour la détection de force réagissent aux changements de température et au chauffage optique, partant de la température ambiante jusqu'à aux basses températures.

Résumé de thèse vulgarisé pour le grand public en anglais

To measure tiny forces at the nanoscale one may use suspended nanowires, that act like pendulum. Those nanowires, made of Silicon Carbide, are several hundreds of nanometres wide but thousand time more long. This high aspect ratio allows for sensitive detection of small scaled forces, as well as having a 2D resolution of the forces. However, in order to increase the sensitivity of the nanowires at cold

temperatures, one needs to characterise well the thermal properties of those mechanical probes. This is the work of this PhD. We implemented several techniques in order to better understand how heat propagates in our nanowires, as well as how it changes its mechanical properties. To do so, we also observed the subtle interaction of the nanowires with incoming visible light.

We thus present our results and exploratory work concerning how the nanowires we use for force sensing, react to temperature changes and to optical heating from room to low temperatures.